STUDY IN THE PREPARATION OF POLY(4-VINYLPYRIDINE) BASED NANOPARTICLES AND THEIR APPLICATON AS AN EFFECTIVE ADSORBENT FOR THE RECOVERY OF PALLADIUM FROM AQUEOUS SOLUTIONS

WEE KIN HO

(B. Eng. (Hons.), NUS)

A THESIS SUBMITTED

FOR THE DEGREE OF DOCTOR OF PHILOSOPHY

DEPARTMENT OF CHEMICAL & BIOMOLECULAR ENGINEERING

NATIONAL UNIVERSITY OF SINGAPORE

2011

Acknowledgements

I would like to sincerely express my greatest gratitude to my thesis supervisor, A/P Bai Renbi, for his unreserved support and guidance throughout the course of this research project. His guidance, constructive criticisms and insightful comments have helped me in getting my thesis in the present form. He has shown enormous patience during the course of my PhD study and he constantly gives me encouragements to think positively. More importantly, his passion in scientific research will be a great motivation for my future career undertakings.

In addition, I wish to express my heartfelt thanks to all my friends and colleagues in the research group, Dr. Liu Changkun, Dr. Han Wei, Dr. Li Nan, Dr. Liu Chunxiu, Ms. Han Hui, Ms. Liu Cui, Ms. Zhang Linzi, Mr. Zhu Xiaoying, Dr. Zhao Yong-Hong, Dr. He Yi, Dr. Miao Jing, and other supporting staff for administrative work and laboratory support of the Department of Chemical and Biomolecular Engineering as well as Division of Environmental Science and Engineering, especially Ms. Jamie Siew, Ms. Sylvia Wan, Ms. Susan Chia, Ms. Li Fengmei, Mr. Sukiantor bin Tokiman, Mr. Mohammed bin Sidek and others. I would also like to thank the FYP students who I have worked with along the journey, Ms. Wee Ming Hwee, Ms. Lee Chow Jin and Ms. Tu Wenting. Without their generosity and timely help, I would not be able to complete all the tasks and targets I set out.

Last but not least, I would like to dedicate this thesis to my parents and younger brother, who have been supporting me all the time. Without their love, encouragement and understanding, I would not have completed my doctoral study.

Table of Contents

Summary

Nanomaterials have been gaining increasing popularity in recent years, including in environmental applications. However, in spite of their great potentials and versatilities, practical engineered applications of nanomaterials in environmental protection or pollution control has encountered various problems, such as they could be easily lost in the process and their recovery and reuse impose technical challenge and economic burden. In this project, we attempted to address these problems by synthesizing polymeric nanoparticles through an improvised emulsion polymerization method so that the prepared nanoparticles would be economically viable for up-scale, and simultaneous recovery and reuse. Initially, the major effort was focused on the development of the polymerization systems that led to the preparation of highly mono-sized nanoparticles as an adsorbent. Subsequently, the adsorptive separation behavior performance of the prepared nanoparticles for a precious metal, palladium(II), was investigated through batch adsorption and coupled adsorption-filtration processes.

Poly(4-vinylpyridine) or P4VP nanoparticles of a highly uniform size were synthesized in a wide size range (70 – 650 nm) and they were studied for efficient recovery of palladium in aqueous solutions. The P4VP nanoparticles were prepared through a surfactant-free emulsion polymerization (SFEP) method from 4-vinylpyridine (4VP) as the monomer, with divinylbenzene (DVB) as the crosslinker, and 2.2'-azobis(2-aminopropane) dihydrochloride (V50) as the free-radical polymerization initiator. By changing the mode and rate at which the monomer was added, as well as by adding additional hydrophilic co-monomers such as poly(ethylene glycol) methyl ether methacrylate (PEGMA) and (2-(methacryloyloxy) ethyl) trimethylammonium chloride (MATMAC), highly monodispersed P4VP

nanoparticles in a wide size range were obtained. It was found that the P4VP nanoparticles prepared in this study could serve as a highly efficient nanoadsorbent for the recovery and concentration of palladium (II) from metal-laden acidic solutions. Due to the well-swollen nature, the interior functional groups within the structure of the prepared P4VP nanoparticles were accessible to ions, ionic complexes and molecules from the surrounding solution, which contributed to enhanced adsorption capacity. Both adsorption isotherm and kinetic studies demonstrated that the lightly-crosslinked P4VP nanoparticles could rapidly sequestrate palladium with a high uptake capacity up to 6 mmole-Pd(II)/g-nanoparticles. The prepared P4VP nanoparticles displayed good binding ability towards Pd(II) even at low Pd(II) concentrations. To improve the potential for repeated use of the prepared nanoparticles, DVB was substituted with long-chain crosslinkers – poly(ethylene glycol) dimethacrylate (PEGDM) with molecular weights of 550 and 750, and the resulting P4VP nanoparticles were found to be able to swell and deswell reversibly without flocculation, while the structural integrity remained intact in the cyclic pH-swing challenge tests, as confirmed by electron microscopy. The lightly-crosslinked, P4VP nanoparticles prepared in this study showed much better palladium adsorption performance, as compared to other adsorbents or bulk analogues of P4VP, such as crosslinked P4VP resins (Kononova *et al.*, *Hydrometallurgy* 48 (1998), 65-72) or P4VP-derivatived biopolymers (Baba and Hirakawa, *Chem. Lett.* (1992), 1905-1908). Experiments conducted for concentrating and eluting palladium from the P4VP nanoparticles showed the effectiveness for their use as a nanoadsorbent that can find great potentials in other environmental applications as well, such as for heavy metal removal from aqueous solutions.

The adsorptive removal of palladium (II) in aqueous solutions with P4VP nanoparticles as adsorbent was further investigated in more details, such as spectroscopic study, adsorption isotherm and kinetic modeling. Both FT-IR and XPS analyses revealed that strong chemical binding took place during the Pd(II) adsorption process on P4VP nanoparticles, which may involve coordinative binding and ion-exchange mechanisms. The adsorption process appeared to be coupled with the deswelling of the swollen P4VP nanoparticles. The monitoring of particle size-evolution of the swollen P4VP nanoparticles using dynamic light scattering (DLS) analysis showed that the deswelling of swollen P4VP nanoparticles in the "static adsorption" test typically finished within about 10 seconds upon contact with the Pd(II) solutions, but not with other metal solutions, e.g. Cu(II) and Ca(II). The timescale of the deswelling process ($\tau_{deswelling}$) was much smaller than the time duration in which Pd(II) adsorption took place, suggesting that the Pd(II) adsorption was diffusion-controlled ($De \ll 1$). The adsorption kinetics was modeled with 2-*p* model (D_{eff}, k_f) which accounts for simultaneous occurrence of pore-diffusion (within pore fluid) and film-mass transfer and 1-*p* model (D_{eff}) that assumes negligible film-transfer resistance, with the aid of orthogonal collocation on finite element (OCFE) method. It was shown that the Pd(II) adsorption coupled with the deswelling of the P4VP nanoparticles obeys the Fickian's law of diffusion, by substituting the values at equilibrium/deswollen state for the physical parameters (R, ε). The adsorption kinetics was systematically studied by varying various experimental parameters, for instance, initial Pd(II) concentration, solution pH and P4VP nanoparticle size, and fitted using the 2-*p* model. The values of film mass transfer coefficient obtained in this work are in good agreement with that reported by Nagata (1975), whereas the observed retardation effect ($D_{eff}/D_0 < 1$) could be correlated to the physical parameters of the swollen P4VP

network using Amsden's model (2001). The 2-*p* model and the numerical solution method developed in this work were found to be useful for predicting Pd(II) adsorption performance and uptake rate of the P4VP nanoparticles.

To better understand the effects of particle sizes and concentrations on membrane fouling by the P4VP nanoparticles, the separation performance and filtration of monodispersed nanoparticle suspensions were studied under unstirred, dead-end filtration mode. Several analysis tools were used to analyze the fouling mechanisms. Two batches of chemically identical P4VP nanoparticles with two distinct sizes (60 nm and 250 nm) were chosen. Asymmetric-type mixed cellulose ester membrane with a pore size rating at 0.1 μm (100 nm), that lies between the two nanoparticle sizes was used. Different fouling mechanisms were discussed. These studies provided a more fundamental understanding as to how the ratio of particle size of nanoparticles to membrane pore size would affect the efficiency and production throughput of the membrane-based separation process for nanoparticle recovery. The identification of dominant fouling mechanism as well as the transition in internal fouling to external fouling as a function of nanoparticle concentration and physical dimension of the nanoparticles present in the suspensions was discussed in details, which provided useful information that can facilitate the design and process optimization to minimize nanoparticles fouling in the membrane separation processes.

List of Tables

List of Figures

Nomenclature

Abbreviations:

Adj. R^2	Adjusted squared correlation coefficient
DF	Degree of freedom
DI	Deionized
DLS	Dynamic light scattering
DVB	Divinylbenzene
EDL	Electric double layer
EGDMA	Ethylene glycol dimethacrylate
FESEM	Field-emission scanning electron microscopy
FTIR	Fourier-transformed infra-red spectroscopy
ICP-OES	Inductively coupled plasma optical-emission spectrometer
IPD	Intraparticle diffusion
LLS	Laser light scattering
MATMAC	(2-(Methacryloyloxy) ethyl) trimethylammonium chloride
MCE	Mixed cellulose ester
MF	Microfiltration
OCFE	Orthogonal collocation on finite elements
Pd(II)	Palladium (II)
P4VP	Poly(4-vinylpyridine)
P4VP060	Poly(4-vinylpyridine) nanoparticles with diameter of 60 nm
P4VP250	Poly(4-vinylpyridine) nanoparticles with diameter of 250 nm
PEGDM	Poly(ethylene glycol) dimethacrylate
PEGMA	Poly(ethylene glycol) methyl ether methacrylate

RMSE	Root-mean square of errors
SE	Standard errors
SEM	Scanning electron microscopy
SS	Sum of squared errors
TEM	Transmission electron microscopy
UF	Ultrafiltration
UV/VIS	Ultraviolet/visible light
V50	2.2’-Azobis(2-aminopropane) dihydrochloride
XPS	X-ray photoelectron spectroscopy

List of Symbols

Langmuir Isotherm Model

q_{eqm}	Adsorption capacity for solute at equilibrium (mmole/g)
q_{max}	Maximum adsorption capacity (mmole/g)
b	Affinity constant (L/mmole)
c_{eqm}	Solute concentration at equilibrium (mmole/L)

Combined Diffusion Models (1-*p*, 2-*p*)

C_0	Initial concentration (mmole/L)
$S_{swollen}$	Swelling ratio at swollen state (-)
$\varepsilon_{swollen}$	Porosity at swollen state (-)
S_{eqm}	Equilibrium swelling ratio (-)
ε_{eqm}	Equilibrium porosity (-)
D_{eff}	Effective diffusivity (cm^2/s)
k_f	Mass transfer coefficient through external film (cm/s)
Bi	Biot number (-)

Membrane Filtration Analysis

J	Filtrate flux (m^3/m^2-s)
ΔP	Transmembrane pressure (kPa)
R_{total}	Total resistance (m^{-1})
R_m	Resistance of clean membrane (m^{-1})
t	Filtration time (s)

CHAPTER 1

INTRODUCTION AND RESEARCH OBJECTIVES

1.1 Overview

With strategic importance and great economic interest, platinum group elements (PGMs) such as palladium (Pd) have attracted significant attention for their extraction and recovery, and the related analytical quantification and environmental monitoring, as well as separation techniques (Rao and Reddi, 2000; Bernardis *et al.*, 2005). For example, palladium possesses good catalytic activity and hence becomes one of the most expensive metals. Because of its limited crustal abundance, the huge demands for palladium in various industries such as for automobile emission control, electric and electronic devices, metal alloys as well as pharmaceutical manufacturing have continually stimulated the further research and development in novel separation media (solid phase adsorbents, extractants) and advanced separation technologies for the effective and efficient recycling and reuse of palladium. As a major application in chemical synthesis or manufacturing where palladium is commonly used as a catalyst, leaching of palladium particles from the heterogeneous supports such as silica, carbon etc., or palladium nanoparticles in the homogeneous process could occur, which results in the loss of the active catalyst and causes metal impurities in the product stream or metal pollution in the effluent (Yu *et al.*, 2004; Ji *et al.*, 2005; Yu *et al.*, 2005). The risk associated with the direct leaching of palladium which is non-biodegradable into the aqueous environment is also a concern, especially in view of the recent interest in deploying the possibility of using palladium-catalyzed hydrodechlorination treatment for groundwater or wastewater remediation (McNab *et al.*, 2000; Mackenzie *et al.*, 2006).

Separation plays a vital role in the recovery or removal of palladium that leaches out or exits in the process stream or effluent. Conventional separation technologies that

may be used to recover palladium as well as other PGMs, such as chemical precipitation and solvent extraction etc., often involve multiple-stage operations and can require huge amounts of input in chemicals (precipitants, organic extractants etc.). These technologies are gradually replaced with more efficient and environmentally benign alternatives, for instance, adsorption or ion-exchange chromatography, because the amount of palladium or other PGMs to be recovered or removed in solutions are usually at relatively low concentrations (Bernardis *et al.*, 2005). For example, technological advancements have been made in recent decades for various novel adsorbents to overcome the shortcomings of the conventional separation technologies. Some of those adsorbents (or resins) synthesized showed high sequestration capacities. However, the existing problems in those adsorbents may include that the separation process often took long equilibrium time to achieve completion (Ruiz *et al.*, 2002), or the adsorbents had low binding affinity towards palladium ions, Pd(II) (Kumaresan *et al.*, 2008). Therefore, new adsorptive nanomaterials, for instance, magnetite nanoparticles (Uheida *et al.*, 2006a; Uheida *et al.*, 2006b; Rossi *et al.*, 2007; Vatta *et al.*, 2007), titanate nanotubes (Kochkar *et al.*, 2009) and mesoporous nanosilica (Kang *et al.*, 2004) etc., have been prepared and investigated for their efficacy in decontamination of palladium-laden waste solution or recovery of palladium. Because of the high specific surface areas of these nanomaterials, short contact times (< 30 minutes) for the completion of the adsorption process were typically observed (Uheida *et al.*, 2006a; Uheida *et al.*, 2006b). Nevertheless, in spite of the advantages of rapid adsorption uptake kinetics, those prepared nanomaterials had found little direct practical applications due to their low adsorption uptake capacities (≤ 0.5 mmole/g). As a result, further post-synthesis surface-functionalization is often required to improve either the selectivity or the extraction efficiency of these nanomaterials.

These post-treatments however were often found to make the subsequent elution of the adsorbed Pd(II) or the regeneration of those prepared adsorbents difficult (Uheida *et al.*, 2006b; Vatta *et al.*, 2007).

Other types of nanomaterials that can display high binding capacity towards metal ions, such as poly(amidoamine) (PAMAM) dendrimers, have also been explored (Diallo *et al.*, 1999). Because of the abundance of chargeable amine groups residing within the dendrimer, the PAMAM dendrimers have showed a copper binding capacity of up to 308 to 451 mg-Cu/g, which is significantly higher than conventional ion-exchange or chelating resins reported (Diallo *et al.*, 2003). To recover these nanomaterials from process stream after their use, Diallo *et al.* (2005) investigated the "dendrimer-enhanced ultrafiltration" (DEUF), i.e. the coupling of ultrafiltration process with the separation of dendrimer-Cu(II) complexes. It was reported that economic filtration for the separation of these dendrimer was possible because these nanoscale macromolecules are highly monodispersed in their size distribution, and hence the copper-laden dendrimers could be fully rejected with a properly selected membrane (in terms of material and molecular weight cut-off combination). Nonetheless, the commercially available dendrimers are expensive, e.g. one gram of G6 PAMAM dendrimers costs approximately USD 880 (Dendritech, 2009) and therefore the applications of the dendrimer-based technology have been scarce in environmental engineering. Their high material cost also excluded our consideration in this study in using them to prepare nanoadsorbent for palladium recovery.

For nanotechnology to become affordable and economically feasible in environmental applications, cost-effective preparation of the nanoparticles or related nanomaterials as

the effective adsorbents should be made available. Polymeric nanoparticles, also sometimes known as nanogel/microgel particles, have shown such prospects. Polymeric nanoparticles, in general, are characterized as spherical, three-dimensional covalently crosslinked polymer network in the colloidal size range (50 nm – 5 μm). They can swell or shrink, depending on the surrounding solvent conditions. These particles have widely been studied in recent years because of their relatively low preparation cost and fast response in volume transition triggered by environmental change. A number of applications of various types of polymeric nanoparticles have been developed, such as in controlled delivery of drugs and proteins (Eichenbaum *et al.*, 1999; Serpe *et al.*, 2005), for nanoreactors (Antonietti *et al.*, 1997), as microlenses assembly for detection of protein (Kim *et al.*, 2005), for heavy metal scavenging in water purification (Snowden *et al.*, 1993; Morris *et al.*, 1997) and for enhanced oil-recovery from oil fields (Dawson and Le, 1996), etc. These nanoparticles are commonly synthesized via the emulsion- or dispersion-based free-radical polymerization (FRP) method, and the products are usually in the form of colloidal dispersions. They can also be synthesized to possess specific stimuli-responsive properties (e.g., pH-sensitive or thermal-responsive etc.) such that they would swell or shrink corresponding to changes in the environmental conditions surrounding them (e.g. change in pH, ionic strength or temperature) (Pelton, 2000). Polymeric nanoparticles are therefore promising substitutes for dendrimers to obtain high-capacity nanoadsorbents. While many types of nanoparticles have been prepared for various applications in other fields, there has only been a few reports on the use of polymeric nanoparticles for environmental applications so far, for example, lead adsorption with poly(acrylic acid)-based nanoparticles (Snowden *et al.*, 1993; Morris *et al.*, 1997).

Pyridine is a six-membered aromatic nitrogen heterocyclic molecule that has relatively low energy π^* orbitals that can act as good acceptors of metal d-orbital electron density in the metal-ligand backbonding (Steel, 1990), leading to the formation of coordinative bondings, through donating the electron lone pair from pyridine to the metal ion coordinated. In general, soft acids like palladium, as categorized by the hard and soft acid and bases theory (HSAB) (Pearson, 1963), would interact strongly with the functional groups containing sulfur or nitrogen atom. In the literature, poly(4-vinylpyridine) (P4VP), a pyridine containing polymer, has been used as an adsorbent and investigated for the adsorption of heavy metal ions such as cadmium Cd (II), copper Cu (II), mercury Hg (II), nickel Ni (II) (Chanda and Rempel, 1993; Talanova *et al.*, 1999), or precious metal ions including silver Ag (I), gold (III), palladium (II) and platinum (II) (Talanova et *al.*, 2001; Kumaresan *et al.*, 2008). Many of these studies have shown good adsorption performance of P4VP. Therefore, it is of great research and practical interest in this research project to develop P4VP-based nanoparticles as adsorbents and examine their separation applications, especially for palladium recovery or removal from aqueous solutions.

Through literature study and preliminary experimental investigation, we found that many of the current state-of-art emulsion- or dispersion-based polymerization techniques are either lacking of synthetic flexibility or are uneconomic for preparing P4VP-based nanoparticles desired in this development. For example, the commonplace practices have been using multiple-step organic syntheses (Ma and Fukutomi, 1991) and many of them used precursor chemicals that are either proprietary (Takahashi *et al.*, 1997) or hazardous (Dupin *et al.*, 2006). In addition, as demonstrated by some researchers (Davis *et al.*, 1995; Pathak *et al.*, 2000),

monodispersed P4VP nanoparticles may be prepared from a surfactant-free emulsion polymerization (SFEP) method (Ferguson *et al.*, 2002), but the approaches were however not able to manipulate the final particle size while preserving the size monodispersity. Hence, the SFEP method needs to be improved to allow for preparing monodispersed P4VP-based nanoparticles in a wide size range in this study.

To enable the prepared P4VP nanoparticles to be readily reused as an adsorbent, an effective separation technology should be examined to recover the nanoparticles from the process streams after use. One such potential technology is considered to be the membrane separation technology (Zeman and Zydney, 1996; Cheryan, 1998). Many types of filtration membranes have been investigated for the separation of nanoscale colloids or nanoparticles from solutions. For instance, recycling of dendrimers for chemical catalysis or copper ion adsorption has been successfully conducted with either nanofiltration (Jesüs and Flores, 2008) or ultrafiltration membranes (Diallo *et al.*, 2005). However, the major problem for this application is membrane fouling. The major fouling mechanisms may include concentration polarization, pore-blocking and cake formation ("caking"). Especially, pore-blocking may cause irreversible membrane fouling that can result in the permanent loss of the membrane's permeability. Ideally, these fouling phenomena should be minimized as the purification, fractionation and recovery of industrially-important nanoparticles which function as catalysts or adsorbents, would require the separation process to not only fully retain them but also preserve their original physical properties (dimensions, shapes and crystallinity) and functionality, after multiple cyclic processes.

For effective and economic filtration by membrane-based separation technology, the prepared P4VP-based nanoparticles need to be narrowly-distributed in their sizes. Thus, with a membrane of pore size that is smaller than the diameter of the P4VP nanoparticles, the problem of internal fouling of the used membrane, e.g. clogging/blocking of pores caused by the nanoparticles entering the pores, can be limited or even completely eliminated. Cross-flow filtration mode may also be used to reduce the external fouling phenomenon such as concentration polarization and cake formation. Hence, one of the most important aspects in this study is to obtain highly uniform or monodispersed P4VP nanoparticles. With these particles, a membrane of proper pore size can be selected for their separation and recovery. The relative size of the nanoparticles to the selected membrane pores will be examined to understand its impact on the separation/rejection efficiency of the membrane filtration process as well as the extent of membrane fouling.

The prepared nanoparticles, to function as nanoadsorbents in aqueous solutions, should be colloidally stable and mechanically robust so that their size and shape, as well as specific surface area of the nanoparticles could be preserved after use. These particles should be porous or highly-swellable so that the binding sites or reactive moieties within the particles are also accessible (to solute ions or molecules from the surrounding solutions), thereby giving rise to high adsorption capacities and fast kinetics. To fully separate them from treated effluents or waste solutions for regeneration and reuse, nanoparticles of good monodispersity in terms of size and shape are extremely desired, so that membrane separation technology can be readily applied to separate and recover the nanoparticles.

1.2 Objectives and Scope of Present Study

The overall objective of this doctoral research project is to prepare novel polymeric nanoparticles, particularly P4VP-based nanoparticles, with desired material properties that enable them to be used as effective adsorbents for the removal of metal ion, and especially for the separation and recovery of palladium ions from aqueous solutions. Methods will be developed to prepare the desired P4VP nanoparticles. The physical properties of the P4VP-based nanoparticles will be examined and their adsorption performance will be investigated. Further improvement in the properties and performances of the prepared P4VP nanoparticles will be attempted. The separation and recovery of the nanoparticles will be performed with a membrane filtration system and their fouling and permeation characteristics of the membrane system will be examined. The specific scope of the research project may be listed as follow:

1. To prepare highly monodispersed P4VP or P4VP-based nanoparticles of different sizes in a wide size range.
2. To examine the adsorption performance for palladium in acidic solutions with the prepared nanoparticles.
3. To improve the property and performance of the prepared P4VP nanoparticles for their stability under harsh process conditions (e.g. high salinity, cyclic changes in solution pH), and for their reusability in multiple cycles of the adsorption-regeneration process.
4. To investigate the separation and recovery of the nanoparticles by a membrane filtration system for its feasibility and effectiveness.

1.3 Organization of the Thesis

The contents of this thesis revolve around and branch out from the central theme of the doctoral research project, i.e. the preparation and use of P4VP-based nanoadsorbents for palladium adsorption, as well as their separation and recovery with a membrane filtration system. Based on the work done this doctoral research project, the results are presented in the following order:

- Chapter 1 gives a brief overview on the area of interest for this research project, including the backgrounds, the development needs, and the research objectives.
- Chapter 2 reviews the implication of nanotechnology and various adsorptive nanomaterials emerged in recent years for metal ion adsorption/removal, and the methods for preparing P4VP-based nanoparticles are surveyed. The major types of separation technologies that are used for nanoparticle separation are briefly reviewed also.
- Chapter 3 describes the preparation of monodispersed P4VP and P4VP-based nanoparticles. The mechanical robustness and stability of the prepared nanoparticles are examined to assess their potential for applications even under harsh conditions.
- Chapter 4 evaluates the efficacy of the nanoparticles as an adsorbent for palladium. The adsorption capacity, isotherms, and kinetics are investigated. The potential for practical application through cyclic adsorption-desorption-regeneration processes is examined. The possible adsorption mechanisms involved are also discussed.
- Chapter 5 describes the modeling work done characterizing the mass transfer phenomenon involved in the adsorption process and the impacts of various process parameters on the palladium adsorption kinetics. The contributions of

pore diffusion and external film diffusion to the observed rapid sequestration kinetics are discussed.

- Chapter 6 describes the separation performance using a membrane system for the recovery of the P4VP nanoparticles. Specifically, the effects of relative particle size to membrane pore size on the separation/rejection performance and the fouling phenomenon of the membrane are discussed.
- Chapter 7 summarizes the results and findings obtained from this doctoral research project. Some recommended works of potential values that could improve the developed preparation method for producing P4VP nanoparticles, and enhance the understanding on the membrane fouling phenomenon associated with nanoparticle separation are described.
- Finally, additional data for Chapter 3 that may be of help to the readers, and the formulation of the orthogonal collocation on finite element formulation that is used to obtain the numerical solutions for the diffusion models discussed in Chapter 5 are included in the Appendix A and Appendix B respectively.

CHAPTER 2

LITERATURE REVIEW

2.1 Nanotechnology and Its Implications

Recent advances in nanoscale science and engineering has provided the ability to create objects measuring between 1 to 100 nm in at least one dimension. In the last few decades, many novel material properties have emerged as material dimension or particle size decreases, and enters the nanoscale regime, mainly due to the quantum effects (Klabunde et *al.*, 1996). For example, highly reactive calcium oxide nanoparticles were synthesized and proven to be more effective than its bulk analogue in destructive adsorption of chlorinated hydrocarbons (Koper *et al.*, 1993). In practice, almost all of the environmental remediation or water treatment techniques related to heavy metal removal from aqueous solutions have relied heavily on adsorption process at solid-liquid interfaces. Hence, it is logically to explore nanotechnology for new generations of adsorbents, because nanoparticles exhibit high specific surface area, as compared to their bulk or larger-scale analogues, which could contribute to more surface reactive sites for adsorption or reaction to take place.

One of the key characteristics of an ideal environmental remedial agent, for instance an adsorbent, should possess high capacity, fast sequestration kinetic as well as good selectivity. Clearly, higher treatment throughput could be achieved if the remedial agent reduces the concentration of the target pollutant within a short time scale. The selectivity can be especially vital if the remediation process is to remove a specific target pollutant at trace level, such as arsenic, in the presence of various competing compounds or species, e.g. phosphate or perchlorate, that are at much higher concentrations. In addition, remedial agent with high remedial capacity would reduce the dosage and thus lower the material cost. All of these requirements have led many environmental scientists and engineers to look beyond the traditional materials and

explore new treatment methodologies that may incorporate nanoparticles of high reactivity, selectivity and capacity as adsorbents. For example, with those new developments, more small-scale and household-based heavy metal removal systems may be installed, at a fraction of current cost, especially in areas that lack central treatment infrastructures, for instance in Bangladesh where ground water pollution by geogenic arsenic are common (Smedley and Kinnburgh, 2002). So far, inorganic and polymeric materials engineered by nanotechnology with promising metal ion removal capabilities have attracted immense research interests. The following will give a brief overview on the various types of nanoparticles for adsorptive removal of metal ions from aqueous solutions.

2.2 Review of Nanoparticles as Adsorbents for Metal Ion Removal

To remove metal ions from aqueous solution as effective and efficient as possible, the remedial agents, i.e. the adsorbents, should optimally possess high density of binding site or chemical functional groups (e.g. –COOH, –NH, –SH etc.) which have selective affinity towards the metal ions, located at the solid-liquid interface (Alexandratos and Crick, 1996; Zagorodni, 2007). In addition, these binding sites should be accessible for metal ion binding or adsorption to take place, which can be achieved by making the adsorbents as porous as possible (i.e. high specific surface area or pore volume), while the pore sizes are big enough for the metal ions to diffuse and travel to the interior binding sites located on the pore surface (Guyot, 1988; LeVan and Carta, 2008). Alternatively, the adsorbents can be engineered and synthesized to have nanoscale dimensions, which would enhance their performance for metal ion removal, via either higher surface density of binding sites, or reduced mass transfer resistance

(diffusion through the adsorbent particles). In the following sections, various types of novel nanoparticles or adsorbents with nanoscale dimensions are reviewed, and their pros and cons are discussed.

2.2.1 Iron-based Nanoparticles

2.2.1.1 Introduction

Over the past few decades, extensive research efforts have led to the discovery of many novel metal and metal oxide nanoparticles which display many unprecedented properties (Rotello, 2004). For instance, Haruta reported that gold nanoparticles of ~10 nm could catalyze carbon monoxide oxidation at low temperature, whereas gold in bulk is not catalytically active at all (Haruta, 1997). However, current efforts in application of metal and metal oxide nanoparticles for water/wastewater decontamination such as metal ion removal have focused almost solely on iron-based nanoparticles or their subcolloidal particles. Iron-based nanoparticles are inexpensive, easily scalable and highly reactive towards a wide array of organic and inorganic pollutants (Zhang, 2003). Being the most widely utilized nanoscale remedial agents, iron-based nanoparticles have been extensively studied in their synthesis methods and structure-property relationships. The reliable performance and wide acceptance has rendered iron-based nanoparticles to be the model metallic nanoparticles for environmental applications, including over 20 actual field remediation projects using nanoscale zero-valent iron (nZVI) (Li *et al.*, 2006).

Generally, iron rapidly oxidizes in air or corrodes in water. This high reactivity of iron with respect to water and oxygen which are ubiquitous in either laboratory or actual field-remediation condition, gives rise to passivation of the iron nanoparticles as the

passivation layer serves as a protective layer to the nanoparticles in aqueous environment. Hence the iron nanoparticles often consist of core/shell structures, where the shell consists of iron oxide/hydroxide and the particle core is zero-valent iron. These special structures not only lead to their stability against further passive corrosion as well as the dissolution-related processes during actual field application, but also complicate the analysis on their decontamination mechanism, such as the competition between electrostatic attraction ($Fe(OH)_2$, $Fe(OH)_3$, Fe_2O_3) and reduction (Fe^0).

The oxide shells of iron-based nanoparticles in general can be expressed stoichiometrically as FeOOH (Li and Zhang, 2006), which is similar to that of goethite (α-FeOOH). The surface binding sites commonly found on the FeOOH surface are singly-coordinated (≡Fe(OH)H) and triply-coordinated (≡Fe_3O(H)) oxygens (Hiemstra *et al.*, 1996). Like other mineral oxides, these surface binding sites undergo protonation or deprotonation, and become either negatively-charged (≡$FeOH^{-1/2}$, ≡$Fe_3O^{-1/2}$) or positively-charged (≡$FeOH_2^{+1/2}$, ≡$Fe_3OH^{+1/2}$), depending on the solution pH and the intrinsic point-of-zero-charge (pH_{pzc}) of these binding sites. Heavy metal ions in contact with these binding sites will be adsorbed and removed from the bulk liquid phase, according to the general schemes as shown in Eq. (2.1) to Eq. (2.4) (Benjamin *et al.*, 1982). These processes, taking place on the nanoparticle surface, are mainly based on electrostatic interaction by nature, and hence no specific selectivity could be derived. As a result, the binding sites could easily be occupied by other environmental species of abundance, e.g. phosphates or sodium ions.

Protonation: $$\overline{Fe-OH} + H^+ = \overline{Fe-OH_2^+} \quad (2.1)$$

Deprotonation: $$\overline{Fe-OH} = \overline{Fe-O^-} + H^+ \quad (2.2)$$

Cation adsorption: $$\overline{Fe-OH} + M^{n+} + mH_2O = \overline{Fe-M(OH)_m^{n-m-1}} + (m+1)H^+ \quad (2.3)$$

Anion adsorption: $$\overline{Fe-OH} + A^{n-} + mH^+ = \overline{Fe-OH_{m+1}A^{m-n}} \quad (2.4)$$

These useful binding sites for metal ion removal are located on the external surface of the iron nanoparticles, as these nanoparticles are predominantly non-porous and their solid cores are impervious and non-penetrable. To enhance their remedial performance (e.g. higher adsorption capacity), the iron nanoparticles are often made in the size range of 1-100 nm, so as to afford higher specific surface areas. Without proper dispersants or surface-modifying additives (Saleh *et al.*, 2007), the nanoparticles prepared have high tendency to aggregate (Zaitsev *et al.*, 1999; Nurmi *et al.*, 2005), which is further aggravated by their magnetic properties (Phenrat *et al.*, 2007).

Various synthetic methodologies producing metallic or metal oxide nanoparticles are available (Cushing *et al.*, 2004). Due to the straightforwardness and scalability, chemical synthesis methods, such as liquid-phase reduction and controlled chemical co-precipitation, have long been favored by environmental technologies and scientists over traditional top-down approach such as mechanical milling (Huber, 2005; Li *et al.*, 2006). Standard "wet-chemistry" techniques can be used to alter the surface

functionality of the synthesized nanoparticles. The following sections briefly discuss the synthesis and applications of various iron-based nanoparticles. The representative examples are tabulated in Table 2.1.

2.2.1.2 Pristine zero-valent iron (Fe^0) nanoparticles

Iron nanoparticles are often prepared by liquid-phase reduction through reducing an iron salt or an iron oxide, with or without the presence of a surfactant. The surfactants, if present, could self-assemble in the solution into micelles and prevent the agglomeration of the formed iron nanoparticles. The most commonly used reductant in both basic research and industry is sodium borohydride ($NaBH_4$). The as-synthesized zero-valent iron nanoparticles oxides spontaneously. Thus, core/shell nanoscale zero-valent iron (see Figure 2.1) was obtained, popularly through borohydride reduction of ferric or ferrous salts, and studied for the performance and the mechanism in heavy metal removal (Kanel *et al.*, 2005; Kanel *et al.*, 2006; Li and Zhang, 2006; Li and Zhang, 2007). Kanel *et al.* (2005, 2006) demonstrated that the pristine zero-valent iron nanoparticles with diameter of 1-120 nm could remove As(III) and As(V) via a rapid adsorption step followed by co-precipitation with the surface corrosion by-products. The aging of the pristine zero-valent iron yields magnetite (Fe_3O_4), ferrous hydroxide ($Fe(OH)_2$) and ferric hydroxide ($Fe(OH)_3$) which react with As(III) and convert the neutral $HAsO_4^0$ to oxyanions, $H_2AsO_4^{1-}$ and $HAsO_4^{2-}$ in the range of pH = 6 – 9. The negatively-charged species are then adsorbed and undergo surface complexation on the positively-charged surface of iron nanoparticles (pH_{pzc} ~ 8.0). In this process, the high redox activity present in the iron nanoparticles system is essential for transformation of toxic contaminants into adsorbable form or co-precipitation products. Nevertheless, leaching of adsorbed As(III) and As(V) was also

observed due to the weak electrostatic attraction between the adsorbed species and the binding sites.

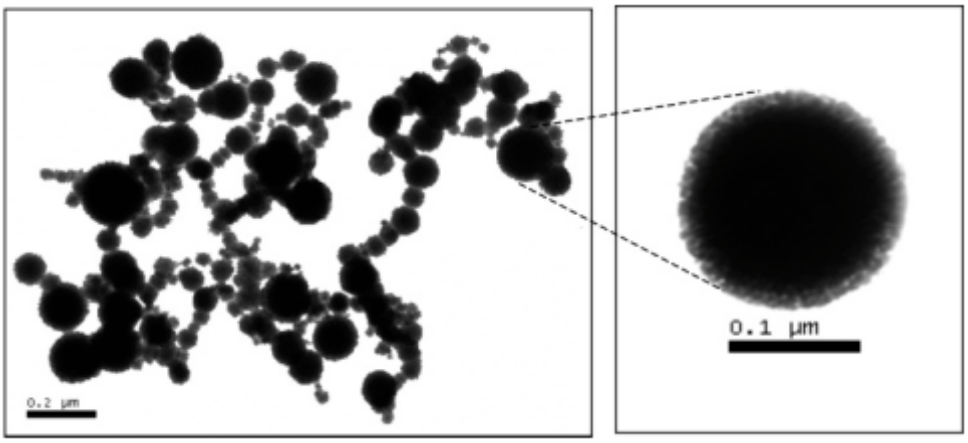

Figure 2.1 Transmission Electron Micrography (TEM) pictures of iron nanoparticles (Li and Zhang, 2006) (reprinted with permission; Copyright (2006), American Chemical Society).

The composition of the various corrosion by-products continually changes as aging proceeds, hence contributing to the variable mixed-valence nature of the core/shell nanoparticles. Li and Zhang (2007) further demonstrated that the oxidized shell layer of the iron nanoparticles contains the adsorption sites where heavy metal removal occurs. Heavy metal ions such as Ni(II), diffusing through the oxide-shell, would not only be adsorbed, but also be sequestrated by the zero-valent iron core via reductive precipitation. It has been noted that the removal capacity of core/shell iron nanoparticle with zero-valent iron core is always higher than that found in iron oxide nanoparticles. For example, a Ni(II) sequestration capacity of 130 mg/g was obtained for the core/shell iron nanoparticles, whereas a modest value of 25 mg/g was reported for maghemite (γ-Fe_2O_3) nanoparticle (Hu et al., 2005a). Even though the former has higher remedial capacities, their reuse potential is however lower. In most cases, the core/shell iron nanoparticles could not be regenerated with a simple acidic elution

because the redox reaction and/or co-precipitation with iron corrosion by-products are irreversible.

2.2.1.3 Modified iron-based nanoparticles

Many researchers often apply post-synthesis treatment to modify the pristine iron-based nanoparticles. Functional materials such as stable noble metal, metal oxide, low molecular weight organic molecules and polymers are often added to complement the pristine nanoparticles or augment additional functionality which enables the resulting iron-based nanoparticles to deliver better heavy metal remediation (higher adsorption capacity) or optimal process characteristics (increased lifespan for cyclic reuse). One of the most feasible routes has been to fabricate iron oxide-based nanoparticles (e.g. Fe_3O_4 or Fe_2O_3) and apply them directly for metal ion removal. Due to their inertness, these oxide nanoparticles often undergo further chemical modification to enhance their adsorption performance.

By varying the types and concentrations of precursor metal salts during the controlled chemical co-precipitation, different nanoscale ferrites ($MeFe_2O_4$, Me = Mn, Co, Cu, Mg, Zn, Ni) have been obtained (Hu *et al.*, 2007). It was demonstrated that the adsorption performance of nanoscale ferrites could be maximized by optimizing the elemental composition of the nanoparticles. It was determined that the highest adsorption capacity of 31 mg/g for Cr(VI) was achieved for jacobsite nanoparticle ($MnFe_2O_4$). Regeneration of the nanoscale ferrites in their work was investigated and it was found that the chemical redox reaction between the Mn(II) and the Cr(VI) caused the poor recovery. Regeneration of nanoscale adsorbents is not widely investigated as most of the iron-based nanoparticles remove heavy metal ions through

a combination of both surface adsorption and redox reaction. Remedial capacity and performance would undoubtedly degrade during treatment and eventually becomes exhausted. Simple pretreatment was attempted successfully by Hu *et al.* (2005b) to convert all lower valent Mn to its highest valence. It was reported that the modified jacobsite nanoparticles could be used and regenerated for multiple cycle of use without drop in performance in successive runs.

Binding sites found on iron-based nanoparticles consist mostly of oxygen-donor-atoms or protonated ion-exchange sites, which has little or no affinity towards some of the more toxic heavy metals, for example, Hg(II) and Pb(II). Surface modifications via various "wet-chemistry" routes are often carried out. These modified nanoparticles could serve as nanoscale carrier for specific metal-coordinating ligands which are softer Lewis base, such as ligands containing either sulfur-donor-atom (e.g. thiol groups) or nitrogen-donor-atom (e.g. amine groups). Yantasee, *et al.* (2007) obtained surface-modified iron nanoparticles carrying dimercaptosuccinic acid, via the ligand-exchange method. The modified nanoparticles showed a high adsorption capacity of 227 mg/g-nanoadsorbent for Hg(II). High heavy metal affinity of the modified nanoparticles also promoted a more rapid adsorption kinetics, for instance, 99 wt% of 1 ppm Pb(II) was removed within a minute.

Another type of hybrids iron-based nanoparticles was obtained by encapsulating pre-synthesized iron nanoparticles with a polymer that carries desired heavy metal-selective binding sites. Shih and Jang (2007) utilized Fe_3O_4 nanoparticles as seed and allowed the precursor monomer ethylenedioxythiophene to adsorb onto the seed nanoparticles under acid etching-mediated conditions, followed by polymerization.

The poly(3,4-ethylenedioxythiophene) (PEDOT) polymer encapsulated the parent seeds and the resulting hybrid nanoparticles displayed remarkably high heavy metal sequestration capacity. For instance, the maximum adsorption capacity for Hg(II) could exceed 400 mg/g-modified nanoparticles.

Without further chemical modification, iron nanoparticles, in general, have low adsorption capacity for metal ion removal. Bulk of the binding sites available for metal ion adsorption are located on the external surface of the nanoparticles, which may be easily lost as a result of irreversible aggregation of these nanoparticles. These nanoparticles therefore display low potential to function as effective nanoadsorbent for palladium sequestration and recovery.

Table 2.1 Survey of literature on iron-based nanoparticles and related metal ion removal applications.

Type of nanoparticles	**Particle size** (nm)	**Target metal ion**	**Major binding sites or functional groups for metal ion removal**	**Reference**
Zero-valent iron nanoparticles				
Nanoscale zero-valent iron (NZVIs)	1-120	As(III), As(V)	Initially the sites are amorphous Fe(II)/Fe(III), magnetite (maghemite). As treatment proceeds, initial reactive sites gradually transform into lepidocrocite and more crystalline magnetite.	Kanel *et al.*, 2005; Kanel *et al.*, 2006.
Maghemite nanoparticles	~10	Cr(VI)	The major binding site is hydroxyl groups of iron oxide.	Hu et al., 2005a.
Core/shell nanoscale zero-valent iron (Fe(0)/Fe(III))	10-200	Zn(II), Cd(II), Pb(II), Ni(II), Cu(II), Ag(I), Cr(VI), Hg(II)	Simultaneous adsorption and co-precipitation may occur, depending on the standard redox potential difference between the Fe^0 and the incoming heavy metal. Major binding site is ≡Fe-OH.	Li and Zhang, 2006; Li and Zhang, 2007.
Modified iron-based nanoparticles				
Modified jacobsite (MnFe2O4)	~10	Cr(VI)	The major adsorptive components are MnO_2 and Fe_2O_3.	Hu et al., 2005b.
Nanoscale ferrites, MeFe2O4 (Me = Mn, Co, Cu, Mg, Zn, Ni)	~20	Cr(VI)	For $MnFe_2O_4$, the major driving force for adsorption is chemical redox reaction between Mn(II) and incoming Cr(VI).	Hu et al., 2007.
Magnetic nanoparticles encapsulated by Poly(3,4-ethylenedioxythiophene) (PEDOT)	~11	Ag(I), Hg(II), Pb(II)	The major binding sites are the O-donor-atoms and S-donor-atoms of the PEDOT.	Shih and Jang, 2007.
Magnetite nanoparticles modified with dimercaptosuccinic acid	~6	Hg(II), Co(II), Cu(II), As(V), Ag(I), Cd(II), Tl(III), Pb(II)	The major binding site responsible for remarkable heavy metal binding is thiol groups originated from the dimercaptosuccinic acid added.	Yantasee *et al.*, 2007.

2.2.2 Surfactant-based Micelles

2.2.2.1 Introduction

Micelle is nanoscale subcolloidal aggregates formed by surfactants or amphiphilic polymers when their concentrations in solutions exceed a critical micelle concentration (CMC) or critical aggregate concentration (CAC) (Figure 2.2).

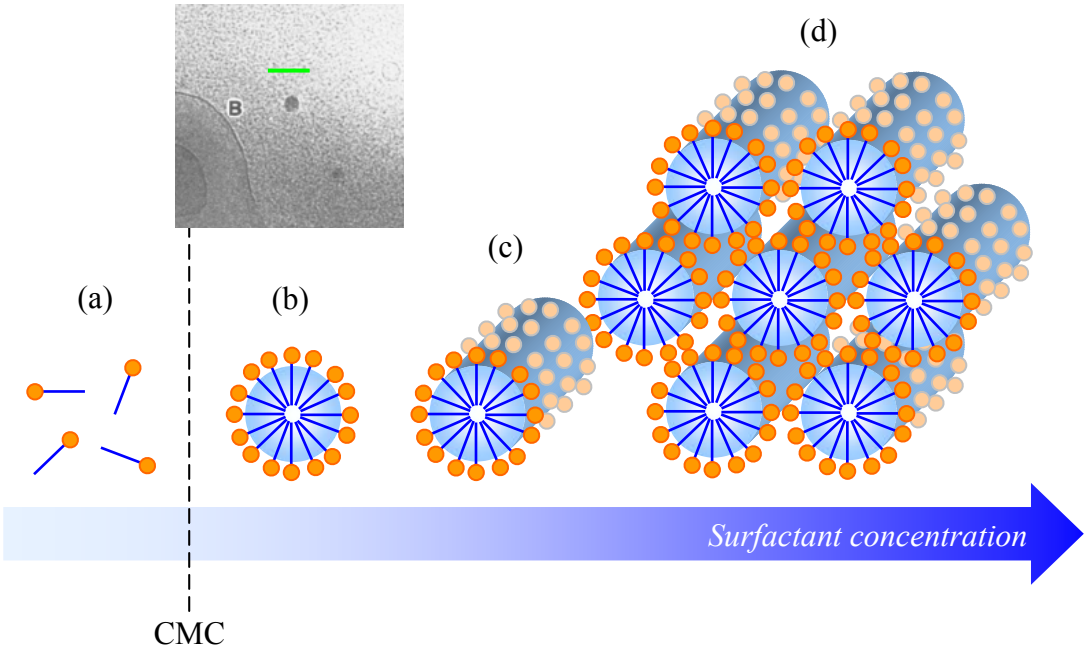

Figure 2.2 The inset is Cryo-Transmission Electron Micrography (Cryo-TEM) picture of vitrified, hydrated of 10 mM ditetradecyldimethylammonium acetate (DTAA) solution (Bellare *et al.*, 1988) (reprinted with permission; Copyright (1988), American Chemical Society). The scale bar denotes 100 nm. Self-assembly of surfactant molecules: (a) free surfactant molecules, (b) spherical micelle, (c) rod, (d) hexagonally packed rods.

Upon micellization, the sizes of these nanoscopic structures formed spans the range from 0.1 nm to 50 nm, depending on both aqueous environmental conditions (pH, background electrolyte, temperature) as well as the precursor surfactant's architecture (Hunter, 2001). Above the CMC, the excess surfactants will associate or micellize, whereas the rest will remain as monomer. The simplest micelles are spheres but as surfactant concentration increases the micelles grow and form rods or even larger

structures, such as hexagonally packed rods etc., at higher surfactant concentrations. The first direct visual evidence of surfactant-based micelles as nanoparticles was reported by Bellare *et al.* (1988).

Surfactants are basic materials in a variety of industrial products or essential constituents for chemical formulations such as detergents, paints, cosmetics, pharmaceuticals, pesticides, or plastics. The wide applications of surfactants owe to their amphiphilic structure, consisting of polar head groups, such as cationic ammonium groups or anionic sulfate groups, and non-polar tails which are usually alkyl chains (Figure 2.3). Nonionic block copolymers with proper selection of head groups and tails could display similar surface-active properties, such as lowering interfacial free energies at oil/water or water/solid interfaces by adsorbing onto the liquid/liquid interface or solid surface. One of the engineering applications is pretreatment of ultrafiltration membrane with surfactant solution in order to reduce fouling on ultrafiltration membrane by bovine serum albumin through electrostatic and/or steric repulsion by the adsorbed polar head groups, hence resulted in higher flux (Fane *et al.*, 1985).

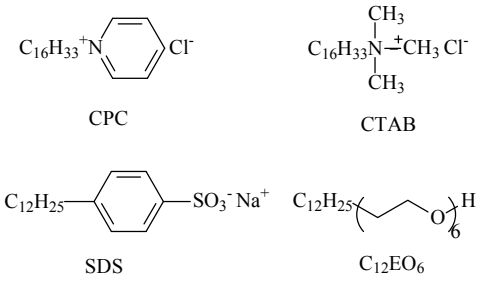

Figure 2.3 Chemical structures of representative surfactant widely used today (CPC: cetylpyridinium chloride, CTAB: cetyltrimethylammonium bromide, SDS: sodium dodecyl sulfate, $C_{12}EO_6$: hexaethylene glycol *n*-dodecyl ether).

Similar to the iron-based nanoparticles discussed earlier, most of the available binding sites (i.e. the charged groups or the ionizable functional groups) for metal ion adsorption are located on the external surface of the micelles. The first work on utilizing surfactant-based micelle for separation of organic solutes and monovalent/multivalent ions was proposed by Leung (1979). After the solubilization of organic solutes and the binding of ions of opposite charge to the charged micelles' surfaces are complete, the spent surfactant-micelle solution is filtered with a ultrafiltration system. The combination of the nanoscale micelles and the membrane filtration process allowed the use of nanoparticles in continuous operation and avoided the "particle size-backpressure" dilemma encountered in conventional packed-bed chelating ion-exchanger systems. Since then, there have been extensive research activities using the micelle-membrane filtration process (see page 32 for Table 2.2).

The use of surfactant-based micelles can be generalized in the two categories as follows. Micellar-enhanced ultrafiltration (MEUF) refers to the process whereby association of metal ions occurs via ion-exchange with the charged head groups on the micelles' surfaces. The heavy metal ions to be removed are electrostatically bound to the charged surface of the micelles which are equivalent to that of strong cationic or anionic ion-exchange resins. MEUF is relatively simple and straightforward though only moderate performance has been achieved due to the non-selective binding involved in the Coulumbic electrostatic attraction between species of opposite charges (Scamehorn, *et al.*, 1994).

Micellar aggregates are able to enhance the aqueous solubility of hydrophobic substances which otherwise are only sparingly soluble in water. The enhancement in

the solubility arises from the fact that the micellar cores mainly consist of hydrophobic alkyl chains, and can serve as compatible microenvironment for water-insoluble solute molecules. This phenomenon of enhanced solubility is referred to as 'solubilization'.

To enhance the remedial capacity or the metal ion affinity, hydrophobic extractants or chemically-derivatized chelating molecules are preloaded into the micelle's core prior to actual treatment (Klepac *et al.*, 1991). The removal of metal ions from aqueous solution takes place when the metal ions undergo multidentate complexation or chelation with the micelle-solubilized hydrophobic extractants. Coupling this adsorption process with ultrafiltration for micelle recovery, this process is then referred as ligand-modified micellar-enhanced ultrafiltration (LM-MEUF).

2.2.2.2 Surfactant-micelle for water/wastewater treatment

Any multivalent heavy metal species present will tend to adsorb or bind preferentially on the micelle surface due to electrostatic attraction. If a anionic surfactant is used, multivalent cationic species in solution will bind to the micellar nanoparticles. Scamehorn *et al.* (1994) explored the use of SDS (see Figure 2.3) micellar system for the removal of divalent metal ions. At a surfactant concentration of 100 mM, 96% removal efficiency was achieved with the MEUF for all divalent metal ions studied. They demonstrated that the separation efficiency is solely based on their valence (cation charge), with no display of selectivity towards specific metal species. Juang *et al.* (2003) investigated the similar SDS micellar system, with a wide range of experimental conditions, including solution pH, membrane molecular weight cut-off (MWCO) and material, as well as molar ratio of surfactant to metal ions. Only limited success was achieved to separate trivalent cations from divalent cations by varying

molar ratio of surfactant to metal ions. Otherwise, the MEUF displays no selectivity at all without the aids of additional ligands.

Since various divalent cations are removed with approximately the equivalent rejection in MEUF, selective sequestration of heavy metals ions was attempted by researchers through LM-MEUF, wherein an appropriately selected extractant was synthesized and solubilized (Klepac *et al.*, 1991; Tondre *et al.*, 1993; Fillipi *et al.*, 1997; Hebrant *et al.*, 1998). In contrast to ordinary micelles, these ligand-modified micelles can offer preferential removal of specific metal ion with higher selectivity. Amphiphilic ligand and surfactant was added to water under conditions where micellization was favored. Klepac *et al.* (1991) demonstrated that Cu(II) could be preferentially removed from the solutions containing both Cu(II) and Ca(II). They also even showed that the cationic charge of the micellar nanoparticles assisted to repel uncomplexed non-target Ca(II) due to the "ion-expulsion effect" (Christian *et al.*, 1989), whereas the specific complexation of Cu(II) by the amphiphilic extractant was not retarded at all. Tondre *et al.* (1993) proposed a strong analogy between the LM-MEUF and classical solvent extraction process, wherein the hydrophobic core of micelles acts in similar capacity as the organic solvent phase in the latter. The Cu(II) removal performance by such system was affected by the same design parameters, for instance, the hydrophilic-lipophilic balance of the extractant or the ionization state of the extractant selected (Ismael and Tondre, 1993; Tondre et al., 1997). Fillipi *et al.* (1997) investigated the regeneration of the retained Cu(II)-extractant-micelle complexes by standard acid stripping in a 4-stage operation. One of the competitive advantages of LM-MEUF compared to solvent extraction is that the former could exploit the difference in the complexation kinetics between metal ions (Ismael and

Tondre, 1993). Kinetic-selective separation of Co(II) from a solution containing both Ni(II) and Co(II) was made possible, which had been impossible in standard solvent extraction.

Tondre et al. (1997) investigated the electrochemical behaviors between copper ions bound through the usual ion-exchange and complexation by the organic ligands in the core. Through cyclic voltammetry, the researchers compared the electroreduction behaviors of copper ions between MEUF and LM-MEUF and confirmed that copper ions removed through the latter process cannot be reduced the same manner in former as copper ions forms stable complexes with 11-hydroquinone solubilized. Nonetheless, leakage of unassociated surfactant as monomer through membrane permeation occurs inevitably even at 100 mM of SDS (Scamehom *et al.*, 1994). This leakage problem was observed to be more severe in tangential ultrafiltration when the shearing action degrades the cohesion of the micelles (Tounissou *et al.*, 1996). This may be unacceptable because surfactant-bound harmful metal ions can escape into the permeate stream and release into the environment.

Decontamination of As(V)-laden water using MEUF has been carried out also (Gecol *et al.*, 2004; Beolchini *et al.*, 2006; Iqbal *et al.*, 2007). Conventional nanofiltration and reverse osmosis were found to remove over 90% As(V). However, both processes required high operating pressure for proper treatment throughput (Gecol *et al.*, 2004). Cationic surfactants and micelles were able to bind As(V) species such as $H_2AsO_4^-$ and $HAsO_4^{2-}$ through electrostatic interaction, and later separated by ultrafiltration. Optimization of As(V) rejection was studied by Iqbal *et al.* (2007) via comparative analysis of a series of commercially available cationic surfactants. As(V) removal

efficiency is closely related to the characteristics of surfactants such as CMC and type of head groups. At surfactant concentration of 10mM, CPC-based micellar system retained almost 97% of As(V) whereas the benzalkonium chloride (BC)-based system only removed 57% due to much higher CMC. Leakage of As-bound surfactants or micelles through permeate was severe (~0.9 mM) and post-treatment with powdered activated carbon (PAC) was used for polishing.

Beolchini *et al.* (2006) reported that an 89% removal could be achieved with lower surfactant concentration and membranes with bigger pore size (20 and 50nm, compared to 5-10 kDa in other's work). Lower surfactant leakage in permeate (~0.2 mM) was observed as less surfactant was used in the diafiltration process (0.9 to 2.5 mM). They reported lower As(V) retention when CPC concentration in feed was increased from 0.75 mM to above its CMC. They hypothesized that flocculation or co-precipitation might have happened (as it did at higher concentrations of both CPC and As(V)), resulted in nanoscale flocs or micro-precipitates, which caused the system performance deteriorating. The interactions between CPC and As(V) in lower surfactant systems was still unclear. It is possibly that the higher feed concentration of As(V) at ppm level, could have contributed to the phenomenon.

Gecol *et al.* (2004) experimentally explored the As(V) rejection by charged membranes in the absence of surfactants. Regenerated cellulose membranes with a higher negative surface charge than polyethersulfone membranes was found to have higher retention of negatively charged As(V), due to the "Donnan exclusion effect" on charged membrane. Upon surfactant addition, 100% of As(V) retention was achieved with regenerated cellulose membranes of 5 kDa with lower permeate flux, regardless

of the feed concentration of As(V). In addition, other conditions such as concentration of competiting co-ions such as phosphate, and solution pH also affect the final As(V) removal performance (Gecol *et al.*, 2004; Iqbal *et al.*, 2007).

Widespread chromate pollution is another potential environmental application of MEUF. Flux decline in MEUF for Cr(VI) removal has been investigated systematically (Gzara and Dhahbi, 2001; Baek and Yang, 2004; Ghosh and Bhattacharya, 2006). The MEUF studied by Baek and Yang (2004) could remove 99% and 80% of chromate and nitrate respectively after optimization, due to the higher affinity between the pyridinium head groups and chromate ions. Chromate ions could be removed at surfactant concentrations where no micelles exist, due to the concentration polarization and the "Donnan-exclusion effect" (Gzara and Dhahbi, 2001).

Concentration polarization is the predominant cause for flux decline, especially where the surfactant concentration is lower than CMC (Gzara and Dhahbi, 2001). Accumulation of surfactant molecules in the vicinity of membrane surface occurs as the surfactant monomers are retained by the membrane during permeation. As the accumulation proceeds, the surfactant concentration at the membrane surface eventually becomes larger than CMC and a gel layer is formed. For the similar CPC-Cr(VI) micellar system, Ghosh and Bhattacharya (2006) found that the permeate flux decreased as the Cr(VI) concentration increased; however the permeate flux increased linearly with the transmembrane pressure. They also observed that the concentration polarization was negligible as the permeation flux remained stable throughout the whole course of ultrafiltration in an unstirred batch cell, in contrary to the conclusions

of Gzara and Dhahbi (2001). This discrepancy is probably due to the reason that the micellar aggregation layer forms quickly above the membrane surface in the former; whereas the shearing force along the membrane surface in the tangential flow systems disrupts the initial formation.

Nonionic surfactants were used as micellar carrier of heavy metals extractant (Tondre *et al.*, 1993) or to form mixed micelles (Fillipi *et al.*, 1999). Fillipi *et al.* (1999) incorporated a nonionic surfactant into anionic surfactant solution. Both surfactants associated simultaneously and the nonionic component caused charged anionic head groups to be further away from each other, hence less repulsion. Micelles could form below the original CMC of the anionic surfactant. Besides the spherical micelles, other forms of micellar nanostructures used in MEUF or LM-MEUF such as microemulsions (Ismael and Tondre, 1992) and vesicles (Hebrant *et al.*, 1997) were also experimentally explored too.

Careful examination of environmental clean-up technologies always precedes actual pump-and-treat field applications. Before the environmental application with nanomaterials actually takes place, risk assessment on its possible harm to human and ecological health must be done (Tratnyek and Johnson, 2006). For instance, *in-situ* remediation requires delivery of relevant nanoparticles to affected subsurface zone. The toxicity and the mobility of nanoparticles, as well as its fate and transport in long-term, for instance the potential of the nanoscale remedial agents of being trapped in contaminated porous soils, sediments and aquifers, must be properly addressed (Li *et al.*, 2006).

As surfactant leakage can add substantial expense to the separation or make the process effluent stream environmentally unacceptable, the ultimate success of remediation using MEUF or LM-MEUF, to a large extent depends on the surfactant recovery and reuse (Nivas *et al.*, 1996; Sabatini *et al.*, 1998; Rouse *et al.*, 2004). The use of biodegradable surfactants derived from microorganism such as bacteria or yeast was another attractive option as an cost-effective and non-toxic way for remediation of dredged sediments contaminated with heavy metals (Mulligan *et al.*, 2001). Nonetheless, the major technological limitations are still the surfactant monomer-micelle equilibrium, which often results in leakage of surfactant monomer through the membrane into the permeate stream. In addition, pumping actions incurred during MEUF in tangential flow mode would induce further surfactant loss through the membrane due to shear-induced mechanical breakdown of micelles (Brackman, 1991; Tounissou *et al.*, 1996). Despite the benign nature of the surfactant, the surfactant-metal ion complexes permeates through the membrane and pending concerns from environmental regulators might call for additional downstream facilities to act as a polishing step for the permeate stream. In most instances, an ultrafiltration or even nanofiltration step with a smaller pore size membrane has to be installed, which translates to higher capital investment as well as operation expenditure. As a result, the overall economic attractiveness of the MEUF process dwindles. These drawbacks which are associated with the fundamental operating principles of MEUF have excluded the preparation of nanoadsorbents from surfactant-based micelles for palladium sequestration in this study.

Table 2.2 Survey of literature on surfactant-based micelles and related metal ion removal applications.

Surfactant	Target metal ions	Remark	Mechanism	Reference
Ionic micelles				
CPC	As(V)	Polyethersulfone (PES) and regenerated cellulose (RC) membranes (MWCO: 5, 10kDa). 100% As(V) removal could be achieved after optimization.	MEUF	Gecol *et al.*, 2004.
CPC	As(V)	Ceramic membrane (Dp: 20, 50 nm). Low surfactant concentration was employed.	MEUF	Beolchini *et al.*, 2006.
BC, CPC, CTAB, ODA	As(V)	RC membrane (MWCO: 3, 10kDa). Arsenate removal is highly dependent on the surfactant concentration	MEUF	Iqbal *et al.*, 2007.
CPC, CTAB	Cr(VI)	Polysulfone (PS) membrane (MWCO: 10kDa). Above CMC, micelles are sieved; below CMC, charge repulsion between the membrane and surfactant unimer, 50% rejection only.	MEUF	Gzara and Dhahbi, 2001.
CPC	Cr(VI)	PES membrane (MWCO: 10kDa). One of the few studies that address the modeling of metal ion adsorption on micelles.	MEUF	Ghosh and Bhattacharya, 2006.
CPC	Cr(VI)	RC membrane (MWCO: 3, 10kDa). Competitive binding between common anions (NO_3^-) and CrO_4^- is addressed.	MEUF	Baek and Yang, 2004.
CTAB	Cu(II)	RC membrane (MWCO: 6kDa), ligand: LIX-54. Rejection of copper ions greater than 99% could be achieved, even in the presence of Ca(II).	LM-MEUF	Fillipi *et al.*, 1997.
CPC	Cu(II)	CA membrane (MWCO: 5kDa), ligand: N-n-dodecyl-iminodiacetic acid. Copper specific ligand was solubilized within cationic micelles	LM-MEUF	Klepac *et al.*, 1991.
SDS	Cd(II), Cu(II), Zn(II)	CA membrane (MWCO: 1, 5kDa). Rejection of at least 96% of all the divalent metal ions was achieved, at SDS concentration of 100mM.	MEUF	Scamehorn *et al.*, 1994.
SDS	Co(II), Cu(II), Zn(II), Cr(III)	Polyamide thin-film composite membrane (MWCO: 1, 2.5, 8kDa) and PES membrane (MWCO: 2, 5kDa). Surfactant precipitation as mean of recovery. It remains difficult to selectively separate various metal ions of same valence.	MEUF	Juang *et al.*, 2003.

Nonionic micelles				
$C_{12}EO_6$, CTAB	Cu(II)	Cellulose membrane (MWCO: 10kDa), ligand: C*n*NHMePyr (*n* = 4,8,10,12,14,16)	LM-MEUF	Tondre *et al.*, 1993.
$C_{12}EO_6$, CTAB/1-butanol	Cu(II), Ni(II), Zn(II)	Cellulose membrane (MWCO: 10, 30kDa), ligand: 8-hydroxyquinoline, Kelex-100	LM-MEUF	Ismael and Tondre, 1993.
$C_{12}EO_6$, CTAB	Cu(II)	Cellulose membrane (MWCO: 10kDa), ligand: Kelex-100, C*n*NHMePyr (*n* = 12,16). Ion expulsion effect due to Donnan equilibria could no be neglected in modeling the yield of extraction.	LM-MEUF	Hebrant *et al.*, 1998.
Mixed micelles				
SDS & NPE	Zn(II)	CA membrane (MWCO: 5 kDa). High rejections of Zn(II) ions below the CMC of pure SDS, in the presence of NPE.	MEUF	Fillipi *et al.*, 1999.
Microemulsions				
CTAB/1-butanol	Co(II), Ni(II)	Cellulose membrane (MWCO: 10kDa), ligand: Kelex-100. Kinetic-controlled selective removal of Co(II) from mixture was achieved.	LM-MEUF	Ismael and Tondre, 1992.

*Note: Dp: Membrane pore size, nm.
MWCO: Molecular weight cut-off, Dalton (D) or kilo Dalton (kD)
BC: Benzalkonium chloride
$C_{12}EO_6$: Hexaethylene glycol *n*-dodecyl ether
C*n*NHMePyr: 6-[(alkylamino) methyl]-2-(hydroxymethyl) pyridines
CTAB: Cetyltrimethylammonium bromide
CPC: Cetylpyridinium chloride;
SDS: Sodium dodecyl sulfate
DMDAB: dimethyldi-*n*-alkylammonium bromides
diC_{12}NMePyr: 6-[(di-*n*-dodecylamino)methyl]-2-(hydroxymethyl)pyridine
Kelex-100: 7-(4-ethyl-1-methyloctyl)-8- hydroxyquinoline
LIX-54: 1-phenyl-3-isoheptyl-1,3-propanedione
LM-MEUF: Ligand-modified micellar-enhanced ultrafiltration
MEUF: Micellar-enhanced ultrafiltration
NPE: Nonlyphenol polyethoxylate
ODA: Octadecylamine acetate;
Triton X-100: Polyoxyethylene octyl phenyl ether

2.2.3 Dendrimers

2.2.3.1 Introduction

Dendrimers consist of spheroid or globular macromolecules wherein a core, interior branching and terminal surface branching are covalently bonded in a three-dimensional manner (Tomalia and Fréchet, 2002). Dendrimers are constructed through either divergent or convergent method whereby a set of repeating chemical synthesis procedures that build up from the molecular level to the nanoscale region. Through each repetition, the dendrimers' generation is increased by one, and their size as well as their surface functionalities increases. Similar to other synthetic linear polymer, macromolecules, or polymeric microgels, the properties of dendrimers such as reactivity are eventually determined by the generation (shells) and chemical composition of the core, interior branching and surface functionalities. Dendrimers are hence regarded as spherical "soft" nanoparticles with sizes in the range of 2-20 nm of very low polydispersity (Figure 2.4). These nanoparticles are highly customizable through chemical modification of their surface groups or synthesis with various starting core materials. This extra synthetic versatility offers interesting variation to their original properties. For instance, dendrimers can be made soluble in appropriate media (polar or non-polar) (Bosman *et at.*, 1999). The well-defined size and shape, architecture as well as rich chemical functionalities on the surface and interior of dendrimers make them good candidates for various applications of scientific and industrial importance, such as biomedical, electronics, sensors and coatings (Dykes, 2001).

As compared to iron nanoparticles and micelles/ligand-modified micelles, dendrimers are undoubtedly better candidate as nanoscale adsorbents because of their much higher

density and variety of binding sites for metal ion removal. Due to the intrinsic affinity of the amine groups and carboxylates towards metal ions, Ottaviani *et al.* (1994) explored the complexation between Cu(II) and anionic starburst dendrimers, with the aid of electron paramagnetic resonance spectroscopy (EPR). Not only the oxygen atoms of the surface carboxylate groups would bind Cu(II) and, cooperative binding of Cu(II) through the oxygen atoms and interior nitrogen atoms occurred too. Due to the high accessibility of the interior chemical functionalities with mobile ions and molecules, dendrimers have been considered as excellent substitutes for water-soluble chelators in soil-washing remediation (Xu and Zhao, 2005; Xu and Zhao, 2006) as well as nanosensors for detection of trace level cobalt ions in aqueous sample (Balzani *et al.*, 2000).

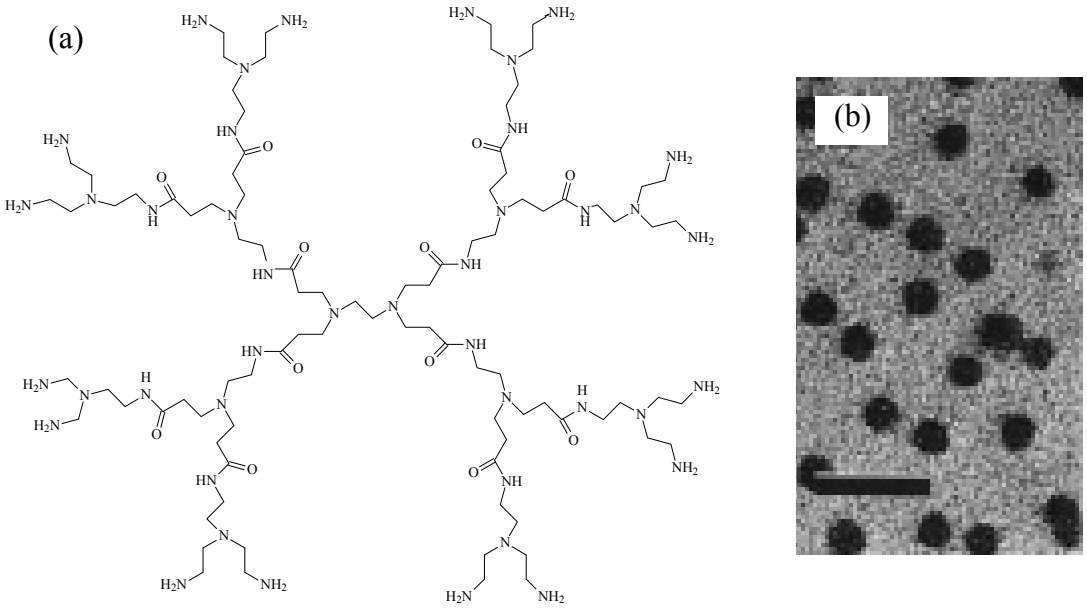

Figure 2.4 (a) Illustrative diagram of a G2 Poly(amidoamine) (PAMAM); (b) cryo-TEM micrograph of G10 PAMAM (scale bar indicates 50 nm) (Jackson *et al.*, 1998) (reprinted with permission; Copyright (1998), American Chemical Society).

2.2.3.2 Dendrimers for water/wastewater treatment or resource recovery

Poly(amidoamine) (PAMAM0 dendrimers are relatively more often investigated due to the rich abundance of chargeable amine groups throughout the dendrimers (Figure 2.4). The first environmental application of dendrimers was reported by Diallo *et al.* (1999) at CalTech. The PAMAM dendrimers of various generations acted as high capacity chelating agents and effectively removed Cu(II) from synthetic wastewater. Depending on the background electrolyte concentration, solution pH as well as the generation number of dendrimers, the Cu(II) binding capacity of PAMAM dendrimers was found to range from 308 to 451 mg/g, which is significantly higher than conventional ion-exchange or chelating resins (Diallo *et al.*, 2003).

For environmental nanotechnology to become affordable and economically feasible, cost-effective manufacturing of these nanoparticles or related nanomaterials should be made available. Another critical step in ensuring the overall feasibility is to integrate a recovery and reuse operation with the nanoparticle-based technologies. Diallo *et al.* (2005) investigated the "dendrimer-enhanced ultrafiltration" (DEUF), i.e. the coupling of ultrafiltration process with separation of dendrimer-Cu(II) complexation, and showed that the copper-laden dendrimers could be fully rejected by optimizing the types of membranes used as well as their MWCO. The retained Cu(II)-dendrimer complexes could be regenerated through pH adjustment.

The attractiveness of the DEUF owes to the defined shape and size of the dendrimer as well as its high intrinsic binding capacity. Unlike conventional low-molecular weight chelating agents such as ethylenediamine tetraacetic acid (EDTA), the DEUF process could recover the remedial agents by choosing ultrafiltration membrane with a greater

MWCO, without the use of high pressure membrane processes such as reverse osmosis and nanofiltration. Dendrimers have lower hydrodynamic volumes in comparison to their linear polymer analogue with the same molecular weight (Bosman *et al.*, 1999). The viscosity of dendrimer solution would only increase with molecular weight up to certain generation, and it is always lower than their linear polymer analogue, which render them to be more energy efficient in tangential/cross-flow filtration than their polymeric counterpart, i.e. polymeric chelating agents of polymer-enhanced ultrafiltration process (PEUF).

Contrary to surfactant-based nanoparticles, i.e. micelles, the dendrimers acquire stable covalently globular nanostructures without thermodynamic restriction on the particle-forming threshold concentration, e.g. the CMC for the former. The leakage of dendrimers through membranes with an appropriate MWCO is highly unlikely. Thus the loss of dendrimers by shear-induced mechanical breakdown is minimum in DEUF, be it in dead-end or tangential filtration systems that are commonly found in water/wastewater treatment practice nowadays. Diallo *et al.* (2005) examined the fouling phenomenon of the DEUF system. More severe membrane fouling was observed for PAMAM-polyethersulfone membrane system whereas PAMAM-regenerated cellulose membrane system only experienced a slight drop in flux. The PAMAM dendrimers for generation 3, 4 and 5 have hydrodynamic diameters of 3.5, 5 and 5.4 nm respectively, which are comparatively larger than the equivalent pore size of the membrane used. Diallo *et al.* (2005) attributed the fouling in the case of polyethersulfone membrane to particle deposition, whereas surface adsorption was the main fouling mechanism for the regenerated cellulose membrane. As a high pressure of 5 bar was required to obtain acceptable flux in the DEUF system, the claimed

advantages such as reduced operating costs and lower energy expenditure are still in doubts. In fact, the membrane molecular weight cut-off investigated is comparable to those of MEUF as discussed before. Theoretically, higher flux would only be achieved by selecting membranes with higher MWCO. However, this would require the use of higher generation dendrimers (i.e. larger dendrimers). As the globular-shape dendrimers become more rigid as the generation number increases, the accessibility of interior binding sites is reduced (Ottaviani *et al.*, 1994).

Rether and Shuster (2003) explored the modification of the sequestration selectivity of the PAMAM dendrimers of generation 2.5, by functionalizing the surface groups with benzoylthiourea groups. In contrast to the original PAMAM dendrimers, the benzoylthiourea-modified PAMAM dendrimers could retain Cu(II) with a retention of >90% even at pH = 4. In the presence of various water-soluble complexing agents such as ammonia and triethanolamine, Cu(II) and Ni(II) would still be fully removed by the modified PAMAM dendrimers. Their work showed that post-synthesis chemical modification of the dendrimers was feasible but there was insufficient data to show whether the reactions were strictly selective towards the surface terminal groups.

Unlike Cu(II) removal in DEUF as discussed before, removal of metal ions from metal-laden soil or sand will only utilize surface or near-surface functional groups of dendrimers because the binding to interior groups is diffusion-controlled. Situation is further exacerbated when the dendrimer becomes larger as generation increases (Ottaviani *et al.*, 1994; Ottaviani *et al.*, 1997). Xu and Zhao (2005) explored the efficacy of PAMAM dendrimers of different terminal groups as recoverable extracting

agents for in-situ flushing of Cu(II)-contaminated soil. Fixed-bed column elution studies with copper-laden sandy soil were carried out to compare the copper elution and recovery by different types of dendrimers. Almost 90% of Cu(II) was removed using 66 bed volumes with PAMAM dendrimers with terminal carboxylic acid groups at 0.10% (w/w) and solution pH 6.0. In addition, it was also shown that dendrimers of lower generation could remove soil-sorbed Cu(II) more effectively than that of higher generation, on a equal weight basis. This is probably due to that the heavy metals removal from contaminated soil is a non-equilibrium process; hence the mass transfer of dendrimers as well as the availability of accessible binding sites have significant influence on the dynamic column elution's performance. Hence, the less bulkier the dendrimers are, the higher Cu(II) removal could be achieved at the same elution rate.

As discussed earlier, dendrimers possess larger size and well-defined shape, in contrast to other low molecular weight extracting agents such as pyridine-2,6-dicarboxylic acid (DPA), aminoethyl ethanolamine (AEEA), tetramethyl ethylenediamine (TEMED) and EDTA. About 72% recovery of the spent dendrimers of generation 4 was achieved by using a centrifugal nanofiltration filter (Xu and Zhao, 2005). This possibly implies that some dendrimers disintegrated during the column elution test. Hence the smaller fragments passed through the nanofiltration filter and were not recovered.

With the aid of EPR spectroscopy, Ottaviani *et al.* (1997) reported that the dendritic nanostructures of all generation eventually degraded after 60 days of aging at neutral solution pH, whereas complete decomposition was observed for dendrimers of generation 4 and lower. Stability of such precisely engineered highly branched

macromolecules is therefore questioned. The overall high cost of the dendrimers (Dendritech, 2009) could have thwarted any further efforts for a full-scale environmental remediation application. By sacrificing the symmetry as well as the precisely engineered microstructures of the dendrimers, polymeric nanoparticles of bigger or comparable dimensions as well as rich chemical functionalities can be another economically viable candidates for environmental applications.

Table 2.3 Survey of literature on dendrimers and related metal ion removal applications.

Generation number and terminal groups	Target metal ions	Remark	Reference
G_n-NH_2 (n: 3,4,5,6,7,8)	Cu(II)	The first study that reports significant enhanced chelating capacity in nanostructured polymer.	Diallo *et al.*, 1999.
G_n-NH_2 (n: 3,4,5)	Cu(II), Co(II), Ni(II), Na(I), Mg(II), Ca(II)	RC and PES membrane (MWCO: 5, 10kDa) was used in ultrafiltration. Fouling by dendrimers on polymeric membrane is examined. Particle-deposition model is proposed.	Diallo *et al.*, 2005.
G_n-NH_2 (n: 1, 1.5, 4); G_m-COOH, (m: 1.5, 4.5); G4-OH	Cu(II)	Centrifugal PES ultrafilter (MWCO: 1kDa) The first study that reports the use of dendrimers as recoverable chelating agents for soil washing.	Xu and Zhao, 2005.
G_n-NH_2 (n: 1, 4); G1.5-COONa	Pb(II)	97% of dendrimers is recovered using nanofiltration device (MWCO: 1kDa)	Xu and Zhao, 2006.
$G_{2.5}$-NH_2	Cu(II), Co(II), Hg(II), Ni(II), Pb(II), Zn(II)	Cellulose membrane (MWCO: 3kDa), the dendrimer was modified with benzoylthiourea for selective and enhanced removal of specific heavy metals Competitive binding between common water soluble complexing agents and modified dendrimer was investigated. No study on membrane fouling.	Rether and Schuster, 2003.

Notes: G_n: generation number
-NH_2: amine group
-COOH: carboxylic acid group
-OH: hydroxyl group
-Sac: succinamic acid group
-Gly: glycidyol group
-Ac: acetamide group

2.2.4 Polymeric Nanoparticles

2.2.4.1 Introduction

Polymeric nanoparticles (10 – 500 nm) represent a wide category of macromolecules or molecular aggregates that have been researched and developed over the last few decades. Polymeric nanoparticles or otherwise known as latexes or polymeric microgels, share some similarities to surfactant micelles (for example, polymeric nanoparticles possess amphiphilic properties too). Other than that, polymeric nanoparticles differ greatly from surfactant micelles, in terms of both physical dimension as well as microstructures. One of the distinct dissimilarities is perhaps that the surfactant-based micelles would only maintain their structure provided that the CMC is reached or exceeded, whereas the size and shape of polymeric nanoparticles will remain relatively stable after manufacturing.

Due to the enormous technical and economical importance, various types of polymeric nanoparticles have been synthesized via a vast array of "heterophase polymerization" routes, which have been established and continually advanced in polymer-emulsions industry (Ma, 1999; Tauer, 2004). One of the most important commercial processes is emulsion polymerization. In emulsion polymerization, the emulsion-polymers can be synthesized efficiently in water as solvent with various process configurations (batch, semibatch and continuous). Emulsion polymerization could be further sub-divided, depending on the types of polymerization initiator and stabilizer utilized. For examples, the emulsion polymerization employs water-soluble initiator with all kind of stabilizer, and often yields polymeric nanoparticles of 5 nm to 10 μm in diameter, with a good size-monodispersity.

The simplest form of polymeric nanoparticles, in the form of latexes (also known as emulsion polymer or polymeric dispersion), has been manufactured in high tonnage around the globe and constitutes a major volume of polymer manufacturing nowadays. The major applications of latexes or polymeric nanoparticles include those in paint and coating, paper and paperboard, packaging and adhesives etc. Antionetti and Tauer (2003) estimated that about 25% of the total amount of synthetic polymers produced worldwide (approximately 2 x 10^8 metric tons per annum at that time) is prepared via various heterophase polymerization routes. This rough estimate implies that a minimum financial value of 50 billion € was generated annually. In fact, the environmental applications of these polymers are not new at all. For instance, water soluble polymers are being applied at every water/wastewater's coagulation/flocculation units.

Other emerging application areas for polymeric nanoparticles are biomedical and pharmaceutical science, for instance, protein bioseparation and drug-delivery (Kawaguchi, 2000). The concept of immobilizing reagents or probes on polymer support for use in chemistry and biology has received a great deal of attention. Since the activity of supported reagents depends on the accessibility of the active sites and is often limited by intraparticle-diffusion (Guyot, 1988), considerable efforts have been made to develop new polymer supports with improved capacity, accessibility and selectivity (Okay, 2000; Sherrington, 2001). This issue has tremendous implication on the environmental applications. For instance, it is well known that the chelating resins (diameter of 0.3-1.2 mm) have slow kinetics despite their high affinity towards heavy metals cations (Sengupta and SenGupta, 2002). A variety of polymeric nanoparticles with different surface functional groups for instance, amine groups or epoxy groups,

can be readily synthesized from scratch (Ma, 1999) or through surface-functionalization (Kawaguchi, 1999; Wang *et al.*, 2003). Besides surface chemistry, the morphology of polymeric nanoparticles can be varied as well (Figure 2.5). Hence, the polymeric nanoparticles may serve as nanoscale polymer supports, for instance, nanocarrier for precious metal catalyst (Biffis, 2001). Larpernt *et al.* (2003) demonstrated that polymeric nanoparticles can be dendronized at ease and the resulting nanoparticles could be used as an inexpensive substitute for applications involving dendrimers.

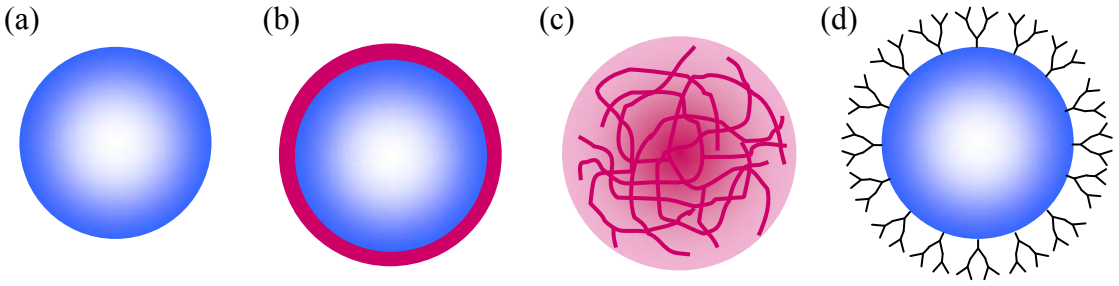

Figure 2.5 General morphology of polymeric nanoparticles: (a) homogeneous sphere; (b) core/shell sphere; (c) microgel; (d) dendronized sphere.

In general, the synthetic processes whereby these polymeric nanoparticles are manufactured are well-established and scalable. Despite the various advances in synthesis and functionalization of polymeric nanoparticles in recent decades, relevant environmental applications of these nanoparticles remain rare. This may be due to the misconceptions including difficulty in recovery and reuse of nanoparticles, and high synthesis/manufacturing cost. The manufacturing industry of polymer-emulsions is well established world-wide, so is the associated downstream separation process. Filtration processes such as microfiltration and ultrafiltration have already been accepted by industry as major operation for separation of latex emulsions (Cheryan, 1998). In the following section, research literature on polymeric nanoparticles are outlined to illustrate their remediation potential.

2.2.4.2 Polymeric nanoparticles for water/wastewater treatment

One of the first environmental applications of polymeric nanoparticles was investigated by Snowden and Vincent (1993) who have studied the applicability of using of poly(N-isopropylacrylamide) (PNIPAAm) colloidal microgels or nanoparticles for removal of heavy metals such as Pb(II) and Cd(II) (Table 2.4). The binding sites for metal ions were derived from the thermal initiator molecules used. Hence the removal capacity for both heavy metals ions was limited as the ratio of initiator to N-isopropylacrylamide was kept small in all the synthesis. For instance, the adsorption capacity achieved for Pb(II) was only 0.4 mmole/g at solution pH 6.0. This shortcoming was overcome by Morris *et al.* (1997) by copolymerizing PNIPAAm nanoparticles with a co-monomer, acrylic acid. They reported an improved performance, for example, the specific adsorption capacity for Pb(II) at pH 8.0 to be 2.4 mmole/g, which they attributed to the favorable Coulumbic attraction between carboxylate groups and positively charged lead species. Kanazawa *et al.* (2004) experimentally demonstrated that the adsorption kinetic by nanoparticles prepared was significantly improved, as compared to their bulk analogue. For instance, the former took only 100 minutes to attain adsorption equilibrium, while the latter required 100 hours at least.

Antonietti *et al.* (1995) explored the synthesis of metal-chelating nanoparticles by one-step functionlization via miniemulsion polymerization approach. Polymeric nanoparticles of 13 to 19 nm were obtained successfully. The bipyridine-based metal-chelating groups are located on the surface of the nanoparticles and are accessible. It was observed that the complexation completed within minutes. In addition, the nanoparticle solution remained colloidally stable after metal ion adsorption, which

indicates that the cooperative binding event occurs between every two neighboring bipyridine groups solely.

Polymeric nanoparticles could acts as better nano-carrier than that of LM-MEUF as discussed earlier. Recent advances in polymer science and technology provide a great variety of efficient tool for surface-functionlization of polymeric nanoparticles or latexes (Wang *et al.*, 2003). Specific ligands could be grafted or second polymer layer could be deposited onto the particle surfaces, resulting in a change in surface functionalities and morphologies. The grafted ligands are covalently bonded and highly accessible to the multivalent ions or molecules in surrounding environment; whereas for LM-MEUF, the hydrophobic ligands are solubilized within the core of micelles and the sequestration kinetic is therefore lower. Amigoni-Gerbier *et al.* (1999; 2002) explored the synthesis and application of cyclam-grafted nanoparticles as recoverable chelating agents. Due to the small size (13 – 20 nm) of the nanoparticles, the nanoparticle suspension was stable and transparent. The cyclam ligands binds specifically copper ions with high selectivity, in the presence of other cations. The loading of cyclam ligands of 0.73 mmole/g is one-fold higher than those obtained by other approaches reported elsewhere (Amigoni-Gerbier *et al.*, 2002). Fast chelation kinetics was observed and about 85-90% utilization of the available ligands is easily achieved. The nanoparticles remain stable after dialysis or Cu(II) complexation. The binding capacity of 0.6 mmole-Cu(II)/g of the resulting nanoparticles plus its ease of preparation demonstrates its competitive edge over others, for instance PAMAM dendrimers of generation 8, which has a Cu(II) binding capacity of 0.65 mmole/g (Diallo *et al.*, 1999).

Chen *et al.* (2003) modified the surface-aminated polystyrene nanoparticles with azo-chromophore. It was found that the ligand-modified nanoparticles remain adsorptive towards Pb(II) after 3 cycles of adsorption/desorption processes. Bell *et al.* (2006) synthesized polymer nanoparticles with core/shell structure. They demonstrated that the heavy metals sequestration selectivity could be altered by grafting a macrocyclic ligand. The original core/shell nanoparticles is selective towards mercury ions solely; whereas the modified nanoparticles would only adsorb Co(II) despite presence of thousand-fold excess of other heavy metals ions, such as mercury. Therefore, the polymeric nanoparticles could be conveniently engineered or tailored to display specific remedial function such as selective sequestration of heavy metals.

Another research area which receives considerable attention recently is the synthesis of biopolymer-based nanoparticles for environmental application (Qi and Xu, 2004; Chang and Chen, 2005). Chitosan is a natural polysaccharide with rich functionalities. Due to its non-toxicity and low cost, chitosan has been studied extensively in various areas such as biomedicine and water/wastewater treatment (Li and Bai, 2006). Chang and Chen (2005) carboxylated the chitosan polymer and later covalently bonded to magnetite nanoparticles, whereas Qi and Xu (2004) obtained the chitosan nanoparticles through simple ionic-gelation nucleation method, wherein tripolyphosphate (TPP) acts as ionic crosslinker. Both groups of authors reported high Cu(II) removal capacity. However, chitosan nanoparticles obtained via ionic-gelation has a critical drawback: they gradually disintegrate in aqueous media over days or aggregate in alkaline solution (pH 9.0) (López-León *et al.*, 2005). This is mainly due to the weak electrostatic interactions between chitosan chains and TPP molecules, as proven by the complete disintegration of spherical chitosan nanoparticles into

dissolved polymer chains in solution of high ionic strength (125 mM of KNO_3). Like any other adsorbents, a systematic physicochemical examination should accompany the remedial assessment of nanoparticles in order to fully understand their potentials and pitfalls.

Polymeric nanoparticles resemble dendrimers minus of latter's' precise intramolecular structure and symmetry, and therefore they should perform as effective as dendrimers because of their high volumetric binding site density. Under right solution condition, these binding sites that reside within the polymeric nanoparticles could become available for sequestrating metal ions in surrounding aqueous solutions, for instance, when the polymeric nanoparticles are fully swollen.

Table 2.4 Survey of literature on polymeric nanoparticles and related metal ion removal applications.

Type of polymeric nanoparticles	**Particle size** (nm)	**Target metal ions**	**Major functional groups for metal ion binding**	**Remarks**	**Reference**
Core/shell polystyrene-*graft*-poly(vinylamine)	~500	Pb(II), Cu(II)	Bare nanoparticles: amine group and amide group. Modified nanoparticles: residual amine group and azo-chromophore (imine group, amide group and hydroxyl group)	Adsorption efficiency of Pb(II) was enhanced, but the resulting nanoparticles did not display exclusive selectivity towards Pb(II). This is because the copper ions have access to the amine groups buried beneath the corona.	Chen *et al.*, 2003.
Core/shell polystyrene-*co*-poly((2-acetoacetoxy)ethyl methacrylate)	~70	Hg(II), Co(II)	Bare nanoparticles: xanthate (thiolate group) and oxygen donor on the ester group. Modified nanoparticles: NH_2-capten (secondary amine group and thiolether groups)	Selectivity in heavy metals sequestration (ppb level) can be engineered onto the particle surface by grafting a macrobicyclic ligand. Kinetic selective binding of Co(II) in the presence of 1000-fold excess of Cd(II), Pb(II), Hg(II) is achieved.	Bell *et al.*, 2006.
Poly(N-isopropylacrylamide) microgel (PNIPAAm)	~550	Pb(II), Cd(II)	The electrostatic interaction conferred to the microgel comes from the thermal initiators which possess sulfate group, carboxylic group and amidine group respectively.	Desorption of metal ion could be triggered by heating. Both absorption as well as adsorption was proposed to account for the incomplete desorption.	Snowden *et al.*, 1993.
Poly(N-isopropylacrylamide) microgel	~900 (>pH =6), ~650 (<pH = 4)	Pb(II)	Poly(acrylic acid) (carboxylic acid group)	Acrylic acid was copolymerized in the formulation to enhance the lead removal capacity. The presence of the additional acidic group within the gel network imparts pH dependence on microgel size.	Morris *et al.*, 1997.
Poly(N-isopropylacrylamide) microgel with metal chelating	~750	Cu(II)	N-(4-vinyl)benzyl-ethylenediamine (amine group)	The thermosensitive microgel was incorporated metal ion chelation ability via copolymerization. The drastic increase in adsorption rate was observed, compared to bulk analogue in previous work. Molecular imprinting technique was employed in this work too.	Kanazawa *et al.*, 2004.

Polystyrene nanoparticles	13-19	Ni(II), Co(II), Cr(II), Cu(II), Pd(II)	These co-monomer were synthesized and used in synthesis: 4-methyl-4'-2,2'-bipyridine, 6'methyl-2,2'-bipyridine-6-ylmethyl methacrylate, 4-(6'-methyl-2,2'-bipyridin-6-ylmethoxy)butyl methacrylate (bipyridine group)	Attempt was made to polymerize pyridine-containing monomer directly was unsuccessful. Instead, pyridine-containing nanoparticles were synthesized via copolymerization with styrene as main monomer. Results show that the pyridine moieties are located on the surface.	Antonietti *et al.*, 1995.
Polystyrene nanoparticles	13, 15, 20	Cu(II)	Vinylbenzyl-cyclam (cyclam: 1,4,8,11-tetraazacyclotetradecane)	Fast adsorption kinetic towards copper ion was reported. Synthetic methodology adopted herein allows 1-fold higher of cyclam loading. 40-70% of cyclam is located on the particle surface and hence has good access to copper ions, which allows spontaneous and stochiometric binding between cyclam and copper ion. The remaining buried in core undergo diffusion-limited complexation.	Amigoni-Gerbier *et al.*, 1999.
Polystyrene nanoparticles	13, 15, 20	Cu(II), Zn(II)	Vinylbenzyl-cyclam (cyclam: 1,4,8,11-tetraazacyclotetradecane)	The UV/Vis spectroscopy revealed that the ligand accessibility is closely correlated with the particle size. Selective sequestration of copper ion in presence of large excess of competing ion does take place.	Amigoni-Gerbier *et al.*, 2002.
Biopolymer—chitosan nanoparticles	40, 100	Pb(II)	Pristine amine groups and polyphosphoric groups derived from the ionic gelation	Freeze-drying was applied to lower the crystallinity of the chitosan nanoparticles, which led to better sorption performance.	Qi and Xu, 2004.
Magnetic nanoparticles coated by chitosan	13.5	Cu(II)	Pristine amine groups from chitosan	A Cu(II) high adsorption capacity based on chitosan content is reported, attributed to high specific surface area.	Chang and Chen, 2005.

2.3 Preparation of Poly(4-vinylpyridine)-based Nanoparticles

Because of the useful adsorption properties of poly(4-vinylpyridine) (P4VP) (Steel, 1990; Chanda and Rempel, 1993; Talanova *et al.*, 2001), the preparation of P4VP-based nanoparticles is therefore pursued in this work. Various approaches reported in the literature for synthesizing P4VP-based nanoparticles with high pyridine content are generally in lack of synthetic versatility or they rely on tedious experimental steps. Many studies showed that 4VP should be copolymerized with another hydrophobic co-monomer such as styrene (Sty) (Wang and Pan, 1999; Ni *et al.*, 2001) or *N*-isopropylacrylamide (NIPAM) (Pinkrah *et al.*, 2003) to facilitate coagulum-free formation of nanoparticles. The successful surfactant-free preparation of nanoparticles made of homopolymer of 4VP with cationic initiator (V50) (particle diameter = 357 nm) was first reported by Davies *et al.* (1995). Pathak *et al.* (2000) also prepared P4VP nanospheres with a diameter of around 500 nm and showed that those nanospheres could function as a catalyst support. However, both group made no attempt to investigate the effects of various experimental parameters for the nanoparticle synthesis.

Another polymerization system which had successfully produced P4VP particles of high 4VP content (more than 90%) was based on the dispersion polymerization method reported by Takahashi *et al.* (1997), who prepared P4VP particles of 1 – 2 μm in size. Their recipe requires the use of proprietary poly(styrene-*b*-butadiene)-based surfactants. Moreover, the synthesis was conducted in organic solvent (mixture of *N*,*N*-dimethylformamide and toluene) which has to be highly anhydrous, and therefore

effort-demanding. Ma and Fukutomi (1991) developed a preparative technique based on the emulsion polymerization approach and produced nanoparticles of the sizes in the range from 70 to 700 nm. Their success in size control relied on preparing the polymerizable quaternized poly(4-vinylpyridine) polymer through tedious multistep procedures, and the polymer acted as a electrosteric surfactant for the subsequent emulsion copolymerization with 4VP. Dupin *et al.* (2006) successfully prepared narrowly-dispersed polymeric nanoparticles made of 2-vinylpyridine, an isomer of 4VP, through batch emulsion polymerization wherein both a non-polymerizable surfactant (trialkyl quaternary-ammonium, Aliquat® 336) and poly(ethylene glycol) methacrylate were added to control the particle size. Though the emulsion polymerization method could be easily performed with the addition of conventional surfactants or emulsifiers (Gilbert, 1995), a few severe drawbacks have been encountered during the application. Conventional surfactant molecules (e.g. SDS, CTAB and CPC, see Figure 2.3) stabilize the particle suspensions by adsorbing to the particle surface via weak physical forces, and could be easily desorbed when the particle suspensions are subjected to intense shearing or repeated freeze-thaw cycles, or even leached out upon prolonged exposure to water (Capek, 1999; Wilkinson *et al.*, 1999). One approach to alleviate this problem is to replace conventional surfactants with their polymerizable analogues that have carbon-carbon double bonds and can be covalently grafted onto the particles (Capek, 1999; Capek, 2000).

With some modifications, the surfactant-free emulsion polymerization (SFEP) method is employed and studied in this work because of its ease of preparation, high reproducibility and good size monodispersity (Song and Poehlein, 1990; Fritz *et al.*, 1997). Mechanistically, a typical SFEP comprises the following steps based on the

"homogeneous-coagulative nucleation" theory (Feeney *et al.*, 1987; Gilbert, 1995): the decomposition of water-soluble initiator molecules gives rise to charged free radicals which react with molecularly-dissolved monomers to form oligomeric radicals that also function as charged stabilizers formed *in-situ* (Song and Poehlein, 1989; Li and Salovey, 2000). These radicals propagate further and react with more monomers in the aqueous phase until the oligomeric radicals attain a critical degree of polymerization. Precursor particles are then formed when these radicals precipitate. These precursor particles are colloidally unstable and would coagulate to produce larger stable particles as the precursor particles only contain few *in-situ* stabilizers. Once they acquire adequate colloidal stabilization, the major locus of polymerization would shift to these stable particles that are swollen with the monomers. These particles continue to grow in size till they are exhausted of the monomers. Nanoparticles formed from SFEP are generally monodispersed in size because the particles are formed so fast that they emerge essentially at the same time and are allowed to grow equally thereafter (Ferguson *et al.*, 2002). Polymeric nanoparticles which are narrowly distributed in size are desired in this study because they can be readily removed using a membrane separation system, in a similar manner as those of DEUF or MEUF discussed earlier. Their size monodispersity also allows for straightforward investigation on their size-dependence properties.

2.4 Technologies for Nanoparticle Separation and Recovery

Various separation technologies have been studied for their use in separation, fractionation, purification or recovery of a wide range of nanoparticles. Most of the as-prepared nanomaterials or nanoparticles may be contaminated by chemical impurities, unreacted or residual precursors. For examples, the major impurities encountered with

polymeric nanoparticles or colloids consist of unreacted monomer, low molecular weight oligomers, emulsifiers, buffers, bacteria and fungi, and various byproducts of the polymerization, etc. (Wilkinson *et al.*, 1999). Purification and cleaning of these contaminated nanoparticles is therefore critical for them to meet safe and sustainable commercial end-use or industry requirements. Because of their high specific surface areas and many chemical-related surface activities, nanoparticles have attracted many attentions in their safety, health and environment related issues (Makino *et al.*, 2008). Many studies have demonstrated the potential adverse effects of nanoparticles on the well-being of environment and human health (Altken *et al.*, 2004). The toxicology and the potential toxic effects of these nanoparticles on organisms in natural environments are also largely unknown (Colvin, 2003; Liu, 2006). Effective control of the transport and fate of these nanoparticles is therefore crucial in view of these possible catastrophic impacts.

Some major separation techniques which enjoy wide popularity nowadays are reviewed in the following section. Other emerging separation techniques such as nanoprecipitation (Jesús and Flores, 2008) or anti-solvent addition (Myakonkaya *et al.*, 2010) are not reviewed as these techniques are still in their infant stage and are not used in this study. The major factors determining the usefulness and potential for further process intensification include the recovery efficiency of the separation process (process yield), the separation selectivity, the complexity of the separation technique, the capital and operating costs, as well as the possible alteration of the physicochemical properties of the pristine nanoparticles.

2.4.1 Centrifugation/Ultracentrifugation

One of the commonly employed techniques for separating impurities from nanoparticle suspensions, or washing of nanoparticles on laboratory-scale is centrifugation or ultracentrifugation followed by decantation (Calvo *et al.*, 1997; Govender *et al.*, 1999). However, the irreversible nanoparticle aggregation may occur (Wilkinson *et al.*, 1999), and the re-dispersion of the nanoparticles became difficult. The average particle sizes were significantly affected by the pelletization or caking of the nanoparticles, after subjecting to the high centrifugal force (Chiellini *et al.*, 2003). Unsatisfactory separation of the nanoparticles would occur when the centrifugation force applied is insufficient to pull the very fine, dense nanoparticles towards the center of centrifugation (Dalwadi *et al.*, 2005). Purification of very fine nanoparticles, e.g. 3 nm gold nanoparticles, was often difficult, even with the aid of high-speed ultracentrifugation (~ 60,000 rpm) (Kanaras *et al.*, 2002). This technique may be simple to use on preparative-scale for nanoparticle separation. However, its potential for scale-up to meet industry requirements is limited due to its restricted volume-handling capacity and high installation cost.

2.4.2 Magnetic Separation

Magnetic or magnetically susceptible nanoparticles are easily remotely manipulated and can be removed from the nanoparticle suspensions by applying an external magnetic field (Huber, 2005). The magnetic separation method is particularly suited for the iron-based nanoparticles, e.g. the Fe_3O_4 magnetite nanoparticles described earlier due to their inherent magnetic susceptibility. Nonetheless, the magnetic properties of the nanoparticles are greatly influenced by their chemical compositions and sizes (Ozin, 1992). Yavuz *et al.* (2006) demonstrated that the highly

monodispersed magnetitie nanocrystals responded to magnetic field differently, depending on the particle sizes. For instance, they showed that the very fine nanocrystals (~ 4 nm) could not be retained at all by the low field applied, while the larger nanocrystals (~ 20 nm) were permanently adsorbed onto the ferromagnetic wire-filled column upon removal of magnetic field. Successful retention of the 16 nm nanocrystals was achieved at low field gradients (< 100 T/m). The maghemite nanoparticles obtained by Hu *et al.* (2005) displayed paramagnetism which they attributed to the small size of the nanoparticles (~ 10 nm) (Watson *et al.*, 2000).

Superparamagnetic iron oxide nanoparticles, which are able to respond to an external magnetic field without any permanent magnetization, can be captured magnetically and re-dispersed again after removal of the magnetic field. This particular feature prolongs their dispersion stability since no residual magnetization is observed upon the removal of magnetic field (Huber, 2005, Xu and Sun, 2007). Superparamagnetic surface-modified jacobsite nanoparticles that could rapidly sequestrate Cr(VI) were readily magnetically separated and regenerated after the metal ion adsorption reached equilibrium, as demonstrated by Hu et al. (2005b). Besides, size-based fractionation of polydispersed nanoparticles can be carried out too, as demonstrated by Kelland (1998) and Yavuz *et al.* (2006).

Despite the ease of use and immediate advantage, the use of magnetic field in separating the iron-based or iron oxide nanoparticles suffers several inherent drawbacks. Some of these problems that need to be addressed prior to actual environmental application are as follow. The magnetic interaction among the nanoparticles that are not superparamagnetic would lead to irreversible aggregation

(Nurmi *et al.*, 2005) after prolonged exposure to magnetic field (Phenrat *et al.*, 2007). The value of the saturation magnetization of the iron oxide nanoparticles is often low, as compared to their bulk analogues. Their weaker magnetic strength would render their separation to be less efficient. Additional polymer coatings that are either physically adsorbed or chemically reacted onto the surfaces of the nanoparticles would shield the nanoparticles, thereby lowering their saturation magnetization (Rosensweig, 1985). Magnetic separation may not be applicable for separation of polymeric nanoparticles as these nanoparticles are not magnetically susceptible.

2.4.3 Pressure-Driven Membrane Filtration

Pressure-driven membrane filtration technology has long been used for cleaning, purification and size-based fractionation of a wide range of natural or synthetic colloids, cells and proteins through steric exclusion mechanism (Cheryan, 1998; Zeman and Zydney, 1996). Two major types of membranes used for these applications are ultrafiltration (UF) membranes and microfiltration (MF) membranes. Generally, the UF membranes have pore size ranging from 1 nm to 0.1 μm, which enable them to be used for separating or purifying macromolecular solutes and very fine nanoparticles, for instance, protein concentration and buffer exchange. The MF membranes typically have larger pore size, ranging from 0.05 μm to 10 μm, making them particularly suited for ultrapure water production in semiconductor manufacturing plants and removal of pathogens and viruses. As compared to other separation methods, the membrane-based technology is often favored because of its overall techno-economic potentials: low energy consumption, low system footprint, high throughput capacity and ease of up-scale.

Cross-flow or tangential flow filtration has found wide use in many industry nowadays (Ripperger and Altmann, 2002). Dalwadi *et al.* (2005) experimentally investigated and compared the performances of commercially available diafiltration centrifugal device (DCD), ultracentrifugation and tangential flow filtration (TFF) systems for the removal of excess poly(vinyl alcohol) from the polylactide nanoparticles (mean particle size ~ 300 nm). The purification of the polylactide nanoparticles with the TFF system in concentration mode (MWCO = 300 kDa, operating pressure = 2.75 to 10 psi), which consists of ultrafilter operated in cross-flow mode, was demonstrated to be more efficient than dialysis and DCD, while the impact on the recovery yield, size and stability of the nanoparticles was reduced considerably. Sweeney *et al.* (2006) reported the rapid purification of water-soluble gold nanoparticles of 3 nm, using a continuous TFT (100 kPa, polysulfone ultrafiltration membrane of MWCO = 70 kDa) operated in diafiltration mode, i.e. constant hold-up volume. In addition, the high-resolution size separation of a bimodal mixture of gold nnaoparticles (1.5 nm, 3.1 nm) was also successfully conducted, by selecting a diafiltration membrane with appropriate pore size or MWCO (in this case, the selected MWCO of the membrane was 50 kDa). Separation of polydispersed nanoparticles into several more monodispersed fractions was demonstrated as well.

The major drawbacks associated with the membrane filtration for nanoparticles are the concentration polarization on the membrane surface, and the internal fouling of the membrane. In addition, the efficiency of separation/rejection of fractionation is often a complex function of various process conditions. As demonstrated by Brans *et al.* (2007), the fractionation of bi-dispersed nanoparticle suspensions was complicated by the particle size ratio and the choice of transmission regime, cross-flow velocity as

well as membrane morphology. For example, the use of microsieve filter with regular pore size led to more in-pore fouling while the random depth deposition vanished. During the filtration process, the nanoparticles in the process fluids are pulled towards the membrane surface. These nanoparticles would deposit and accumulate on the membrane surface, provided that the dimensions of the nanoparticles are larger than the surface pore size of the membrane. These deposited materials impose additional hydraulic resistance and decrease the process productivity. The nanoparticles that are smaller than the membrane pore size may enter the pores and transmit through the membrane, leading to low recovery yield. Or else, the nanoparticles can adsorb and aggregate onto the pore wall, or even plug the membrane pore completely. To alleviate the fouling problems, many effective process strategies and cleaning methods have been extensively researched and optimized (Zeman and Zydney, 1996; Nidal *et al.*, 2005). Because of the simplicity and wide industrial use, the membrane filtration would be used for the nanoparticle separation in this work. However, to avoid membrane fouling, particularly by pore-blocking, highly uniform P4VP nanoparticles will be prepared and used in this study.

2.4.4 Electric Field-Assisted Separation

Other than those discussed above, direct current (DC) or alternating current (AC) electric fields were also studied for their ability to control and manipulate the transport and separation behavior of nanoparticles. The first theoretical analysis for the electric-field assisted cross-flow filtration ('electro-filtration') was given by Henry *et al.* (1977). Many researchers have studied the separation performance of the electric field-enhanced cross-flow filtration for nanoparticle separation (Weigert *et al.*, 1999; Lin *et al.*, 2007; Molla and Bhattacharjee, 2008). Most nanoparticles or colloids are

charged in their suspending mediums, such as water. The superimposition of DC electric field normal to the cross-flow direction would generate electrophoretic movement of the charged nanoparticles away from the membrane surface during filtration. Lin *et al.* (2007) experimentally demonstrated the size separation of polydispersed nanoparticle suspensions (γ-Al_2O_3 particles with mean size of 209 nm, and SiO_2 particles with mean size of 76-126 nm) by varying the electrostatic field strength. Many efforts were spent on minimizing the colloidal fouling of membrane with such process. For example, Weigert *et al.* (1999) demonstrated that the permeation flux for the microfiltration of silica particles can be enhanced by ten folds when an external electric field was applied across the cross-flow filtration module. Repulsive dielectrophoretic (DEP) force may be imposed on the suspending particles (of lower dielectric constant than that of the surrounding medium) when an AC is applied to an optimally designed parallel microelectrode array embedded in the membrane (Molla and Bhattacharjee, 2005). By applying an electric field of appropriate strength, the particles can be repelled from the regions of high electric field intensities (i.e. the microelectrode embedded membranes). Molla and Bhattacharjee (2008) reported a rejection percentage of about 80 % for 2 μm polystyrene particles with nylon mesh filter with a pore size rating of 10 μm.

The first successful case of membrane-less, dielectrophoresis-based field flow fractionation for nanoparticles was reported by Du *et al.* (2008) for separating the ultrathin gold nanoplates (227 nm in diameter and 30 nm in thickness) from a mineral mixture (zircon and quartz). A separation efficiency of 88% was achieved at field strength of 31667 V/m, without dosing of hazardous chemical. Another membrane-less electric-field enhanced separation was the free flow electrophoresis reported by

Ho *et al.*, 2009. The successfully simultaneous purification and size fractionation of polydispersed CdTe nanoparticles (2.7 – 8.7 nm) in aqueous solutions into several partitions with better size monodispersity was conducted, while their original optical (fluorescence) properties were preserved. The separation of the nanoparticles was achieved by applying a high DC field applied through the hydraulic channel in which the nanoparticles solution was pumped along. The applied field induced the nanoparticles' movement in the transverse direction, in which their velocity is linearly proportional to their electrophoretic mobility, or charge-to-size ratio. Though there are extensive research efforts to advancing these innovative separation techniques, these electric-field based techniques are however not energy-friendly as high electric field strengths are often required and the associated energy loss through electrothermal effect can be significant (Du *et al.*, 2008). Furthermore, the separation efficiency of these technologies is highly dependent on the process variables, such as solution composition, salt content, flow velocity, etc. (Ho *et al.*, 2009), therefore additional pretreatment of the nanoparticle suspensions prior to entering the separation may be necessitated to meet the stringent process conditions.

2.5 Membrane Fouling Behavior in Nanoparticle Filtration

The relative size of contaminants and membrane pores is usually regarded as the primary factor in determining the occurrence of surface fouling and internal plugging (Wakeman, 2007). The membrane fouling behavior in nanoparticle filtration is similar to that of colloidal fouling (Wiesner and Aptel, 1996). Membrane fouling generally refers to the alteration in membrane properties arising from adsorption or deposition of suspended matters on the membrane surface or within the membrane pores. Membrane fouling can be classified as internal fouling and external fouling in general.

Internal fouling usually refers to deposition and absorption of small particles or macromolecules within the internal pore structure of membranes (e.g. (c) of Figure 2.6), whereas external fouling refers accumulation of large rejected particles on top of the membrane surface (e.g. (d) of Figure 2.6).

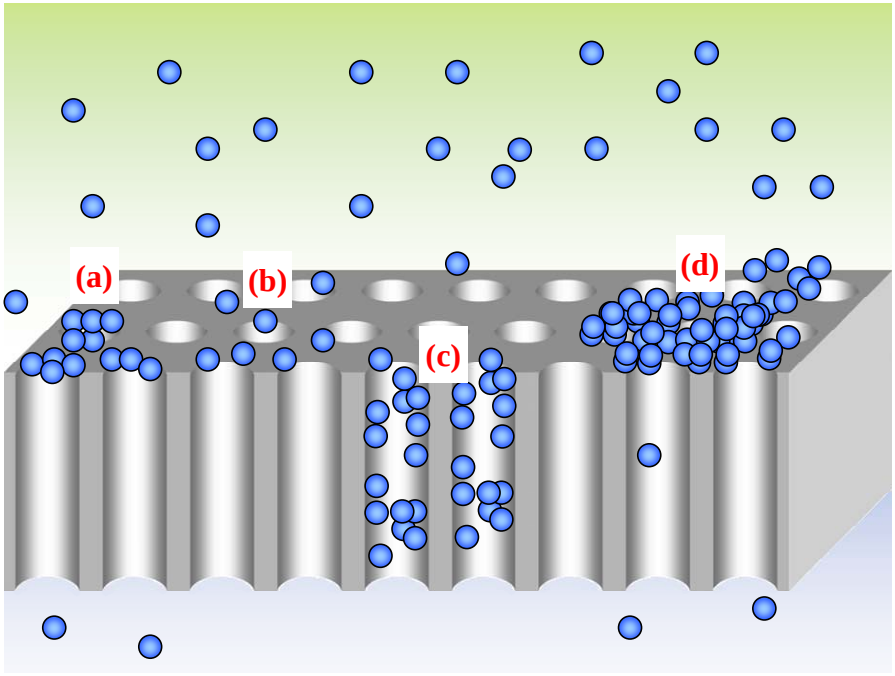

Figure 2.6 Schematic representations of the various mechanisms in membrane fouling by particles: (a) complete blocking, (b) intermediate blocking, (c) pore constriction, and (d) cake filtration.

Base on the blocking filtration theory (Hermia, 1982), the filtrate flux decline during colloidal fouling of membrane can be caused by the four mechanisms: complete blocking, pore constriction (standard blocking), and intermediate blocking and cake filtration (Ho, 2001; Alexia *et al.*, 2008). These mechanisms are schematically shown in Figure 2.6. For constant pressure filtration, a common frame of power law relationship was developed as the governing equation to include all fouling mechanisms (Hermia, 1982; Alexia *et al.*, 2008):

$$\frac{d^2t}{dV^2} = k\left(\frac{dt}{dV}\right)^n \text{ or } \frac{dJ}{dt} = -kJ\left(JA_0\right)^{2-n} \tag{2.5}$$

where t is the filtration time, V is the filtrate volume, $J = \frac{1}{A}\frac{dV}{dt}$ is the filtrate flux, A is the effective filtration area of the membrane, and k and n are filtration constants. The exponent (n) characterizes the filtration model, with $n = 0$ for cake filtration, $n = 1$ for intermediate blocking, $n = 3/2$ for pore constriction, and $n = 2$ for complete pore blocking. The mathematical expressions for the integrated form of the blocking law model in Eq. (2.5) for different values of exponent n are summarized in Table 2.5.

Table 2.5 Summary of mathematical expressions derived from Hermia's Blocking Law for different fouling mechanism.

Model types	n	Integrated form
Complete Blocking	2	$V = J_0\left(1 - e^{-kt}\right)$
Pore Constriction Model	3/2	$\frac{t}{V} = \frac{k}{2}t + \frac{1}{J_0}$
Intermediate Blocking	1	$kV = \ln\left(1 + ktJ_0\right)$
Cake Filtration	0	$\frac{t}{V} = \frac{k}{2}V + \frac{1}{J_0}$

(a). Complete blocking: this model describes the clogging or sealing of pore entrances or pore mouths. The amount of effective area open for flow movement is reduced. This model is valid for particles which have a very similar size to the membrane pores. The particles seal the pores (surface or bulk) and do not accumulate on each other.

(b). Intermediate blocking: this phenomenon is characterized by having the pore partially blocked by the particles or particle assemblage on top of the membrane pore entrances. Every particle reaching a pore will contribute to blockage and particles accumulate on each other. Both intermediate blocking and complete blocking cause apparent reduction in the total

number of pores available for filtration. The classical pore blockage model predicts that the plot of the filtration flux versus filtration volume is linear.

(c). Pore constriction (standard blocking): this model describes the particle accumulation inside the membrane on the pore walls, wherein the particles that are much smaller than the pores.The classical pore constriction model predicts that t/V should be linear with t. Particles pass through the pores and deposit on the surface of the pores.

(d). Cake filtration: Particles which are much larger than that the membrane pores are retained on the surface by the permeation pull, without entering the pores. The particles deposit and accumulate on the membrane surface, forming a permeable cake of increasing thickness, which poses hydraulic resistance to filtration by contributing to the boundary layer resistance. This model includes deposition due to concentration polarization. The amount of particles or foulants accumulated is proportional to the filtrate volume. The classical cake filtration predicts that a plot of t/V should be linear with V.

Pore constriction is only possible for membrane with relatively large pores that are easily accessible to the particles. Pore blockage and cake filtration usually dominate when the pores are smaller than the particles. Both pore blockages and pore constrictions are classified as internal fouling and cake filtration is external fouling.

CHAPTER 3

PREPARATION AND CHARACTERIZATION OF HIGHLY MONODISPERSED POLY(4-VINYLPYRIDINE) BASED NANOPARTICLES

3.1 Introduction

For effective removal and recovery of palladium from acidic medium, the adsorbents should ideally possess high remedial capacity and rapid sequestration kinetics. In addition, these nanoparticles need to be completely separated from the treated solutions for adsorbent regeneration and reuse. Many adsorbents developed in recent years for decontamination of palladium-laden solutions have shown their limitation and hence further innovation and synthesis efforts are needed. Emerging adsorbents, such as those based on nanotechnology or nanomaterials have been developed to meet these increasingly stringent requirements. For example, the magnetite nanoparticles (Uheida *et al.*, 2006a; Uheida *et al.*, 2006b; Rossi *et al.*, 2007; Vatta *et al.*, 2007) were prepared and investigated for their efficacy in decontamination of palladium-laden waste solutions or for palladium recovery. For these adsorptive nanomaterials, the contact time for adsorption equilibrium is typically short (< 30 minutes) (Uheida *et al.*, 2006a; Uheida *et al.*, 2006b), attributed to their high specific surface areas. However, these nanoadsorbents have low uptake capacity because of their low surface density of binding sites for metal ion adsorption. Additional post-synthesis chemical modification is required to improve either their selectivity or remedial capacity, which unavoidably makes the recovery of palladium inefficient due to the difficulty in their regeneration (Uheida *et al.*, 2006b; Vatta *et al.*, 2007).

To overcome that shortcoming of low binding site density, alternative nanomaterials for metal ion adsorption, such as poly(amidoamine) (PAMAM) dendrimers were explored (Diallo *et al.*, 2003). Because of the high volumetric density of chargeable amine groups residing within the dendrimer, the PAMAM dendrimers were demonstrated to have a binding capacity for copper removal, in the range of 308 to

451 mg-Cu/g,. In addition, the sequestration kinetics of these nanoscale adsorbents was rapid because of their nanoscale dimensions. Despite their superior adsorption performance, the separation and reuse of these dendrimers required the use of ultrafiltration grade membrane with tight selective layer of very small pore size (Diallo *et al.*, 2005). Furthermore, commercially available dendrimers are expensive (Dendritech, 2009). These drawbacks have thwarted the direct application of these nanoscale polymeric adsorbents.

Polymeric nanoparticles have appeared to be low-cost alternatives to dendrimer-based nanomaterials. By sacrificing the precisely engineered, symmetric microstructures of the dendrimers, the substitution of dendrimer-based adsorbents with monodispersed polymeric nanoparticles that have similarly rich chemical functionalities and high volumetric binding site density, becomes a technologically and economically viable approach for palladium adsorption. To date, there have been a number of reports on the preparation and use of polymeric nanoparticles for metal ion adsorption, for instance, lead adsorption with poly(acrylic acid)-based nanoparticles developed by Snowden *et al.* (1993) and Morris *et al.* (1997), and mercury removal with surface-modified poly(styrene-*co*-2-(acetoacetoxy)ethylmethacrylate) nanoparticles (Bell *et al.*, 2006). To prepare nanoparticles that are highly adsorptive for metal ion adsorption, the polymers or monomers (e.g. 4-vinylpyridine) that are based on pyridine or pyridyl groups are chosen as the precursors for nanoparticle synthesis in this work. Many poly(4-vinylpyridine)-based (P4VP) adsorbents have been investigated for adsorption of heavy metal ions (Chanda and Rempel, 1993; Talanova *et al.*, 1999), or precious metal ions (Talanova et *al.*, 2001; Kumaresan *et al.*, 2008).

To develop and engineer P4VP based functional polymeric nanoparticles that are simultaneously effective and robust for palladium adsorption or other target applications, a holistic examination of the polymerization recipe (selection of monomer, crosslinker, experimental conditions etc.) and synthesis procedure is needed (Klein and Daniels, 1997). To prepare monodispersed P4VP nanoparticles for palladium adsorption desired in this project, a two-pronged approach that was based on the surfactant-free emulsion polymerization (SFEP) method was developed in this work. Many polymerization approaches reported for synthesizing P4VP-based nanoparticles with high 4-vinylpyridine (4VP) content are generally in lack of synthetic versatility or relying on tedious experimental steps (Ma and Fukutomi, 1991; Takahashi *et al.*, 1997). For example, the emulsion polymerization approach developed by Dupin *et al.* (2006) made use of non-polymerizable trialkyl quaternary-ammonium surfactant (Aliquat® 336) that could be easily desorbed when the nanoparticle suspensions are subjected to intense shearing or repeated freeze-thaw cycles, or even leached out upon prolonged exposure to water (Capek, 1999; Wilkinson *et al.*, 1999). One approach to alleviate this problem is to replace the conventional surfactants with their polymerizable analogues that have carbon-carbon double bonds and can be covalently grafted onto the particles (Capek, 1999; Capek, 2000). With some modifications, the SFEP method is employed and studied in this work because of its ease of preparation, high reproducibility and good size monodispersity (Fritz *et al.*, 1997; Ferguson *et al.*, 2002).

In order to synthesize nanoparticles that possess the above desired properties for palladium recovery and removal from aqueous solutions in this work, 4VP was employed as the main monomer to prepare P4VP nanoparticles of high size

monodispersity. P4VP nanoparticles with narrow particle size distribution can also provide the advantage for easy separation and recovery by a membrane system similar to the DEUF or MEUF process.

3.2 Materials and Methods

3.2.1 Chemicals

The monomeric precursors and crosslinkers used in this work are shown in Figure 3.1, including 4-vinylpyridine (4VP), divinylbenzene (DVB), 80 mol% of 1,4-divinyl content) 2.2'-azobis(2-aminopropane) dihydrochloride (V50) (all are of the highest purity available, supplied by Sigma-Aldrich). Both 4VP and DVB were distilled under reduced pressure to remove their polymerization inhibitor and impurities, and were stored in argon at -20 °C. Poly(ethylene glycol) methyl ether methacrylate (PEGMA) with nominal molecular weight of 2080, (2-(methacryloyloxy)ethyl) trimethylammonium chloride (MATMAC), ethylene glycol dimethacrylate (EGDM), and poly(ethylene glycol) dimethacrylate (PEGDM) with molecular weights of 550 (n = 9) ad 750 (n = 13) were used as received. Palladium (II) chloride ($PdCl_2$) (99.9%, 59.9% as metal) was from Alfa Aesar. Sodium chloride (NaCl), thiourea (TU), sodium hydroxide (NaOH), hydrochloric acid (HCl) and nitric acid (HNO_3) are of analytical grade and were used without further purification in this work.

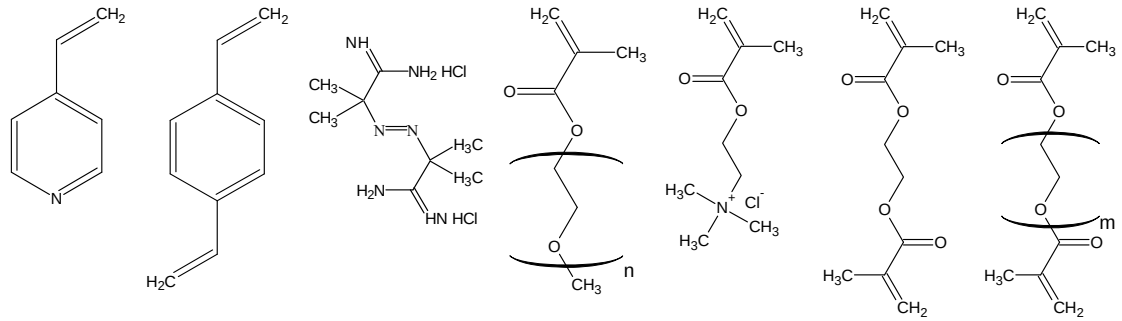

4VP	DVB	V50	PEGMA (n=46)	MATMAC	EGDM	PEGDM (m=9, 13~14)

Figure 3.1 Chemical structures of the monomeric precursors, crosslinkers and thermal initiator used in this work.

3.2.2 Synthesis of P4VP Nanoparticles

Pristine P4VP nanoparticles were synthesized through a surfactant-free emulsion polymerization (SFEP) method via either an *ab-initio* or a semicontinuous feed ("semibatch" or "starved-fed") approach, with the recipes given in Table 3.1. The *ab-initio* synthesis was conducted as follow. A 250 ml three-neck round bottom flask was fitted with a reflux condenser, a nitrogen inlet valve for inert gas blanket, and a mechanical overhead stirrer. The flask containing 197 ml of deionized water was heated to 70 °C, stirred at 300 rpm, and degassed vigorously with clean N_2 gas for 30 minutes, after which the gas flow was reduced to provide a gentle inert gas blanket. Then, a pre-mixed blend of 4VP (monomer) and DVB (crosslinker) (0.5 wt.% relative to that of 4VP) was injected in one-shot to the flask and the content was mixed for 15 minutes. The polymerization was then commenced by addition of a small amount of V50 dissolved in 3ml of deionized water. The content in the flask turned milky within the first 5 minutes of the polymerization, and was allowed to react for 6 hours before quenching the reaction by cooling the reaction to room temperature. In the case of semibatch polymerization, the reaction time was extended to 8 hours and a LC-10AD high pressure double-piston pump (Shimadzu, Japan) was used for injecting the

mixture of monomer and crosslinker at a constant flow rate into the flask, after V50 injection. Under the "monomer-starved" condition with no monomer (except the initiator and water-soluble co-monomers) in the initial charge, the polymerization rate would be reduced (Sajjadi and Brooks, 1999). Hence, the reaction mixture only turned milky or opalescent 30 minutes after the initiator was injected. The polymerization led to the production of P4VP nanoparticles suspended or dispersed in aqueous solutions. The nanoparticle suspension was filtered with a fritted-glass filter, and the retained coagulum formed was oven-dried and weighed to determine the amount of coagulum formed. Other P4VP-based nanoparticles, i.e. P4VP-PEGMA and P4VP-PEGMA-MATMAC nanoparticles crosslinked by DVB were synthesized by adding additional co-monomers into the water phase prior to commencing the polymerization, based on the ratios indicated in Table 3.2. Synthesis of PEGMA-P4VP nanoparticles copolymerized with other crosslinkers (EGDM, PEGDM) was also carried out by simply substituting the DVB with EGDM or PEGDM during the preparation of the pre-mixed blend.

Table 3.1 Surfactant-free emulsion polymerization recipes used in this work ([DVB] = 0.5 wt./wt.%-4VP)

Code	Monomer	Co-monomer(s)			Feed Mode	Yield		Particle Size				
	4-VP [g/100ml solution]	PEGMA [wt./wt.%-4-VP]	MATMAC [wt./wt.%-4-VP]	Initiator [wt./wt.%-4-VP]	Feed Rate [g/min]*	Conversion [%]	Coagulum [wt./wt.%-4VP]	D_n [nm]	D_w [nm]	D_{DLS} [nm]	PDI [-]	$N_p \times 10^{-15}$ [1/liter]
A-1	1.0	-	-	2.5	*One-shot*	99.0	nil	161.5	162.4	172.2 ± 2.9	1.006	4.03
A-2	1.5	-	-	2.5	*One-shot*	99.1	nil	239.3	242.1	248.9 ± 5.2	1.012	1.86
A-3	1.5	-	-	5.0	*One-shot*	98.2	1.5	354.0	356.9	364.1 ± 9.0	1.008	0.57
A-4	1.5	-	-	5.0	0.30	99.1	0.2	245.8	249.3	265.2 ± 1.3	1.014	1.72
A-5	1.5	-	-	5.0	0.10	96.8	0.1	180.9	185.8	196.6 ± 2.8	1.027	4.21
A-6	1.5	-	-	5.0	0.05	97.9	0.1	164.8	166.6	174.9 ± 1.9	1.011	5.63
A-7	1.5	-	-	2.5	0.05	99.0	0.2	132.4	135.9	136.5 ± 0.9	1.026	10.97
A-8	3.0	-	-	2.5	*One-shot*	98.3	42	-	-	851.4 ± 122.2	-	-
A-9	5.0	-	-	2.5	*One-shot*	98.9	85	-	-	1243.6 ± 239.3	-	-
A-10	5.0	10.0	-	2.5	*One-shot*	97.4	67	-	-	1104.0 ± 278.2	-	-

***** Under the "Feed Mode", the notion of "one-shot" indicates that the experiment was conducted *ab-initio*. Any number in that particular entry indicates that the experiment was conducted in "starve-fed" or semibatch feed mode.

Table 3.2 Surfactant-free emulsion polymerization recipes including hydrophilic co-monomers used in this work. ([DVB] = 0.5 wt./wt.%-4VP)

Code	Monomer	Co-monomer(s)			Feed Mode	Yield		Particle Size				
	4-VP [g/100ml solution]	PEGMA [wt./wt.%-4-VP]	MATMAC [wt./wt.%-4-VP]	Initiator [wt./wt.%-4-VP]	Feed Rate [g/min]*	Conversion [%]	Coagulum [wt./wt.%-4VP]	D_n [nm]	D_w [nm]	D_{DLS} [nm]	PDI [-]	$N_p \times 10^{-15}$ [1/liter]
B-1	1.5	2.5	-	2.5	0.05	96.5	1.3	90.2	93.4	107.6 ± 2.2	1.036	33.82
B-2	1.5	5.0	-	2.5	0.05	94.3	1.1	82.3	83.4	100.6 ± 3.2	1.013	43.50
B-3	1.5	10.0	-	2.5	0.05	93.1	1.4	74.3	77.9	92.5 ± 1.3	1.048	58.30
B-4	1.5	20.0	-	2.5	0.05	92.1	0.9	73.1	75.1	95.3 ± 0.6	1.027	60.63
B-5	1.5	10.0	-	2.5	*One-shot*	94.9	0.5	303.0	306.2	313.6 ± 5.4	1.011	0.088
B-6	3.0	10.0	-	2.5	*One-shot*	95.1	49	-	-	733.7 ± 361.2	-	-
B-7	3.0	10.0	-	2.5	0.05	94.0	20	-	-	223.1 ± 101.9	-	-
C-1	3.0	10.0	5	2.5	*One-shot*	96.2	1.2	623.1	637.9	646.4 ± 19.7	1.024	0.020
C-2	3.0	10.0	5	2.5	0.05	95.7	0.4	79.2	83.1	90.9 ± 0.5	1.049	98.35
C-3	5.0	10.0	5	2.5	0.083	93.3	1.0	101.7	103.6	113.4 ± 0.6	1.019	75.79

***** Under the "Feed Mode", the notion of "one-shot" indicates that the experiment was conducted *ab-initio*. Any number in that particular entry indicates that the experiment was conducted in "starve-fed" or semibatch feed mode.

3.2.3 Cleaning of Nanoparticles

The freshly-prepared nanoparticle suspensions were collected and cleaned by using the SpectraPor® MWCO 12,000-14,000 dialysis bag (Spectrum Laboratory, Inc., CA, USA) in constantly replenished deionized water for a few days to remove any unreacted monomer and initiator, and any low molecular weight polymers formed. The dialysis process was monitored by constantly measuring the ion conductivity of the water phase, and stopped when the conductivity was equal to that of fresh deionized water. The dialyzed nanoparticle suspensions were used as stock solution in subsequent experiments and the solid content (wt.%) of each batch of the nanoparticle suspensions prepared was determined gravimetrically. The typical solid content of the nanoparticle stocks in this work was 1.01 wt.%. Portions of the dialyzed P4VP or P4VP-based nanoparticle stocks were concentrated by centrifugation (9000 rpm), and the collected particle pellets were then vacuum-dried at 60 °C for at least 16 hours. The dried pellets were then stored in a dessicator for subsequent examinations such as elemental and spectroscopic analyses.

3.2.4 Characterization Methods

Electron microscopy. Field Emission Scanning Electron Microscope (FESEM) (JSM-6700, JEOL, Japan) was used to examine the morphology of the nanoparticles prepared. The samples were attached onto the metal sample stub by wet-casting the nanoparticle suspension onto carbon adhesive tape or copper tape, followed by solvent evaporation at room temperature overnight. The air-dried samples were platinum-sputtered before the FESEM observation. The accelerating voltage for the electron beam was set at 5kV for all analyses in the study. For better clarity, nanoparticles with sizes smaller than 100 nm were examined with a Transmission Electron Microscope

(TEM) (JEM 2010F, JEOL, Japan) operated at 200 kV. The P4VP or P4VP-based nanoparticles were wet-casted on 3mm carbon-coated copper grid support, followed by solvent evaporation at room temperature for at least 24 hours. The number- and weight-average diameters (D_n, D_w) as well as polydispersity index (PDI) of the nanoparticles synthesized were calculated as follow (Eqs. (3.1) – (3.3)), based on the size measurements from the electron micrographs (FESEM or TEM).

$$D_n = \frac{\sum n_i D_i}{\sum n_i}, D_w = \frac{\sum n_i D_i^4}{\sum n_i D_i^3}, PDI = \frac{D_w}{D_n} \quad (3.1, 3.2, 3.3)$$

The number concentration of P4VP nanoparticles at the end of each polymerization experiment was calculated as follow (Eq. (3.4)) (Sajjadi and Brooks, 1999):

$$N_p = \frac{6X_{conv}ML}{\pi\rho_p D_w^3} \quad (3.4)$$

where X_{conv} is the degree of conversion measured by gravimetric analysis, ML is the monomer loading (g-4VP/100 ml-solution), ρ_p is the solid density of the polymer (ρ_p = 1.114 g/ml for P4VP). For P4VP-based nanoparticles with the additional co-monomers, same method of calculation was conducted by assuming that the level of incorporation of co-monomers during polymerization was low.

Infrared spectroscopy. Fourier-Transform Infrared (FT-IR) vibrational spectroscopy was applied to determine the chemical functionalities of the samples. Nanoparticle samples were first pelleted by centrifuging sample solutions at 9000 rpm for 30 minutes, after which the clear supernatant was decanted. The collected wet pellets were then vacuum-dried at 40 °C for 16 hours, and then stored in a drying dessicator. The sample was powdered and blended with KBr (Analar® grade) and pelletized into translucent solid discs for transmission modes analysis. Infrared absorption spectra

were recorded at room temperature, over a scan range of 400-4000 cm^{-1} using a computer-interfaced Bio-Rad FTS 135 system with a scan resolution of 4 cm^{-1}.

Bulk elemental analysis. The bulk elemental composition (C, H, N) of P4VP or P4VP-based nanoparticles synthesized in this work was measured with a PerkinElmer 2400 CHNS Elemental Analyzer (EA) (Perkin-Elmer, USA). Two duplicates were made for every sample to check for reproducibility, and the measured compositions were averaged and reported as the representative compositions. The weight percentages of other atoms, such as oxygen (from PEGMA and MATMAC) or chlorine (from V50 and MATMAC) were then inferred from the measured weight percentages of C, H and N measured.

Surface elemental analysis. Semi-quantitative measurements of surface elemental compositions and oxidation states of P4VP or P4VP-based nanoparticles were made using an X-ray photoelectron spectrometer (Kratos XPS System AXIS His-165 Ultra, Kratos Analytical Ltd., U.K.). The XPS spectra were obtained by applying the energy source of monochromatic Al-Kα radiation (1486.7 eV) operated at 150 W (10 mA and 15 kV). The wide scans were conducted from 100 to 1100 eV with a pass energy of 80 eV, whereas the high-resolution spectra for C 1*s*, N 1*s* and O 1*s* were obtained by applying 40 eV. The spectra were deconvoluted and curve-fitted to various oxidation states using the XPSPEAK 4.1 software, with linear baseline correction by fixing a 0 – 5 % of Lorentzian-Gaussian ratio. The full-width at half-maximum (FWHM) of the Gaussian peaks was maintained constant for all components in each spectrum. The elemental ratios of a particular sample were determined using Kratos's VISION, based on the experimentally calibrated relative instrumental sensitivity factor (RSF).

Charging reference for the polymer samples was done by setting the C 1*s* component for C-C/C–H bonds at 284.6 eV. The sample specimens for XPS analysis were prepared by wet-casting the nanoparticle suspensions directly onto freshly-cleaned glass slides which were mounted on the sample holders and then vacuum-dried at room temperature overnight. Prior to analysis, the sample holders were placed in the prechamber for outgassing. All samples were prepared from aqueous solutions of pH 8 ~ 9.

ζ-potential, hydrodynamic diameter and turbidity measurement. A BIC Zeta-Plus particle electrophoresis system (Brookhaven Instrument Corp., USA) was used to measure the electrophoretic mobilities (u_e) of the nanoparticles prepared. The ζ-potentials were then calculated from the measured u_e using Smoluchowski's equation (Smoluchowski, 1921). The effective hydrodynamic diameter (D_{DLS}) of the nanoparticles was measured through dynamic light scattering (DLS), by using the BIC 90Plus particle size analyzer, as well as a BI-9000AT digital autocorrelator integrated with the Zeta-Plus. Each sample was prepared by diluting the nanoparticle suspension by 100 folds, and the solution pH was adjusted using either 0.1 M HCl or 0.1 M NaOH to a desired value. No adjustment of ionic strength (IS) was made unless stated otherwise. The ionic strength was adjusted with 3.0 M NaCl stock solution when necessary. The measured autocorrelation functions were converted into particle size distributions via Stokes-Einstein equation, based on single-exponential cumulant analysis. An HP-Agilent 8453 spectrophotometer equipped with diode-array detector was used to measure the UV/Vis absorbance of nanoparticle suspension at wavelength (λ) = 400 nm ($Abs_{\lambda=400}$). All the measurements were thermostated at 25 °C.

3.2.5 Determination of Critical Coagulation Concentration (CCC).

To determine the CCC of the P4VP-based nanoparticle suspensions, the initial rate of change in turbidity (or absorbance at λ = 500 nm) was assumed to be proportional to the coagulation rate of the colloidal dispersion (Romero-Cano *et al.*, 1998). The weight concentration of the nanoparticle suspensions was adjusted from the nanoparticle stocks prepared to approximately 100 mg/liter, for optimal value of absorbance or turbidity. The rate of change in turbidity was followed as a function of time at a series of increasing salt concentrations ([NaCl] = 5.0×10^{-7} M – 1.2 M), by measuring the UV/Vis absorbance ($Abs_{\lambda=500}$) of the nanoparticle suspensions upon addition of concentrated NaCl solution. To monitor the coagulation kinetic, the cycle time was set to be 0.5 second, to open the optical shutter in the spectrophotometer for all time during measurement. A typical set-up is described as follow: for each experiment, 2.4 ml of nanoparticles solution was accurately pipetted into a quartz cuvette that was mounted in the observation chamber of the spectrometer. Aliquot (0.6 ml) of sodium chloride solution was quickly added and instantly mixed in the cuvette. Thereupon, the kinetic of the coagulation process was measured and recorded. All the measurements were repeated twice and conducted at room temperature (22-24 °C) and the initial pH values of the nanoparticle suspensions were measured and adjusted to approximately 6, as and when necessary.

3.2.6 Reversible Swelling Using pH-Swing Titration

Most adsorption process often undergoes cyclic change in the operating conditions, for example, the exhausted adsorbents being subjected to elution and conditioning before commencing another cycle of adsorption. To verify whether the as-synthesized nanoparticles are robust enough so that they would remain morphologically and

colloidally stable during the cyclic operations, PEGMA grafted P4VP nanoparticles (P4VP-PEGMA) crosslinked by DVB, EGDM and PEGDM (n = 9 and n = 13) were subjected to pH-swing titration as described below. A mixture solution of ca 0.002 wt.% of nanoparticles and 0.1 M NaCl was titrated from pH 8.0 ~ 9.0, in which nanoparticles were first fully collapsed or deswollen, to pH 1.8 ~ 2.0 to fully swell the nanoparticles. The mixture solution was then magnetically stirred (100 rpm) for 30 minutes. Sampling was done at each pH after which the turbidity (UV/Vis absorbance at λ = 400 nm) and the effective hydrodynamic diameter of the nanoparticles were measured for each sampled mixture. The measured turbidity values were corrected for the extra titrant volume added during the pH-titration.

3.2.7 Deswelling Kinetic of Swollen P4VP Nanoparticles Upon Pd(II) Adsorption

To assess whether the P4VP nanoparticles would remain colloidally stable after adsorption of palladium ions, the deswelling dynamics of the P4VP nanoparticles in palladium solutions were monitored with DLS measurement. For instance, aliquot nanoparticle suspension with pre-adjusted pH were mixed rapidly with Pd(II) solution using micropipette, in a transparent cuvette mounted on the BIC 90Plus system, thereupon the measurement was commenced immediately. The light scattering function of the mixture was measured as a function of time. An average size reading for D_{DLS} (nm) was obtained after every 10 seconds of signal acquisition. A shorter sampling interval (< 10 seconds) would cause excessive noise, resulting in large scatters of readings in the first few measurements. There is no effective method to stir the mixture in the cuvette during the measurement ("static adsorption"), and therefore the D_{DLS} trend obtained herein is only a inferred indicator for well-stirred adsorption process, due to the existence of multiple deswelling rates resulting from

inhomogeneous Pd(II) distribution throughout the sample volume caused by the lack of mixing. Typical dosage of nanoparticles for these measurements was 0.05 g/liter. Besides Pd(II), other chloride salts of Ca(II) and Cu(II) were also used to determine the degree of deswelling of the P4VP nanoparticles in the presence of these cations. Optical microscopy was attempted but to no avail, because of the poor contrast of the swollen, sparse polymer network, as well as the poor sub-micron resolution of optical microscope (Fujii *et al.*, 2005).

3.3 Results and Discussion

3.3.1 Synthesized P4VP Nanoparticles

To enhance colloidal stability and size control, a two-pronged approach for producing P4VP nanoparticles was taken in this work. Firstly a mixture of hydrophilic and charged co-monomers was added to increase the amount of surface-bound stabilizing moieties ("hydrophilic co-monomer addition" approach). Secondly, the mixture of monomer and crosslinker was injected semicontinuously to the thermostated reaction mixture such that the rate of polymerization and particle growth could be manipulated by changing the monomer addition rate ("starved-fed" approach). The experimental results obtained in this work, such as D_n, D_w (from FESEM) and D_{DLS} (from BIC Zeta-Plus) are given in Table 3.1 and 3.2, together with their polymerization recipes. In the following discussion, only the values of D_n (D_w has similar value to D_n) are referred and used to make the discussion simpler and to avoid confusion. In general, the measured values of D_{DLS} are larger than the values of D_n because the former includes the contributions from the electrostatic double layer (EDL) as well as the swelling of the surface-bound polymer layer (Gittings and Saville, 1998). Except for Run A-8 to A-9 (Table 3.1), Run B-6 and Run B-7 (Table 3.2) which failed to produce

monodispersed nanoparticles, most of the P4VP nanoparticles prepared are spherical and narrowly distributed in their sizes (Figure 3.2).

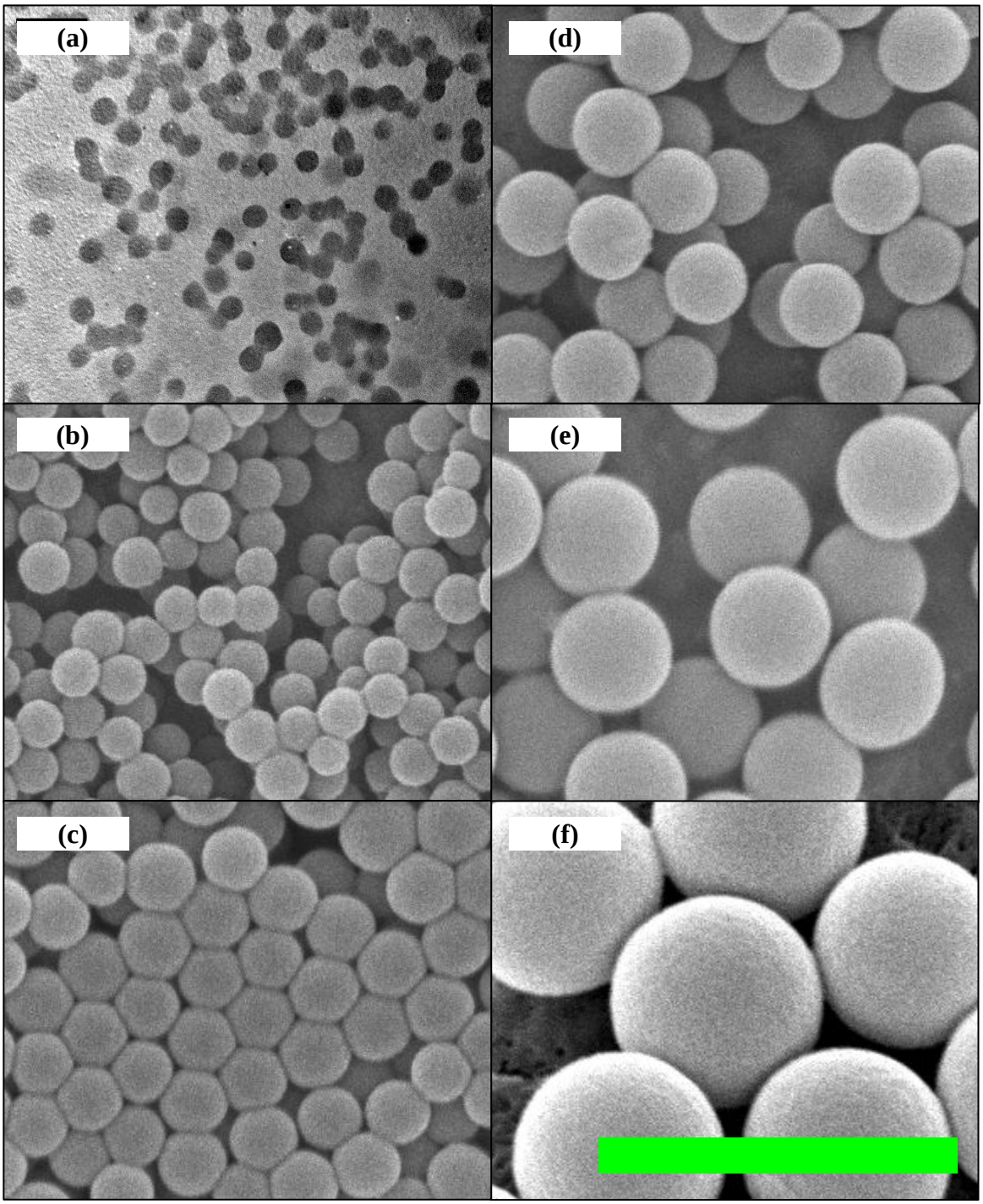

Figure 3.2 Electron micrographs of various P4VP and P4VP-based nanoparticles synthesized: P4VP-PEGMA nanoparticles (a) B-1 (D_n = 90.2 nm); P4VP nanoparticles (b) A-7 (D_n = 132.4 nm), (c) A-5 (D_n = 180.9 nm), (d) A-4 (D_n = 245.8 nm) and (e) A-3 (D_n = 354.0 nm); P4VP-PEGMA-MATMAC nanoparticles (f) C-1 (D_n = 623.1 nm). Scale bar denotes 1 μm.

Pristine P4VP nanoparticles with no co-monomers. P4VP nanoparticles which are electrostatically-stabilized were prepared successfully via the *ab-initio* emulsion copolymerization (Table 3.1, Run A-1 to A-3). To minimize coagulum formation, the solid content of the dispersions was kept at below 3 wt.% (aqueous solubility of 4VP = 2.9 wt.%), similar to those used by other researchers (Davies *et al.*, 1995). As 4VP loading was kept below its solubility limit, almost all monomers were dissolved and well dispersed throughout the reaction volume. The results from Run A-1 to A-3 demonstrated that nanoparticles of good size monodispersity (PDI $\leq$ 1.020) have been successfully obtained through the batch SFEP method, which produced high yields and low coagulum formation. A direct increase in the particle diameter from 161.5 to 354 nm was readily obtained by changing the monomer and initiator concentrations, without any aid of foreign surfactant. An increase in the monomer concentration gave rise to larger particles as more monomer molecules were available during the particle growth stage (see Run A-1 to A-2). The reverse situation was observed for an increase in the initiator concentration (see Run A-2 to A-3). The latter phenomenon was also observed by Shouldice *et al.* (1994). Initiation efficiency is lower when initiator concentration increases, and the rate of production of free radicals becomes reduced, which indirectly retards the rate of formation of *in-situ* cationic stabilizers (from decomposed initiator molecules) (Gilbert, 1995). The initiator molecules are the source for electrostatic charges and ionic strength and thus have both stabilizing and destabilizing effects (Feeney *et al.*, 1987; Ngai and Wu, 2005). In Run A-3, increased initiator concentration probably caused more counter-ions (Cl^-) to dissociate from the initiator molecules and compressed the electrostatic double layer of the precursor particles, resulting in the formation of larger stable particles prior to the particle growth stage.

To probe the smallest particle size that the current SFEP recipe was able to produce, the monomer and crosslinker was pre-mixed and metered into the thermostated reactor at a constant feed rate ("semicontinuous feed approach"). This technique has been shown to be extremely versatile in controlling molecular weight distribution, particle morphology, particle size distribution as well as chemical composition distribution of the polymers synthesized (Leiza and Meuldijk, 2005). Emulsion polymerizations conducted under such condition have been demonstrated to be capable of producing very fine nanoparticles (Ledezma *et al.*, 2007; Sajjadi, 2007). In conventional *ab-initio* SFEP, a stable particle freshly formed from the coagulative nucleation stage would become monomer-swollen and grow at a rate controlled by monomer diffusion from the neighboring monomer droplets. Conversely, the rate of particle growth in a semibatch SFEP is controlled by the monomer addition rate (Wessling, 1968; Sajjadi and Brooks, 2000). The monomer concentration within the particles (C_p) is kept below their saturation concentration ($C_{p,sat}$), i.e. the particles are starved of monomer. The growth of existing particles is effectively delayed and reduced in "monomer-starved" SFEP while the nucleation stage is lengthened, and therefore more monomers are utilized for particle nucleation which favors more particles to be produced (Krackeler and Naidus, 1969; Sajjadi and Brooks, 1999). In this study, at a 4VP loading of 1.5 wt.%, reducing monomer feed rate lengthened the period of particle nucleation and caused an increase in particle number (N_p) along with a decrease in particle diameter (see Run A-4 to A-6). At higher 4VP loadings, the nanoparticles obtained from Run A-6 for example were similar in size to that of Run A-1 that has a lower monomer loading. These results indicate that particle nucleation and growth (N_p, D_p) could be readily controlled by the semibatch feed mode ("monomer-starved condition"), while satisfactory yields would still be obtained (> 95%). By halving the initiator

concentration, the diameter of the nanoparticles prepared was found to be further reduced by 30 nm (see Run A-6 to A-7), probably caused by the same reason as discussed above (see Run A-2 and A-3).

As expected, poor polymerization with massive coagulum formation was observed when the monomer loading was increased above its aqueous solubility (Run A-8 and Run A-9). The formation of coagulum or floc in emulsion polymerization was either caused by loss of colloidal stability in particle dispersions or emergence of different mechanism of polymerization, such as polymerization in monomer droplets (Vanderhoff, 1981). At a higher monomer loading, the solubility limit of 4VP was exceeded and monomer mini-droplets would appear. The oil mini-droplets might consume excessive amount of charged oligomeric radicals and therefore less stabilizers were available to stabilize the surrounding particles, thus intensifying the coagulum formation. Similar phenomenon was observed by Ni *et al.* (2001) and they hypothesized that high molecular weight polymer chains could be formed instantaneously in large quantity due to rapid propagation, which would bridge the nearby particles and result in flocculation when the aqueous phase is oversaturated with 4VP.

PEGMA-grafted nanoparticles (P4VP-PEGMA). Nanoparticles produced from a typical SFEP (i.e. the A-series run in Table 3.1) were generally large (>100 nm) as their precursor particles tend to coagulate manyfolds due to their low surface-charge density or weak colloidal stability (Feeney et al., 1987; Gilbert, 1995). Many researchers have designed and developed a number of novel amphiphilic macromolecular co-monomers for emulsion polymerization to obtain smaller,

uniformly-shaped nanoparticles with narrow particle size distributions. The common chemical structure of those amphiphilic molecules usually contains both poly(ethylene glycol) (PEG) or poly(ethylene oxide) (PEO) block and hydrophobic chain with an unsaturated bond as anchor (Ferguson *et al.*, 1993; Liu et al., 1997; Kawaguchi *et al.*, 2000; Maniruzzaman *et al.*, 2000). By virtue of 'excluded-volume' effect and hydration, PEG chains are extended from the particle surface, thereby enhancing steric repulsions and contributing to colloidal stability of the PEG-grafted nanoparticles. These novel PEG macromonomers are effective in strengthening the stability of polymer dispersions and reducing the particle size. By employing amphiphilic *ω*–methoxy-*α*-*p*-styrelalkyl poly(ethylene glycol) macromonomers (CH_3- $(CH_2CH_2O)n$-$(CH_2)_m$-$C_6H_4CHCH_2$, n = 18, m = 1, 4, 7), Maniruzzaman *et al.* (2000) successfully synthesized ultrafine polystyrene nanoparticles with diameter as small as 30 nm from a simple emulsion polymerization process. Although these amphiphilic co-monomers are very efficient, their immediate technological exploitation is often rare because the synthesis of these molecules is tedious and requires multiple steps of transformation/purification. To reduce the synthetic complexity, another variant of this approach was undertaken to synthesize sterically-stabilized particles by substituting the amphiphilic macromonomers with PEGMA of varying molecular weights (Chen *et al.*, 2000; Tuncel, 2000; Pich *et al.*, 2003). As shown in Table 3.1, an attempt was made by injecting PEGMA, a commercially available polymerizable hydrophilic macromonomer (see Run A-10); however no reduction in particle size was observed. The reason for the failed attempt (Run A-10) is probably as follow: at higher monomer loadings, the monomer oil mini-droplets would function as sinks for non-ionic surfactants, as reported by other researchers (Özdeğer *et al.*, 1997; Okubo *et al.*, 2003). To overcome this problem, the "hydrophilic co-monomer addition" approach

was combined with the semicontinuous feed mode ("starved-fed" approach) and the results of polymerization obtained are tabulated in Table 3.2. The monomer concentration in the thermostated reactor was then low by feeding the monomer semicontinuously at a constant rate (see Run B-1 to B-4 in Table 3.2).

A dramatic reduction of particle size by 40 nm was obtained by adding 2.5 wt.% (relative to 4VP) of PEGMA into the semibatch SFEP system (comparing Run A-7 in Table 3.1, Run B-1 in Table 3.2). Precursor particles formed during the initial stage of polymerization are extremely unstable, and hence tend to coagulate to reduce the interfacial free energy (Gilbert, 1995). Because the size of the precursor particles formed therein was controlled by limited coagulation among the precursor particles, the PEGMA-derived steric stabilizers formed *in-situ* under monomer-starved condition rendered the particles to be better protected against further coagulative aggregation once these stabilizers were adsorbed and grafted onto the particle surfaces. With more PEGMA present, more (charged- and steric-) oligomeric stabilizers produced *in-situ* were available to be adsorbed and grafted onto the growing particles and nuclei, leading to enhanced colloidal stabilization during the coagulative nucleation, due to the presence of the surface-grafted steric layer, i.e. the surface PEG diffuse layer (Run B-1 to B-4). Together with the charged fragments from the initiator molecules consumed, the combined electrostatic and steric repulsion would allow greater surface area of the produced particles to be stabilized; hence smaller P4VP nanoparticles were eventually obtained in this work. Much smaller P4VP nanoparticles of diameter that is close to the smallest P4VP nanoparticles synthesized by Ma and Fukutomi (1991) via the electrosteric-surfactant approach, were also obtained at higher PEGMA concentrations in this study (Run B-3 and B-4). These

results imply that the simple two-pronged approach proposed herein is capable of producing very fine P4VP nanoparticles. Further attempts were made to test whether monomer loading could be increased while colloidal stability is preserved (Run B-5 to B-7). A comparison for the results from Run B-5 and those from Run B-1 to B-4 suggests that the semicontinuous feed is essential to better incorporate PEGMA onto the growing particles surface. Polymer-bridging induced flocculation (de Witt and van de Ven, 1992) and depletion flocculation (Jenkins and Snowden, 1996) may have occurred when the copolymerization was conducted batchwise in a large excess of PEGMA, as evidenced by the increase in particle diameter from 239.3 nm of Run A-2 to 303.0 nm of Run B-5. Similar flocculation-limited growth phenomenon was also observed by Chen *et al.* (1997) for batch emulsion polymerization of styrene, wherein the particle diameter increased by two folds when the non-ionic surfactant (NP40, C_9H_{19}-C_6H_4-O-$(CH_2CH_2)_{40}$-H) was added. The high amount of coagulum or flocs formed from Run B-6 and B-7 was probably caused by polymer-bridging induced flocculation between neighboring PEGMA-grafted nanoparticles (Guillaume *et al.*, 1988; de Witt and van de Ven, 1992), or reduced availability of stabilizer formed *in-situ* through surfactant engulfment (Özdeğer *et al.*, 1997).

Experimental studies reported by Okubo and coworkers (2003, 2006) showed that non-ionic stabilizers could be engulfed by growing particles or monomer oil-droplets, leading to formation of multi-hollow particles that contain solvent-filled spheroids. For example, a severe inclusion of 75% of polyoxyethylene nonyl phenyl ether non-ionic emulsifier added (Emulgen 911, C_9H_{19}-C_6H_4-$O(CH_2CH_2O)_{10.9}H$) inside the growing poly(styrene-co-methacrylic acid) particles was reported by Okubo *et al.* (2003). Undesirable consumption of the non-ionic stabilizers through engulfment

caused catastrophic loss of colloidal stability and thus severe problems in controlling the particle size distribution and polymerization kinetics. These findings suggested that better polymerization and smaller nanoparticles could be obtained in this work because less PEGMA were engulfed and wasted under "monomer-starved" condition (Okubo *et al.*, 2006). By conducting the polymerization under "monomer-starved" condition (Run B-1 to B-4), better polymerization and smaller nanoparticles were indeed obtained in this study.

P4VP-PEGMA-MATMAC nanoparticles. In previous systems (Run A and Run B), the electrostatic repulsion for colloidal stabilization was contributed solely by the cationic charged groups from the azo-based thermal initiators (V50) used. Many studies suggest that the charge formation and electrostatic stabilization during SFEP could be further enhanced by the addition of charged co-monomers (Liu *et al.*, 2000; Vroon *et al.*, 2005). To augment greater amount of charges to the current system, cationic co-monomer MATMAC, which has a strongly charged quaternized amine headgroup, was included alongside with PEGMA (Run C-1 to C-3 of Table 3.2). Because of the diminishing marginal improvement at 20 wt.% of PEGMA (Run B-3), the subsequent runs were conducted at a constant dosage of PEGMA at 10 wt.% (Run B-4).

Unlike other quaternary ammonium based surfactants, MATMAC has no long hydrophobic tail and hence is highly water-soluble. Nonetheless, some MATMAC could be covalently grafted onto polymeric nanoparticles during the emulsion polymerization through its reactive methacrylate group. The addition of MATMAC to the reaction mixture should therefore supplement the *in-situ* formation and supply of electrostatic stabilizers. Comparing Run C-1 and Run B-6, significant improvement in

size monodispersity as well as polymer yield was obtained by adding a small amount of MATMAC. Further evidence on the stability-boosting effect of MATMAC is indicated by the results from Run C-2 and C-3, wherein the monomer loading could be increased up to 5 wt.% successfully without catastrophic coagulation or flocculation observed in Run A-9. The only minor drawback of this approach is that more water-soluble polyeletrolytes are formed, which would preferentially desorb from the growing particles and partition themselves in aqueous phase favorably (Kim *et al.*, 1987; Liu *et al.*, 2000; Voorn *et al.*, 2005). The gravimetric yields from the C-series run were generally lower than that of A-series run because of the loss of these water-soluble polyelectrolytes. Similar phenomenon was observed for B-series run wherein the PEGMA-grafted oligomers or polymers were very water-soluble and could be desorbed from the polymeric nanoparticles during their growth. Despite these shortcomings, the two-pronged approach demonstrated herein is capable of producing narrowly-distributed P4VP nanoparticles (PDI $\leq$ 1.020) of various sizes (70 – 650 nm) (Figure 3.2).

3.3.2 Characteristics of P4VP-based Nanoparticles Prepared

The bulk elemental compositions of the nanoparticles prepared show no significant variations from others because the precursor chemicals other than 4VP were added, if any, only in minor amounts (Table 3.3). The pristine P4VP nanoparticles (with no co-monomers) (A-2 in Table 3.3) ranks the highest in the nitrogen content, followed by the P4VP-PEGMA nanoparticles (B-1 to B-5) and then the P4VP-PEGMA-MATMAC nanoparticles (C-1 and C-2). The decrease in the nitrogen contents for B- and C-series nanoparticles was due to the dilution effect by the co-monomers added in the polymerization. Nonetheless, the high nitrogen contents (9.2 – 9.6 mmole/g) of

these P4VP-based nanoparticles indicate that these nanoparticles would logically possess high binding capacity for palladium ions in subsequent adsorption experiments.

To determine whether there is chemical degradation of 4VP after the polymerization, FT-IR spectroscopy was used to probe the chemical state of pristine P4VP nanoparticles (A-2), PEGMA-grafted P4VP nanoparticles (B-5) as well as MATMAC-augmented PEGMA-grafted P4VP nanoparticles (C-1). As shown in Figure 3.3 (a), the pyridyl group of the P4VP nanoparticles can be clearly identified by the major characteristic band centering at 1600 cm^{-1} which corresponds to the C–N ring stretching of the pyridine ring, together with other remaining absorption bands at 1555, 1495, 1449 and 1420 cm^{-1}, assignable to the C–C ring stretching vibrations, as well as 1220 cm^{-1}, 1068 and 962 cm^{-1}, attributed to the C–C in plane bending, in-plane and out-of-plane rings and C–H bending, respectively (Wu *et al.*, 2003). Out-of-plane C–H deformation bands at 998 and 824 cm^{-1} are also observed. An additional shoulder band (1650 cm^{-1}) next to the C–N ring stretching band observed in spectrum (a) is attributed to the N–H bending of the primary and secondary amines of the initiator molecules incorporated (Silverstein *et al.*, 2005).

Table 3.3 Bulk and surface elemental compositions of various P4VP-based nanoparticles synthesized.

Sample	Code	Bulk elemental composition (EA) [wt.%]				Nitrogen content [mmole/g]	Surface elemental composition (XPS) Atomic ratio [at.%]	
		C	H	N	Others*		N	O
Pristine P4VP nanoparticles	A-2	79.61 ± 0.09	6.69 ± 0.04	13.57 ± 0.18	0.14 ± 0.06	9.69 ± 0.13	11.10	0.00
P4VP-PEGMA nanoparticles	B-1	78.96 ± 0.11	6.79 ± 0.05	13.52 ± 0.12	0.74 ± 0.17	9.65 ± 0.08	15.57	7.10
	B-2	79.36 ± 0.15	6.75 ± 0.03	13.42 ± 0.04	0.47 ± 0.16	9.58 ± 0.03	14.31	6.74
	B-3	78.80 ± 0.20	6.64 ± 0.05	13.36 ± 0.16	1.21 ± 0.08	9.54 ± 0.12	13.11	6.28
	B-4	79.03 ± 0.07	6.75 ± 0.06	13.08 ± 0.05	1.14 ± 0.18	9.34 ± 0.04	12.28	9.26
	B-5	78.76 ± 0.18	6.66 ± 0.02	13.17 ± 0.12	1.41 ± 0.08	9.40 ± 0.09	22.54	12.53
P4VP-PEGMA-MATMAC nanoparticles	C-1	78.53 ± 0.05	6.80 ± 0.09	12.95 ± 0.04	1.73 ± 0.09	9.24 ± 0.03	18.66	12.20
	C-2	78.60 ± 0.10	6.75 ± 0.03	12.89 ± 0.08	1.76 ± 0.21	9.21 ± 0.06	15.63	6.78
Pure PEGMA	-	-	-	-	-	-	0	32.3
V50	-	-	-	-	-	-	37.5**	0

* The weight percentages of other atoms (e.g. oxygen, chlorine) are calculated as follow: wt.% Others = 100 – wt.% C – wt.% H – wt.% N.
** The ratio is calculated from the chemical formula, i.e. $C_8H_{18}N_6 \cdot 2HCl$.

The availability and distribution of PEGMA molecules during the particle formation in the polymerization process is crucial for obtaining fine nanoparticles as discussed above. Neither the presence nor the concentration of PEGMA or MATMAC can be deduced without ambiguity from the results obtained by the EA (Table 3.3), as the EA cannot identify and quantify the individual contribution of oxygen atom and chlorine atom.

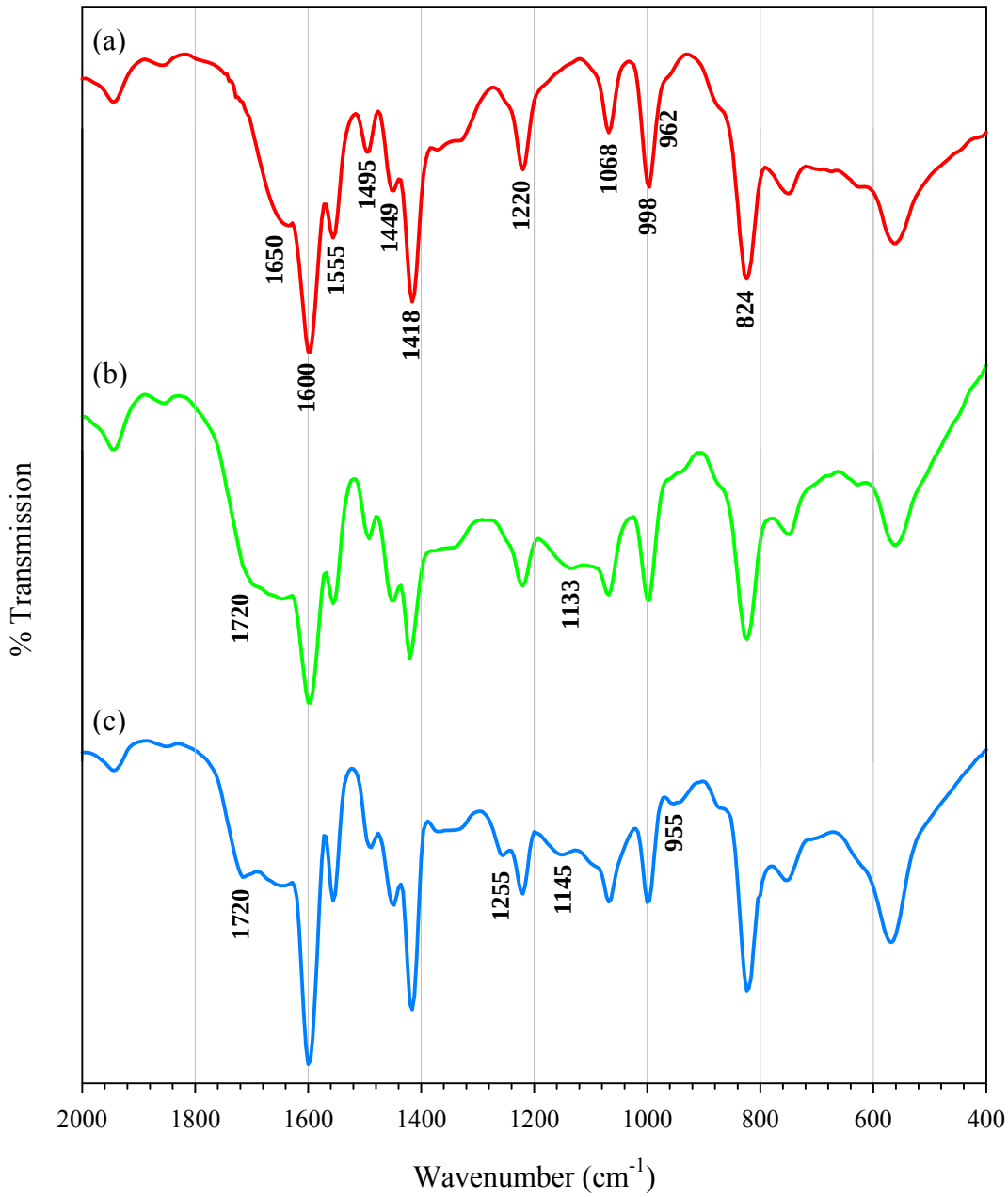

Figure 3.3 FT-IR spectra of the representative P4VP-based nanoparticles synthesized in this work. (a) Prisitine P4VP nanoparticles (A-2), (b) P4VP-PEGMA nanoparticles (B-5) and (c) P4VP-PEGMA-MATMAC nanoparticles (C-1).

In FT-IR spectrum (b) of Figure 3.3, the additional shoulder band at 1133 (s) and small vibration band at 1720 cm^{-1} (s), assignable to the stretching vibrations of –C=O carbonyl groups of methacrylate end-group (Shay *et al.*, 2000) and C–O–C ether groups of PEG chain (Harder *et al.*, 1998; de Zea Bermudez *et al.*, 1999) of PEGMA respectively, provide evidence that PEGMA has been successfully incorporated onto the nanoparticles (B-5). The hydrophilic co-monomers (PEGMA, MATMAC) would partition themselves favorably towards aqueous phase, and be bound onto the particle surface during the polymerization process. Because of their low bulk concentration, the amplitudes of these newly emerged bands are weak and easily masked by more intense bands of the major component of P4VP. The carbonyl stretching band at 1720 cm^{-1} becomes identifiable in spectrum (c). The C–O–C stretching is however shifted from 1133 to 1145 cm^{-1}, possibly due to band masking caused by many overlapping vibration bands in this region. Faint vibration bands at 1255 cm^{-1} and 955 cm^{-1} are caused by N–CH_3 rocking and C–N stretching of the quaternary ammonium groups of MATMAC (Uno *et al.*, 1968), a modest indication of successful tethering of MATMAC onto the P4VP nanoparticles (C-1).

Due to the limited detection and resolution of FT-IR, XPS spectroscopy was applied to further identify and quantify the chemical functionality, specifically present on the surfaces of the P4VP-based nanoparticles. XPS wide scans for various nanoparticles synthesized are shown in Figure 3.4. Major peaks for C 1*s* and N 1*s* are clearly present in all samples. O 1*s* peaks appear in the spectra of P4VP-PEGMA nanoparticles (B-1 to B-5) indicate the presence of poly(ethylene glycol) from PEGMA on the particle surfaces. The signal intensity of O 1*s* peaks relative to that of N 1*s* peaks intensifies from B-1 to B-2, suggesting the increasing enrichment of PEGMA on the particle

surfaces, which is in line with the increasing input of PEGMA in the polymerization recipes as shown in Table 3.2.

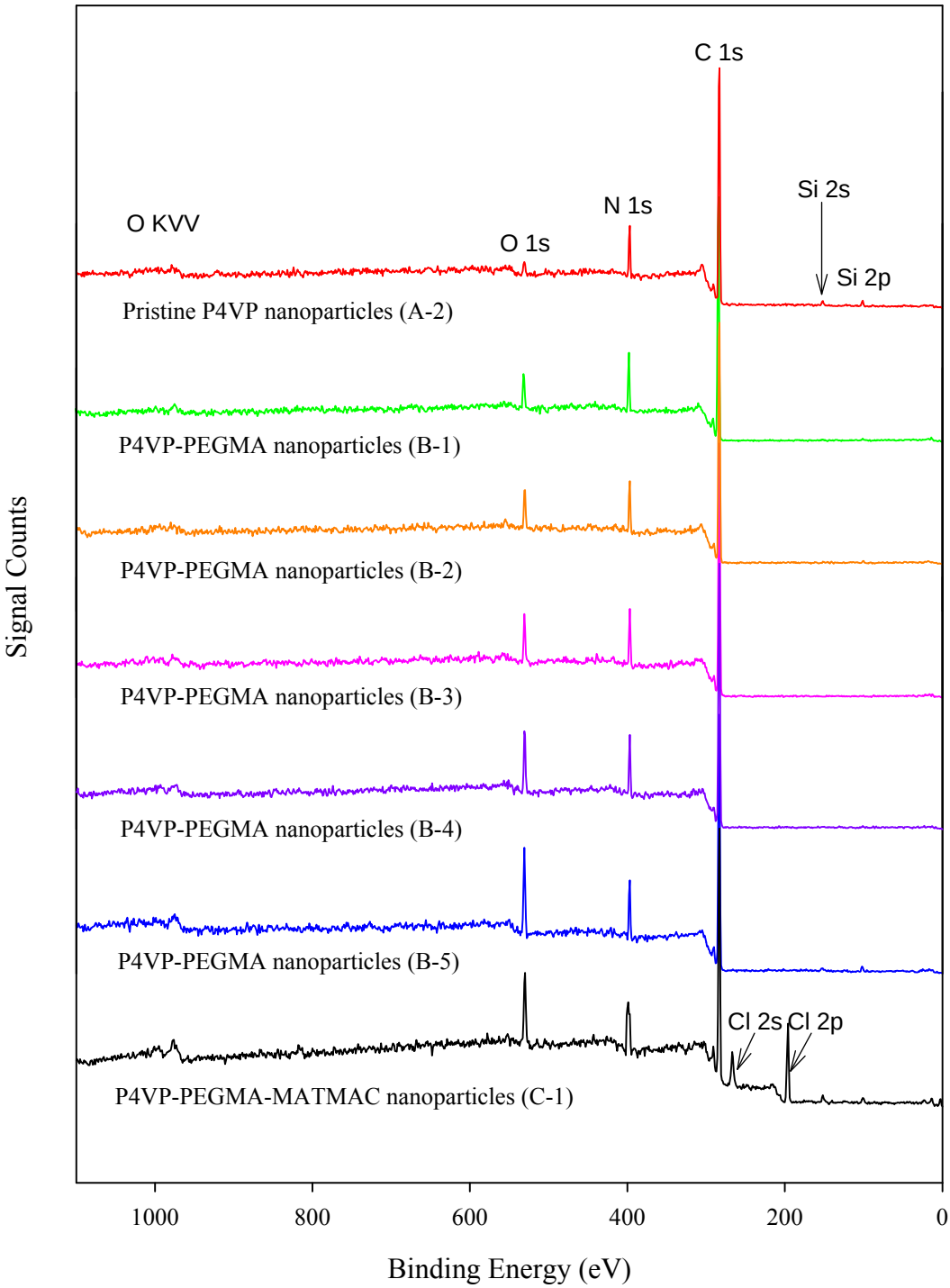

Figure 3.4 XPS wide scan spectra (0 – 1100 eV) of P4VP-based nanoparticles synthesized.

In the spectrum of pristine P4VP nanoparticles, the weak O 1*s* peak together with the two minor peaks in the region of 100 – 200 eV are possibly caused by contamination

originated from silica leached from the glasswares. In the spectrum of C-1, the two peaks (Cl 2*s*, Cl 2*p*) in the region of 200 to 300 eV support the presence of chlorine atoms, thereby evidencing the incorporation of MATMAC in the prepared P4VP-PEGMA-MATMAC nanoparticles.

High-resolution XPS analyses were carried out for the P4VP-based nanoparticles prepared in this study, in order to identify the respective chemical shifts due to the hydrophilic co-monomers covalently grafted on the nanoparticle surfaces. The C 1*s* core-level spectra of various representative nanoparticles are shown in Figure 3.5. The broad band of the C 1s spectra for the pristine P4VP nanoparticles was deconvoluted to reveal three components: the first peak at 284.6 eV is assigned to the C–C/C–H bond while the second and third peaks at 285.19 eV and 285.71 eV are attributed to the –C= bond of the aromatic ring and C–N/C=N bond originated from the pyridyl group (P4VP) and the butyramidine group (V50) (see Figure 3.5 (a)). The copolymerization of 4VP with PEGMA resulted in a new peak at 286.1 eV which is due to the C–O ether group of PEGMA present on the P4VP-PEGMA nanoparticle surface (Figure 3.5 (b)). Following the simultaneous additions of PEGMA and MATMAC, an additional weak peak emerged at 288.5 eV, assignable to O–C=O ester group, located distantly from the main peaks in spectrum (c), suggesting that a minor amounts of MATMAC were incorporated. A significant decrease of the area under the component curve of –C= for phenyl rings in spectra (b) and (c) as compared to that observed in spectrum (a) suggests that the surface enrichment of the PEGMA and MATMAC molecules on the particle surfaces indeed occurred at the expense of P4VP. These results confirm the efficacy of the proposed two-pronged SFEP method in

producing P4VP-based nanoparticles of various sizes by introducing the hydrophilic co-monomers.

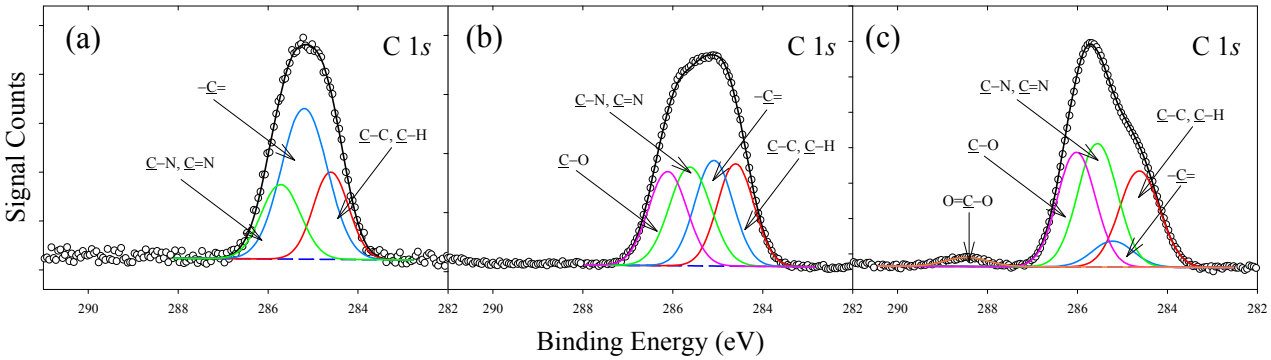

Figure 3.5 C 1*s* XPS spectra recorded for (a) pristine P4VP nanoparticles (A-2), (b) P4VP-PEGMA nanoparticles (B-5), and (c) P4VP-PEGMA-MATMAC nanoparticles (C-1) respectively.

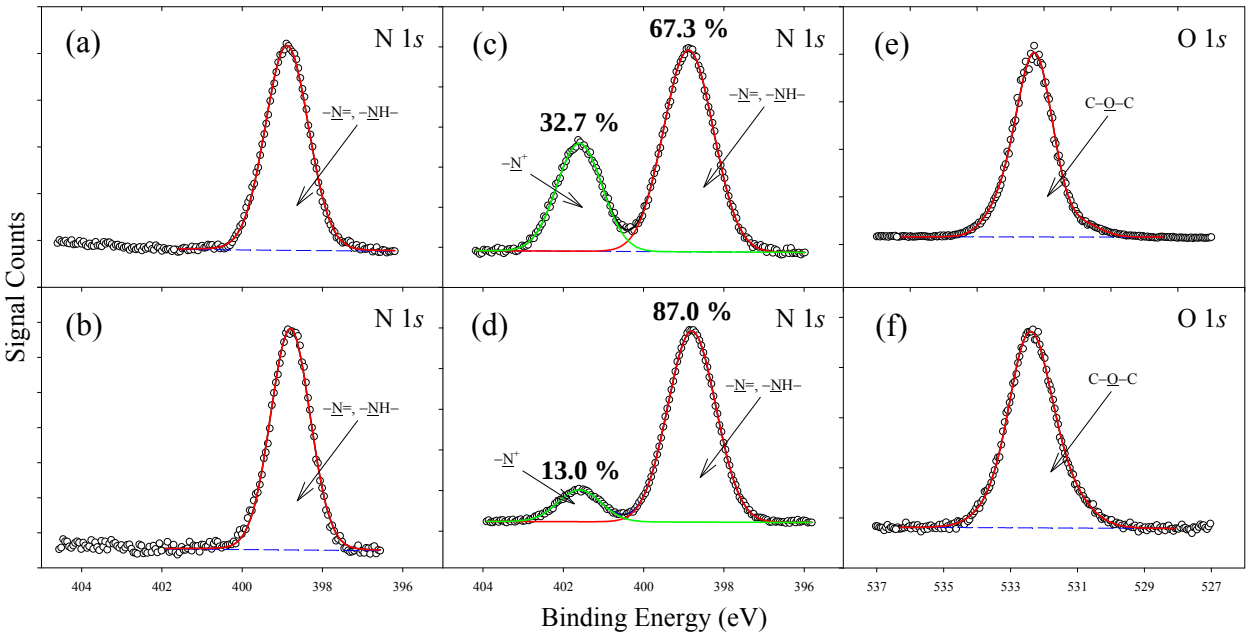

Figure 3.6 XPS high-resolution scans of various P4VP-based nanoparticles synthesized. N 1*s* spectra of (a) pristine P4VP nanoparticles (A-2), (b) P4VP-PEGMA nanoparticles (B-5), and P4VP-PEGMA-MATMAC nanoparticles (C-1 & C-2 respectively) (c) and (d). Spectra (e) and (f) are O 1*s* scan for B-5 and C-1, respectively.

As shown in Figure 3.6 (a) and (b), the N 1*s* XPS spectra for both pristine P4VP nanoparticles (A-2) and P4VP-PEGMA nanoparticles (B-5) display the characteristic peak at 398.8 eV, assignable to the lumped contribution from the nitrogen atoms of

the pyridyl group (–N= of 4VP) and amidine group (C–N/C=N of V50) (Beamson and Briggs, 1992). Due to the proximity in their binding energies (399.9 eV –N= of 4VP, 399.7 eV for C–N/C=N of V50), further deconvolution of the N 1*s* spectra into these subcomponents was not possible under the current instrumental resolution. Nonetheless, the incorporation of MATMAC in the P4VP-PEGMA-MATMAC nanoparticles (C-1 and C-2) clearly resulted in a new peak centered at 401.6 eV as observed in N 1*s* spectra (c) and (d). The new peak, which is absent in spectrum (a) and (b), is attributed to the nitrogen atom of the quaternary ammonium group ($–N^+$) from MATMAC. The emergence of an intense and broad peak at 532.5 eV in the O 1*s* spectra of samples B-5 and C-1 (see Figure 3.6 (e) and (f)) further verify that the surface oxygen atoms mostly come from the C–O–C ether group of the PEG chains grafted from PEGMA. The C=O carbonyl group from MATMAC is not discernible and may have been masked by the C–O–C peak in the spectrum, due to the high molar percentage of C–O–C per molecule of PEGMA (degree of polymerization = 46, i.e. 46 repeated units of C–O–C versus 1 unit of C=O).

To provide additional supporting information, the elemental compositions of the nanoparticle surfaces modified by the hydrophilic co-monomers were calculated from the photoelectron peak areas recorded for each element in the XPS spectra. The area ratios of these elements were further corrected according to the instrumental sensitivity factor experimentally determined to yield the actual atomic proportions. The atomic percentages of nitrogen and oxygen atoms of the P4VP-based nanoparticles are shown in Table 3.3. As can be found from the table, the compositional variations of the P4VP-based nanoparticles' surfaces can be correlated to the co-monomers added (i.e. DVB, PEGMA and MATMAC). The atomic

percentage of surface nitrogen atom experimentally determined from the pristine P4VP nanoparticles (A-2) is only 11.1 %. This value is however closer to the theoretical ratio of 12.5 % for P4VP than the 9.9 % reported for similar P4VP nanoparticles prepared by Davies *et al.* (1995).

As expected, steep rises in surface O at.% (referred as "O at.%" unless otherwise stated) from B-series and C-series nanoparticles were observed when PEGMA was added. During the synthesis of the P4VP-PEGMA nanoparticles (B-series) via the "starved-fed" approach, a counterintuitive decrease in oxygen at.% was observed when the amount of PEGMA added was raised from 2.5 to 10 wt.% (B-1 to B-3). It was shown earlier in Table 3.2 that, as more nanoparticles were stabilized at a higher PEGMA concentration (i.e. higher N_p), the number of PEGMA molecules grafted on the surface of each particle decreased. When there was only little increase in N_p (B-3 and B-4 in Table 3.2), the PEGMA molecules in excess would attach onto existing particles, resulting in higher surface coverage per particle with PEGMA as indicated by the increase in O at.% from 6.28 to 9.26 in Table 3.3. As compared to other B-series nanoparticles (B-1 to B-4), B-5 had the highest O at.% which supports and strengthens the earlier proposition that the more particles were available, the lower amount of PEGMA was attached to the existing particles, and vice versa. Similar trend in surface stabilizer concentration was also witnessed in C-series nanoparticles. Besides, the area ratios of the $-N^+$ peak decreased from C-1 to C-2 (see Figure 3.6 (c) and (d)), indicating that a less amount of MATMAC molecules was available for each individual particle when more particles were nucleated and present in the system.

Surface enrichment of PEGMA molecules on the particle surface (B-series and C-series) can be confirmed by comparing the values of surface O at.% (XPS) with that of bulk O at.% (EA) in Table 3.3. To calculate the latter, the bulk elemental compositions (wt.%) determined were first converted to molar composition by dividing each element's atomic percentage by its own atomic weight. To err on a conservative side, the values under the category of "Others" were assumed to be contributed by oxygen atoms (atomic weight = 16 g/mole) solely. The bulk O at.% calculated for B-series and C-series nanoparticles has a range of 0.20 – 0.77 at.%. These values are significantly lower than the surface O at.% shown in Table 3.3 (6.28 – 12.53 at.%). The PEG layers which consists of a molecular weight of roughly 2,000 Da, when grafted onto liposome surfaces, has a hydrodynamic thickness of 4.5 nm (Cohen and Khorosheva, 2001). Hence, a loose steric layer of finite thickness (few nanometers) comprising PEGMA molecules should envelope each particle from the B-series and C-series (Polverari and van de Ven, 1994; Pich *et al.*, 2003). Due to the limited sampling depth of XPS (5 – 10 nm) (Bai and Zhang, 2001), the presence of this steric layer would reduce the elemental contribution from the P4VP base polymer beneath the layer (Deslandes *et al.*, 1993). In addition, the initiator molecules (V50) would preferentially reside in the aqueous phase or on the particle-liquid interface due to its hydrophilicity. The values of N at.% of particle surface for P4VP-PEGMA nanoparticles were therefore generally higher than that of pristine P4VP nanoparticles from the XPS analysis (Table 3.3) as more signals from V50 were collected instead. Similar reasoning could be used to account for the decreasing trend in N at.% for B-series and C-series nanoparticles. At a fixed concentration of V50 and MATMAC, the more particles present in the system, the lower amount of V50 or MATMAC was available for reacting onto each particle. Examining all these spectra altogether, one

may confirm that the added hydrophilic co-monomers have been successfully copolymerized and the majority of them was grafted onto the surfaces of the nanoparticles.

3.3.3 Colloidal Stability Enhancement by Copolymerization with PEGMA

To further confirm whether the grafting of PEGMA molecules in the B-series and C-series were effective, the colloidal stability of the pristine P4VP nanoparticles (i.e. A-4 in Table 3.1, D_{DLS} = 265.2 nm) that were solely stabilized through the positively charged repulsion was compared to that of the representative PEGMA-grafted nanoparticles (i.e. B-5 in Table 3.2, D_{DLS} = 313.6 nm) of comparable size. PEG-based surfactants or polymers when adsorbed or chemically grafted onto the particle surfaces were demonstrated to enhance the colloidal stability of the particles (Ottewill and Satgurunathan, 1988; Romero-Cano *et al.*, 1998). The typical coagulation kinetics as measured are presented in Figure 3.7. Figure 3.7 (a) shows that the absorbance of the pristine P4VP nanoparticle suspension (A-4) which were electrostatically-stabilized first dropped to a lower value in a very short time (< 2 or 3 seconds), which was caused by the dilution with the concentrated NaCl solution added. After the initial drop, the curve gradually increased, indicating that the resulting NaCl concentration has exceeded the critical coagulation concentration. When the CCC is exceeded, the particles undergo rapid coagulation under the influence of Brownian motion, as the electrostatic repulsive forces vanish as a result of compression of the EDL surrounding the particles. At lower salt concentrations, the coagulation process proceeds at a much slower rate (Fortuny *et al.*, 2004).

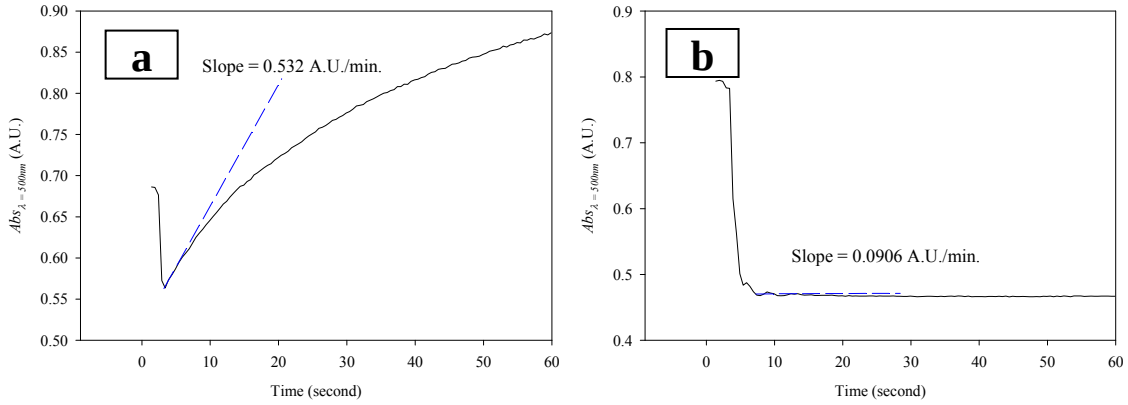

Figure 3.7 The kinetics of coagulation for (a) electrostatically-stabilized P4VP nanoparticles (A-4, D_{DLS} = 265.2 nm), and (b) P4VP-PEGMA nanoparticles (B-5, D_{DLS} = 313.6 nm), where the [NaCl] = 0.0428 M and 1.3 M, respectively. A.U. refers to the absorbance unit.

On the contrary, the absorbance remained relatively constant after the initial dip for the P4VP-PEGMA nanoparticle suspension (Figure 3.7 (b)), even when the salt concentration exceeded 1.3 M. Similar kinetic experiments were repeated for different salt concentrations, and the rates of change were then assessed by fitting straight lines to the initial portions of the kinetic curves (after the dip). The slopes of the fitted straight lines were measured and plotted as a function of [NaCl], as shown in Figure 3.8.

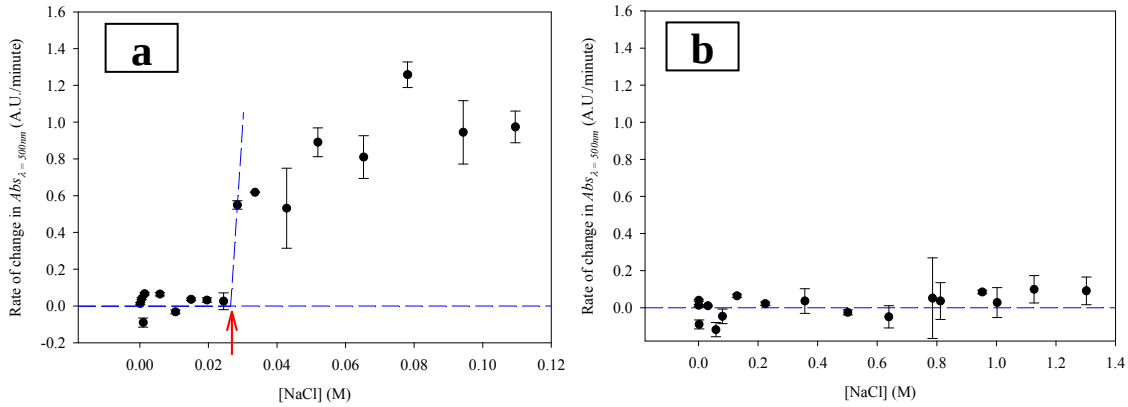

Figure 3.8 The CCC plots for the P4VP-based nanoparticle suspensions: (a) electrostatically-stabilized P4VP nanoparticles (A-4, D_{DLS} = 265.2 nm), and (b) P4VP-PEGMA nanoparticles (B-5, D_{DLS} = 313.6 nm). The arrow indicates where the phase transition occurs.

When the suspensions of the P4VP nanoparticles were solely stabilized by the positively-charged surface amidine groups (extended measurements of ζ–potentials of these nanoparticles are shown in Figure A-1 of the Appendix-A), the CCC plot in Figure 3.8 (a) displays a transition in the measured rates of change in turbidity (marked by the arrow), indicating that phase transition, i.e. the colloid coagulation occurred. As more salts were present, more freely moving ions were available. The electrostatic repulsion interaction was reduced gradually upon the increment of electrolyte concentration in the surrounding solution. The thickening of the ion atmospheres around the nanoparticles compressed the electrostatic double layer.

In the contrary, the P4VP-PEGMA nanoparticles (B-5) were much more colloidally stable as demonstrated in Figure 3.8 (b). The additional stabilizing power was originated from the short steric layer of poly(ethylene glycol) grafted on the nanoparticles, which has been confirmed in the previous section. It is therefore demonstrated that the PEGMA chemically grafted onto the nanoparticles could enhance drastically the colloidal stability of the P4VP nanoparticles, thereby protecting the nanoparticles from flocculation/coagulation. The contribution of this steric layer is however neither accounted nor predicted by the traditional DLVO theory (Israelachvili, 1992; Romero-Cano *et al.*, 1998). The enhanced repulsive interactions can be explained as follow: when two particles with surfaces bearing grafted or adsorbed polymer chains are brought towards each other, an additional repulsion force arise due to either the osmotic repulsion caused by polymer chains interpenetration or reduced entropy from the compression between polymer chains (Israelachvili, 1992). This additional steric interaction can be related to the major physical characteristics of the polymer chains, for instance, the average thickness of

the polymeric coils covering the external surface, and the density and molecular weight of the adsorbed (or grafted) polymers (Vincent *et al.*, 1986).

3.3.4 pH-Dependent Swelling of P4VP-based Nanoparticles

P4VP and P4VP-based copolymers used in this study are well known for their pH-responsiveness due to the ionizable pyridyl group (Gil and Hudson, 2004). The swellability is controlled chiefly by their affinity for the surrounding solvent, and is a function of the chemical composition of the monomer and co-monomer, and the amount of crosslinker incorporated in the nanoparticles. As the nanoparticles become more swollen, higher amount of interstitial spaces or voids are available to accommodate influx of water or solvent from surrounding reservoir (increased "sponginess"), implying that the internal functional groups become more accessible for adsorption should these nanoparticles be used as adsorbents. The equilibrium porosity (or equilibrated water content or solvent uptake) of swollen nanoparticles or colloidal microgels is directly proportional to its degree of swelling (LeVan and Carta, 2008).

The swelling behaviors of the P4VP or P4VP-based nanoparticles prepared in this study were examined under various solution pH (Figure 3.9). Upon protonation (say at pH 3), the P4VP-based nanoparticles become swollen in the acidic environment, attributed to the Columbic repulsion between the neighboring protonated pyridyl groups. This can lead to an expansion in the overall dimensions, in particular, the hydrodynamic diameters of the nanoparticles. Due to the film-forming nature of the swollen P4VP, the particle sizes of these P4VP-based nanoparticles at low pH values could only be inferred from the DLS measurement. As shown in Figure 3.9 (a), when

the P4VP-PEGMA nanoparticle suspension was gradually acidified, the swelling of these nanoparticles containing varying amounts of crosslinkers (synthesized in the same manner as Run B-5 with different [DVB]), continuously increased from pH 5 to 2, as indicated by the ratio D/D_0, where D is the value of D_{DLS} of the nanoparticles at that particular pH and D_0 is the D_{DLS} of the nanoparticles in fully deswollen/collapsed state (i.e. at pH 6 – 8). As the crosslinker concentration increased, more crosslinking nodes were available to restrain the electrostatic repulsion-dominated swelling of the polymer network. Consequently, the degree of swelling (D/D_0) decreased from 2.9 to 1.9 when [DVB] increased from 0.5 wt.% to 4.0 wt.% (Figure 3.9 (a)). This is due to the diminishing polymer-polymer interaction when the charge repulsion was gradually increased from pH 5 to pH 2, because the degree of protonation became higher in a more acidic environment. This swelling property is in good agreement with another experimental result reported for poly(2-vinylpyridine)-based nanoparticles (Loxley and Vincent, 1997). The butyramidine groups of the initiator V50 mainly consists of primary and secondary amines, which have a characteristic pK_a value in the range of 9 to 11 that is higher that the pK_a value of the pyridyl groups (pK_a = 5.3). It may be expected that the butyramidine group will be completely protonated and the P4VP nanoparticle is positively charged even at neutral pH (i.e. pH 6 – 8). From pH 6 downwards, as the solution became more acidified, the nanoparticles were more positively charged due to the ionization of the pyridyl groups in the acidic environment. The measured ζ-potentials of the various P4VP-based nanoparticles are tabulated in Table 3.4. For instance, the values of both the ζ-potentials and the D_{DLS} of the P4VP-PEGMA nanoparticles crosslinked with DVB, were increased by almost one-fold when the pH was decreased from ca 6 to 1. The polydispersity of the D_{DLS} measured remained relatively small (< 0.02) during the acidification-induced swelling,

implying that these nanoparticles remained monodispersed even when they were fully swollen. These data altogether indicate that the P4VP-based nanoparticles are swellable and porous at low pH, hence they are suited for metal ion adsorption in acidic palladium-laden solution.

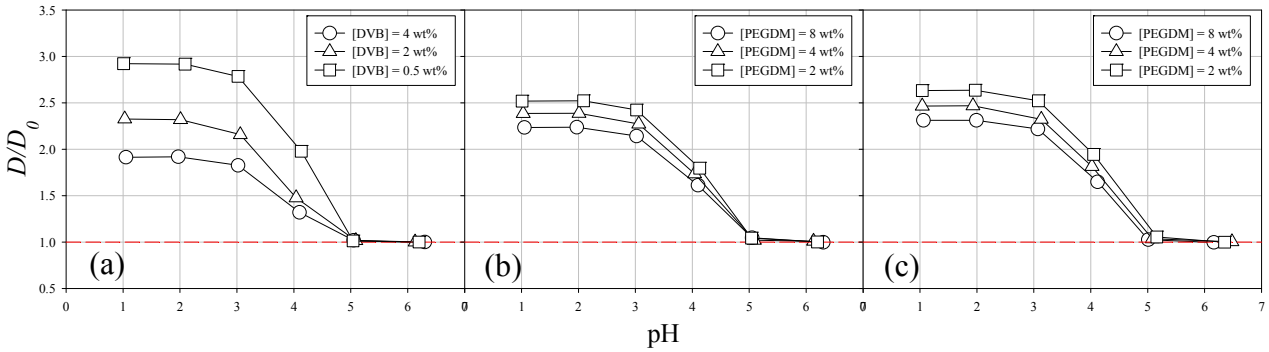

Figure 3.9 pH variation of hydrodynamic diameter of PEGMA-grafted P4VP (P4VP-PEGMA) nanoparticles prepared according to Run B-5 in Table 3.2, crosslinked by (a) DVB, (b) PEGDM (n = 9) and (c) PEGDM (n = 13), at ionic strength = 0.1 M. The solution pH was decreased from 6 to 1 by addition of acid. Note that the error bars are too small to be shown clearly.

Table 3.4 pH-dependent swelling of P4VP-PEGMA nanoparticles (prepared according to Run B-5 in Table 3.2)

Type of crosslinker	Crosslinker input		(Start of 1st cycle)			(Fully swollen state)			(End of 1st cycle, fully collapsed state)		
	[wt.% based on monomer]	[mole% based on monomer]	pH	D_{DLS} [nm] (μ)	ζ-potential [mV]$	pH	D_{DLS} [nm] (μ)	ζ-potential [mV]	pH	D_{DLS} [nm] (μ)	ζ-potential [mV]
DVB	2.0	0.0154	6.32	290.1 (0.004)	23.8 ± 2.2	1.07	631.4 (0.015)	43.1 ± 5.2	6.10	829.4 (0.443)	24.4 ± 5.7
	4.0	0.0308	6.40	306.8 (0.005)	24.8 ± 4.8	1.08	587.2 (0.005)	52.3 ± 4.6	6.07	700.8 (0.314)	26.6 ± 3.3
EGDM	2.0	0.0101	6.23	300.4 (0.005)	27.8 ± 1.2	1.03	745.1 (0.005)	47.3 ± 2.3	6.40	336.7 (0.156)	25.2 ± 4.2
	4.0	0.0203	6.52	305.6 (0.028)	25.4 ± 1.8	1.04	692.1 (0.005)	44.8 ± 6.0	6.34	303.3 (0.136)	27.2 ± 4.8
PEG-DM											
n = 9	2.0	0.00363	6.29	302.5 (0.005)	25.4 ± 1.4	1.05	762.4 (0.005)	46.4 ± 2.3	6.45	303.4 (0.005)	25.0 ± 4.1
	4.0	0.00727	6.81	314.5 (0.005)	26.2 ± 1.1	1.00	751.2 (0.005)	46.8 ± 2.2	6.76	312.4 (0.009)	27.0 ± 2.0
n = 13~14	2.0	0.00267	6.66	306.9 (0.005)	24.2 ± 2.5	1.02	808.1 (0.005)	48.8 ± 1.9	6.11	347.1 (0.046)	25.0 ± 1.2
	4.0	0.00533	6.46	317.0 (0.023)	24.4 ± 4.8	1.01	781.5 (0.005)	45.8 ± 2.9	6.20	320.6 (0.031)	27.3 ± 3.5

* All tests were conducted at 0.1 M NaCl. Relatively higher salt content was used to alleviate the dilution caused by addition of acid/base during the titration, as well as a preliminary test of the nanoparticle stability towards high ionic strength medium.
** μ denotes the polydispersity, as given by the cumulant analysis of the DLS data. Value of 0.000 – 0.020 indicates monodispersity, whereas 0.020 – 0.050 implies near monodispersity.
$ For reference, ζ-potentials of pristine nanoparticles (A-2) are 45.36 ± 1.8 mV and 27.19 eV ± 2.3 mV at 0.01 M and 0.1 M NaCl respectively (pH 6.1).

Together with the electron micrographs shown in Figure 3.2, the results confirm that the prepared nanoparticles exhibited a narrow particle size distribution at all solution pH (pH 1 to pH 6), with good shape and size stability which can be attributed to the crosslinker incorporated that stabilized the polymeric network generated during the polymerization process. However, an unexpected flocculation of the nanoparticles was observed when the swollen nanoparticles samples were back-titrated back to neutral pH (see Table 3.4 for DVB's entries). As a consequence, significant polydispersity in the particle sizes was observed from the DLS measurement. It was suspected that the hysteresis was due to sub-optimal selection of the crosslinker (defect of polymeric network), rather than the colloidal destabilization since the back-titrated PEGMA-grafted nanoparticles remained positively-charged (see the ζ-potentials measured at the end of 1st cycle of titration in Table 3.4).

3.3.5 pH-Swing Titrametric Swelling of P4VP-Based Nanoparticles

It is important to study whether the robustness of the nanoparticles prepared can be further enhanced, i.e. to swell and deswell reversibly without hysteresis during acidification and neutralization in a cyclic manner. Physicochemical and morphological stabilities of nanomaterials are crucial in evaluating their full-scale potential for actual applications. In the literature, use of difunctional or multifunctional crosslinkers has been industrially important and indispensable in various polymer formulations. Polymeric nanoparticles with weak, inadequate crosslinking would lose its shape and particle integrity when the particles are subjected to cyclic, harsh treatment (pH, salinity, temperature etc.). For instance, chitosan nanoparticles prepared from ionic-crosslinking between protonated amine groups along chitosan chains and tripolyphosphate (TPP) gradually disintegrated in

water over days, or even dissolved spontaneously when came into contact with high salinity solution (125 mM KCl) (López-León *et al.*, 2005).

It is highly probable that the use of DVB might have caused the hysteresis problem, as identified in the previous section (see Table 3.4 for DVB's entries). The hydrophobic crosslinker, i.e. DVB, is more reactive than other common monomers (styrene, N-isopropylacrylamide etc.), and their copolymerization always leads to early and quick DVB congregation at the initial stage of the polymerization (Okasha *et al.*, 1979). This disparate reactivity caused uneven intraparticle distribution of crosslinking, and gave rise to inhomogeneous microgel structure, consisting of a strongly crosslinked core surrounded by a diffuse and loosely crosslinked shell when the polymeric nanoparticles are swollen (Funke, 1996; Downey *et al.*, 2001). Fernández-Nieves *et al.* (2004) reported that the internal distribution of crosslink within the poly(2-vinylpyridine) microgels crosslinked with 0.25 wt.% DVB was inhomogeneous in both swollen and collapsed states. Furthermore, they demonstrated that the density profile with the particles could only be described with exponentially decaying function.

Use of long, flexible crosslinkers which comprises ethylene glycol as repeating units in synthesis of microgel particles and polymer latexes has been reported (Kratz *et al.*, 2002; Leobandung *et al.*, 2002; Hazot *et al.*, 2003; Bouvier-Fontes *et al.*, 2005). It was proposed that incorporation of long-chain, flexible crosslinker could reduce intramolecular crosslinking and cyclization, and endow the microgel particles with larger network flexibility (Kratz *et al.*, 2002; Ma *et al.*, 2004). To determine whether a change of crosslinker can alleviate the stability problem observed, a few new batches of P4VP-PEGMA nanoparticles were synthesized according to the recipe for Run B-5

in Table 3.2, except that the original crosslinker, DVB was substituted by other commercially-available crosslinkers (i.e. EGDM, PEGDM (n = 9 and 13)) and the concentrations were increased. Low crosslinker concentration, e.g. 0.5 wt.%, was not used because their molar concentration would be too low for meaningful discussion (see Table 3.4 for the molar percentages).

These new batches of P4VP-PEGMA nanoparticles (crosslinked with EGDM and PEGDM) were also studied for their pH-dependent swelling behavior, and their D_{DLS} and ζ–potentials were measured (see Table 3.4). Generally, these nanoparticles display similar features to those crosslinked with DVB, e.g. the pH-dependence of swelling, except that the hysteresis in D_{DLS} after the 1st cycle of acidification-neutralization became smaller in magnitude, and the polydispersity in particle sizes were remarkably reduced (see Table 3.4). To explore further the beneficial roles of these long-chain crosslinkers, the P4VP-based nanoparticles crosslinked with 4.0 wt.% of these crosslinkers were subjected to pH-swing titrametric swelling test. The results are shown in Figure 3.10, wherein the changes in the turbidity values (i.e. $Abs_{\lambda=400}$) are also shown.

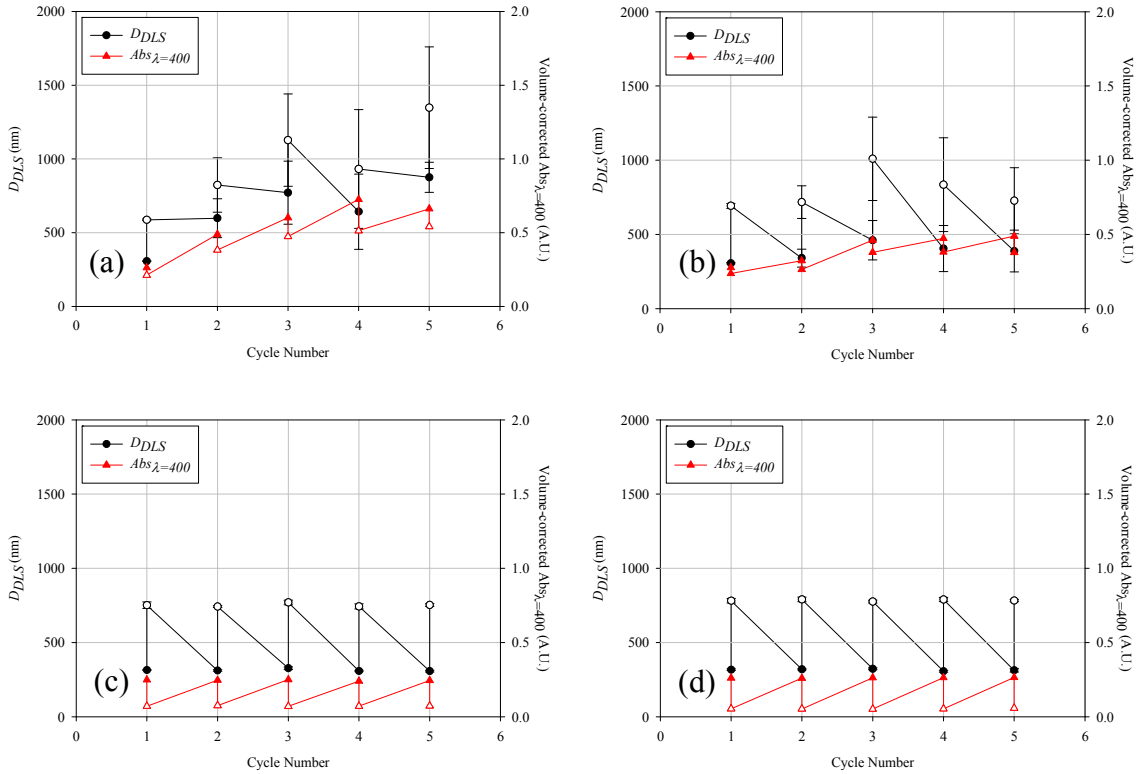

Figure 3.10 pH-swing titrametric swelling curves of P4VP-PEGMA nanoparticles (prepared according to Run B-5 in Table 3.2, D_{pte} ~ 300 nm) at ionic strength of 0.1 M. The nanoparticles are crosslinked with (a) 4 wt.% of DVB, (b) 4 wt.% of EGDM, (c) 4 wt.% of PEGDM (n=9), or (d) of PEGDM (n=13). Filled symbols are referred to fully collapsed nanoparticles (deswollen state); whereas hollow symbols denote fully swollen state at pH ~ 1.0 – 1.1.

As shown in Figure 3.10 (a), the DVB-based nanoparticles lost their stabilities and flocculated during the test. The increase in $Abs_{\lambda=400}$ over five cycles indicated that either more aggregates or larger aggregates were formed. The clumps of these DVB-based particles can be clearly observed in the FESEM micrographs (Figure 3.11 (a)). Even though substituting DVB with EGDM improved the morphological integrity after the cyclic swelling-deswelling (see Figure 3.11 (b)), the aggregation of these EGDM-based nanoparticles was still unavoidable (see Figure 3.10 (b)). When DVB was replaced with both types of PEGDM crosslinkers, the distribution of the crosslinker molecules may be more uniformly distributed throughout the nanoparticles, and hence the microstructural integrity was better retained when repeated swelling-

deswelling took place (Figure 3.10 (c) and (d)). There was also no appreciable difference in the dimension of the PEGDM-based nanoparticles throughout all the titrametric cycles (see Figure 3.11 (c) and (d)).

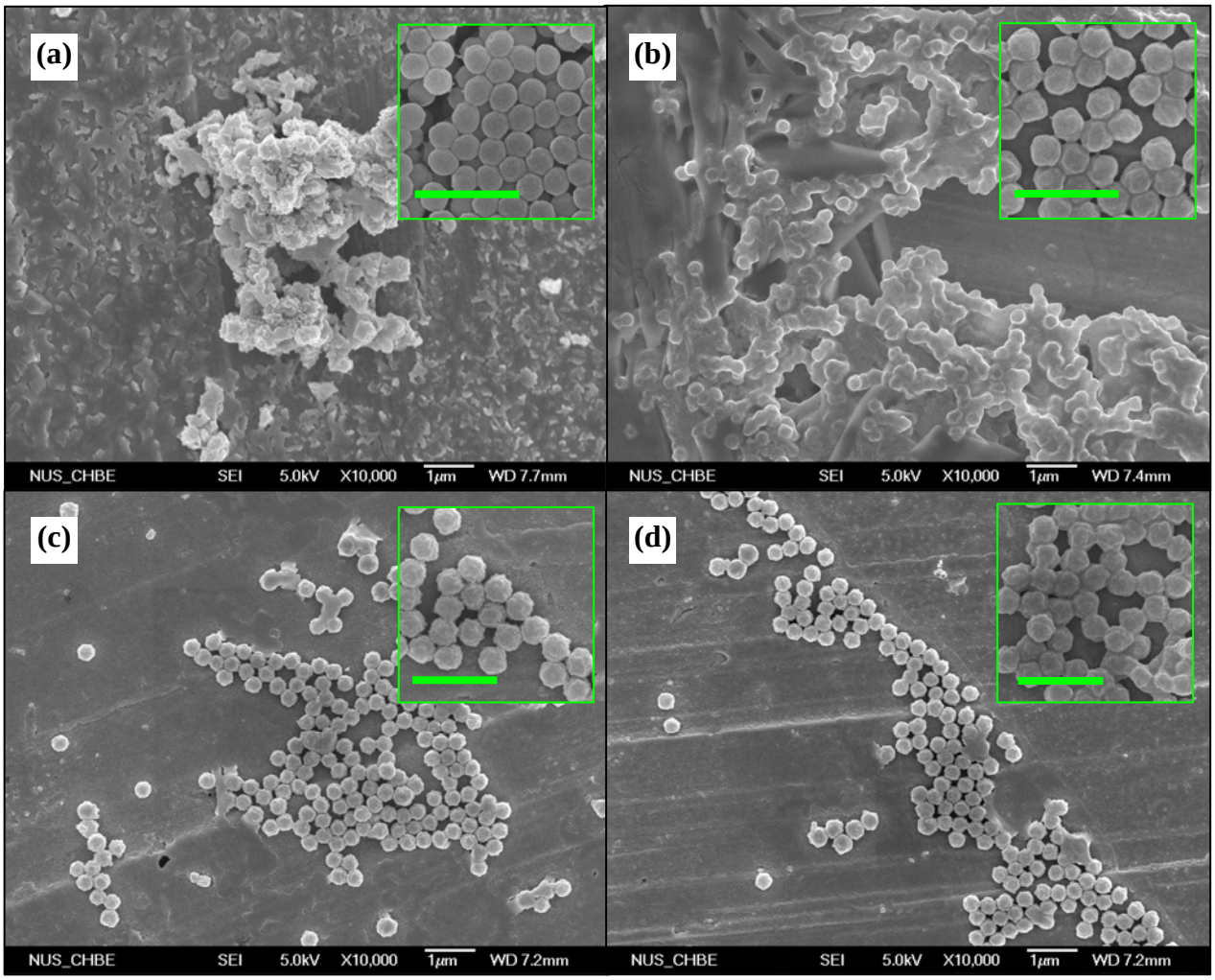

Figure 3.11 Electron micrographs of P4VP-PEGMA nanoparticles (B-5) crosslinked with (a) 4 wt.% of DVB, and (b) 4 wt.% of EGDM, (c) 4 wt.% of PEGDM (n=13), and (d) 4 wt.% of PEGDM (n=9) (wet-casted from dilute suspensions that had undergone five cycles of pH-swing titration, final pH at which the nanoparticles were casted from, pH ~ 8-9). Insets are the pristine nanoparticles that are not subjected to titration (scale bar denotes 1μm).

The results in this study therefore demonstrated that replacing short-chain divinyl crosslinker (DVB, EGDM) with flexible long-chain crosslinker (PEGDM) can effectively minimize the hysteresis of the nanoparticles during the cyclic swelling-deswelling process. Their pH-dependent swelling behaviors were similar to that of

DVB (see Figure 3.9 (b) and (c)). The degree of swelling decreased as more PEGDM molecules were present, indicating that the PEGDM crosslinkers were successfully incorporated, which strengthened the polymeric network despite their lower molar percentages than that of their counterparts (DVB, EGDM) (see Table 3.4). Amalvy *et al.* (2004) synthesized tertiary-amine containing microgels with poly(propylene glycol) diacrylate (PPGDA) and observed a similar reversibility in swelling transition (pH 9 → pH 4 → pH 9).

The underlying mechanisms for enhanced stabilization of the polymeric networks with long-chain crosslinker have been experimentally investigated by other researchers. Abdurrahmanoglu and Okay (2008) experimentally probed the structure-modifying effect of poly(ethylene glycol) dimethacrylate crosslinkers with varying spacer lengths during the microstructure evolution of the poly(acrylamide) hydrogels, by monitoring the rheological properties, degree of swelling and change in gel turbidity as a function of spacer length. Higher elastic modulus and more restrained swelling were observed for the hydrogels that were synthesized with larger, more flexible crosslinkers. They attributed the observed phenomenon to the higher propensity of the long-chain crosslinker to undergo intermolecular crosslinking. During the *ab-initio* free-radical polymerization, short-chain crosslinkers are generally more susceptible to cyclization (formation of loop), leading to lower crosslinking efficiency and crosslinking density (Anseth and Bowman, 1994; Kannurpatti *et al.*, 1998). Similar observation was obtained by Bouvier-Fontes *et al.* (2005) who investigated the effect of the size of diacrylate ester on seeded semicontinuous emulsion copolymerization of butyl acrylate.

During polymerization, a crosslinker molecule first adds to a propagating polymeric radical by consuming one double bond, after which the polymeric radical continues to propagate and lengthen itself by adding more monomers and crosslinkers. The remaining pendant double bonds could react with another propagating polymeric radical (intermolecular crosslinking), thereby forming crosslink nodes, or react with the radical end on the same chain (intramolecular crosslinking or cyclization) (Tobita and Hamielec, 1989). Crosslinkers with short spacer length are generally more prone to the latter scenario because the separation distance between propagating radical and pendant double bonds is shorter, resulting in higher local concentration of pendant double bonds in the vicinity of propagating radicals (Kannurpatti *et al.*, 1998; Yu *et al.*, 2007).

Hazot *et al.* (2003) observed that the polymerization reactivity and crosslinking efficiency are higher when the crosslinkers employed are more water-soluble during the synthesis of poly(N-ethylmethacrylamide) microgels. During the polymerization, water-soluble crosslinkers could dissolve and be fully dispersed in the continuous phase, resulting in less local agglomeration of crosslinker molecules. The more ethylene glycol groups the molecule possesses, the higher the aqueous solubility of PEGDM is. Therefore, the local rate of addition of these crosslinker to the growing networks is more homogeneous throughout the whole reaction volume.

It is therefore hypothesized as follow as to how large, flexible difunctional crosslinkers (e.g. PEGDM) were incorporated once the polymerization was commenced: the greater spacer length between the two reactive methacrylate groups allowed each end to distance itself from one another, leading to lower local

concentration of the dimethacrylates in close proximity of propagating polymeric radicals. Other incoming monomers, monomeric radicals and propagating oligomers therefore had greater probability to add to the dimethacrylates, hence giving rise to more sparsely distributed crosslink nodes, increased network connectivity and higher crosslinking efficiency. In addition, the more hydrophilic PEGDM was more uniformly distributed in the aqueous phase, and its diffusive transport through aqueous phase, between surrounding solution and growing particles, could occur more readily. As a result, the resulting polymer networks were homogeneously and efficiently crosslinked, which allows for producing more robust P4VP nanoparticles that are capable of swell and deswell reversibly during pH-swing titration.

3.3.6 Palladium-induced Deswelling of P4VP Nanoparticles

Besides colloidal stability and morphological stability during pH-swing titration, the robustness of the P4VP nanoparticles in the presence of target metal ions should be assessed as well. To determine whether the P4VP nanoparticles would remain stable and well-dispersed after sequestration of palladium ions, the change in mean particle size and polydispersity of swollen P4VP nanoparticles was examined as a function of contact time (Figure 3.12). Swollen P4VP nanoparticles at low pH are structurally equivalent to hydrogel in good solvent, whereby the extent of swelling as well as the associated mass transport phenomena such as diffusion, uptake and release of solute by the polymeric network are mainly determined by three important structural parameters (Peppas *et al.*, 2000): the polymer fraction in the gel network (φ), the number average molecular weight between crosslinking nodes ($\overline{M}_c$) and the mesh size (or pore size) of the gel network. For most metal-sequestrating hydrogels and ion-

exchange resins, the swollen polymeric matrix undergoes deswelling when metal-binding event takes place.

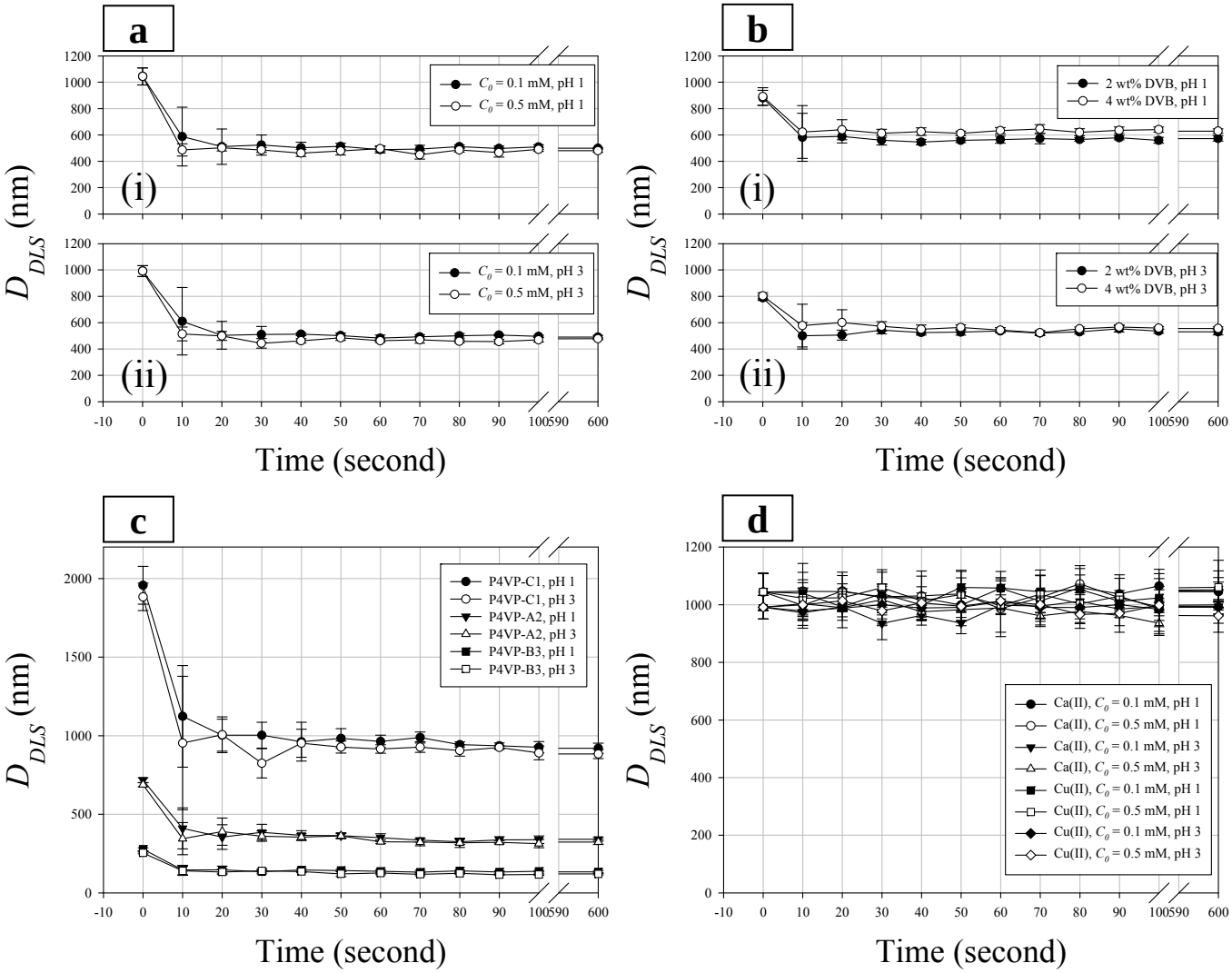

Figure 3.12 Plots of deswelling of swollen P4VP nanoparticles during static adsorption (without stirring), i.e. (a) deswelling of P4VP-A3, (b) deswelling of P4VP-A3 whose [DVB] are varied where C_0 = 0.1 mM, (c) effect of particle size on desweling kinetic C_0 = 0.1 mM, and (d) deswelling of P4VP nanoparticles in the presence of other metal ions. [DVB] = 0.5 wt.% unless otherwise mentioned. The solid lines are to guide the eye.

The dynamics of the variation of D_{DLS} of the P4VP nanoparticles as a function of time were monitored in a "static adsorption" set-up (Figure 3.12). In the experiments, prior to mixing the nanoparticles with Pd(II) solution, the P4VP nanoparticles were swollen to various extents, depending on the solution pH and the crosslinking degree. Once the Pd(II) adsorption commenced, rapid deswelling of P4VP nanoparticles was observed,

regardless of initial Pd(II) concentration or solution pH (see Figure 3.12 (a), (b) and (c), and Table 3.5). Figure 3.12 (a) shows that the swollen P4VP nanoparticles with 0.5 wt.% DVB became collapsed upon contact with Pd(II), and the degree of swelling was larger for higher Pd(II) initial concentration (also see Table 3.5).

Table 3.5 Deswelling of P4VP nanoparticles (P4VP-A3) in the presence of metal ions. [DVB] = 0.5 wt.% (equilibrium time = 10 minutes).

	pH	C_0 (mM)	D_{DLS} (nm)	ε (-)*
No metal ions	1.02	-	1044.2 ± 64.3	0.958
	3.01	-	991.2 ± 41.1	0.950
Pd(II)	1.09	0.12	499.1 ± 5.1	0.612
	1.01	0.52	490.8 ± 13.8	0.592
	3.05	0.13	480.7 ± 12.2	0.566
	3.03	0.54	477.8 ± 7.5	0.557
Ca(II)	1.02	0.11	1044.8 ± 33.6	0.958
	1.08	0.55	1049.4 ± 68.1	0.958
	3.07	0.12	993.8 ± 58.3	0.951
	3.02	0.51	999.4 ± 11.1	0.952
Cu(II)	1.03	0.12	1051.2 ± 42.9	0.958
	1.04	0.54	1060.3 ± 93.8	0.960
	3.02	0.10	991.0 ± 23.4	0.950
	3.00	0.57	961.6 ± 56.9	0.946

* Assuming the nanoparticles are fully collapsed at pH ~ 8-9 (i.e. the nanoparticles are totally deswollen initially at neutral condition), the equilibrium porosity (ε) or equilibrated water uptake (EWC) is calculated as follow, $\varepsilon_{eqm} = 1 - \varphi_{eqm} = 1 - \left(\frac{D_{DLS,0}}{D_{DLS,eqm}} \right)^3$, where φ_{eqm} is the polymer fraction of the nanoparticles.

As higher amounts of crosslinker were incorporated, lesser extents in the deswelling were observed (Figure 3.12 (b)), implying that stiffer networks restricted the contraction due to having more crosslinking nodes. Pd(II)-induced deswelling was also observed for the P4VP nanoparticles with different particle size ($D_{DLS,0}$ = 90.8 nm for P4VP-B3; $D_{DLS,0}$ = 245.6 nm for P4VP-A2; $D_{DLS,0}$ = 648.2 nm for P4VP-C1), as demonstrated in Figure 3.12 (c). The error bars might be excessively large for the first 30 seconds, caused by dead zones or velocity distribution arises from absence of

external mixing. Due to the limitation of our current light scattering set-up, the deswelling dynamics within less than 10-second intervals could not be further refined.

Metal ions-induced deswelling. Many studies reported the manipulation of phase behaviors of polyelectrolytes, proteins and colloids in aqueous solution by adding multivalent cations which could interact strongly with the surface and interior negatively charged groups, forming multipoint contacts centered at the complexed cations. Depending on the polymer or colloid concentration, the polyelectrolytes or colloids would undergo aggregation (interchain-complexation or intermolecular crosslinking), deswelling/shrinking (intrachain-complexation or intramolecular crosslinking) or a combination of both (Peng and Wu, 1999; Peng and Wu, 2001a; Peng and Wu 2001b; Lin *et al.*, 2002). For linear or branched polymers, it was reported that the transition from intrachain-complexation to interchain-complexation occured when the multivalent cation concentration exceeded a critical concentration (Peng and Wu, 1999). Coagulation of colloidal particles could be induced as well when the amount of added multivalent cations exceeds the critical coagulation concentration (Gregory, 2006).

The sequestrated Pd(II) collapsed the swollen P4VP nanoparticles to a large extent, for instance, the equilibrium porosity (ε) decreased from ca 0.96 to 0.60 at pH 1 after Pd(II) adsorption (Table 3.5). This should be caused by the chemical binding of Pd(II) to the pyridyl or pyridinium groups residing in the swollen P4VP networks, as pyridyl groups of P4VP are soft-donor ligands for Pd(II) (Pearson, 1963). Morris *et al.* (1997) observed that the diameter of anionic microgel particles (carrying carboxylic acid groups) decreased in the presence of Pb^{2+} at neutral or higher pH. They postulated that

the collapse of microgel particles was caused by the complexation of Pb^{2+} with the negatively charged carboxylate groups. Peng and Wu (2001a) explored further on the effect of different type of metal ions on the deswelling/aggregation behavior of lightly crosslinked poly(N-vinyl-caprolactam-*co*-sodium acrylate) (P(VCL-*co*-SA)) microgels using simultaneous static and dynamic laser light scattering spectroscopy (SLS, DLS). Their results reveal that Hg^{2+} is highly efficient in collapsing the microgels and lead to profound shrinking, by ionic crosslinking; whereas other divalent metal ions (Cu^{2+}, Ca^{2+}) can only cause weak or negligible deswelling of microgels. The extent of the microgel deswelling triggered by different metal ions follows the order of strength for hard-soft acid-base (HSAB) interaction between the cations and carboxylate groups (Pearson, 1963). Hg^{2+}, being the softest electron acceptor, could coordinately bind to the two carboxylate groups (the electron donor), resulting in more preferential partitioning in the polymer phase, stronger 'inner-sphere' complexation and hence increased proximity of the coordinated carboxylate groups.

The presence of interchain or inter-microgel aggregation could be checked by examining whether there is multimodal splitting of hydrodynamic size distributions (Lin *et al.*, 2002; Rasmusson *et al.*, 2004). From Table 3.5 and Figure 3.12, it is shown that the collapsed nanoparticles after adsorbing Pd(II) remained narrowly monodispersed (small error bars), and splitting of particle size distribution is clearly absent. This result implies that the intraparticle Pd(II)-pyridyl groups complexation is dominant, hence leading to minimal interparticle complexation and aggregation (Peng and Wu, 2001b; He *et al.*, 2008). These results suggest that even though the P4VP nanoparticles would be partially collapsed after Pd(II) sequestration, the deswollen

particles remain colloidally stable. The experiments also showed that other types of metal ions (Ca(II), Cu(II)) did not collapse the swollen nanoparticles at all, in the range of concentrations concerned (Table 3.5). The dimensions of P4VP nanoparticles remained unchanged throughout the 10 minutes of DLS measurement (Figure 3.12 (d)). As both types of metal ions are cationic at low pH and harder than Pd(II), their complexation to the pyridyl groups is unlikely to occur, especially when the pyridyl groups become positively charged at low pH. Considering that the square-planar coordination geometry for Pd^{2+} cation requires four ligands, it is highly probable that either the coordinative binding or anion-exchange of Pd(II) by P4VP is at least of bidentate nature, in order to form intramolecular crosslinking that leads to nanoparticles deswelling collectively.

3.4 Conclusion

The spherical, narrowly-dispersed P4VP or P4VP-based nanoparticles with a size in the range of 70 – 650 nm were successfully synthesized with the proposed two-pronged approach based on the surfactant-free emulsion polymerization method (SFEP) in this work. Selection of co-monomers and crosslinkers in the polymerization recipe was of crucial importance in determining the mechanical robustness of these prepared nanoparticles in terms of colloidal and morphological stabilities. The use of PEGMA in a "starved-fed" manner could produced very fine nanoparticles (~ 70 nm), while the PEGMA molecules once grafted onto the nanoparticle surfaces would confer enhanced salt-tolerance towards coagulation. As shown from the cyclic pH-swing swelling-deswelling tests, the nanoparticles crosslinked with flexible, long chain PEGDM remained intact and well-dispersed after five cycles of pH-swing swelling-deswelling. The high nitrogen content measured for these nanoparticles implies that

the P4VP nanoparticles have high volumetric density of the binding sites. Together with their tremendous swellability in acidic pH and sponge-like porous structure, these nanoparticles can be expected to show good adsorption performance for palladium ions from aqueous solutions.

CHAPTER 4

ADSORPTION BEHAVIOR AND PERFORMANCE OF P4VP NANOPARTICLES FOR PALLADIUM RECOVERY: ADSORPTION MECHANISMS, ISOTHERMS, KINETICS AND ADSORBENT REGENERATION

4.1 Introduction

In the previous chapter, the successful preparation of P4VP or P4VP-based nanoparticles of various sizes with high uniformity have been described. The robustness of the P4VP nanoparticles has also been demonstrated through pH-swing swelling-deswelling tests etc. To facilitate further deployment of these prepared nanoadsorbents for actual environmental applications, for instance, resource recovery and reuse of precious metal, such as palladium, more detailed studies that describe all the relevant process behaviors and rates, for e.g., adsorption isotherms, kinetics and separation performance would be important. The adsorption isotherms and kinetics data can aid engineers and technologists to evaluate and predict the rates and performances of the processes. Measuring and predicting pollutant transport and uptake rates are also critical to the design and operation of batch and fixed-bed adsorption systems for environmental protection or resource recovery (Tien, 1994; Do, 1998).

As the prepared P4VP nanoparticles were shown to swell significantly in acidic solutions, the resulting highly porous, charged polycationic network resembles a "nano-sponge". The "sponge-like" structure of the P4VP nanoparticles should facilitate the diffusive penetrative movement of palladium ions through the open, swollen network, thereby resulting in high accessibility and utilization of the interior pyridyl binding sites. In this chapter, the prepared P4VP nanoparticles were evaluated for their performance in sequestrating and recovering palladium, in terms of adsorption isotherms and kinetics. The adsorption mechanism of Pd(II) with P4VP nanoparticles was also examined in depth, by probing the nature of Pd(II) binding to the nanoparticles. The recovery of palladium from spent P4VP nanoparticles was

investigated, and a simple proof-of-concept demonstrating the repeated adsorption-desorption-regeneration processes with the P4VP nanoparticles was also included.

4.2 Materials and Methods

4.2.1 Materials

The monomeric precursors, crosslinker and initiator used to prepare the nanoparticles in this chapter are the same as those described in section 3.2.1 of Chapter 3, as shown in Figure 3.1. Palladium (II) chloride ($PdCl_2$) (99.9%, 59.9% as metal) purchased from Alfa Aesar was used in the adsorption experiments. Other chemicals, including sodium hydroxide (NaOH), hydrochloric acid (HCl) and nitric acid (HNO_3) were of analytical grade and used without further purification.

4.2.2 Synthesis of P4VP Nanoparticles

The P4VP nanoparticles used for the spectroscopic investigation and adsorption study were synthesized using the two-pronged surfactant-free emulsion polymerization (SFEP) method described in section 3.2.2 of Chapter 3, via either *ab-initio* or semicontinuous feed ("semibatch" or "starved-fed") approach. The recipes used are given in Table 3.1 and Table 3.2. The freshly-made nanoparticle suspension was collected and cleaned the same way described in section 3.2.3 of Chapter 3. The cleaned nanoparticle suspension was used as stock for subsequent adsorption experiments and spectroscopic investigation, and the solid contents (wt.%) of each stock was determined gravimetrically.

4.2.3 Characterization Methods

Spectroscopic methods to probe Pd(II) binding. Fourier Transform-Infrared (FT-IR) vibrational spectroscopy was performed on Bio-Rad FTS 135 system to examine the change in chemical functionality of the nanoparticle samples after Pd(II) adsorption. The analysis was done as described in section 3.2.4 of Chapter 3. The binding between the nanoparticles and the adsorbed Pd(II) was also examined through X-ray photoelectron spectroscopic analysis (Kratos XPS System AXIS His-165 Ultra, Kratos Analytical Ltd., U.K.). The analysis was similarly done as described in section 3.2.4 of Chapter 3. To determine the relative abundance of pristine, hydrogen-bonded, Pd(II)-bound and protonated pyridyl groups (pyridinium), the area under each component peak of N 1*s* spectra was calculated and summed up to yield the ratios.

Particle size measurement. Effective hydrodynamic diameter (D_{DLS}) of the swollen nanoparticles at various pH were measured, based on the principle of dynamic light scattering (DLS), as described in section 3.2.4 of Chapter 3.

Potentiometric titration. To measure the degree of ionization or protonation of the pyridyl groups of the nanoparticles prepared, various batches of cleaned samples of P4VP-A3 nanoparticles with several crosslinker concentrations were first dispersed in diluted HCl solution of pH 1.1-1.2. The nanoparticles dispersion was titrated by using a computer-interfaced pH-autotitrator (Titrino 799 GPT, Metrohm, Switzerland) (precalibrated using certified pH buffer solutions). The pH titration was conducted by dropwise addition of 0.1 N NaOH (aq) in forward direction, and repeated in reverse direction with 0.1 N HCl (aq).

4.2.4 Adsorption Isotherms Experiments

The P4VP and P4VP-based nanoparticles were evaluated for their maximum adsorption capacity (q_{max}) and adsorption affinity (b) for palladium ions, i.e. Pd(II), through adsorption isotherm experiments. As palladium ions are mostly found in acidic chloride solutions (Iglesias *et al.*, 1999), the palladium stock solutions for the adsorption experiments were first prepared by dissolving palladium chloride salt in warm, acidified (HCl) deionized water, with gentle stirring. The resultant orange/reddish color solution was then filtered through a 0.45 μm syringe filter to remove any undissolved or colloidal palladium chloride. The final concentrations of the filtered palladium stock solutions were measured with an inductively coupled plasma optical-emission spectrometer (ICP-OES, Perkin Elmer Optima DV 3000, USA). The stock solutions of P4VP nanoparticles and palladium chloride were adjusted to the desired pH with HCl monitored through a pH meter (Titrino 799 GPT, Metrohm, Switzerland). A typical set up for the batch adsorption experiment is as follow: 0.75 ml of a P4VP nanoparticle stock solution was mixed with 2 ml of palladium chloride stock solution at a concentration of 2.0 mM and a pH of 2.3. The mixture was then combined with 7.25 ml of deionized water to give a final volume of 10 ml. The pH of the resultant solution was 3.0, and the initial palladium concentration was 0.4 mM in this case, which were confirmed by pH measurement and ICP analysis. The procedure was repeated for other initial palladium concentrations, in order to determine the adsorption isotherm. After an equilibration period of 1 hour (at room temperature), the mixture solution was centrifuged at 9000 rpm for 30 minutes, and the clear supernatant was filtered through a 0.2 μm syringe filter to remove any residual nanoparticles. The palladium chloride stock solution and the filtered supernatants were analyzed for palladium concentration by the ICP-OES.

The pH values of the solution before and after the batch adsorption experiment were measured and found to be relatively constant (ΔpH < 0.05). To examine the effect of pH values on the adsorption performance, the pH of the solutions was adjusted using HCl and NaOH solutions to a level in the range of pH 3 to pH 1 (palladium ions would precipitate out from pH 4.0 or higher at the concerned concentrations, resulting in the formation of palladium colloids (Byrne and Kump, 1993)). The palladium solution at pH ~ 0 was prepared by directly mixing concentrated HCl with the palladium stock solution in appropriate proportion. The resulting dosage of the nanoparticles for a typical batch adsorption experiment was approximately 0.75 g for 1 liter of palladium solution. The equilibrium adsorption capacity (q_{eqm} or q) was calculated using Eq. (4.1):

$$q_{eqm}\left(\frac{mmole-solute}{gram-adsorbent}\right)=\frac{V\left(c_0-c_{eqm}\right)}{m_p} \tag{4.1}$$

where V is the total volume of the mixture solution (ml), m_p is the mass of nanoparticles added in the mixture solution (mg), and c_0 (mM) and c_{eqm} (mM) are the initial Pd(II) concentration and the equilibrium (or final) Pd(II) concentration at end of adsorption, respectively. The typical palladium concentrations used in these experiments were in the range of 0.1 to 1.0 mM and the pH values investigated were 0 to 4. A minimum of 12 experiments was conducted at each pH to compile the adsorption isotherm curve. Some selected samples with Pd(II) adsorbed were collected for further characterization using FT-IR and XPS.

4.2.5 Adsorption Kinetic Experiments

The palladium adsorption kinetics by P4VP or P4VP-based nanoparticles were also investigated. To accurately follow the adsorption kinetics, the change in the palladium concentration of the solution during the adsorption process (at room temperature) was monitored as a function of time, by periodically sampling at short intervals (5 or 10 seconds), and analyzing residual palladium concentrations in the samples. The adsorbent dosage was determined via trial-and-error to keep it low enough to minimize the back-pressure as well as to allow for rapid separation of the nanoparticles with a 0.1 μm or 0.2 μm syringe filter. The typical dosage for the kinetic experiments was 20 mg (dry weight) nanoparticles for every 400 ml of the palladium solution used. The mixture was magnetically stirred at 500 rpm throughout the kinetic experiment.

4.2.6 Regeneration and Reuse of P4VP Nanoparticles

Several types of eluents or stripping agents were screened to evaluate their potentials in desorption of sequestrated palladium from the exhausted P4VP nanoparticles, at a liquid/solid ratio (L/S) of 1.0 ml/mg. Palladium-loaded nanoparticles (PEGMA-grafted nanoparticles crosslinked with 4.0 wt.% of PEGDM (n = 9), B-5) were prepared in a similar manner described earlier for the adsorption experiment. In short, 40 ml solution containing 2 mg of nanoparticles and 0.2 mM of palladium ions at pH 3 was prepared and stirred for 1 hour. The mixture was then centrifuged and 39 ml of the supernatant was removed. The supernatant was analyzed with ICP-OES to determine the residual palladium concentration. The residual volume was then mixed with a selected eluent of an appropriate concentration to obtain a L\S ratio of 1.0. The mixture was then ultrasonicated for 5 minutes and later vortexed for another 30

minutes to fully re-disperse the nanoparticles. The desorbed solution was centrifuged and supernatant was sampled and filtered before measuring the palladium concentration. Duplicates of two were prepared to check for reproducibility of each experiment.

The regeneration and reuse of the nanoparticles (B-5) for multiple cycles were investigated batchwise with an in-house assembled filtration system. The filtration of the nanoparticle suspension was carried out with a UHP 47 ultrafiltration dead-end stirred cell (Advantec MFS, Japan), wherein the operating pressure of 68.9 kPa (10 psi) was precisely controlled via the computer-interfaced pressure controller (Alicat Scientific PCD, USA) with an accuracy of ± 0.5 % to which the nitrogen cylinder was connected. The solution was first placed inside a PVC pressure vessel, to which the stirred cell was connected to. Upon pressurization, the solution was pressed from the vessel to the stirred cell (stirring speed = 500 rpm) where a membrane filter (PVDF GVWP04700, pore size = 0.22 μm, Millipore, USA) was housed. Permeate was collected and weighed by an electronic balance serially linked to a PC for automated data collection at fixed time intervals. Data acquisition program written via LabVIEW^{TM} (National Instruments, Austin, Texas) was used to communicate with the pressure controller and to collect permeate-weight data over time. Typically, 500 ml of a solution containing 25 mg of the nanoparticles and 0.2 mM of palladium ions (pH 3) was prepared and equilibrated for 1 hour. After the adsorption, the nanoparticles were separated by the filtration system. The filtration was paused when 497 ml of permeate was collected. Then, 22 ml of a selected eluent was added to the retentate (concentrate) (3 ml) and stirred for 30 minutes. The mixture was filtered through the membrane again until 22 ml of permeate containing the eluted Pd(II) was collected.

To increase the recovery, another portion (17 ml) of acidified solution (pH 3) was added and the mixture was filtrated to yield retentate of 3 ml. The nanoparticles in the retentate was then mixed with a freshly prepared Pd(II) solution and the whole filtration and regeneration process was repeated. A total of five cycles of this process was conducted. The palladium concentrations in the collected permeates (22 ml + 17 ml) were measured and the recovery efficiencies were calculated for each of the five cycles.

4.3 Results and Discussion

4.3.1 Pd(II) Adsorption Isotherms

Adsorption Isotherm. An adsorbent should ideally have a high sequestration capacity for the target metal and would work effectively even at very low metal concentrations. Only a few adsorbents reported in the literature may meet such criteria. Most of the commercial anion-exchange and thiol-modified resins investigated for Pd(II) adsorption have shown a adsorption capacity of 1 – 2 mmole-Pd/g. Biopolymer-based adsorbents such as chitosan flakes or beads have been examined for palladium adsorption (Ruiz *et al.*, 2000). It was reported that chitosan adsorbed most palladium at pH 2 through electrostatic interaction (with a capacity of up to 1.7 mmole-Pd/g), while the actual amount sequestrated depended greatly on the presence of anions (chloride or sulphate), due to the change of the palladium speciation in the aqueous system. Guibal *et al.* (2002) also reported a palladium adsorption capacity of 3.6 mmole-Pd/g by using rubeanic acid derivative of chitosan containing additional sulfur ligands.

To allow for clear elucidation of adsorption/ion-exchange mechanism that may govern the removal of Pd(II), only the P4VP nanoparticles crosslinked with the non-polar, inert crosslinker, DVB, were used for study in this section, i.e. P4VP-A3 ([DVB] = 0.5 wt.%) (Table 3.1 of Chapter 3). Other types of P4VP nanoparticles were excluded due to possible interference from the acid-base interaction among the trimethylammonium groups, poly(ethylene glycol) spacer and dissolved Pd(II). Under the experimental conditions investigated in this study ([Pd] = 0.1 – 1.0 mM, [HCl] = 0.001 – 1 M), the palladium ions would mostly exist in the form of chloropalladate complexes, such as $PdCl_4^{2-}$, $PdCl_3^-$, $PdCl_2^0$ and $PdCl^+$ (Baes and Mesmer, 1978; Ruiz et *al.*, 2000). As pH decreases, or equivalently chloride concentration increases (since only HCl is used), the palladium speciation would shift in proportion towards more negatively-charged species ($PdCl_4^{2-}$, $PdCl_3^-$). When the P4VP-based nanoparticles become highly positively-charged, as indicated by the ζ-potentials measured (See Table 3.4 of Chapter 3), the protonated pyridyl groups on the nanoparticles can interact easily with the incoming palladium species which are negatively charged via anion-exchange mechanism.

To evaluate the efficacy of the P4VP nanoparticles as adsorbents for Pd(II) sequestration, the Pd(II) adsorption isotherms of the pristine P4VP nanoparticles (A-2) were studied as a function of pH (Figure 4.1 (a) in page 129). Other P4VP-based nanoparticles (i.e. B-series and C-series) would display similar performance as that of A-2 since their chemical functionality and nitrogen contents were shown to be approximately similar in Chapter 3, and the hydrophilic co-monomers were only added in minor amounts. Figures 4.1 (a) and (b) show the results from the adsorption isotherm experiments. These curves resemble to that of the saturation-type pattern as

characterized by the Langmuir isotherm model, indicating that the vacant active sites for adsorption decreased as the residual metal ion concentration increased. The optimal pH for the highest sequestration capacity appeared to be pH 3 ([HCl] = 0.001 M), while the adsorption seemed less favored at lower pH values, where the saturated adsorption capacity were lower as the pH values decreased. Chloride anions may compete strongly with the chloropalladate species for the positively-charged pyridinium groups on the nanoparticles (Ruiz *et al.*, 2000; Ruiz *et al.*, 2002). At a higher [HCl], more chlorides would be bound to the pyridinium group and fewer binding sites are available for chloropalladate adsorption, resulting in lower adsorption capacity at the adsorption equilibrium.

Various mathematical expressions have been developed to describe adsorption isotherms (Tien, 1994). The Langmuir isotherm model has been shown to be successful in describing adsorption equilibrium data of various types of adsorbent. The Langmuir isotherm assumes a surface with homogeneous binding sites, equivalent sorption energies, and no interaction between sorbed species. In a mathematical form, the model has often been given as below:

$$q_{eqm} = q_{\max} \frac{b \cdot c_{eqm}}{1 + b \cdot c_{eqm}} \tag{4.2}$$

where q_{eqm}, q_{max}, b and c_{eqm} are the adsorption uptake for the solute at adsorption equilibrium, the maximum adsorption capacity, the affinity constant and the solute concentration at adsorption equilibrium, respectively. The adsorption data in Figure 4.1 (a) could be well fitted by the Langmuir isotherm model, with satisfactory goodness-of-fit such that the adjusted correlation coefficients (Adj. R^2) are in the range of 0.96 – 0.99 (see Table 4.1).

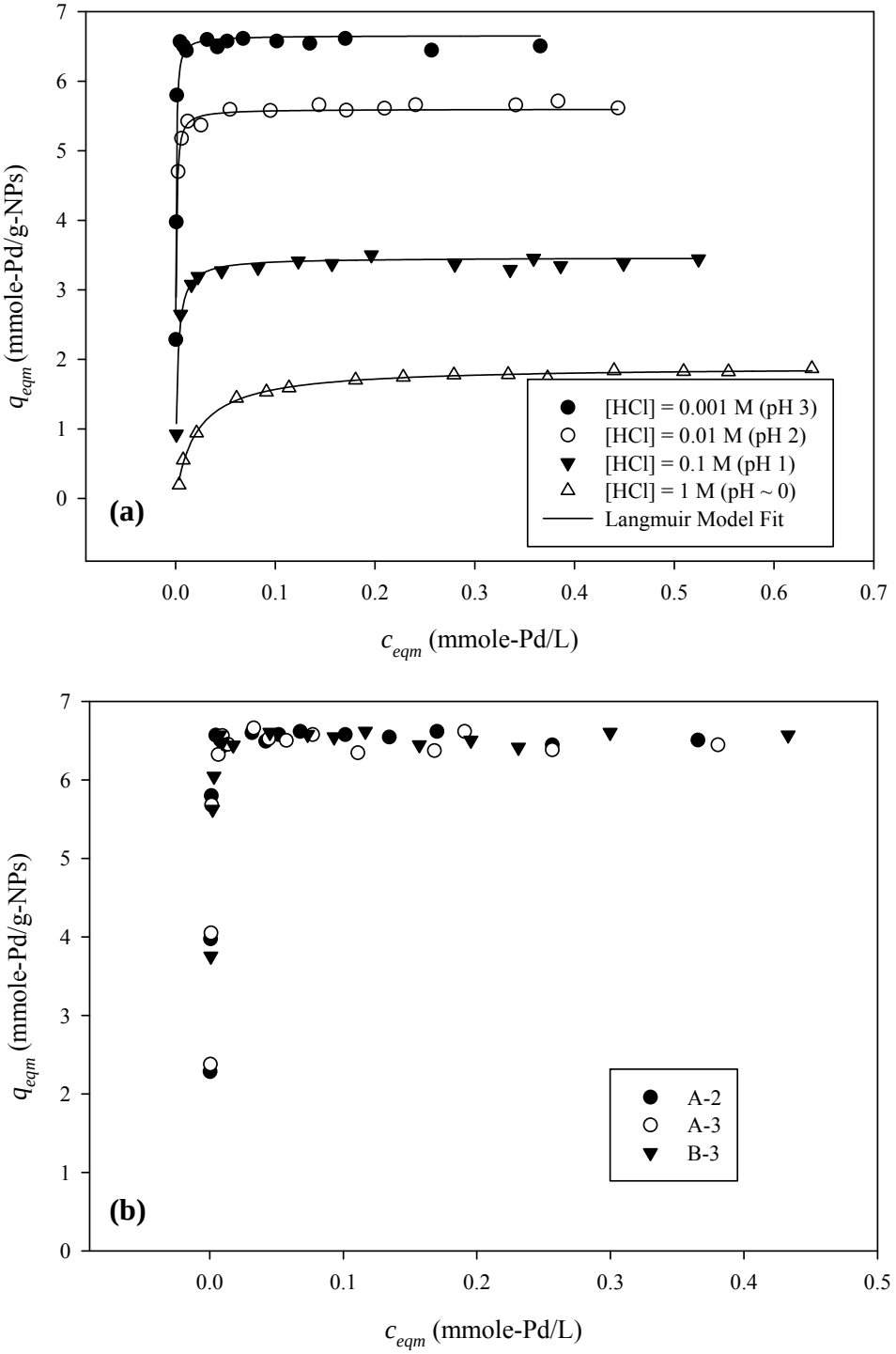

Figure 4.1 Adsorption isotherm plots for (a) effect of pH (pristine P4VP nanoparticles, A-2), and (b) effect of particle size ([HCl] = 0.001 M, pH 3). The actual D_{DLS} of the swollen P4VP-based nanoparticles measured prior to adsorption are as follow: A-2: 698.4 ± 18.8 nm; A-3: 982.2 ± 46.2 nm; B-3: 260.8 ± 10.2 nm.

The chemical moieties or binding sites responsible for metal ion capture of most nanoscale adsorbents reported in the literature, for instance, the magnetite nanoparticles (Uheida *et al.*, 2006a; Uheida *et al.*, 2006b), are located on the external surface. The P4VP nanoparticles resemble the PAMAM dendrimers in which the binding sites are distributed throughout the entire macromolecular entity. To verify this proposition, another set of adsorption experiments was carried out to determine if there is additional enhancement in palladium binding capacity when smaller P4VP nanoparticles were used in the adsorption isotherm experiments. As shown in Figure 4.1 (b), the use of smaller nanoparticles did not appear to improve the adsorption uptake amounts despite the higher specific surface area. This is because the access hindrance to interior binding sites was largely reduced for the P4VP nanoparticles of all sizes when they were fully swollen. In addition, the adsorption isotherm curve measured for the P4VP-PEGMA nanoparticles (B-3) was almost similar to others, which supports the proposition made. Similar phenomenon was also reported by Ruiz *et al.* (2002).

Table 4.1 Fitted parameters of the Langmuir isotherm model for Figure 4.1 (a).

Conditions	Model parameters fitted*				Goodness-of-fit[$]	
	q_{eqm}	SE**	b	SE	Adj. R^2	RMSE
	(mmole/g)		(liter/mmole)			
pH 3 ([HCl] = 0.001 M)	6.655	0.0744	3062	318.0	0.9608	0.2451
pH 2 ([HCl] = 0.01 M)	5.599	0.0434	2103	166.5	0.9639	0.1437
pH 1 ([HCl] = 0.1 M)	3.426	0.0237	533.3	41.89	0.9855	0.07761
pH ~ 0 ([HCl] = 1 M)	1.896	0.0146	47.75	2.508	0.9955	0.03431

* The model parameters are calculated using nonlinear least-squares fitting.
** SE: standard errors.
[$] Adj. R^2: adjusted correlation coefficients; RMSE: root-mean square of standard errors.

Palladium adsorption capacity. It is clear from Table 4.1 that the P4VP-based nanoparticles synthesized in this work can have an adsorption capacity up to 6.655 mmole/g, that outperformed not only most of the reported nanomaterials but also other developed adsorbents reported in the literature, in terms of capacity and affinity; as

summarized in Table 4.2 (page 132). Unlike other nanomaterials as listed in Table 4.2 whose palladium uptake capacities are mostly lower than that of commercially available chelating resins and other polymeric resins recently reported (Chen *et al.*, 1998; Hubicki *et al.*, 2006; Hubicki *et al.*, 2008), the adsorption isotherms of the P4VP nanoparticles displayed a favorable adsorption curve with high capacities (see Figures 4.1 (a) and (b)). Baba and Hirakawa (1992) reported an adsorption capacity of 6 mmole-Pd/g for a chitosan polymer grafted with pyridyl groups but the residual palladium concentration was excessively high at 30 mM. The residual palladium concentration measured for the P4VP nanoparticles to achieve maximum adsorption capacity was however only at 0.1 to 0.2 mmole-Pd/L, for all the pH values investigated, which is remarkably lower than that reported by other researchers who worked on the similar polymer (Baba and Hirakawa, 1993; Talanova *et al.*, 2001). The low residual palladium concentration required to achieve maximum adsorption capacity can be characterized by the binding affinity (*b*) of the P4VP nanoparticles prepared as shown in Table 4.1. For instance, the values of binding affinity of the nanoparticles for Pd(II) adsorption at pH 3 and 2 (3062 and 2103 liter/mmole) are higher than that of other adsorbents reported ((Table 4.2). High binding affinity towards palladium has also been observed for PEI-grafted and crosslinked chitosan beads (Ruiz *et al.*, 2002), which sequestrated Pd(II) mainly through the imine groups (secondary amine) and quaternized imine groups (tertiary amine).

Table 4.2 Adsorption capacity for palladium with various adsorbents reported in literature.

Adsorbents*	Pd(II) adsorption performance**	Reference
Nanomaterials:		
Pristine Fe_3O_4 nanoparticles (D_{pte} ~ 10 nm)	q_{eqm} = 0.103 mmole-Pd/g-adsorbents at c_{eqm} = 0.55 mmole-Pd/liter.	Uheida *et al.*, 2006a
Thiol-modified (-SH) Fe_3O_4 nanoparticles (D_{pte} ~ 10 nm)	q_{eqm} = 0.295 mmole-Pd/g-adsorbents at c_{eqm} = 0.927 mmole-Pd/liter.	Rossi *et al.*, 2007
Nonylthiourea-coated (CH_3-$(CH_2)_7$-CH_2-NH-CS-NH_2) Fe_3O_4 nanoparticles (D_{pte} ~ 10 nm)	q_{max}***= 0.076 mmole-Pd/g-adsorbents, b = 414 liter/mmole.	Uheida *et al.*, 2006b
Diethylenetriamine-functionalized silica-coated Fe_3O_4 nanoparticles (D_{pte} ~ 63 nm)	Extraction efficiency = 80 – 100 % of Pd during first cycle, from waste solution of 7.5 mg-Pd/liter.	Vatta *et al.*, 2007
Hydrogenotitanates (HNTs-1) nanotubes ($D_{o,NT}$ ~ 20 nm)	q_{eqm} = 1.13 mmole-Pd/g-adsorbents at c_{eqm} ~ 0.8 mmole-Pd/liter.	Kochkar et al., 2009
Thiol-functionalized mesoporous silica (Thiol-SBA-15) (D_{pore} = 7.3 nm)	q_{eqm} = 1.6 mmole-Pd/g-adsorbents at c_{eqm} ~ 2.2 mmole-Pd/liter.	Kang *et al.*, 2004
Chelating and ion-exchange resins:		
Poly(acrylonitrile) beads crosslinked by divinylbenzene, and modified by thiosemicarbazide (H_2N-CS-$NHNH_2$)	C_T = 4.05 mmole-Pd/g-adsorbents.	Chen *et al.*, 1998
Duolite GT-73 resins with thiol groups	q_{eqm} = 0.262 mmole-Pd/g-adsorbents at c_{eqm} ~ 1.8 mmole-Pd/liter.	Iglesias *et al.*, 1999
XE-305 resins functionalized with triisobutylphosphine sulphide (spacer: -$S(CH_2)_2(OCH_2CH_2)_2$-)	C_T = 0.7 mmole-Pd/g-adsorbents.	Sánchez *et al.*, 2000
Amberlite IRC-718 resins with iminodiacetate groups, and Duolite ES-346 resins with amidoxime groups	q_{eqm} (Amberlite IRC-718) = 1.10 mmole-Pd/g-adsorbents. q_{eqm} (Duolite E-346) = 1.90 mmole-Pd/g-adsorbents.	Hubicki *et al.*, 2006
Poly(*p*-vinylbenzoyl chloride-*co*-divinylbenzene) functionalized with imidazole groups	q_{max}***= 1.7 mmole-Pd/g-adsorbents, b = 169 liter/mmole.	Parodi *et al.*, 2008
Poly(styrene-co-divinylbenzen)-based strongly basic anion exchangers – Varion ATM (Type 1) resins (trimethyl ammonium groups) and Varion ADM (Type 2) resins (dimethyl ethanol ammonium groups), and polyacrylate-based weakly basic anion exchanger – Varion ADAM resins (dimethylamino groups)	C_T (Varion ATM) = 1.45 mmole-Pd/g-adsorbents. C_T (Varion ADM) = 1.39 mmole-Pd/g-adsorbents. C_T (Varion ADAM) = 2.15 mmole-Pd/g-adsorbents.	Hubicki *et al.*, 2008
Biopolymer-based adsorbents:		
Chitosan (95% deacetylated), modified with 2-pyridinecarboxaldehyde and crosslinked by chloromethyl(oxirane)	q_{eqm} = 5.80 mmole-Pd/g-adsorbents at c_{eqm} ~ 30 mmole-Pd/liter.	Baba and Hirakawa, 1992
Chitosan flake (87% deacetylated), crosslinked by glutaraldehyde	q_{max}***= 181.3 mg-Pd/g-adsorbents (1.70 mmole/g), b = 5.59 liter/mg (594.9 liter/mmole).	Ruiz *et al.*, 2000
Chitosan flake (87% deacetylated), crosslinked by glutaraldehyde, further derivatized with Rubeanic acid	q_{max}***= 389.4 mg-Pd/g-adsorbents (3.66 mmole/g), b = 1.74 liter/mg (185.2 liter/mmole).	Guibal *et al.*, 2002
Chitosan beads (87% deacetylated) crosslinked by glutaraldehyde, further grafted with poly(ethylene imine) (PEI) ((-CH=CH-NH-)$_n$) (PEI-GA), or grafted with thiourea ($(NH_2)_2CS$) (3:2:1 BH)	q_{eqm} (PEI-GA) = 3.96 mmole-Pd/g-adsorbents at c_{eqm} ~ 0.05 mmole-Pd/liter. q_{eqm} (3:2:1 BH) = 3.10 mmole-Pd/g-adsorbents at c_{eqm} ~ 0.1 mmole-	Ruiz *et al.*, 2002

	Pd/liter.	
Wood powder-derived crosslinked lignin adsorption gels, crosslinked by phenol and modified with primary amine (PA) and ethylenediamine (EN)	q_{eqm} = 0.38 mmole-Pd/g-adsorbents at c_{eqm} ~ 1.5 mmole-Pd/liter (PA-lignin). q_{eqm} = 0.213 mmole-Pd/g-adsorbents at c_{eqm} ~ 1.5 mmole-Pd/liter (EN-lignin).	Parajuli *et al.*, 2006
L-Lysine modified crosslinked chitosan resins (LMCCR)	q_{max}***= 109.5 mg-Pd/g-adsorbents (1.03 mmole/g), b = 1.58 liter/mg (168.1 liter/mmole).	Fujiwara *et al.*, 2007
Porous chitosan microspheres (100% deacetylated), crosslinked by chloromethyl(oxirane), and modified with 1,2-ethylenedisulfide (EDSC) (D_{pte} ~ 143 μm)	q_{eqm} = 2.33 mmole-Pd/g-adsorbents at c_{eqm} ~ 3.5 mmole-Pd/liter.	Kanai *et al.*, 2008
Biopolymers (gelatin and sodium alginate) capsules immobilized with ionic liquid (Cyphos® IL 101, tetradecyl(trihexyl)phosphonium chloride)	q_{max}***= 181.1 mg-Pd/g-adsorbents (1.70 mmole/g), b = 0.096 liter/mg (10.2 liter/mmole).	Vincent *et al.*, 2008
Adsorptive membrane:		
Bayberry tannin immobilized collagen fiber (BTICF) membrane	q_{eqm} = 0.74 mmole-Pd/g-adsorbents at c_{eqm} = 0.49 mmole-Pd/liter.	Wang *et al.*, 2005
Bayberry tannin immobilized collagen fiber (BTICF) membrane	q_{eqm} = 0.27 mmole-Pd/g-adsorbents at c_{eqm} = 0.33 mmole-Pd/liter.	Ma *et al.*, 2006
Polyethylene hollow fiber membrane, modified with nucleic acid bases (adenine)	C_T = 0.26 mmole-Pd/g-adsorbents (obtained from permeation mode).	Yoshikawa *et al.*, 2008
Vinylpyridine-based resins or adsorbents:		
Poly(4-vinylpyridine) modified with dithizone	q_{eqm} = 0.98 mmole-Pd/g-adsorbents at c_{eqm} = 0.055 mmole-Pd/liter.	Shah and Devi, 1997
Pyridine-carboxylic amphoteric exchanger (VP-14K)	q_{eqm} ~ 1.4 mmole-Pd/g-adsorbents at c_{eqm} ~ 50 mmole-Pd/liter.	Kononova *et al.*, 1998
Poly(4-vinylpyridine) copolymer (crosslinker:monomer=2:1)	q_{eqm} = 1.92 mmole-Pd/g-adsorbents at c_{eqm} = 10 mmole-Pd/liter.	Talanova *et al.*, 2001
Poly(4-vinylpyridine) powder (Aldrich, 2 wt.% crosslinked) (D_{pte} ~ 250 μm)	q_{eqm} = 3.61 mmole-Pd/g-adsorbents at c_{eqm} = 1.62 mmole/liter.	Chen *et al.*, 2007
Poly(4-vinylpyridine) resins crosslinked by divinylbenzene ([DVB] = 4, 8, 12 wt.%)	q_{eqm} = 4.28 mmole-Pd/g-adsorbents at c_{eqm} ~ 27 mmole/liter ([DVB] = 8 wt.%); q_{eqm} = 4.35 mmole-Pd/g-adsorbents at c_{eqm} ~ 8 mmole/liter ([DVB] = 4 wt.%)	Kumaresan *et al.*, 2008

* D_{pte}, $D_{o,NT}$ and D_{pore} denote average particle diameter, outer diameter of nanotube and pore diameter, respectively.

** All values (q_{eqm}, q_{max} etc.) are obtained from adsorption isotherm studies conducted at room temperature (25 or 30 °C). Representative values of (q_{eqm}, c_{eqm}) pair experimentally measured is shown when only partial isotherm is available, whereas q_{max} and b are shown when isotherm modeling is available in the relevant literature. Only total adsorption capacity (C_T) is given when adsorption isotherm data is absent.

*** The values (q_{max}, b) were fitted using Langmuir adsorption isotherm.

4.3.2 Adsorption Mechanisms: Coordinative Binding and Anion-Exchange

The separation and adsorption performance of weak anion-exchangers or nitrogen-based electron-donor ligands such as primary, secondary or tertiary amines and pyridines can be complicated and difficult to interpret (Zagorodni, 2007). Pyridine-based ion-exchange resins are known to be capable of coordinative binding of metal ions in acidic solutions, and they have been used for chromatographically separating actinides (An) from lanthanides (Ln) from radioactive wastes originating from the reprocessing of spent nuclear fuels (Ikeda *et al.*, 2004a; Ikeda *et al.*, 2007). Unlike other anion-exchangers with tertiary amine groups or quaternary ammonium groups, the binding sites of the pyridine-based adsorbents have low pKa, which implies that there is still a considerable amount of unprotonated pyridyl groups available for coordinative binding of cations at low pH. Despite the presence of concentrated acid and high counter-ion concentration, the adsorption mechanism of trivalent actinides on the pyridine-based adsorbents in alcoholic-hydrochloric acid has been proposed to be largely coordinative ('inner-sphere' complexation) in nature, despite competition from protonation of pyridyl groups (Ikeda *et al.*, 2004a; Ikeda *et al.*, 2007).

In hydrochloric acid media ([Pd(II)] = 0.1 – 1.0 mM, [HCl] = 0.001 – 1 M), the palladium ions mostly exists in the form of chloropalladate complexes, such as $PdCl_4^{2-}$, $PdCl_3^-$, $PdCl_2^0$ and $PdCl^+$, which can be expressed in a general form of $PdCl_n(H_2O)_{4-n}^{2-n}$ after taking into account of hydration (Baes and Mesmer, 1978; Ruiz et *al.*, 2000). Depending on the degree of protonation of the pyridyl groups as well as the actual Pd(II) speciation distribution, Pd(II) can be adsorbed onto positively charged pyridine moiety in acidic or slightly acidic aqueous system, by means of electrostatic attraction;

or bound to the P4VP nanoparticles via chelation/complexation through the lone electron pairs in the pyridine groups that are soft-donor type ligands.

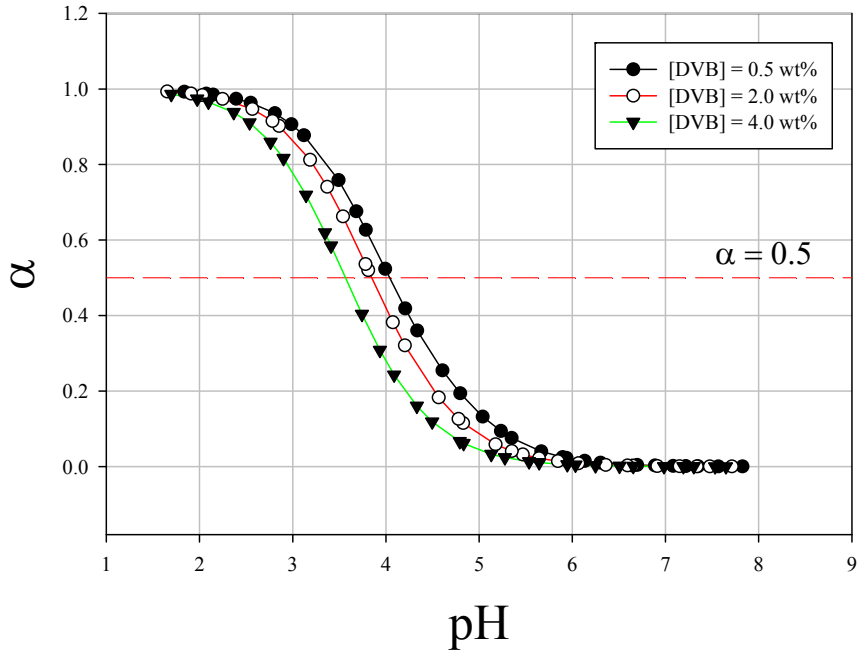

Figure 4.2 Plot of potentiometric titration of P4VP-A3 as a function of crosslinker concentration.

Figure 4.2 illustrates that the pyridine moiety of P4VP is always protonated (especially below pH 4) to different extents, depending on the pH of the system as well as the crosslinker concentration (Dupin *et al.*, 2006). As shown earlier, the lower the pH the lower the amount of Pd(II) adsorbed by P4VP. Chloride ions in the solution would bind to the metal cations, hence forming metal complexes. These counterions were in excess and free in solution and could compete for protonated pyridine groups, and hence upset the coordination or ion-exchange process between palladium ions or associated complexes and pyridyl groups of P4VP. Clearly, the protonation behaviors of pyridyl groups, as well as the speciation of Pd(II) in the presence of chloride (from either precursor salts or counterions introduced by HCl used in pH adjustment) contributed to the decreased adsorption capacity observed. To understand the

palladium binding mechanisms involved during the adsorption process, spectroscopic tools were used to probe the changes in the chemical oxidation states.

FT-IR spectroscopy. FT-IR was used to investigate whether the Pd(II) sequestration by the P4VP nanoparticles was by chemisorption (direct coordination or ion-exchange) or physisorption (van der Waals interaction etc.) or both. Figure 4.3 shows the FT-IR spectra of the P4VP nanoparticles and those adsorbed with different amounts of Pd(II) species at solution pH values of 1 and 3, respectively. For the P4VP nanoparticles with no Pd(II) adsorbed, the frequency band at 1600 cm^{-1} which is characteristic of the ring-stretching modes for the phenyl-like pyridyl rings is known to shift to higher frequencies upon hydrogen bonding or protonation (Harnish *et al.,* 2005). The appearance of a band at 1636 cm^{-1}, as shown in in spectra (i) of Figure 4.3 (a) and (b), accompanied by the shifting of the C–N vibrational peak at 1600 cm^{-1} to 1603 cm^{-1} after Pd(II) adsorption, confirms the existence of pyridinium group and hydrogen-bonded pyridyl groups on the P4VP nanoparticles, respectively. The shift of the absorption band was relatively small (3 – 6 cm^{-1}), indicating possibly due to hydrogen bond formation because the protonation of the pyridyl groups would normally bring a shift of 35 to 40 cm^{-1} (Ikkala *et al.*, 1995).

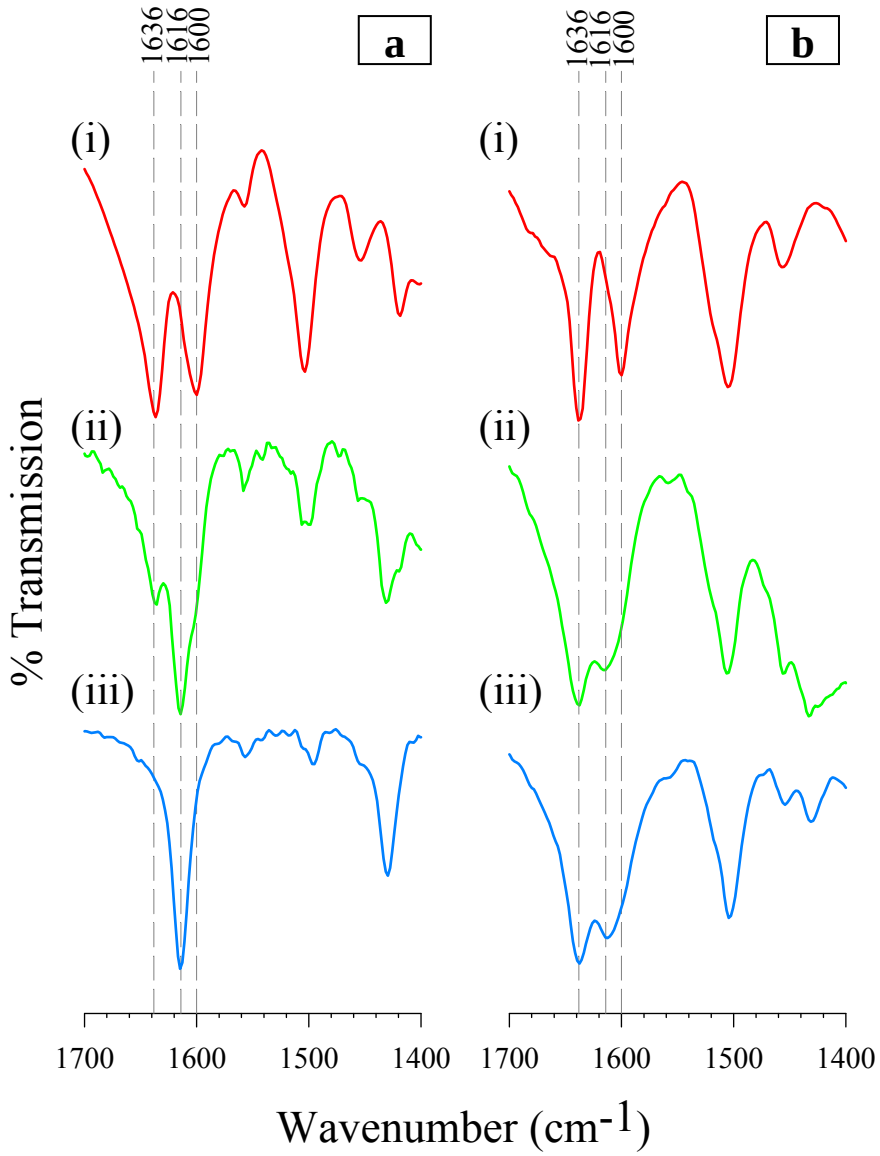

Figure 4.3 FT-IR spectra of P4VP-Pd with various adsorbed amounts of Pd (II) at pH = 3 (a) and pH 1 (b). The pristine samples without adsorbed Pd are shown in (i) of each pH. The Pd loading for samples in (a) are (ii) 2.57 mmole-Pd/g-P4VP, and (iii) 6.15 mmole-Pd/g-P4VP, whereas that of (b) are (ii) 1.57 mmole-Pd/g-P4VP, and (iii) 3.36 mmole-Pd/g-P4VP.

The spectra (ii) and (iii) of Figure 4.3 (a) and (b) clearly demonstrate that the P4VP nanoparticles, after Pd(II) adsorption, shows a 16 cm^{-1} shift from 1600 cm^{-1} to 1616 cm^{-1}. Pyridine molecules could act as Lewis base ("LPY") which the neutral pyridyl group could donate its electron lone-pair, or alternatively, as Brønsted base ("BPY") in their protonated form (Parry, 1963; Lefrancois and Malbois, 1971). The infra-red vibrational spectra of these two binding modes can be clearly differentiable in the

region of 1400 – 1700 cm^{-1} (Parry, 1963), which is largely associated with the in-plane vibration of the pyridine ring. Studies of infrared spectra of pyridine coordinated with metal ions (Kopylova *et al.*, 1973), or hydrogen-bonded to alkylphenol (Ruokolainen *et al.*, 1996), or ionically complexed with poly(styrenesulfonic acid) (Zhou *et al.*, 1998), showed that the most affected bands of P4VP are those concerned with the stretching modes of the pyridine ring: 1598 and 993 cm^{-1}. Upon formation of hydrogen bonding or metal-ligand coordination bonding, these bands shift to higher frequencies, as a consequence of change of electronic distributions in the pyridine ring, due to the formation of stronger bond. Kopylova *et al.* (1973) reported a band shift of 10 – 20 cm^{-1} toward shortwave region, by the valency vibration of the unprotonated pyridyl group at 1600 cm^{-1}. Burshtain *et al.* (2004) observed a shift of 17 cm^{-1} for Cd^{2+}-pyridine complexation, whereas Ruokolainen *et al.* (1995) reported an 18 cm^{-1} shift for Zn^{2+}-pyridine complexation system. Therefore, the 16 cm^{-1} shift observed herein is attributed to the coordinative binding of Pd(II) with the unprotonated pyridyl groups.

In Figure 4.3 (a), the symmetric peak (1616 cm^{-1}) in spectrum (iii) contrasts sharply with that of spectrum (ii) and (i), suggesting that the high Pd(II) loading in P4VP-Pd of spectrum (iii) caused the disappearance of pyridinium groups. In other words, there is a competitive binding for pyridyl group between proton and Pd(II). At pH 3, as P4VP adsorbs higher amount of Pd(II), the extent of competitive proton-binding, i.e. protonation, diminished, indicated by diminution of 1636 and 1505 cm^{-1} bands from (iii) to (ii) of Figure 4.3 (a), which was also observed by Harnish *et al.* (2005).

There is however a hint in the infra-red spectrum in Figure 4.3 (a) that the binding of chloropalladates by P4VP had displaced a fraction of the protons bound (at pH 3) from the pyridinium groups as the band intensity around 1636 cm^{-1} was reduced; the proton displacement reaction eventually ceased when the Pd adsorption took place at a higher proton concentration environment (for e.g., pH 1 in Figure 4.3 (b)). This was indicated by the 1616 cm^{-1} peaks in spectra (ii) and (iii) of Figure 4.3 (b) because these peaks appeared not as intense as those of pH 3 in spectra (ii) and (iii) of Figure 4.3 (a), implying that the Pd(II)-pyridyl group interaction at low pH was more inclined towards anion-exchange. Both unbound and chemisorbed pyridinium salts have been previously shown to have similar strong vibration band in the region of 1636 – 1640 cm^{-1}, unlike that of neutral pyridine molecules (Basila *et al.*, 1964; Glazunov and Odinokov, 1982; Riseman *et al.*, 1982). For instance, no noticeable difference in vibration band assignment (1400 – 1700 cm^{-1}) was observed when the chloride in the pyridinium salts was replaced with bulkier anions, for instance, $SbCl_6^-$ (Glazunov and Odinokov, 1982). There was almost no change in the peak intensities or positions from spectrum (ii) to spectrum (iii) of Figure 4.3 (b) even though the Pd(II) loading was doubled.

XPS spectroscopy. Similar chemical shifts were observed via x-ray photoelectron spectroscopy as well (see Table 4.3). The resultant N 1*s* core-level spectra are shown in Figure 4.4, wherein each spectrum was curve-fitted to three components, i.e. neutral pyridyl group (–N=), hydrogen-bonded pyridyl group (=N---H) and pyridinium group ($=N–H^+$) with binding energies of ca. 398.5, 400.0 and 401.0 eV, respectively.

Table 4.3 XPS determined binding energies (BE) for N 1*s* of P4VP-Pd (P4VP-A3).

Sample	Functional Group	BE (eV)	%*
(a) pH 3 ([HCl] = 0.001 M)			
(i) no Pd(II)	=N–	398.6	71.4
	=N---H	399.8	12.2
	$=N–H^+$	401.0	16.4
(ii) q_{eqm} = 2.57 mmole-Pd/g-P4VP	=N–	398.4	32.8
	$=N---Pd^{2+}$	399.6	62.3
	$=N–H^+$	401.3	4.9
(iii) q_{eqm} = 6.15 mmole-Pd/g-P4VP	=N–	398.5	3.6
	$=N---Pd^{2+}$	399.6	90.2
	$=N–H^+$	401.2	6.2
(b) pH 2 ([HCl] = 0.01 M)			
(i) no Pd(II)	=N–	398.6	40.0
	=N---H	400.1	13.4
	$=N–H^+$	401.0	46.6
(ii) q_{eqm} = 3.10 mmole-Pd/g-P4VP	=N–	398.4	28.6
	$=N---Pd^{2+}$	399.6	34.8
	$=N–H^+$	401.0	36.6
(iii) q_{eqm} = 5.23 mmole-Pd/g-P4VP	=N–	398.4	17.1
	$=N---Pd^{2+}$	399.6	56.5
	$=N–H^+$	401.1	26.4
(c) pH 1 ([HCl] = 0.1 M)			
(i) no Pd(II)	=N–	398.5	4.4
	=N---H	400.1	9.8
	$=N–H^+$	401.1	85.8
(ii) q_{eqm} = 1.57 mmole-Pd/g-P4VP	=N–	398.4	4.1
	$=N---Pd^{2+}$	399.6	15.8
	$=N–H^+$	401.1	80.1
(iii) q_{eqm} = 3.36 mmole-Pd/g-P4VP	=N–	398.3	2.6
	$=N---Pd^{2+}$	399.6	23.9
	$=N–H^+$	401.3	73.5

* The proportions of each function group in respective spectrum is calculated by firstly curve-fitting the raw signals and later calculating the area under each peak.

The neutral pyridine nitrogen at 398.3 – 398.6 eV has been reported to undergo a positive chemical shift of 2.0 – 2.5 eV upon formation of pyridinium ions (Tan *et al.*, 1990; Houben *et al.*, 1996; Olah *et al.* 2004). In spectra (i) of Figure 4.4 (a), (b) and (c), 401.0 – 401.3 eV for protonated pyridyl group was observed, as well as hydrogen-bonded nitrogen at 399.8 – 400.1 eV, which could be originated from the intermolecular hydrogen bonding of butyramidine group of the radical initiator (V50) grafted and pyridyl group (Davies *et al.*, 1995). The content of hydrogen bonded pyridyl nitrogen, as well as that of pyridinium ions observed strengthened as pH

decreased, due to the increased proton or hydrogen ion concentration within the polymeric network of P4VP.

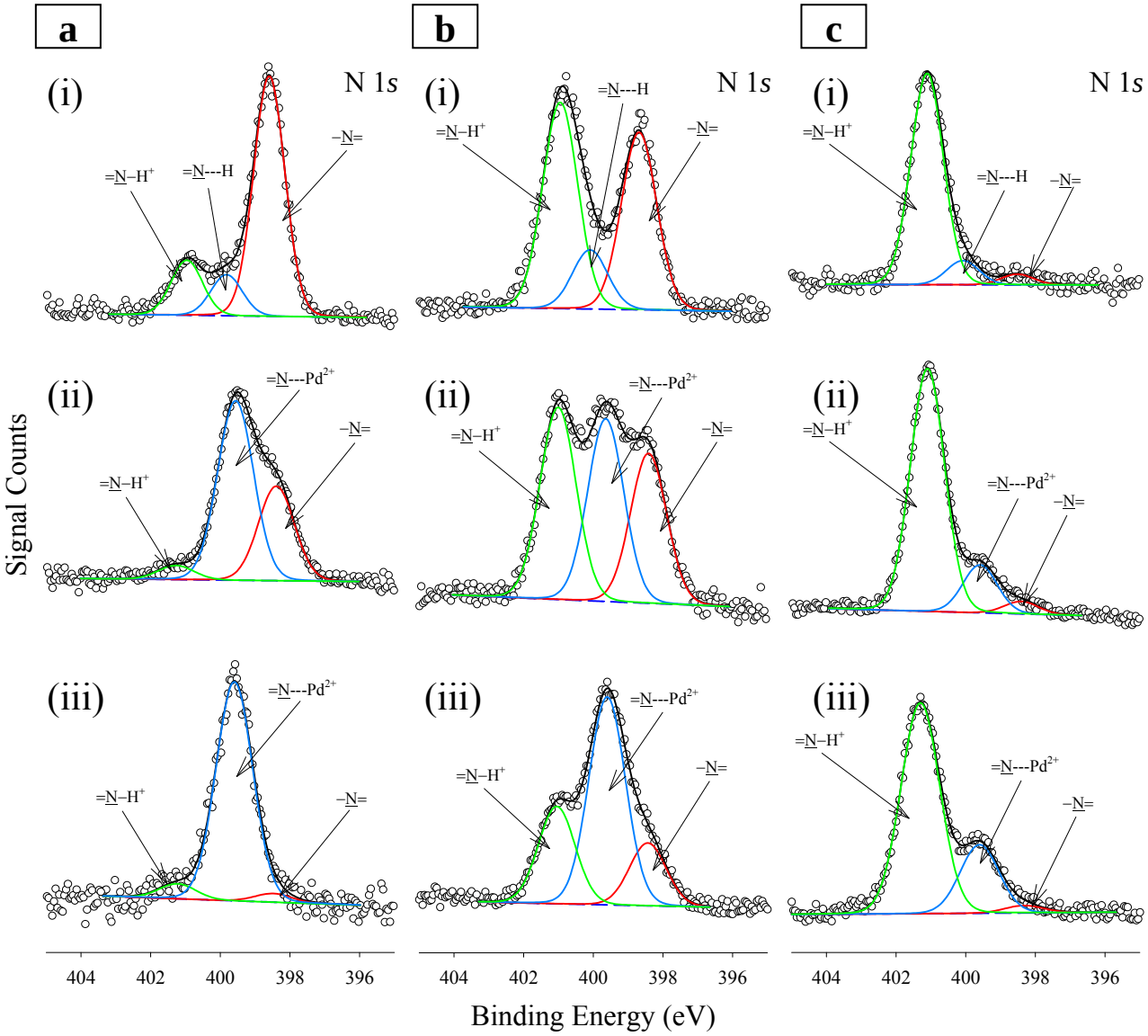

Figure 4.4 XPS N 1*s* spectra of P4VP-Pd at various pH, i.e. (a) pH 3, (b) pH 2 and (c) pH 1. The pristine samples without Pd(II) are shown in (i) for each pH. For (a), (ii) q_{eqm} = 2.57 mmole-Pd/g-P4VP (iii) and q_{eqm} = 6.15 mmole-Pd/g-P4VP. For (b), (ii) q_{eqm} = 3.10 mmole-Pd/g-P4VP (iii) and q_{eqm} = 5.23 mmole-Pd/g-P4VP. For (c), (ii) q_{eqm} = 1.57 mmole-Pd/g-P4VP (iii) and q_{eqm} = 3.36 mmole-Pd/g-P4VP.

The mineral acid, i.e. HCl, used in pH adjustment in this work has been reported to be able to volatize upon vacuuming prior to XPS analysis (Zhai *et al*, 2003). This experimental artifact would cause an underestimation of the protonation degree of the

pyridyl groups as probed by XPS spectroscopy, which possibly resulted in the discrepancy between the pH titration curves (Figure 4.2) and the XPS results herein, and the rather broad peak range for hydrogen-bonded nitrogen. Nonetheless, the XPS results are still useful for describing the protonation behavior of the pyridyl group of the P4VP nanoparticles qualitatively at least.

The values of N 1*s* BE of the pyridyl group shifted to higher frequencies after Pd(II) adsorption, as shown in Table 4.3, and spectra (ii), (iii) of Figure 4.3 (a), (b) and (c). Similar shift in N 1*s* BE was also observed by other researchers for complexation of metal ions with pyridine-moieties (Lyons *et al.*, 1988) or primary/secondary amine groups (Li and Bai, 2005). The N 1*s* peaks appeared to be broadened and each broadened peak could be deconvoluted into three components, i.e. residual neutral pyridyl group (–N=), Pd(II) bound pyridyl group (=N---Pd^{2+}) and pyridinium group (=N–H^{+}), wherein their binding energies depend on the actual microenvironment surrounding the nitrogen atoms of concern. The binding energies for both uncharged pyridyl group and pyridinium group remained uncharged, except for that of =N---Pd^{2+} which centered at 399.6 eV and was lower than the BE of the hydrogen-bonded (399.8 – 400.1 eV). It is assumed that at high loading of Pd(II), the second component peak is attributed to the Pd(II)-pyridyl group complexes solely, because the hydrogen bonding is remarkably weaker than the metal cation-pyridyl bonding (Goh *et al.*, 1998) and can be disrupted and replaced by the latter easily. This assumption could be indirectly inferred from the respective frequency shifts from the C–N vibrational peak in IR spectrum shown in Figure 4.3 (H-bonding: 3 cm^{-1}, metal cation-pyridyl group coordination bonding: 16 cm^{-1}). A positive chemical shift of 1.0 – 1.2 eV for metal cation-pyridyl bonding as observed here, is in agreement with the values reported in

literature (Yang *et al.*, 2001; Pardey *et al.*, 2005), indicating that partial charge transfer from the nitrogen lone pair to palladium has occurred, without any significant broadening of FWHM.

For Pd(II) adsorption at pH 3, both the height and area ratio of =N---Pd^{2+} peak increased when the P4VP sequestrated more Pd(II) (see spectra (ii) and (iii) of Figure 4.4 (a)). At pH 3, direct coordination to (Pd) by uncharged pyridyl groups would occur. A part of the pyridinium groups was deprotonated to release more uncharged pyridyl nitrogen-atoms when the [HCl] in the surrounding reservoir was relatively low. Consequently, the =N---Pd^{2+} peaks grew at the expense of =N–H^+ peaks (the pyridinium groups), as shown in Figure 4.4 (a). Similar trends are observed for Pd(II) adsorption at pH 2 and 1 (spectra (ii) and (iii) of Figure 4.4 (b) and (c)), except that it is weaker in the latter due to higher [HCl] available at lower pH. The chemical potential to expel the previously bound proton from the pyridinium groups was reduced significantly as there were more protons in the solution (Eq. (4.3)). The deprotonation reaction of pyridinium group was effectively depressed when the [HCl] was increased to 0.1 M, i.e. pH 1 (see Figure 4.4 (c)). This may explain why the adsorption capacity decreased as pH was decreased (Figure 4.1).

$$-C_5H_5N - H^+ \longleftrightarrow -C_5H_5N : +H^+ \qquad (4.3)$$

The Pd 3*d* spectra of the P4VP-Pd complexes, as shown in Figure 4.5, at all pH exhibited sharp signals characterized by BE of 337.7 – 337.9 eV. The Pd $3d_{5/2}$ peak for $PdCl_2$ (II) has been reported to be at 337.5 eV and 337.9 eV for K_2PdCl_4 (II), whereas Pd^0 line and PdO line are both centered at 335.1 and 336.9 eV, respectively (Gniewek *et al.*, 2005). The BE observed for the P4VP-Pd complexes are rather close

to the BE of 337.4 eV for chitosan-Pd adsorption complex reported by Kramareva *et al.* (2004). Therefore, the Pd(II) sequestrated by the P4VP nanoparticles were neither chemically reduced nor precipitated onto the P4VP nanoparticles, further supporting the conclusion that Pd(II) are chemisorbed to the swollen P4VP networks.

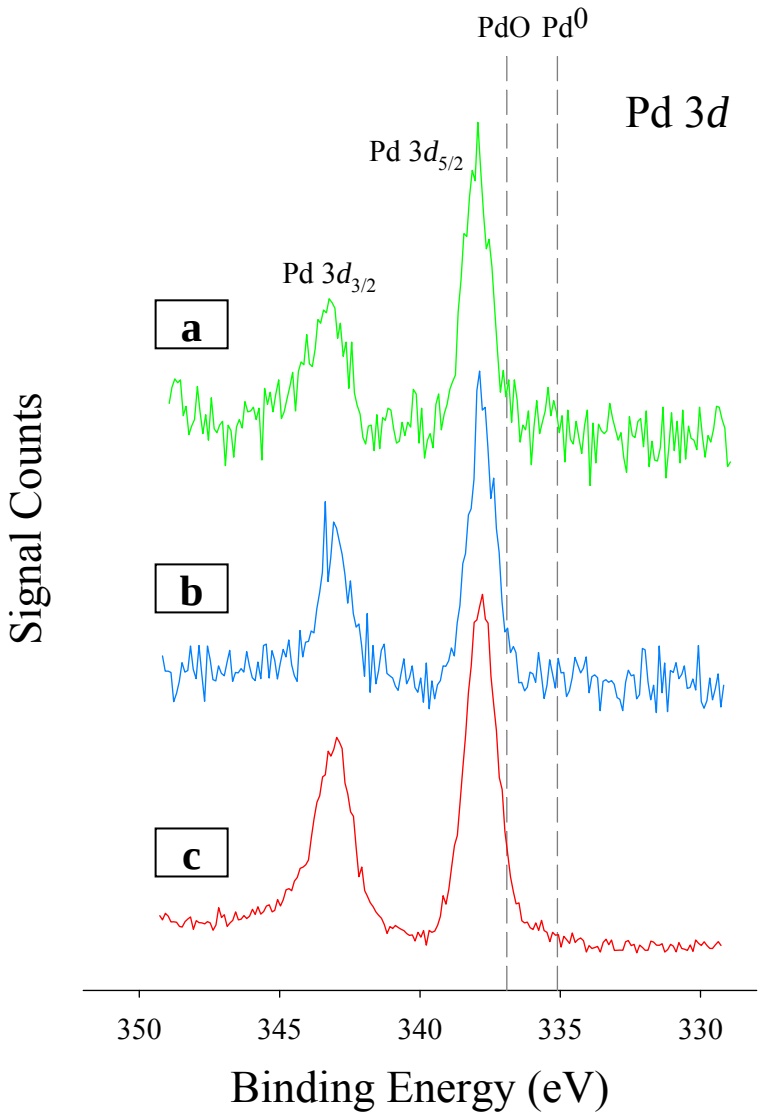

Figure 4.5 XPS Pd 3*d* spectra of P4VP-Pd at various pH. The Pd loading for these samples are (a) q_{eqm} = 1.57 mmole-Pd/g-P4VP at pH 1, (b) q_{eqm} = 3.10 mmole-Pd/g-P4VP at pH 2, and (c) q_{eqm} = 2.57 mmole-Pd/g-P4VP at pH 3.

Similar to FT-IR analysis, the XPS analysis is unable to discriminate between the Pd(II) bound and Cl^- bound pyridinium groups because both Pd(II) and Cl^- were electrostatically adsorbed to the positively-charged groups. Nonetheless, both FT-IR

and XPS results show that the interactions between the pyridyl groups and Pd(II) complexes were strong and the Pd(II) adsorption involved a combination of ionic and coordinative bindings (chemisorption). To accommodate both the coordinative binding and the anion-exchange mechanisms, a tentative schematic for these plausible reactions is listed as follow (Eq. (4.4) to (4.7)). For a d^8 metal cation, the square-planar coordination geometry for Pd^{2+} requires four ligands (Baes and Mesmer, 1978). In current system, the candidates that can act as ligand include water molecules, chloride ions and pyridyl groups which is a strong base and can displace one or two water molecules from $PdCl_n(H_2O)_{4-n}^{2-n}$ and occupy the vacant coordination site on the Pd^{2+} core.

Coordinative binding of chloropalladates:

Monodentate:

$$-C_5H_5N: + \left[PdCl_n\left(H_2O\right)_{4-n}\right]^{2-n} \longleftrightarrow \left\{\left(-C_5H_5N\rightarrow\right)\left[PdCl_n\left(H_2O\right)_{3-n}\right]\right\}^{2-n} + H_2O, \quad where \;\; n = 0-2 \qquad (4.4)$$

Bidentate:

$$2\left(-C_5H_5N:\right) + \left[PdCl_n\left(H_2O\right)_{4-n}\right]^{2-n} \longleftrightarrow \left\{\left(-C_5H_5N\rightarrow\right)_2\left[PdCl_n\left(H_2O\right)_{2-n}\right]\right\}^{2-n} + 2\,H_2O, \quad where \;\; n = 0-2 \qquad (4.5)$$

Anion-exchange of chloropalladates:

Monodentate:

$$-C_5H_5NH^+ + \left[PdCl_n\left(H_2O\right)_{4-n}\right]^{2-n} \longleftrightarrow \left\{\left(-C_5H_5NH\right)\left[PdCl_n\left(H_2O\right)_{4-n}\right]\right\}^{3-n}, \quad where \;\; n = 3, 4 \qquad (4.6)$$

Bidentate:

$$2\left(-C_5H_5NH^+\right) + \left[PdCl_n\left(H_2O\right)_{4-n}\right]^{2-n} \longleftrightarrow \left\{\left(-C_5H_5NH\right)_2\left[PdCl_n\left(H_2O\right)_{4-n}\right]\right\}^{4-n}, \quad where \;\; n = 3, 4 \qquad (4.7)$$

4.3.3 Pd(II) Adsorption Kinetics

An effective adsorbent should also have fast adsorption kinetic for the target metal ions. The kinetics of Pd(II) adsorption with the P4VP-based nanoparticles (crosslinked with 0.5 wt.% DVB) were studied as a function of particle size and the results are shown in Figure 4.6, wherein the particles have the following dimensions in their swollen state at pH 3, i.e. (pristine P4VP nanoparticles) A-2: 698.4, A-3: 982.2; (P4VP-PEGMA nanoparticles) B-3: 260.8 nm. As shown in Figure 4.6, it took only less than two minutes for the nanoparticles to attain adsorption equilibrium at an initial Pd concentration of 0.1 mM. More rapid removal was observed at higher initial concentrations and the adsorption reached equilibrium within the first 10 seconds. As expected, the smaller nanoparticles could sequestrate the Pd(II) more rapidly. Uheida *et al.* (2006b) reported that the nonylthiourea-coated nanoparticles achieved adsorption equilibrium for Pd(II) adsorption within less than 5 minutes. Much longer adsorption equilibrium time were reported for other adsorbents such as crosslinked chitosan beads (Ruiz *et al.*, 2000) and polymeric resins (Parodi *et al.*, 2008). For instance, Parodi *et al.* (2008) reported that more than 8 hours was required to achieve equilibrium when treating dilute palladium solution (C_0 ~ 0.2 mM) with the resins (100 mg). A long contact time of 6 – 8 hours was necessary for the PEI-grafted crosslinked chitosan beads (Ruiz *et al.*, 2002) to attain completion despite their high Pd(II) adsorption capacity. Conversely, the short diffusion path offered by most nanomaterials as well as the P4VP nanoparticles herein could shorten the treatment time drastically. Besides high surface/volume ratio, the P4VP nanoparticles were fully swollen at the pH concerned (see Figure 3.9 in Chapter 3), hence the accessibility to the interior binding sites (pyridyl group) was unhindered, because the polymeric

network imbibed lots of solvent or water so that the palladium ions or chloropalladates could travel freely by diffusion into the porous core networks of the nanoparticles.

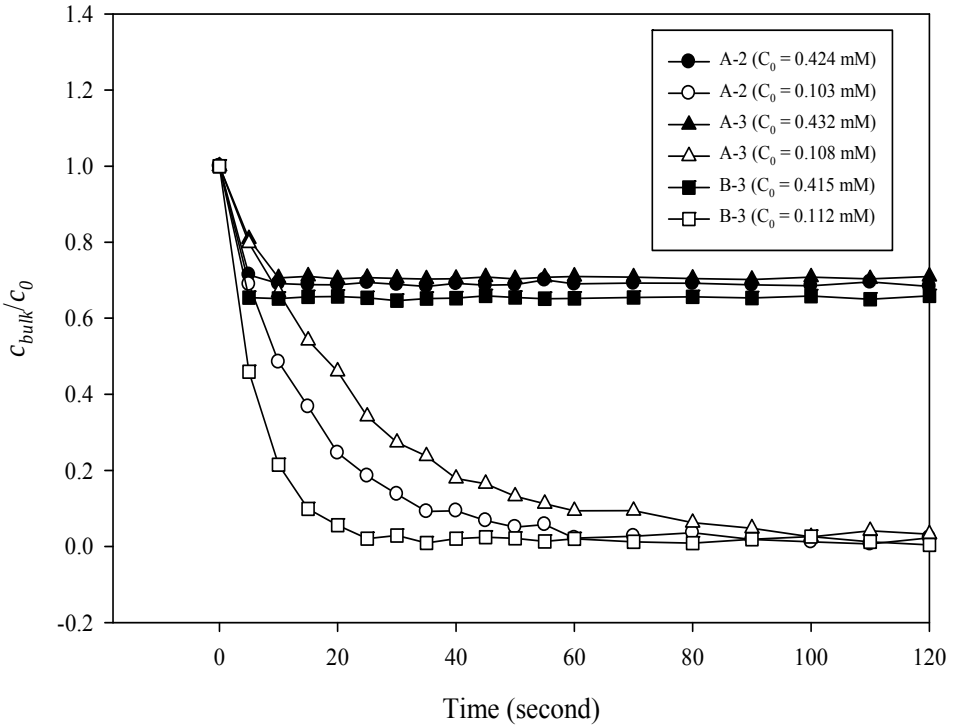

Figure 4.6 Kinetics of Pd(II) adsorption by P4VP nanoparticles, at pH 3 ([HCl] = 0.001 M). The actual D_{DLS} of the swollen P4VP-based nanoparticles measured prior to adsorption are as follow: A-2: 698.4 ± 18.8 nm; A-3: 982.2 ± 46.2 nm; B-3: 260.8 ± 10.2 nm.

4.3.4 Recovery of Pd(II)

Uncontrollable destabilization or mechanical breakdown of nanoparticles would render the repeated use of these nanoadsorbents difficult and expensive. To address this concern, the stability of the P4VP-based nanoparticles was investigated. The robustness of the nanoparticles was significantly enhanced by copolymerization with PEGMA by replacement of the hydrophobic crosslinker (DVB) with PEGDM (Chapter 3). In addition, the ease and extent at which the sequestrated Pd(II) could be desorbed or eluted from the exhausted or used P4VP nanoparticles would determine not only the technological feasibility but also the economic attractiveness of the prepared adsorbent. In some cases, the undesirably strong attraction between the

binding sites of an adsorbent and Pd(II) has been shown to decrease the recovery of the adsorbed Pd(II) (Iglesias *et al.*, 1999; Abiman *et al.*, 2008). The recovery of Pd(II) from the Pd(II) laden P4VP-PEGMA nanoparticles was examined by first screening a pool of selected desorption agents or eluents in this work (see Table 4.4). As most the palladium adsorption took place in an acidic environment, simple acid elution (HNO_3 and HNO_3) with molarity of 1.0 and 2.0 could not desorb the adsorbed Pd(II) quantitatively. Thiourea has been reported by many researchers for palladium elution (Shah and Devi, 1997; Fujiwara *et al.*, 2007; Vincent *et al.*, 2008; Kanai *et al.*, 2008). A much improved recovery of 97 % was obtained with an acidified solution containing 0.1 M thiourea, while a slightly-enhanced recovery at 99 – 100 % can be achieved at a thiourea concentration higher than 0.5 M. Though increasing eluent concentration could achieve much higher recovery, their marginal improvement may not justify the higher chemical cost incurred. In the following cyclic regeneration experiments, an acidifed solution containing 0.1 M thiourea was therefore used.

Table 4.4 Palladium desorption using various eluents.

Eluents	Desorption % (from pH = 3)
[HCl] = 1.0 M	37.4 ± 1.2
[HCl] = 2.0 M	47.5 ± 2.5
[HNO_3] = 1.0 M	19.8 ± 0.8
[HNO_3] = 2.0 M	28.9 ± 2.9
[HCl] = 0.001 M, [Thiourea] = 0.1 M	97.2 ± 3.3
[HCl] = 0.001 M, [Thiourea] = 0.5 M	100.2 ± 2.0
[HCl] = 0.001 M, [Thiourea] = 1.0 M	99.5 ± 2.6

The cyclic regeneration and reuse of P4VP-PEGMA nanoparticles was investigated via the filtration method described earlier. The results are shown in Figure 4.7 for five cycles of the adsorption-desorption process. The recovery efficiencies of an acidified thiourea solution at two concentrations (0.1 M and 1.0 M) were all above 95%, in agreement with that in Table 4.4. However, at a high thiourea concentration of 1.0 M,

the recovery efficiencies of the cycles from the second cycle onwards were generally lower than that of the first cycle. This may be caused by the trace amount of residual thiourea remaining in the concentrate (or retentate) after the desorption, which could compete with the nitrogen-atom binding site for Pd(II). The lower thiourea concentration at 0.1 M resulted in lower or negligible residual amount of competing ligands and therefore the recovery remained relatively constant throughout the five cycles investigated. No hysteresis or loss in adsorption capacity was observed and the total amounts of palladium from adsorption and consecutive desorption were in good agreement. It is therefore concluded that the acidified thiourea solution of 0.1 M is sufficient for quantitative Pd(II) recovery and regeneration of the prepared nanoparticles. Many adsorbents lack specific binding site for metal recovery and therefore are often chemically treated to boost their binding affinity. Nevertheless, an overly high affinity may complicate the desorption process and reduce the recovery of Pd(II) from the exhausted adsorbents. As a result, less binding sites are available for adsorption in the following cycle of adsorption-desorption process, due to the incomplete elution/desorption of Pd(II) sequestrated in previous cycles. Vatta et al. (2007) reported that the Pd(II) extraction and desorption efficiency of diethylenetriamine-modified magnetite nanoparticles could drop to below 50% after 4 cycles of adsorption-desorption process. The chemically-modified Fe_3O_4 nanoparticles (Uheida *et al.*, 2006b) has a modest Pd(II) recovery of 66 % with 0.5 M thiourea solution, which is remarkably lower than the 96 % for the pristine Fe_3O_4 nanoparticles (Uheida et al., 2006a).

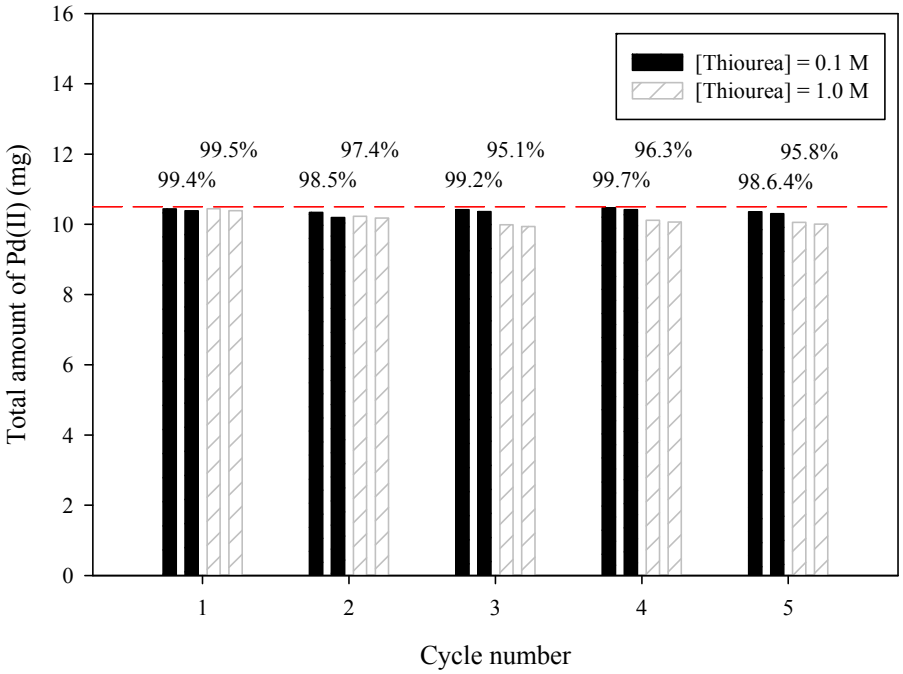

Figure 4.7 Recovery of Pd(II) from metal-laden P4VP-PEGMA crosslinked with 4 wt.% PEGDM (n = 9) with 0.1 M thiourea ([HCl] = 0.001 M) and 1 M thiourea ([HCl] = 0.001 M) as eluents. The percentages shown are the recovery efficiency for each cycle, whereas the horizontal dash line denotes the amount of Pd(II) added per cycle.

4.4 Conclusion

The P4VP nanoparticles prepared were demonstrated to be highly effective for palladium sequestration and recovery. The adsorption capacity for palladium obtained with the P4VP nanoparticles are approximately 1.9 to 6.6 mmole/g depending on solution pH values, wherein the highest adsorption capacity was obtained at pH 3, where the competitive binding between the chloride ions and chloropalladates were lesser. Both XPS and FT-IR confirmed that the pyridyl groups of the P4VP polymeric network are able to sequester the Pd(II) through chemisorption. As the acid concentration in the surrounding reservoir was increased, the amounts of Pd(II) adsorbed were decreased. The P4VP nanoparticles also displayed very high binding affinity towards Pd(II). The desorption and recovery of palladium adsorbed can be effectively achieved in an acidified thiourea solution ([HCl] = 0.001 M, [Thiourea] = 0.1 M). Short contact times (< 2 minutes) were observed for the palladium adsorption

to reach equilibrium. Satisfactory performance for the repeated cycles of adsorption-desorption-regeneration process was achieved with a microfiltration system. The P4VP nanoparticles remained adsorptive and reusable after five cycles in the tests. The successful Pd(II) adsorption and elution demonstrated in this work indicates that the P4VP-based nanoparticles are of great prospect for application in palladium removal and recovery from aqueous solutions.

CHAPTER 5

MODELING OF ADSORPTION KINETICS FOR PALLADIUM ADSORPTION WITH P4VP NANOPARTICLES

5.1 Introduction

The adsorption performance of the prepared P4VP-based nanoadsorbent for palladium has been examined in Chapter 4. More detailed studies on the modeling that can describe the relevant process rate and behaviors would be important for facilitating the use of the developed nanoadsorbents in actual environmental applications, such as for resource recovery and reuse of precious metals, e.g. palladium. It has been pointed out that measuring and predicting pollutant transport and uptake rates are critical to design and operation of both batch and fixed-bed adsorption processes, for environmental protection or resource recovery (Tien, 1994; Do, 1998). Model equations which have been thoroughly studied and validated can assist process engineers and technologists to design, evaluate and predict the performances of the treatment processes.

From a macroscopic viewpoint, accurate modeling with physically sound phenomenological models or thermodynamic partitioning models would also offer a greater insight on the complex interplay between various rate-controlling processes (e.g. pore diffusion, surface diffusion, or a combination of both, in addition to possible inclusion of film-/boundary-layer-diffusion) during Pd(II) adsorption, thereby allowing for a better understanding of the adsorbent performance. Diffusional transport rates of solutes are always lower than that of molecular (or self-) diffusion in free solution as a result of geometric obstruction and hydrodynamic hindrances arising from the intrinsic microstructure and topology of an adsorbent (Muhr and Blanshard, 1982; Amsden 1998). Further assessment on how the various parameters of adsorbent structure affect the diffusive transport rates would assist in preparing improved formulation for new adsorbent development to achieve more efficient separation performance.

In this chapter, the kinetics of Pd(II) adsorption with P4VP nanoparticles was examined in depth through modeling studies. As the swollen P4VP nanoparticles possess porous networks which are positively charged at low pH, modeling of the adsorption kinetic data was carried out to determine whether the adsorption process follows Fickian's laws of diffusion, which is built on the premise that the deswelling is more rapid than the Pd(II) diffusion process. The governing kinetic parameters (such as D_{eff} and k_f) that can accurately reflect the transport rates of Pd(II) within the swollen P4VP networks will be determined. The effect of external (film diffusion) mass transfer resistance on the adsorption process will also be assessed and discussed.

5.2 Materials and Methods

5.2.1 Materials

The nanoparticles used to obtain the experimental adsorption data were prepared with the same method as described in section 3.2.1 of Chapter 3. The specific recipes of these nanoparticles for preparing these nanoparticles are given in Table 5.1. The chemicals used in the adsorption kinetic experiments are the same as described in Chapter 4.

Table 5.1 Surfactant-free emulsion polymerization recipe[a] used in this chapter.

Code	Monomer	Co-monomer(s)				Feed Mode	Yield		Particle Size
	4-VP [g/100ml solution]	PEGMA [wt./wt.%-4-VP]	MATMAC [wt./wt.%-4-VP]	DVB [wt./wt.%-4-VP]	Initiator [wt./wt.%-4-VP]	Feed Rate [g/min]	Conversion [%]	Coagulum [wt./wt.%-4VP]	$D_{DLS,0}$[b] [nm]
For adsorption kinetic study									
P4VP-A2	1.5	-	-	4.0	2.5	*One-shot*	>99	0.2	245.6 ± 3.5
P4VP-A3	1.5	-	-	4.0	5.0	*One-shot*	>99	2.2	359.2 ± 7.4
P4VP-B3	1.5	10.0	-	4.0	2.5	0.05	~91	2.4	90.8 ± 3.3
P4VP-C1	3.0	10.0	5	4.0	2.5	*One-shot*	~94	2.2	648.2 ± 12.1
P4VP-C1-[DVB] = 2.0 wt.%	3.0	10.0	5	2.0	2.5	*One-shot*	~94	2.5	640.7 ± 15.3
P4VP-C1-[DVB] = 0.5 wt.%	3.0	10.0	5	0.5	2.5	*One-shot*	~96	1.2	646.4 ± 19.7

[a] This recipe was reported in our Chapter 3.
[b] $D_{DLS,0}$ refers to particle size measured from the nanoparticles which are fully deswollen, i.e. at pH 8-9, using DLS.

5.2.2 Characterization Methods

Effective hydrodynamic diameter (D_{DLS}) of the swollen nanoparticles at various pH were measured, based on the principle of dynamic light scattering (DLS), as described in section 3.2.4 of Chapter 3. The sample loading (wt.%) for each combination of nanoparticles and pH was first optimized by trial-and-error, to maximize the signal intensity while allowing sufficient light transmission before the actual measurement. Each sample was then prepared to the predetermined concentration and the solution pH was adjusted using either 0.1 M HCl or NaOH. The ionic strength was fixed at 0.1 M. The measured autocorrelation functions were converted into particle size distributions via Stokes-Einstein equation, based on single-exponential cumulant analysis. All the measurements were thermostated at 25 °C.

5.2.4 Adsorption Isotherms Measurement

The Pd adsorption isotherms of P4VP-C1 nanoparticles were examined to determine the actual maximum adsorption capacity (q_{max}) and adsorption affinity (b) of the P4VP nanoparticle prepared (The adsorption isotherms of pristine nanoparticles, i.e. A-series were examined in Chapter 4). The preparation of the palladium stock solution as well as the details for the adsorption istotherms experiment conducted as described in Chapter 4. The residual Pd(II) concentrations were measured, and the equilibrium adsorption capacity (q_{eqm} or q) was calculated as described in section 4.2.4 of Chapter 4 (Eq. (4.1)). The solution pH before and after batch adsorption, was measured using pH meter and found to be relative constant (ΔpH ~ 0.01 – 0.05). The obtained adsorption isotherms were then fitted to the Langmuir model (Eq. (4.2) in section 4.3.1 of Chapter 4) to extract the values of the physical parameters (q_{max}, b) that describe the adsorption characteristics of the adsorbents.

5.2.5 Adsorption Kinetic Measurement

To investigate the effect of various experimental conditions on the resulting adsorption kinetics, a series of kinetic experiments wherein the experimental variables such as stirring speed, pH, initial Pd(II) concentration and type of nanoparticles were varied were conducted. To accurately follow the adsorption kinetics, the change in palladium concentration during adsorption was monitored by periodically sampling at short interval (5 or 10 seconds) for the first 3 minutes, followed by longer interval (30 or 60 seconds) afterwards. The adsorbent dosage for kinetic experiments was 20 mg (dry weight) of nanoadsorbents for every 400 ml of palladium solution. The mixture was magnetically stirred at 300 rpm throughout the kinetic experiment. After the adsorption process was finished, the sampled Pd(II) solutions were measured for transient and final Pd(II) concentrations ($c(t)$ and c_{eqm}). The final $D_{DLS,eqm}$ (nm) of the nanoparticles was measured using the BIC 90Plus particle size analyzer. Although the polymeric nanoparticles or microgel particles may be heterogeneously-crosslinked in which most of crosslinker molecules are congregated in the core (Fernández-Nieves *et al.*, 2000), the swelling transition of the nanoparticles is assumed to be isotropic to allow direct calculation of its properties in this study. The equilibrium swelling ratio S_{eqm} was evaluated using Eq. (5.1):

$$S_{eqm} = \frac{1}{\varphi_{eqm}} = \left(\frac{D_{DLS,eqm}}{D_{DLS,0}} \right)^3 \tag{5.1}$$

where the subscript *0* refers to the reference state where the nanoparticles are fully collapsed (i.e. at pH ~ 8-9 approx.).

Since the extensive swelling of these nanoparticles depends on uptake of the solvent (water) from the surrounding reservoir, the additional space emerged within each

individual swollen P4VP nanoparticle can therefore be quantified as its equilibrated water capacity (*EWC*), which is equal to the equilibrium porosity (ε) of the swollen nanoparticles. The mathematical relationship of these parameters is given as follow (Eq. (5.2)):

$$\varphi_{eqm} = \frac{1}{S_{eqm}} = 1 - EWC = 1 - \varepsilon_{eqm} \tag{5.2}$$

where the polymer fraction at swelling equilibrium (φ_{eqm}) is simply the reciprocal of S_{eqm}, with $\varepsilon_{eqm} = 1 - \left(\frac{D_{DLS,0}}{D_{DLS,eqm}} \right)^3$, where $D_{DLS,0}$ (nm) is the effective hydrodynamic diameter of the swollen nanoparticle prior to adsorption. The equilibrium porosity (or equilibrated water content) of nanoparticle is directly proportional to its degree of swelling (LeVan and Carta, 2008)

5.3 Results and Discussion

5.3.1 Revisiting the Palladium-induced Deswelling Data from Chapter 3

Diffusion-controlled versus swelling-controlled. Brazel and Peppas (1999) proposed the use of the dimensionless numbers – *diffusional Deborah* number (*De*) and the *swelling interface* number (*Sw*), to provide insights on transport behavior of solvent and solute molecules in swellable hydrogel systems. The former number relates the diffusive motion of solvent molecules to the relaxation rate of polymer network, and it is defined in Eq. (5.3):

$$De = \frac{\lambda}{T} = \frac{Polymer \quad relaxation \quad time}{Diffusion \quad of \quad solvent} \tag{5.3}$$

where λ is the characteristic time for the polymer swelling or deswelling, and the T is the characteristic time for solvent diffusion into the hydrogel. If the hydrogel's volume

transition is dominated by either the swelling (polymer relaxation, i.e. De » 1) or solvent diffusion (De « 1), the time-dependence of the overall process is Fickian. On the other hand, the system displays anomalous transport behavior (non-Fickian) when the two processes occur on the same or similar time scale. In addition, De also indicates whether the solute transport through the hydrogel is diffusion-controlled (De « 1) or swelling-controlled (De » 1), by comparing the timescales of these two processes (Lin and Metters, 2006).

The deswelling data shown in Chapter 3 (see Figure 3.12) suggested that the whole deswelling process for various types of swollen P4VP nanoparticles examined practically reached completion within the first ten seconds. Even though the adsorption process was accompanied by deswelling of P4VP nanoparticles, the entire shrinking process essentially ended before the completion of adsorption of palladium, as indicated by comparing the deswelling dynamics and Pd(II) adsorption kinetics shown in Figure 3.12 and Figure 5.1 respectively. During unstirred adsorption ("static adsorption"), the D_{DLS} of all swollen P4VP nanoparticles decreased significantly within the first 10-20 seconds when the nanoparticles were brought in contact with Pd(II) (see Figure 3.12 (a), (b) and (c)), which is similar to that of P2VP microgel particles undergoing pH-jump-induced shrinking transition (Yin *et al.*, 2008). For Pd(II) adsorption, the entire process took ~10 to 150 seconds to reach completion at pH 3; whereas at lower pH, the adsorption proceeded at a faster rate, i.e. less than 5 to 60 seconds, depending on the initial Pd(II) concentration (see Figure 5.2). Except under conditions such as low pH or high initial Pd(II) concentration, the nanoparticles deswelling process typically spanned a shorter time duration as compared to the Pd(II) adsorption. It is however uncertain on this relation under higher C_0 and low pH

because both nanoparticles deswelling and Pd(II) adsorption were too rapid to be measured accurately using the current experimental set-up.

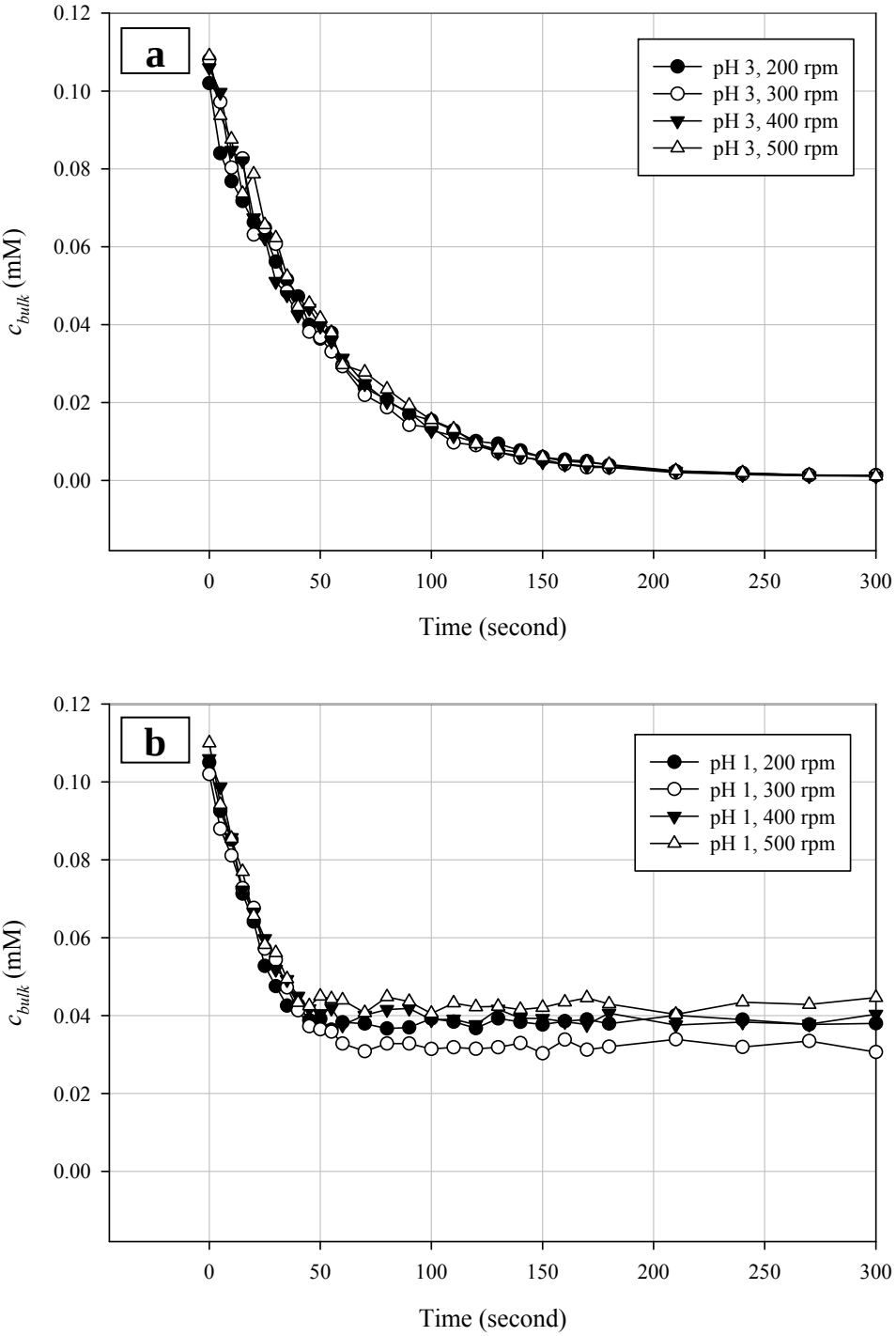

Figure 5.1 Adsorption kinetic of Pd(II) by P4VP-C1 ([DVB] = 4.0 wt.%) as a function of stirring speed at respective pH, (a) pH 3, (b) pH 1. Initial Pd(II) concentration is ca 0.1 mM. The solid lines are to guide the eye.

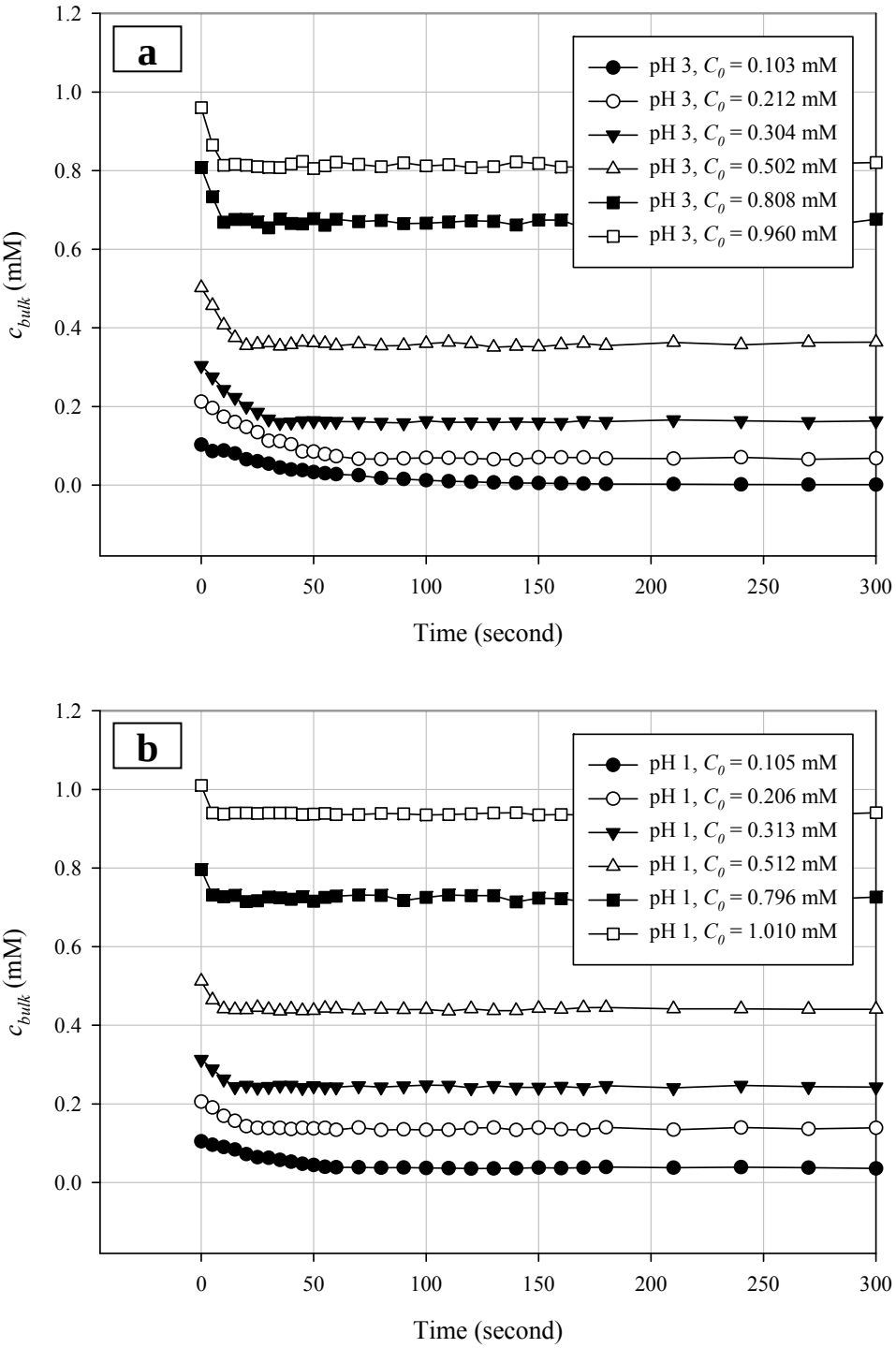

Figure 5.2 Adsorption kinetic of Pd(II) by P4VP-C1 ([DVB] = 4.0 wt.%) as a function of initial Pd(II) concentration at respective pH, i.e. pH 3 (a), and pH 1 (b). The stirring speed is 300 rpm in all cases. The solid lines are to guide the eye.

The characteristic swelling time (τ_{swell}) of a hydrogel (motion of network) is directly proportional to the square of the hydrogel particle dimension (Tanaka and Fillmore, 1979), i.e. $\tau_{swelling} \sim a^2 / D_{H_2O}$, implying that the gel swelling/deswelling process usually completes in tens to hundreds of milliseconds, or lesser, for microspheres or nanospheres. Given their small sizes, the deswelling kinetics of polyelectrolyte/polyionic nanoparticles or microgel particles are always fast and difficult to measure accurately. Nilsson and Hansson (2005) successfully monitored the deswelling kinetics of sodium polyacrylate microgel particles (d_p = 50 – 500 μm), which was induced by the adsorption of the positively-charged surfactant (dodecyltrimethylammonium bromide), with micromanipulator-assisted light microscopy. They found that the typical response time for such hydrogel particles was 100 to 300 seconds, and the measurement became noisy when the particle size was small, probably due to limited resolution of the optical microscopy. To overcome this problem, the swelling-deswelling kinetics of vinylpyridine-based microgel particles has been studied using stopped-flow light-scattering spectroscopy (Dupin *et al.*, 2006). Many researchers have demonstrated that the swelling (or deswelling) transition of pyridine-based polymeric nanoparticles (d_p = 310 – 1100 nm) occurred rapidly, typically in the range of tens of milliseconds (Dupin *et al.*, 2006; Dupin *et al.*, 2007; Yin *et al.*, 2008). For example, the swelling/deswelling of the poly(2-vinylpyridine) (P2VP) microgel particles in response to change in salt concentration or pH of surrounding reservoir has been studied in-depth. Upon acidification, the whole swelling process of P2VP nanoparticles of 1010 nm only took about 30 milliseconds (τ_{swell} = 18.5 milliseconds) (Dupin *et al.*, 2007); whereas the characteristic deswelling time, $\tau_{deswell}$ was only ca 40 milliseconds for P2VP nanoparticles of 1270 nm (Yin *et al.*, 2008).

In this work, to err on the conservative side, the characteristic deswelling time of P4VP nanoparticles during Pd(II) adsorption was taken as 5 seconds, which is at least 100 times larger than the $\tau_{deswell}$ reported (~ 40 milliseconds) in literature. Compared to T = 60 seconds (pH 1) or 150 seconds (pH 3) at C_0 = 0.1 mM (Figure 5.2), the characteristic time-scale (λ) for the relaxation of polymeric network was still smaller than the diffusion time-scale (T), and therefore the dimensionless Deborah number is small ($De \ll 1$), implying that the rate of palladium uptake was diffusion-controlled and did not depend on the swelling (or deswelling) rate of polymer network (Brazel and Peppas, 1999; Lin and Metters, 2006). Yin *et al.* (2008) also suggested that the initial collapse of microgel particles would dominate the first 50-60 milliseconds of the deswelling whereas the diffusion of small molecules (for e.g. ions and salts) would dominates over longer timescales. The observations in this work (Figure 3.12, Figure 5.1 and Figure 5.2) therefore support the proposition made herein that the solute transport in this system followed Fickian's laws of diffusion.

Homogeneous or heterogeneous shrinking. Nilsson and Hansson (2005) modeled the experimental deswelling data and found that the microgel deswelling is controlled by the "stagnant layer" diffusion (through the external film surrounding microgel particles), instead of the mass transfer through the surface collapsed layer (i.e. the skin layer formed due to the polyions/surfactants complexation). Budtova and Navard (1997, 1998) demonstrated that hydrogel deswells in a variety of manners, depending on the interaction between the metal ions and the polyions (charge-bearing hydrogels). For dilute metal conditions (i.e. $C_s/C_{pol} < 10$, where C_s, the salt or metal concentration, is comparable to C_{pol}, the polymer concentration, both calculated in molar unit), the metal ions could penetrate the gel core and bound to the interior network

homogeneously. For concentrated metal conditions (C_s/C_{pol} > 10), a dense, insoluble anisotropic layer would form immediately on the hydrogel surface, following massive binding of metal ions, resulting in the formation of a ring-like skin structure. The skin layer can inhibit further diffusive penetration of metal ions into the swollen gel core. Other researchers had also observed and systematically studied similar phenomenon-formation of collapsed, dense surface layer upon binding of oppositely-charged surfactant (Hansson, 1998; Göransson and Hansson, 2003; Nilsson *et al.*, 2007) or proteins (Kabanov *et al.*, 2004; Johansson *et al.*, 2007) to charged, slightly-crosslinked hydrogels. Nevertheless, the experimental C_s/C_{pol} ratios in this study was in the range of 0.22 to 2.22, which is regarded as "dilute" (in our experiment, C_s = 0.1 – 1.0 M, C_{pol} = 0.45 mole/liter, which is calculated based on the dosage of nanoparticles of 0.05 gram-P4VP/liter and the pyridyl-group density is ca 9.0 mmole/gram-P4VP). This calculation hints that the deswelling of swollen P4VP was probably homogeneous and lacking of any ring-like structure formation or density stratification after Pd(II) sequestration.

5.3.2 Kinetics of Pd(II) Uptake with P4VP Nanoparticles

In this section, P4VP-C1 nanoparticles ([DVB] = 4.0 wt.%) that had a larger size were specifically used for studying Pd(II) adsorption kinetics because other types of P4VP nanoparticles as listed in Table 5.1 had an adsorption process too fast for detailed kinetic study. Various parameters including solution pH, initial Pd(II) concentration, agitation intensity and particle sizes that may influence Pd(II) uptake rate were studied in a manner of batch, well-stirred tank.

Many experimental conditions such as initial metal concentration, nanoparticle dimension or crosslinking degree of the adsorbent employed, the solution pH and the stirring speed etc. can be varied to determine the rate-limiting step(s) or elucidate the complex mass transfer steps involved during the Pd(II) adsorption. In most adsorbent systems, external (bulk and film) mass transfer resistances are known to be negligible as compared to the intraparticle diffusion resistance under well-stirred conditions (Tien, 1994). While this assumption may stand valid for adsorbent particles whose particle size is large, the relative importance of Pd(II) transport through the external stagnant film surrounding the nanoparticles as compared to its diffusive penetration into the nanoparticles is however uncertain for the case in this study.

The dependency of the palladium adsorption kinetic on the stirring speed was investigated from 200 rpm to 500 rpm. As shown in Figure 5.1, there was essentially no change in the Pd(II) uptake rate when the stirring speed was increased, which implies that the bulk phase mass transfer process was not rate-controlling in Pd(II) adsorption on the P4VP nanoparticles. Similar conclusion was made by Kanai *et al.* (2008) for Pd(II) adsorption with chitosan microsphere. Mechanical agitation aids in homogenizing the distributions of both solutes and nanoparticles throughout the stirred tank, therefore eliminating bulk mass transfer resistance. Most of the industrial stirred tanks are baffled, in which the relative dimensions and positioning of the blade assembly as well as tank geometry are designed to enhance mass transfer between phases (i.e. to generate greater mass transfer coefficient). Absence of baffle under strong magnetic stirring causes vortex unavoidably, resulting in less efficient mass transport of solutes across the hydrodynamic boundary layer surrounding the nanoparticles. In this study, the density difference between swollen nanoparticles and

surrounding medium was smaller than that between solid polymeric nanoparticles (in collapsed state) and solution, which may reduce the relative motion between particles and immediate fluid elements.

The results in Figure 5.2 show that the Pd(II) adsorption with the P4VP nanoparticles reached equilibrium faster as initial Pd(II) concentration (C_0) increases. In general, the Pd(II) uptake rate was much faster for lower pH (pH 1, Figure 5.2 (b)) than that of higher pH (pH 3, Figure 5.2 (a)). Similar trend is observed in Figure 5.3, where it is found that the lower pH, the more rapid was the Pd(II) adsorption. This may be due to the lower Pd(II) adsorption capacity at lower pH (see Table 4.1 of Chapter 4), therefore the equilibrium time required for completion of adsorption process was shorter. The influence of other parameters such as the concentration of crosslinker and the particle size on the Pd(II) adsorption kinetic are discussed in the following section.

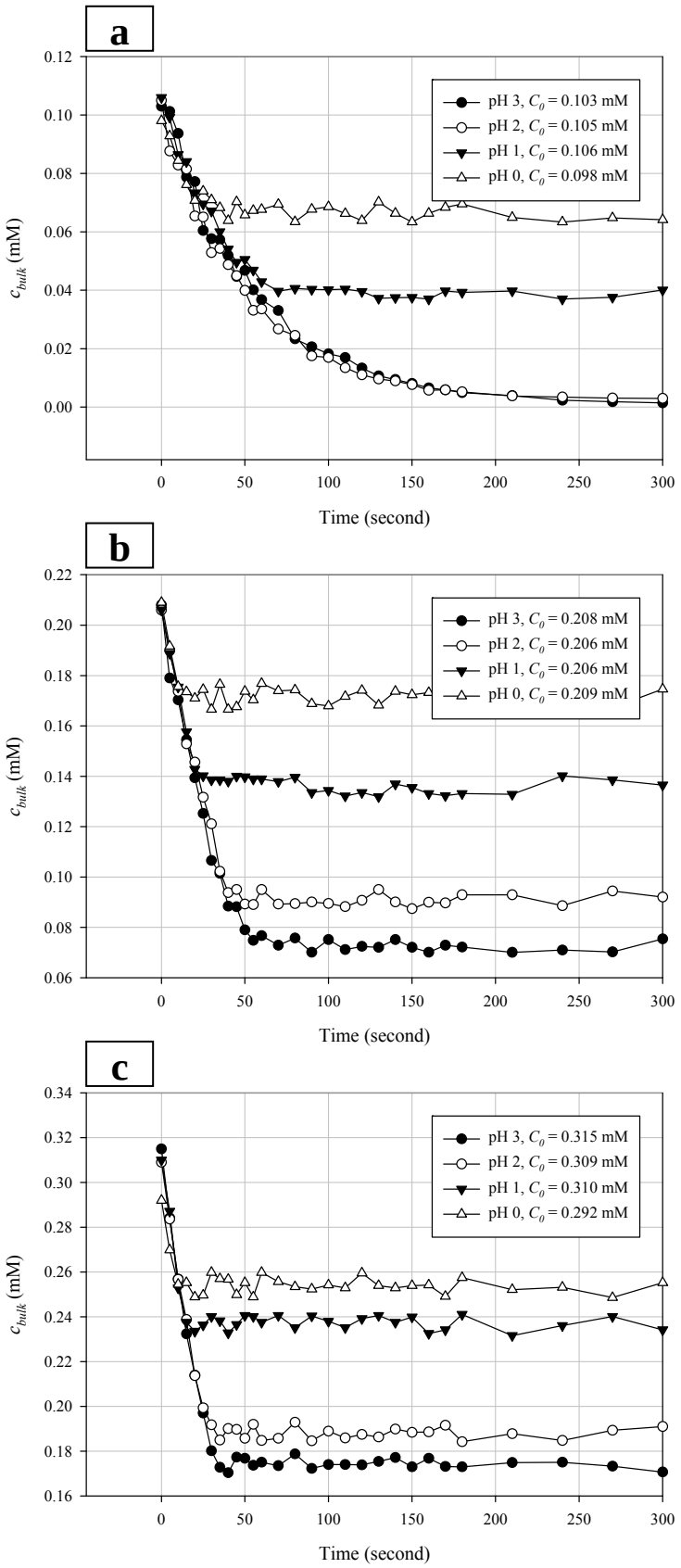

Figure 5.3 Adsorption kinetic of Pd(II) by P4VP-C1 ([DVB] = 4.0 wt.%) at different pH where (a) C_0 = ca 0.1 mM, (b) C_0 = ca 0.2 mM, and (c) C_0 = ca 0.3 mM. The stirring speed is 300 rpm in all cases. The solid lines are to guide the eye.

5.3.3 Diffusion Kinetics Modeling

Diffusion Model. One of the recurring tasks in adsorption studies is to identify the rate-limiting step in the adsorption process. Popular adsorption kinetic models such as Lagergren's Pseudo Second Order (PSO) model have been applied to model adsorption of heavy metal ions, dyes, biomolecules and organic pollutants (Ho, 2006). The model parameters obtained from data fitting may provide information that aids in scale-up of the adsorption system; regrettably they do not offer any insights further into the rate-determining step(s) and solute transport during the adsorption process. More realistic models that consist of differential-algebraic equations and incorporate assumptions made upon the adsorbent structure and dominating transport mechanism(s) for the solute have been studied (Tien, 1994; LeVan and Carta, 2008). In this work, the following models are used for analyzing the Pd(II) adsorption kinetics with P4VP nanoparticles.

(1) ***Intraparticle diffusion (IPD) model*** *(homogeneous pore-diffusion) with negligible external (film diffusion) mass transfer resistance (Bi → ∞) (1-p model) (Table 5.2)*: In this model, it is assumed that all intraparticle mass transfer event occur by diffusion in the solvent-filled pores. One of the popular IPD models for fitting adsorption data is that of Crank (1975). These 1-*p* models mostly operate by assuming the absence of external film transfer resistance or negligible film diffusion while the only adjustable parameter is the effective diffusivity (D_{eff}), which could be further differentiated into either pore diffusivity, surface diffusivity or a lumped approximation of both diffusivities. This approach, albeit oversimplified, manages to yield reasonably satisfactory fits to many adsorption rate data. Many of these fits nonetheless

yield values of solute diffusivity which deviates remarkably from the solute self-diffusion coefficients (Loukidou *et al.*, 2004).

(2) ***Combined film pore-diffusion model*** *with finite external (film diffusion) mass transfer resistance (2-p model) (Table 5.2):* A more accurate description for the various mass transfer events ongoing simultaneously would be to apply a more physically realistic model, such as the combined diffusion model described herein which takes into account of both external film transfer resistance as well as intraparticle diffusion resistance (Do, 1998; LeVan and Carta, 2008). During least-squares analysis, the transport-related parameters (D_{eff}, k_f) are varied iteratively to obtain good fit. The remaining parameters such as porosity (ε), particle radius (R) and adsorbent characteristics (q_{eqm}, b) are determined experimentally as detailed in the experimental section.

Nonetheless, full solutions for these models are often complicated and difficult to obtain; and therefore only approximation solutions were obtained by making certain assumptions, such as absence of film mass transfer, linear adsorption isotherm or infinite volume of batch adsorber (Crank, 1975). To avoid these drawbacks, the full numerical solutions to the models above were obtained using orthogonal collocation on finite elements (OCFE) method (Finlayson, 1980; Do, 1998) (See Appendix B for full OCFE formulation for the models). The OCFE method has been successfully applied in design, optimization and process control of a wide range of industrial processes, for example, phenol removal in cyclic fixed-bed adsorber (Costa and Rodrigues, 1985) and diethylacetal production from heterogeneous acid-catalyzed reaction (Silva and Rodrigues, 2002).

Table 5.2 Differential equations used in modeling the adsorption kinetic based on 1-*p* model or 2-*p* model.

Code	Original form:
DE-1	**Diffusion equation:** $\varepsilon\frac{\partial c}{\partial t}+(1-\varepsilon)\frac{\partial c_\mu}{\partial t}=\frac{1}{r^s}\frac{\partial}{\partial r}\left(r^s\cdot J\right),\ 0\le r\le R$ where $J=\varepsilon D_p\frac{\partial c}{\partial r}$ $c_\mu(t,r)=1000\times\rho_p\times q(t,r)$ **Boundary conditions:** $r=0,\quad \frac{\partial c}{\partial r}=0$ *(geometric symmetry condition)* $r=R,\quad \varepsilon D_p\frac{\partial c}{\partial r}=k_f(c_b-c)$ *(finite film/stagnant layer mass-transfer resistance)* ***(for 2-p model)*** or $r=R,\quad c=c_b$ *(negligible film mass-transfer resistance)* ***(for 1-p model)*** **Initial condition:** $t=0,\quad c=c_i$ *(which is 0, for pore fluid initially filled only with solvents)* **Adsorption isotherm:** $q(t,r)=q_{\max}\frac{bc(t,r)}{1+bc(t,r)}$ *(Langmuir isotherm model)*
DE-2	**Conservation equation:** $V\frac{\partial c_b}{\partial t}=-\frac{(s+1)}{R}(\varepsilon D_p)\frac{\partial c(R,t)}{\partial r}$ **Initial condition:** $t=0,\quad c_b=c_0$

Since these diffusion models require input of adsorption isotherm parameters (q_{max}, b), the adsorption isotherm experiments were repeated for the C-series nanoparticles (P4VP-C1). The adsorption behaviors and performances of P4VP-C1 nanoparticles (See Table 5.3 and Figure 5.4 (a)) are similar to those of P4VP-A3 nanoparticles (Chapter 4), except that the maximum adsorption capacities are slightly lower than but

similar in magnitude to that of prisitine P4VP nanoparticles studied in previous chapter. This is probably due to the dilution of pyridyl group concentration by other co-monomers (DVB, MATMAC and PEGMA) required for synthesis of P4VP-C1. The calculated values of q_{eqm} and b were then input to the kinetic modeling. The adsorption kinetic data were fitted to the model equations (DE-1 and DE-2, see Appendix B for full nomenclature and symbols) depicted in Table 5.2, to determine if the Pd(II) diffusion in P4VP nanoparticles follows 1-*p* or 2-*p* model and whether the Pd(II) transport in deswelling P4VP network obeyed Fickian's laws of diffusion. The differential equations (DE-1 and DE-2) were normalized, non-dimensionalized and rearranged to yield a more manageable form, as shown in Table 5.4. As the binding affinity (b) is high, the Pd(II) species are assumed to be relatively immobile once they are bound onto the P4VP binding sites and the surface diffusion of these solutes along the binding sites is neglected. The effective diffusion coefficient (D_{eff}) fitted from the experimental data is therefore equivalent to the pore diffusion coefficient (D_p).

Table 5.3 Fitted parameters of the Langmuir isotherm model as a function of pH, for Pd(II) adsorption by P4VP-C1 with [DVB] = 4.0 wt.%.

Sample	Model parameters fitted*				Goodness-of-fit	
	q_{eqm}	SE	b	SE	Adj. R^2	RMSE
	(mmole/g)		(liter/mmole)			
pH 3 ([HCl] = 0.001 M)	6.318	0.02147	2716	133.0	0.998	0.0667
pH 2 ([HCl] = 0.01 M)	5.238	0.01856	1978	149.0	0.996	0.0623
pH 1 ([HCl] = 0.1 M)	3.234	0.01037	540.3	23.77	0.998	0.0310
pH ~ 0 ([HCl] = 1 M)	1.919	0.008475	43.82	0.9191	0.999	0.0177

* The model parameters are calculated using nonlinear least-squares fitting.

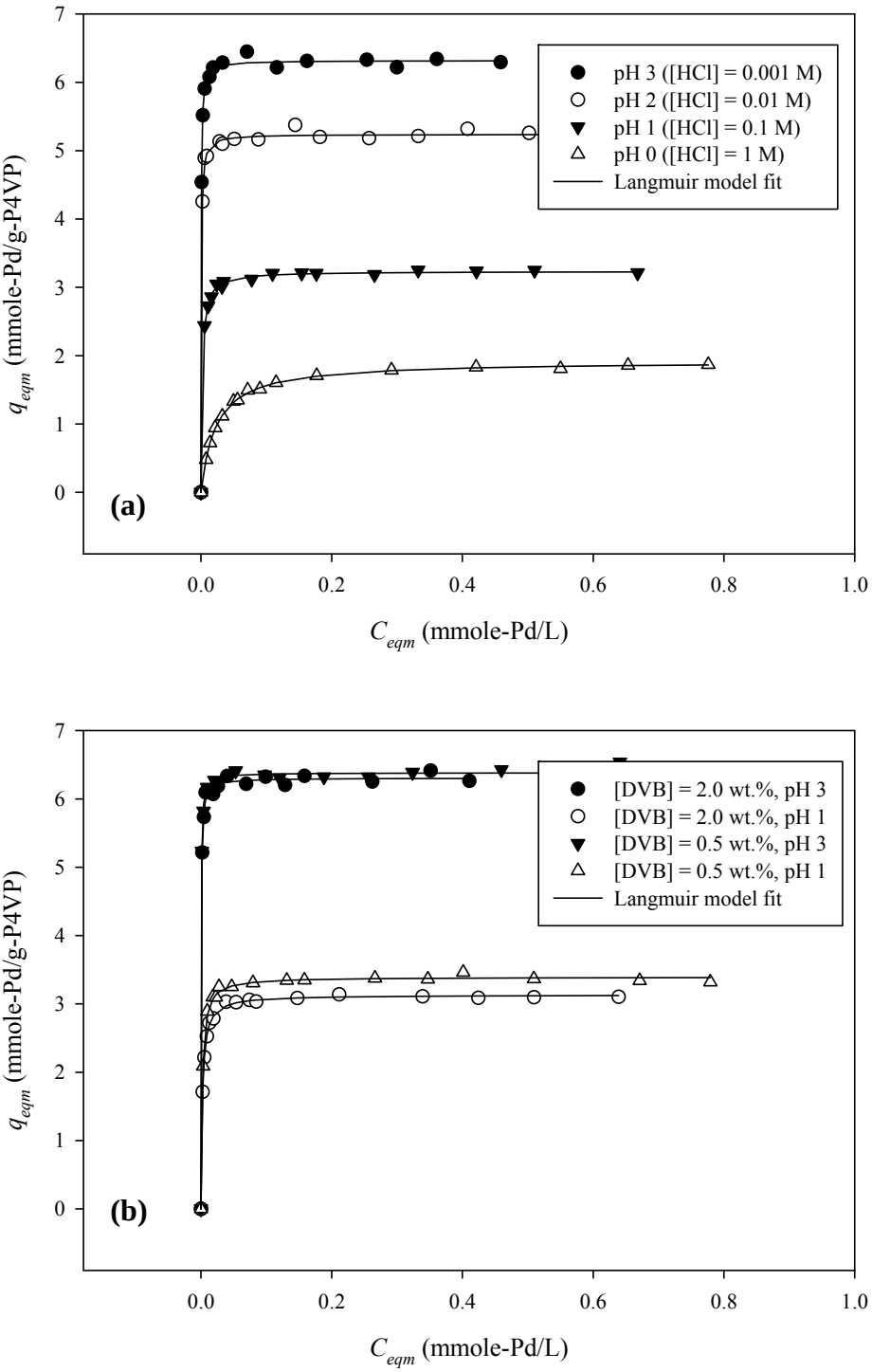

Figure 5.4 Adsorption isotherm plots for Pd(II) adsorption, (a) as a function of pH, by P4VP-C1 with [DVB] = 4.0 wt.%, and (b) as a function of [DVB].

Table 5.4 Dimensionless form of the equations used in modeling the adsorption kinetic.

Code	Non-dimensionalized form:

ND-1 **Diffusion equation:**

$$G(y)\frac{\partial y}{\partial \tau} = \frac{1}{x^s}\frac{\partial}{\partial x}\left\{x^s \frac{\partial y}{\partial x}\right\}$$

or

$$\frac{\partial y}{\partial \tau} = \frac{1}{G(y)}\left[\frac{s}{x}\frac{\partial y}{\partial x} + \frac{\partial^2 y}{\partial x^2}\right],\ 0 \le x \le 1$$

where

$$G(y) = \varepsilon + (1-\varepsilon) f'(c_0 y)$$

$$f'(c_0 y) = \frac{b c_{\mu s}}{\left[1 + b c_0 y\right]^2} \quad \textit{(from Langmuir model)}$$

Boundary conditions:

$$x = 0, \quad \frac{\partial y}{\partial x} = 0 \quad \textit{(geometric symmetry condition)}$$

$$x = 1, \quad \frac{\partial y}{\partial x} = Bi(y_b - y) \quad \textit{(finite film/stagnant layer mass-transfer resistance)} \textbf{\textit{(for 2-p model)}}$$

or

$$x = 1, \quad y = y_b \quad \textit{(negligible film mass-transfer resistance)} \ \textbf{\textit{(for 1-p model)}}$$

Initial condition:

$$\tau = 0, \quad y = y_i \quad \textit{(which is 0, for pore fluid initially filled only with solvents)}$$

ND-2 **Conservation equation:**

$$\frac{\partial y_b}{\partial \tau} = -\frac{(s+1)}{V}\left(\frac{m_p}{\rho_p}\right) Bi\left(y_b(\tau) - y(1,\tau)\right)$$

Initial condition:

$$\tau = 0, \quad y_b = \frac{c_0}{c_0} = 1$$

Transformation of variables:

$$y = \frac{c}{c_0};\ y_b = \frac{c_b}{c_0};\ y_i = \frac{c_i}{c_0};\ x = \frac{r}{R};\ \tau = \frac{\varepsilon D_p t}{R^2};$$

$$c_\mu = f(c) = c_{\mu s}\frac{bc}{1+bc};\ c_{\mu 0} = f(c_0);\ Bi = \frac{k_f R}{\varepsilon D_p}$$

The modeling would become unnecessarily complex if one were to solve the full set of diffusion equations while taking into account of the volume transition (i.e. the variation in volume or physical dimension with respect to time) (Grisham *et al.*, 1990; Narita *et al.*, 1998). For simplicity, we make an assumption that the volume or particle radius remains constant. Physically, this situation is only valid when the deswelling is absent or the deswelling process reaches completion instantaneously at the onset of adsorption, i.e. the volume-transition step outpaces the Pd(II) binding, which was shown to be the case in previous section. To examine the effect of porosity of swollen nanoparticles on the adsorption transient, another two batches of P4VP-C1 nanoparticles with different crosslinker concentrations, i.e. [DVB] = 2.0 wt.% and 0.5 wt.% were synthesized in a similar manner to that described in Chapter 3 (see Table 5.1). Their adsorption capacities were determined via the adsorption isotherm experiments (Table 5.5, Figure 5.4 (b)) and were input to the modeling work.

Table 5.5 Fitted parameters of the Langmuir isotherm model as a function of [DVB] for Pd(II) adsorption by P4VP-C1.

Sample	Model parameters fitted*				Goodness-of-fit	
	q_{eqm}	SE	b	SE	Adj. R^2	RMSE
	(mmole/g)		(liter/mmole)			
[DVB] = 2.0 wt.%, pH 3	6.305	0.02452	2643	211.5	0.997	0.0752
[DVB] = 2.0 wt.%, pH 1	3.132	0.009013	476.3	12.38	0.996	0.0269
[DVB] = 0.5 wt.%, pH 3	6.382	0.02110	3192	219.1	0.998	0.0677
[DVB] = 0.5 wt.%, pH 1	3.393	0.01428	525.0	26.46	0.995	0.0444

* The model parameters are calculated using nonlinear least-squares fitting.

The best-fit coefficients for 2-*p* (D_{eff}, k_f) and 1-*p* (D_{eff} only) models were determined through nonlinear least-squares regression using MATLAB® (R14SP3, The MathWorks, Natick, Massachusetts), and their goodness-of-fit were evaluated, as shown in Table 5.6 (on page 176). The goodness-of-fit by 2-*p* model is generally

better than that of 1-*p* model for the 60 entries of adsorption kinetic data examined and modeled. Nonetheless, similar best fit was observed for data obtained from experiments which were conducted with high initial Pd(II) concentrations (i.e. entry 10-12) or lower pH values (i.e. entry 23-24), and the nanoparticles of higher equilibrium porosity (i.e. entry 38-40). A close examination of the kinetic curves reveals that these counterexamples probably arise when there are too little useful data points in the initial portions of these curves for data-fitting. For example, the Pd(II) adsorptions at pH 1 have instantaneously gone to completion when the initial Pd(II) concentration is higher than 0.5 mM (Figure 5.5 (b) on page 175). This reflects the inadequacy of our current sampling method to follow accurately the Pd(II) adsorption kinetics which were too rapid.

By visual inspection, the 2-*p* model fits better to the collected adsorption kinetics, as shown in Figure 5.5. For both pH (Figure 5.5 (a) and (b)), the prediction by 1-*p* model always falls short of the experimental curves for the initial period of Pd(II) adsorption and overestimate the adsorption process at longer contact time. On the contrary, satisfactory fits between prediction and experimental data were always obtained by using the 2-*p* model. Similar good fits by the 2-*p* model are also shown in Figures 5.6 and 5.7 (on page 179 and 180, respectively). By substituting the equilibrium porosity (ε_{eqm}), q_{max} and b determined through DLS measurement and equilibrium studies, the 2-*p* model could fit the Pd(II) adsorption data by P4VP-C1 nanoparticles of other crosslinker concentrations. The lower the [DVB], the higher value of ε_{eqm} is obtained (Table 5.6). The adsorption of Pd(II) by P4VP nanoparticles with lower [DVB] (Figure 5.7 (c) and (d)) proceeded more rapidly, probably due to the greater mesh size and porosity of the less crosslinked polymer network. Many direct experimental

results have shown that the degree of crosslinking has great influence on the selectivity of separation and binding site accessibility of the crosslinked polymer gels and resins (Alvarez-Lorenzo, 2001; Zagorodni, 2007). Excessive crosslinking reduces the mechanical flexibility and the mesh size of the polymer network, rendering greater diffusional resistance on solutes (Johansson *et al.*, 1991; Amsden, 1998). The smaller P4VP nanoparticles have shorter diffusion path length, which logically results higher Pd(II) uptake rate (Figure 5.7). Both Figures 5.6 and 5.7 demonstrates the universality of the 2-*p* model in predicting the Pd(II) transport in the P4VP nanoparticles with varying level of crosslinking, and its particle size dependence.

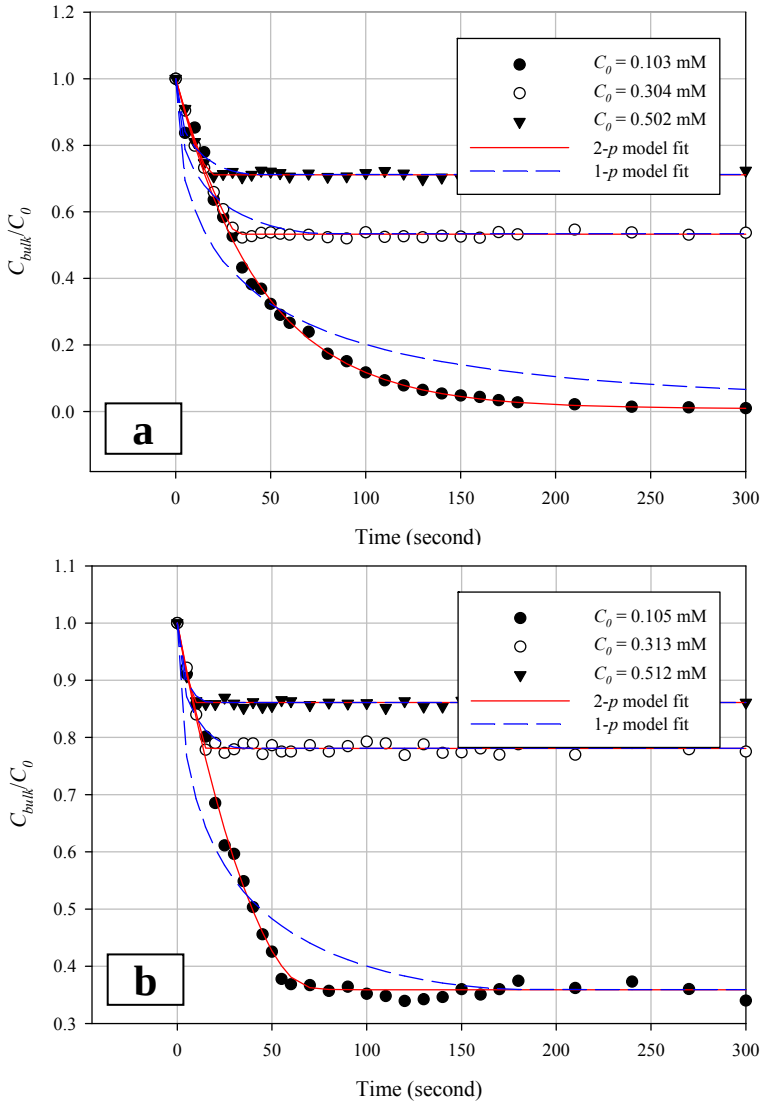

Figure 5.5 Effects of initial Pd(II) concentration on adsorption kinetic, at (a) pH 3 and (b) pH 1, for P4VP-C1 ([DVB] = 4.0 wt.%).

Table 5.6 Experimental conditions for adsorption kinetic experiments and the fitted coefficients.

		Experimental conditions						*(At adsorption equilibrium)*			*2-p model – Combined diffusion model*				*1-p model – Intraparticle diffusion model*			
Entry	Type	[DVB] (wt.%)	Stirring (rpm)	pH	C_0 (mM)	$S_{swollen}$ (-)	$\varepsilon_{swollen}$ (-)	S_{eqm} [a] (-)	ε_{eqm} [b] (-)	q_{eqm} (mmole/g)	$D_{eff}\times10^5$ (cm^2/s)	k_f (cm/s)	Adj. R^2	RMSE	$D_{eff}\times10^7$ (cm^2/s)	Adj. R^2	RMSE	Bi [c] (-)
1	C-1	4.0	300	3.01	0.103	5.877	0.830	2.229	0.551	2.057	0.5721	0.006421	0.995	0.0201	0.6887	0.895	0.0947	0.0860
2	C-1	4.0	300	3.07	0.212	5.770	0.827	2.165	0.538	4.227	0.3591	0.005503	0.996	0.0128	0.9680	0.893	0.0631	0.1191
3	C-1	4.0	300	3.01	0.304	6.229	0.839	2.225	0.550	5.971	0.4015	0.006068	0.996	0.0071	1.0896	0.916	0.0329	0.1160
4	C-1	4.0	300	3.04	0.502	6.124	0.837	2.151	0.535	6.236	0.4203	0.005821	0.982	0.0082	1.0213	0.925	0.0168	0.1080
5	C-1	4.0	300	3.02	0.808	6.269	0.840	2.216	0.549	6.347	0.4032	0.005697	0.910	0.0100	0.9297	0.895	0.0108	0.1084
6	C-1	4.0	300	3.00	0.960	6.023	0.834	2.125	0.529	6.206	1.6861	0.005932	0.968	0.0050	1.1139	0.951	0.0061	0.0276
7	C-1	4.0	300	1.06	0.105	6.905	0.855	2.253	0.556	2.034	0.4881	0.005318	0.993	0.0149	0.9027	0.886	0.0620	0.0830
8	C-1	4.0	300	1.01	0.206	6.917	0.855	2.233	0.552	3.020	0.5122	0.005422	0.977	0.0118	0.8832	0.912	0.0230	0.0810
9	C-1	4.0	300	1.08	0.313	7.218	0.861	2.279	0.561	3.112	0.4647	0.005093	0.974	0.0073	0.8739	0.919	0.0130	0.0831
10	C-1	4.0	300	1.11	0.512	6.822	0.853	2.238	0.553	3.180	0.5339	0.005730	0.960	0.0051	1.0055	0.952	0.0055	0.0820
11	C-1	4.0	300	1.05	0.796	7.083	0.859	2.222	0.550	3.288	0.4953	0.004976	0.811	0.0076	0.9866	0.818	0.0074	0.0770
12	C-1	4.0	300	1.06	1.010	7.114	0.859	2.269	0.559	3.265	0.4144	0.004310	0.976	0.0019	1.3294	0.977	0.0019	0.0790
13	C-1	4.0	300	3.03	0.103	6.151	0.837	2.237	0.553	2.057	0.4006	0.005079	0.994	0.0248	0.5237	0.879	0.1078	0.0969
14	C-1	4.0	300	3.03	0.208	6.173	0.838	2.247	0.555	4.146	0.4051	0.006108	0.994	0.0136	1.0760	0.907	0.0532	0.1150
15	C-1	4.0	300	3.03	0.315	6.274	0.841	2.205	0.546	6.049	0.3990	0.005695	0.996	0.0070	1.0220	0.919	0.0307	0.1100
16	C-1	4.0	300	2.04	0.105	7.050	0.858	2.189	0.543	2.094	0.3120	0.005944	0.995	0.0189	0.8111	0.895	0.0917	0.1472
17	C-1	4.0	300	2.04	0.206	7.074	0.859	2.203	0.546	4.083	2.2859	0.005363	0.991	0.0141	0.9757	0.884	0.0517	0.0181
18	C-1	4.0	300	2.04	0.309	6.855	0.854	2.193	0.544	5.236	0.4342	0.005227	0.992	0.0083	0.9188	0.912	0.0278	0.0929
19	C-1	4.0	300	1.02	0.106	7.234	0.862	2.295	0.564	2.056	0.2903	0.004951	0.993	0.0151	0.7847	0.911	0.0540	0.1289
20	C-1	4.0	300	1.02	0.206	7.191	0.861	2.259	0.557	3.108	0.4829	0.005195	0.969	0.0140	0.7857	0.914	0.0232	0.0819
21	C-1	4.0	300	1.02	0.310	7.209	0.861	2.233	0.552	3.272	0.4987	0.005591	0.953	0.0107	0.9635	0.885	0.0167	0.0858
22	C-1	4.0	300	~ 0	0.098	6.881	0.855	2.247	0.555	1.176	0.4917	0.005005	0.911	0.0238	0.7806	0.858	0.0301	0.0776
23	C-1	4.0	300	~ 0	0.209	7.257	0.862	2.247	0.555	1.624	0.4959	0.005592	0.827	0.0159	0.9028	0.808	0.0167	0.0860
24	C-1	4.0	300	~ 0	0.292	7.200	0.861	2.238	0.553	1.661	0.4914	0.004883	0.812	0.0114	0.8683	0.798	0.0119	0.0760

25	C-1	2.0	300	3.04	0.104	10.271	0.903	2.370	0.578	2.076	0.4594	0.005597	0.996	0.0183	0.6149	0.891	0.0982	0.0908
26	C-1	2.0	300	3.05	0.216	10.365	0.904	2.396	0.583	4.305	0.4698	0.005831	0.990	0.0159	1.0124	0.900	0.0504	0.0921
27	C-1	2.0	300	3.03	0.314	10.224	0.902	2.431	0.589	6.066	0.4689	0.005904	0.994	0.0077	0.9999	0.913	0.0287	0.0929
28	C-1	2.0	300	3.02	0.505	10.295	0.903	2.377	0.579	6.265	0.4729	0.006157	0.983	0.0070	1.0894	0.927	0.0145	0.0970
29	C-1	2.0	300	1.08	0.094	12.542	0.920	2.635	0.620	1.829	0.4479	0.005067	0.990	0.0171	0.8075	0.907	0.0517	0.0814
30	C-1	2.0	300	1.06	0.209	12.655	0.921	2.594	0.615	3.035	0.5002	0.004918	0.951	0.0146	0.7663	0.884	0.0225	0.0710
31	C-1	2.0	300	1.06	0.305	12.493	0.920	2.482	0.597	3.121	0.4502	0.004997	0.938	0.0105	0.8756	0.880	0.0146	0.0813
32	C-1	2.0	300	1.06	0.506	12.805	0.922	2.492	0.599	3.246	0.5370	0.005417	0.888	0.0081	0.9785	0.873	0.0086	0.0738
33	C-1	0.5	300	3.02	0.104	21.935	0.954	3.942	0.746	2.077	0.5152	0.004834	0.994	0.0191	0.7230	0.865	0.0897	0.0642
34	C-1	0.5	300	3.01	0.202	21.680	0.954	4.045	0.753	4.028	0.5374	0.005973	0.950	0.0226	0.9424	0.829	0.0416	0.0760
35	C-1	0.5	300	3.01	0.311	21.854	0.954	4.048	0.753	6.012	0.5574	0.005543	0.968	0.0097	0.9123	0.885	0.0185	0.0680
36	C-1	0.5	300	3.03	0.513	21.761	0.954	3.988	0.749	6.249	0.6206	0.006530	0.944	0.0069	1.1588	0.909	0.0088	0.0720
37	C-1	0.5	300	1.03	0.103	24.663	0.959	4.244	0.764	1.989	0.6518	0.005587	0.942	0.0202	0.8631	0.866	0.0307	0.0587
38	C-1	0.5	300	1.04	0.215	24.998	0.960	4.119	0.757	3.152	0.7443	0.006198	0.860	0.0144	0.8467	0.819	0.0164	0.0570
39	C-1	0.5	300	1.07	0.316	25.255	0.960	4.158	0.759	3.143	0.7394	0.007019	0.726	0.0129	1.3400	0.729	0.0128	0.0650
40	C-1	0.5	300	1.08	0.502	24.917	0.960	4.166	0.760	3.272	0.7045	0.005658	0.734	0.0079	1.5139	0.742	0.0078	0.0550
41	A-2	4.0	300	3.04	0.111	6.192	0.838	2.133	0.531	2.216	0.4060	0.005761	0.999	0.0074	0.3090	0.920	0.9204	0.0428
42	A-2	4.0	300	3.05	0.204	6.140	0.837	2.113	0.527	4.069	0.4104	0.005410	0.996	0.0100	0.4412	0.920	0.9205	0.0399
43	A-2	4.0	300	3.05	0.310	6.241	0.840	2.140	0.533	6.097	0.4126	0.005758	0.994	0.0072	0.4244	0.957	0.9567	0.0420
44	A-2	4.0	300	1.08	0.105	6.971	0.857	2.242	0.554	2.048	0.4785	0.005713	0.994	0.0115	0.4371	0.930	0.9304	0.0351
45	A-2	4.0	300	1.06	0.196	6.919	0.855	2.260	0.558	3.121	0.4940	0.005513	0.976	0.0104	0.4465	0.940	0.9405	0.0327
46	A-2	4.0	300	1.06	0.312	6.811	0.853	2.183	0.542	3.344	0.5180	0.005875	0.972	0.0072	0.6240	0.973	0.9726	0.0338
47	A-3	4.0	300	3.06	0.111	6.229	0.839	2.181	0.541	2.216	0.4057	0.005109	0.998	0.0121	0.3676	0.909	0.9086	0.0550
48	A-3	4.0	300	3.03	0.204	6.059	0.835	2.167	0.539	4.068	0.3971	0.004896	0.997	0.0099	0.5446	0.894	0.8945	0.0539
49	A-3	4.0	300	3.03	0.308	6.169	0.838	2.167	0.539	6.055	0.3890	0.005516	0.997	0.0052	0.5967	0.927	0.9271	0.0620
50	A-3	4.0	300	1.05	0.105	6.932	0.856	2.260	0.558	2.042	0.4892	0.005263	0.994	0.0129	0.5570	0.919	0.9193	0.0461
51	A-3	4.0	300	1.05	0.205	6.889	0.855	2.204	0.546	3.293	0.4890	0.005217	0.986	0.0093	0.5341	0.925	0.9254	0.0463
52	A-3	4.0	300	1.04	0.293	6.826	0.853	2.223	0.550	3.290	0.5274	0.005907	0.975	0.0073	0.6732	0.955	0.9546	0.0484

53	C-1	4.0	200	3.02	0.102	5.821	0.828	2.197	0.545	2.036	0.2350	0.006009	0.994	0.0211	0.6108	0.915	0.9145	0.1971
54	C-1	4.0	300	3.02	0.108	6.335	0.842	2.148	0.534	2.156	0.7465	0.006355	0.995	0.0201	0.7125	0.898	0.8982	0.0665
55	C-1	4.0	400	3.03	0.106	6.548	0.847	2.213	0.548	2.117	0.3982	0.006159	0.996	0.0182	0.6624	0.895	0.8951	0.1189
56	C-1	4.0	500	3.05	0.109	6.198	0.839	2.190	0.543	2.177	0.3985	0.005882	0.995	0.0202	0.6548	0.900	0.9003	0.1141
57	C-1	4.0	200	1.05	0.105	7.078	0.859	2.199	0.545	2.029	0.5689	0.007702	0.993	0.0138	1.3986	0.892	0.8922	0.1044
58	C-1	4.0	300	1.06	0.102	6.959	0.856	2.215	0.549	1.984	0.6124	0.006664	0.995	0.0129	1.1690	0.903	0.9034	0.0835
59	C-1	4.0	400	1.02	0.106	7.021	0.858	2.235	0.553	2.047	0.6103	0.006869	0.991	0.0156	1.2087	0.895	0.8949	0.0860
60	C-1	4.0	500	1.03	0.110	6.981	0.857	2.197	0.545	2.121	0.4474	0.007389	0.991	0.0144	1.3157	0.917	0.9170	0.1273
Means											0.5314	0.005685	0.961	0.0125	0.8556	0.895	0.3292	0.0800

[a] Equilibrium swelling ratio $S_{eqm} = \frac{\varphi_0}{\varphi_{eqm}} = \frac{V_{eqm}}{V_0} = \left(\frac{d_{eqm}}{d_0}\right)^3$, where the subscript *0* refers to reference state where the nanoparticles (or microgel particles) are fully collapsed (i.e. at pH ~ 8-9).

[b] Equilibrium porosity is calculated as $\varepsilon_{eqm} = 1 - \varphi_{eqm} = 1 - \frac{1}{S_{eqm}}$, where φ_0 is assumed to be 1.0 (i.e. the nanoparticles are totally deswollen initially at neutral condition).

[c] $Bi = \frac{k_f R}{\varepsilon D_p}$

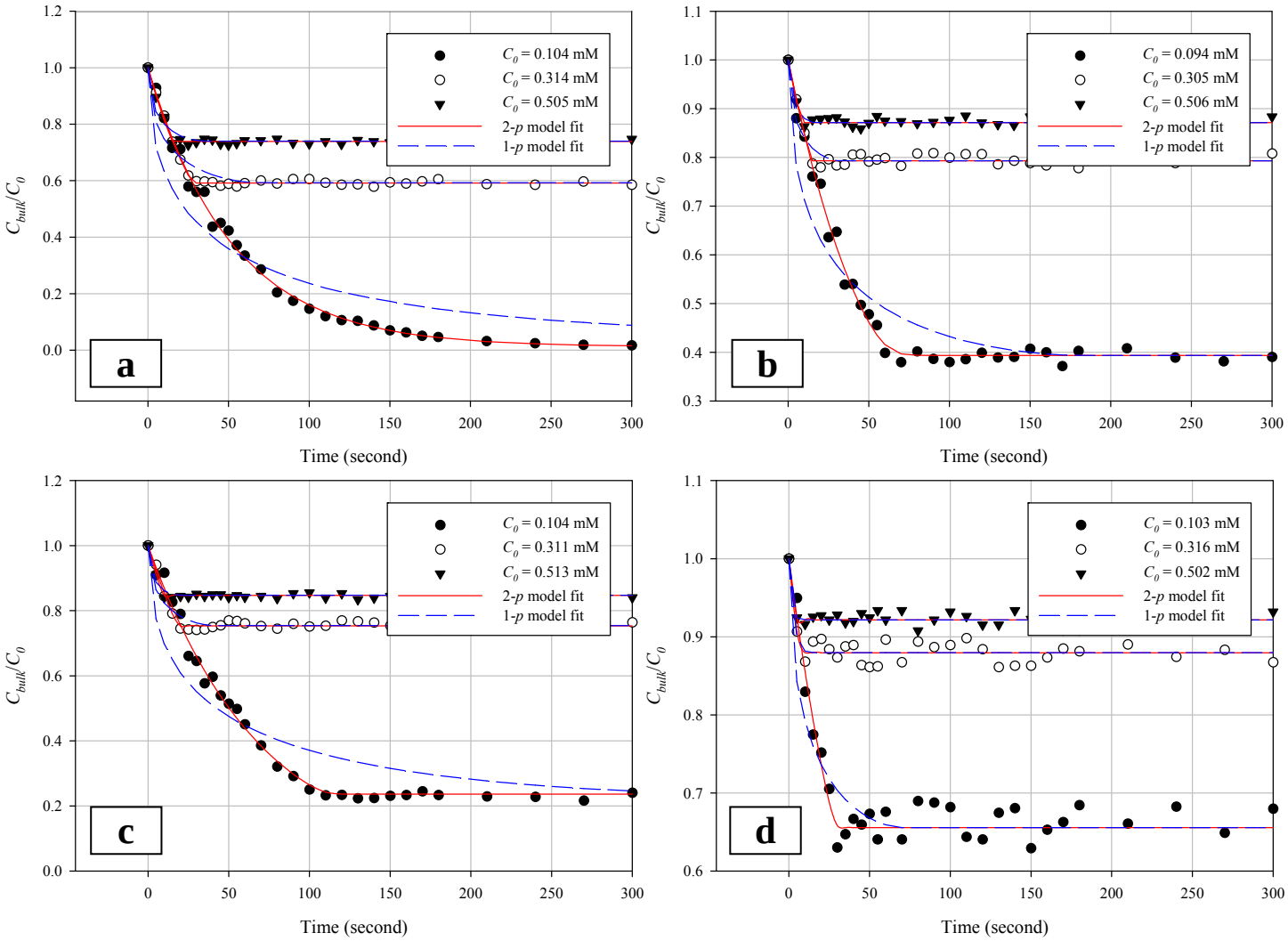

Figure 5.6 Effect of [DVB] incorporated on adsorption kinetic. (a) and (b) are plots for P4VP-C1-[DVB] = 2.0 wt.% at pH 3 and pH 1 respectively, whereas (c) and (d) are plots for P4VP-C1-[DVB] = 0.5 wt.% at pH 3 and pH 1 respectively.

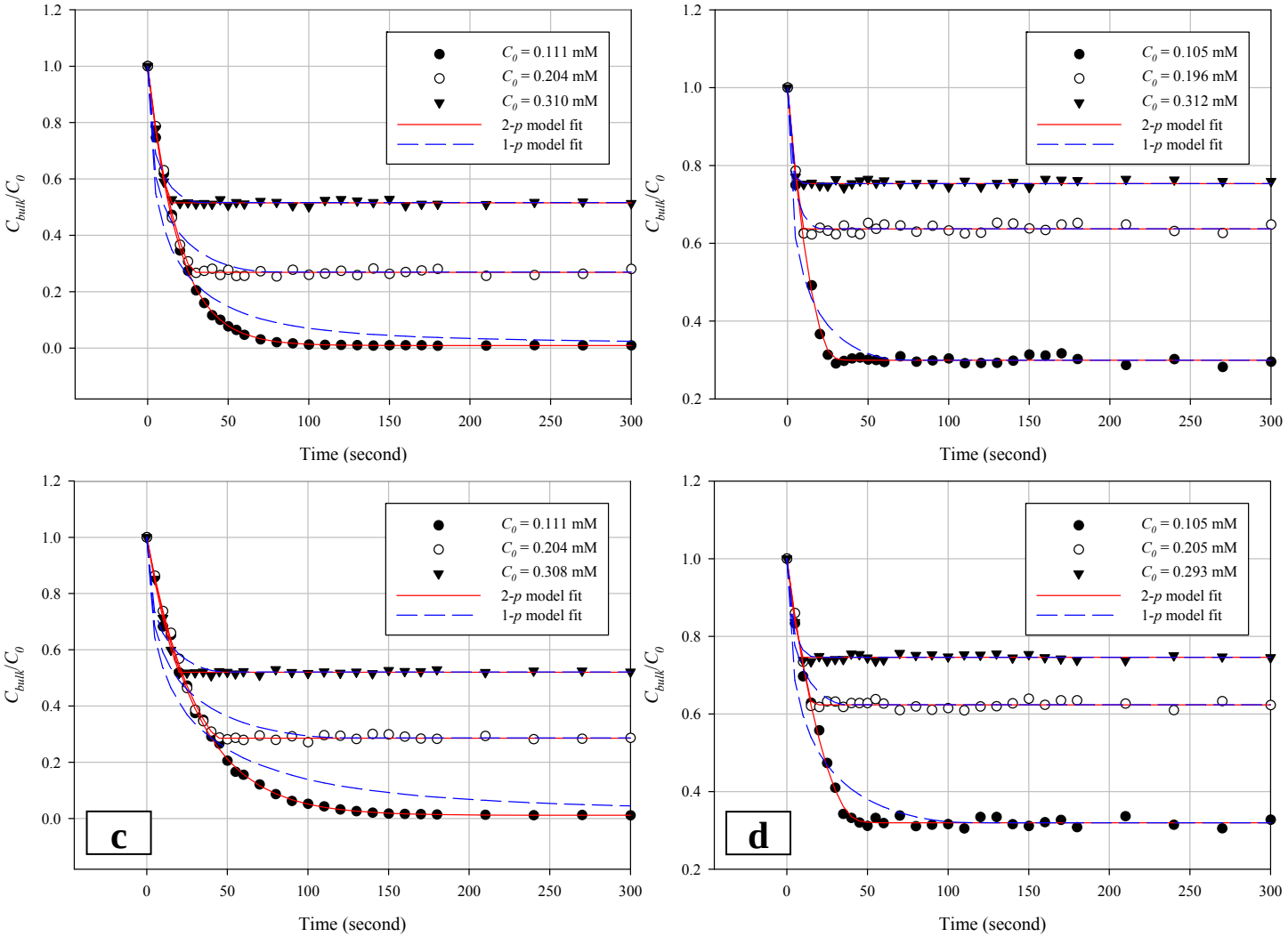

Figure 5.7 Effect of particle size on adsorption kinetic. (a) and (b) are plots of normalized bulk concentration of Pd(II) versus time for P4VP-A2, at pH 3 and pH 1; whereas (c) and (d) are plots for P4VP-A3 at pH 3 and pH 1 ([DVB] = 4.0 wt.%).

Table 5.7 Values of hydrodynamic radius (r_s) for various Pd(II) species

Solute	$D_0 \times 10^5$ (cm^2/s)[a]	r_s (Å)[b]
Pd^{2+}	1.99	1.21
$Pd(NH_3)_4^{2-}$	1.68	1.44
$PdCl_4^{2-}$	1.39	1.74
$PdBr_4^{2-}$	1.04	2.32

[a] Marcus (1997).

[b] The hydrodynamic radius of solute, r_s, is calculated from Stokes-Einstein's equation, i.e. $r_s = \dfrac{k_B T}{6\pi\eta D_0}$.

The average value of D_{eff} fitted in this work is 5.31×10^{-6} cm^2/s (i.e. 0.531×10^{-5} cm^2/s), which is smaller than the self-diffusion coefficients (D_0) of Pd^{2+} and $PdCl_4^{2-}$ (Table 5.7). Ruiz *et al.* (2000) studied Pd(II) adsorption by glutaraldehyde-crosslinked chitosan flakes by fitting the adsorption kinetic data using Crank's equation for IPD model, which assumed linear form of adsorption isotherm for easier computation. The values of D_{eff} fitted from their work fall in the range of $1.15 \times 10^{-11} – 1.43 \times 10^{-8}$ cm^2/s, which is smaller than the D_0 of Pd(II) by at least three orders of magnitude (See Table 5.7). Similar reduced diffusion coefficients were also reported from other studies which modeled the adsorption kinetics for other metal ions-adsorbents. For example, Walcarius *et al.* (2003) studied five different ordered mesoporous silica grafted with amine or thiol groups and modeled their Hg(II) and Cu(II) adsorption kinetics using Crank's IPD model. The fitted diffusion coefficients have a ranges of $10^{-9} – 10^{-11}$ cm^2/s and $10^{-8} – 10^{-10}$ cm^2/s for Hg(II) and Cu(II) respectively.

Estimation of k_f (external film transfer coefficient) and Biot number. Various theoretical analysis as well as semi-empirical correlations has been proposed to model and predict the particle-liquid mass transfer in mechanically-agitated tanks; however studies on particle-liquid mass transfer focusing on microparticles or nanoparticles are limited. Harriott (1962) proposed that, for particles less than 100 μm ('fine particles'), the mass transfer coefficient increases significantly with decreasing particle size, even though the relative slip velocity at the particle-liquid interface is reduced. The validity of Harriott's correlation for fine particles was later refuted by Yagi *et al.* (1984) and Asai *et al.* (1988). Yagi *et al.* (1984) studied the particle-liquid mass transfer of cation-exchange resins in stirred tank, and observed that the mass transfer coefficient decreases as the resins' size decreased from 145 to 25 μm. For example, a tenfold

reduction in k_f was observed when the specific surface area of the particles increased from 60 to 2000 m^2/m^3.

Table 5.8 Reported correlations and limiting coefficient values for solid-liquid mass transfer between fine particles (or microparticles) and liquid proposed by various researchers.

Researchers	Range of particle size (d_p) (cm)	Correlation equations or limiting values of mass transfer coefficient*	Schmidt number (Sc)
Harriott (1962)	0.0005 – 0.8	$Sh^* = k_f^* d_p/D_m = 2 + 0.6(d_p u_T \rho/\mu)^{0.5}(Sc)^{0.33}$, $k_f \approx 2k_f^*$ (Tien 1994), Sh^* ($d_p \rightarrow 0$) ~ 2.0.	325 – 1.08 × 10^5
Nagata (1975)	0.00009 – 0.1	k_f (d_p = 0.9 μm) ~ 0.008 – 0.013 cm/s ($BaSO_4$), k_f (d_p = 10 μm) ~ 0.018 – 0.022 cm/s (Cu^0), k_f (d_p = 10 μm) ~ 0.0085 – 0.011 cm/s ($CaSO_4 \cdot 2H_2O$).	-
Yagi *et al.* (1984)	0.0025 – 0.0145	k_f (d_p = 25.5 μm) ~ 0.02 – 0.03 cm/s (low S_A, DOWEX 50W resins), k_f (d_p = 25.5 μm) ~ 0.002 cm/s (high S_A, DOWEX 50W resins)	490
Asai *et al.* (1988)	0.0005 – 0.096	$Sh_p = [2^{5.8} + (0.61(Re_\varepsilon)^{0.58}(Sc)^{0.33})^{5.8}]^{1/5.8}$, Sh^* ($d_p \rightarrow 0$) ~ 2.0.	269 – 1.13 × 10^4
Armenante and Kirwan (1989)	0.0006 – 0.42	$Sh_p = 2 + 0.52(Re_\varepsilon)^{0.52}(Sc)$, Sh^* ($d_p \rightarrow 0$) ~ 2.0.	420 – 1.3 × 10^5

* $Sh_p = k_f d_p/D_m$, $Re_\varepsilon = (\varepsilon d_p^4/\upsilon^3)^{1/3}$, Sc = υ/D_m. S_A = specific surface area of particles.

There have been diverse views on the asymptotic bounds on value of external mass transfer coefficient for solid-liquid systems that consist of particles of very small sizes ("fine particles"). Most of the correlation equations for mass transfer coefficient reported were derived from experimental data for larger particles (Yagi *et al.*, 1984; Asai *et al.*, 1988; Pangarkar *et al.*, 2002), while there are only a few correlations established for smaller particles (Table 5.8). Asai *et al.* (1988) and Armenante and Kirwan (1989) remarked that, the Sherwood number approaches a limiting value of Sh_p = 2.0 asymptotically, when particle size is further reduced. Conversely, Nagata (1975) and Yagi *et al.* (1984) proposed that the value of external mass transfer coefficient could go lower than that given by Sh_p = 2.0, when the particle size is reduced extensively. Nagata (1975) investigated the mass transfer from submicron

barium sulfate particles of d_p = 0.9 μm, and determined that the mass transfer coefficient is 0.008 ~ 0.013 cm/s, which is similar to that of both copper (~ 0.02 cm/s) and gypsum (~ 0.01 cm/s) microparticles of d_p = 10 μm, regardless of agitation intensity (120 and 650 rpm). He attributed these experimental findings to trapping of an ensemble of fine particles in the Kolmogoroff's smallest turbulent eddies, in which the viscous effect is paramount, and therefore the mass transfer between trapped particles and liquid is dominated by Brownian motion, independent of kinetic energy input (stirring).

The values of k_f fitted from the combined diffusion model in this study are tabulated in Table 5.6. A simple statistical treatment by calculating the mean and the standard deviation (σ) of the population of fitted k_f shows that the population mean is 0.00569 cm/s. The values of fitted k_f show no obvious trend with the operational or experimental variables, and most of the values are contained within the boundaries of ± 1σ or ± 3σ (Figure 5.8). The mean value of k_f (~ 0.006) fitted is essentially of the similar order of magnitude to 0.008 ~ 0.013 cm/s of barium sulphate microparticles reported by Nagata (1975). This agreement implies that the negligible dependence of Pd(II) uptake rate on stirring intensity (Figure 5.1) could be attributed to the existence of asymptotic limit on k_f for film transfer.

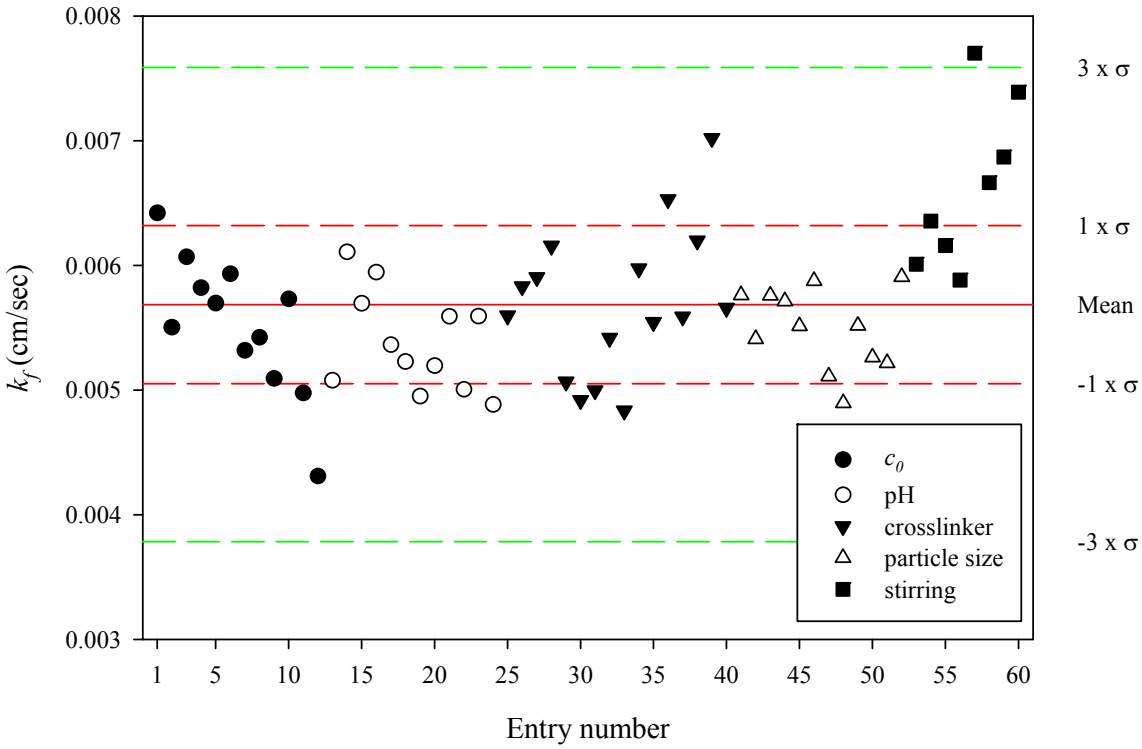

Figure 5.8 Plot of all values of k_f fitted from adsorption kinetic experiments using 2-*p* model. σ refers to the standard deviation of the population of k_f fitted.

To assess and compare the resistances of pore diffusion and film diffusion processes, the Biot number (*Bi*) of the adsorption kinetics was evaluated using Eq. (5.4) (Do, 1998; LeVan and Carta, 2008), using the values of D_{eff} (or D_p) and k_f fitted using the 2-*p* model (Table 5.6).

$$Bi = \frac{k_f R}{\varepsilon D_p} \tag{5.4}$$

For Pd(II) adsorption using P4VP nanoparticles, all the *Bi* values calculated are less than unity (i.e. $Bi < 1$), and their mean is 0.08 as shown in Table 5.6. These low values of *Bi* suggest that the mass transfer resistance contributed by the liquid film or stagnant layer surrounding the nanoparticles is either comparable or greater than the diffusional resistance within the nanoparticles (Tien, 1994; Do, 1998). For most cases,

the pore diffusion or intraparticle diffusion is the rate-controlling mechanism for the solute transport in other adsorbents or ion-exchange resins with sizes of millimeters or hundreds of microns (Tien, 1994; Zagorodni, 2007). For P4VP nanoparticles in this work, the contribution of pore diffusion resistance was remarkably reduced as the diffusional path length was much shorter. Pd(II) adsorption in smaller P4VP nanoparticles would encounter lower pore diffusion, as evidenced by the smaller *Bi* values for entries 41-52 of Table 5.6. Diffusion across the external 'film' or boundary layer surrounding ion-exchange resins becomes prevailing in systems wherein the particles are small, lowly crosslinked and high in solute binding sites, even in the liquid which is intensely agitated (Helfferich, 1962).

Statistical Analysis of Kinetic Model Parameters. Statistical *F*-test was employed to determine if the better goodness-of-fit of two parameters model over that of the one parameter model is statistically justified. The average value of F-ratio for the 60 entries of adsorption kinetic data (as shown in Table 5.9) was computed to be 407.1, which is significantly larger than unity, enforcing the previous regression statistics (Adj. R^2 and RMSE, in Table 5.6) that the 2-*p* model is better in terms of predicting and describing the Pd(II) adsorption process of the P4VP nanoparticles.

Table 5.9 Comparison of the model fits using F-test statistics.

Entry	2-*p* model		1-*p* model		Results					
	DF2	*SS2*	*DF1*	*SS1*	% inc. *DF*	% inc. *SS*	*F-ratio* [a]	DF of Numerator (DFn)	DF of Denominator (DFd)	*p*-value
1	32	0.0129	33	0.2962	3.1%	2192.4%	701.6	1	32	
2	32	0.0053	33	0.1314	3.1%	2390.8%	765.1	1	32	
3	32	0.0016	33	0.0357	3.1%	2115.0%	676.8	1	32	
4	32	0.0022	33	0.0093	3.1%	329.4%	105.4	1	32	
5	32	0.0032	33	0.0038	3.1%	20.4%	6.5	1	32	
6	32	0.0008	33	0.0012	3.1%	55.8%	17.9	1	32	
7	32	0.0071	33	0.1268	3.1%	1689.9%	540.8	1	32	
8	32	0.0045	33	0.0175	3.1%	291.3%	93.2	1	32	
9	32	0.0017	33	0.0056	3.1%	224.8%	71.9	1	32	
10	32	0.0008	33	0.0010	3.1%	23.8%	7.6	1	32	
11	32	0.0018	33	0.0018	3.1%	-0.8%	-0.2	1	32	
12	32	0.0001	33	0.0001	3.1%	0.8%	0.3	1	32	
1-12	**384**	**0.0420**	**396**	**0.6306**	**3.1%**	**1400.9%**	**448.3**	**12**	**384**	**< 0.00**
13	32	0.0197	33	0.3832	3.1%	1849.2%	591.8	1	32	
14	32	0.0059	33	0.0933	3.1%	1485.8%	475.5	1	32	
15	32	0.0016	33	0.0312	3.1%	1871.2%	598.8	1	32	
16	32	0.0115	33	0.2775	3.1%	2315.3%	740.9	1	32	
17	32	0.0064	33	0.0882	3.1%	1283.9%	410.8	1	32	
18	32	0.0022	33	0.0254	3.1%	1055.2%	337.7	1	32	
19	32	0.0073	33	0.0963	3.1%	1212.5%	388.0	1	32	
20	32	0.0063	33	0.0178	3.1%	182.2%	58.3	1	32	
21	32	0.0037	33	0.0093	3.1%	151.6%	48.5	1	32	
22	32	0.0181	33	0.0299	3.1%	64.9%	20.8	1	32	
23	32	0.0080	33	0.0092	3.1%	14.5%	4.6	1	32	
24	32	0.0042	33	0.0046	3.1%	10.7%	3.4	1	32	
13-24	**384**	**0.0949**	**396**	**1.0659**	**3.1%**	**1023.4%**	**327.5**	**12**	**384**	**< 0.00**
25	32	0.0107	33	0.3183	3.1%	2881.5%	922.1	1	32	
26	32	0.0081	33	0.0839	3.1%	939.9%	300.8	1	32	
27	32	0.0019	33	0.0272	3.1%	1317.4%	421.6	1	32	
28	32	0.0016	33	0.0069	3.1%	337.3%	107.9	1	32	
29	32	0.0094	33	0.0881	3.1%	839.1%	268.5	1	32	
30	32	0.0068	33	0.0167	3.1%	144.2%	46.2	1	32	
31	32	0.0035	33	0.0071	3.1%	100.4%	32.1	1	32	
32	32	0.0021	33	0.0025	3.1%	17.4%	5.6	1	32	
33	32	0.0117	33	0.2656	3.1%	2170.5%	694.6	1	32	
34	32	0.0163	33	0.0570	3.1%	249.1%	79.7	1	32	
35	32	0.0030	33	0.0113	3.1%	276.7%	88.5	1	32	
36	32	0.0015	33	0.0025	3.1%	67.2%	21.5	1	32	
37	32	0.0131	33	0.0311	3.1%	137.5%	44.0	1	32	
38	32	0.0067	33	0.0089	3.1%	33.6%	10.7	1	32	
39	32	0.0053	33	0.0054	3.1%	1.9%	0.6	1	32	
40	32	0.0020	33	0.0020	3.1%	-0.2%	-0.1	1	32	
25-40	**512**	**0.1037**	**528**	**0.9345**	**3.1%**	**801.1%**	**256.3**	**16**	**512**	**< 0.00**
41	32	0.0018	33	0.1495	3.1%	8436.7%	2699.8	1	32	
42	32	0.0032	33	0.0698	3.1%	2070.1%	662.4	1	32	
43	32	0.0016	33	0.0125	3.1%	660.9%	211.5	1	32	
44	32	0.0042	33	0.0526	3.1%	1139.4%	364.6	1	32	
45	32	0.0034	33	0.0089	3.1%	158.1%	50.6	1	32	
46	32	0.0016	33	0.0016	3.1%	-0.6%	-0.2	1	32	

47	32	0.0047	33	0.2181	3.1%	4525.6%	1448.2	1	32	
48	32	0.0031	33	0.1141	3.1%	3548.3%	1135.5	1	32	
49	32	0.0009	33	0.0254	3.1%	2829.5%	905.4	1	32	
50	32	0.0053	33	0.0720	3.1%	1248.1%	399.4	1	32	
51	32	0.0027	33	0.0147	3.1%	436.5%	139.7	1	32	
52	32	0.0017	33	0.0032	3.1%	89.6%	28.7	1	32	
41-52	**384**	**0.0344**	**396**	**0.7425**	**3.1%**	**2056.4%**	**658.1**	**12**	**384**	**< 0.00**
53	32	0.0143	33	0.2283	3.1%	1499.4%	479.8	1	32	
54	32	0.0129	33	0.2819	3.1%	2078.1%	665.0	1	32	
55	32	0.0106	33	0.3021	3.1%	2746.2%	878.8	1	32	
56	32	0.0131	33	0.2796	3.1%	2035.7%	651.4	1	32	
57	32	0.0061	33	0.0958	3.1%	1476.6%	472.5	1	32	
58	32	0.0053	33	0.1065	3.1%	1902.6%	608.8	1	32	
59	32	0.0078	33	0.0961	3.1%	1127.0%	360.6	1	32	
60	32	0.0066	33	0.0633	3.1%	858.9%	274.8	1	32	
53-60	**256**	**0.0767**	**264**	**1.4536**	**3.1%**	**1794.0%**	**574.1**	**8**	**256**	**< 0.00**
Total	**1920**	**0.3518**	**1980**	**4.8272**	**3.1%**	**1272.2%**	**407.1**	**60**	**1920**	**< 0.00**

[a] The *F-ratio* is calculated as follow, $F-ratio=\frac{(SS1-SS2)}{SS2}\times\frac{(DF2)}{(DF1-DF2)}$, where *DF* and *SS* are the degrees of freedom and sum of squared errors.

5.3.4 Hindered Diffusion of Ions through Swollen/Deswollen P4VP Network

There have been intensive efforts in modeling and predicting the diffusion of various solutes through either neutral hydrogels or charged gels (polyelectrolyte networks), such as sugars, proteins and polymers (Muhr and Blanshard, 1982; Amsden, 1998; Amsden 2001; Muhr and Blanshard, 1982; Amsden *et al.*, 2002**)**. Many of these diffusion studies reported that the solute diffusion always experiences retardation, i.e. the measured or fitted effective diffusion coefficient (D_{eff}) is smaller than their free solution counterpart (D_0). It is envisioned that the following scenarios might have contributed to the observed retardation effect (i.e. $D_{eff}/D_0 < 1$) : (a) increased hydrodynamic drags, (b) geometrical obstruction, (c) alteration of solvent properties and (d) polymer involvement, during the solute transport through the gel network (Muhr and Blanshard, 1982; Amsden, 1998). To account for this discrepancy, many researchers have put forth different theoretical or semi-empirical formulations to correlate the actual observed values which are fitted from a wide spectrum of adsorption/release data to their reference values at standard states. Various phenomenological models that based on the obstruction effect to account for the hindered movement of solute have been proposed (Table 5.10). One of the popular expressions is that of Mackie and Meares (1955) who relates the retardation effect to the tortuosity (θ) of the porous particles (See Table 5.10). Westrin and Axelsson (1991) made further improvement on that of Mackie and Meares (1955) by accounting for porosity effect (ε), in addition to the tortuosity. Ogston *et al.* (1973) visualized the polymer network consisting of random fibers or cylinders overlapping with each other, where r_s and r_f are solute radius and fiber radius of polymer chain respectively. Amsden (1998) further improved the model proposed by Ogston *et al.* (1973) by incorporating concept of scaling, i.e. the "Obstruction-Scaling" model. During solute

diffusion through swollen neutral hydrogels or polyeletrolyte gels, the solute primarily transport through a series of solvent-filled regions in between the surrounding polymer chains, assembled in a mesh-like manner. To account for electrostatic effect encountered during diffusion in polyelectrolyte gel, Amsden (2001) refined the previous model such that the average radius of the openings between the polymer chains is related to the monomer length (a), the volume fraction (φ), the ionization degree of the polyelectrolyte network (α), and the polymer characteristic ratio (C_∞), by the scaling constant (k_s) which is polymer-specific.

Table 5.10 Summary of obstruction-based models for hindered diffusion.

Model Expressions	Reference
$\frac{D_{eff}}{D_0} = \left(\frac{1}{\theta}\right)^2 = \left(\frac{1-\varphi}{1+\varphi}\right)^2$ (corrected for tortuosity)	Mackie and Meares (1955)
$\frac{D_{eff}}{D_0} = \varepsilon\left(\frac{1}{\theta}\right)^2 = \frac{(1-\varphi)^3}{(1+\varphi)^2}$ (corrected for both porosity and tortuosity)	Westrin & Axelsson (1991)
$\frac{D_{eff}}{D_0} = \exp\left[-\frac{r_s + r_f}{r_f}\sqrt{\varphi}\right]$	Ogston *et al.* (1973)
$\frac{D_{eff}}{D_0} = \exp\left[-\pi\left(\frac{r_s + r_f}{k_s\varphi^{-1/2} + 2r_f}\right)^2\right]$	Amsden (1998)
$\frac{D_{eff}}{D_0} = \exp\left[-\pi\left(\frac{r_s + r_f}{k_s(a\varphi)^{-1/2}(\alpha C_\infty)^{-1/4} + 2r_f}\right)^2\right]$	Amsden (2001)

Table 5.11 Values of physical parameters of P4VP (25 °C) used in this work.

Parameters	Values
M_m (g/mol)	105.14
a (Å)	2.52[c]
$\upsilon_{polymer}$ (cm^3/g)	0.682 (ethanol)[a] & 0.637 (pH 2, HCl)[b]
r_f (Å)[d]	3.88 & 3.75
$r_{f,mean}$ (Å)[e]	3.81
C_∞ (-)	177.69 (pH 3)[f] & 24.02 (pH 1)[g]
α (-)[h]	0.781 (pH 3) & 1.0 (pH 1) for [DVB] = 4.0 wt.%
	0.868 (pH 3) & 1.0 (pH 1) for [DVB] = 2.0 wt.%
	0.904 (pH 3) & 1.0 (pH 1) for [DVB] = 0.5 wt.%

[a] Brandrup *et al.* (1999).
[b] Mika *et al.* (2002).
[c] Nyrkova and Semenov (2005).
[d] The radius of gel fiber (polymer chain) is calculated as follow, $r_f = \sqrt{\frac{M_m \upsilon}{a \pi N_A}}$.
[e] The mean radius of gel fiber is calculated by taking average of the two r_f values.
[f] The polymer characteristic ratio (C_∞) used in this work is estimated as follow: $C_\infty = 2*(l_p/l_{chem}) - 1$ (Flory, 1969), where l_p and l_{chem} are the persistence length and the respectively. The value for l_p is 130 Å (Yoshida, 1997) whereas l_{chem} = 1.455 Å.
[g] Yoshida (1997).
[h] The degree of ionization (α) is determined from the pH titration curves of the P4VP nanoparticles (See Figure 4.2 of Chapter 4).

To understand whether the reduced diffusion coefficients fitted in Table 5.6 can be accounted by the concept of hindered diffusion due to obstruction effect, the data from entries 1-12 and 41-52 were fitted to the obstruction-scaling model (Amsden, 2001). To extend the range of polymer fraction (φ), adsorption data from Pd(II) adsorption by P4VP-C1 nanoparticles with different [DVB] (entries 25-40 of Table 5.6) were included in the modeling. To minimize errors from various sources (human error, DLS error etc.), the experiments of these entries were done in duplicates, and the fitted parameters were averaged and reported. To reduce the number of regressed parameters, many of these model input parameters required such as C_∞ and r_f were either obtained or calculated from various literature source in order to obtain reasonable model fit which is consistent with the physical properties of swollen P4VP network (Table 5.11). The solute radius r_s was estimated from the self-diffusion coefficients of $PdCl_4^{2-}$ (Table 5.7) because the fraction of cationic species such as Pd^{2+} is low in hydrochloric acid media, and the major Pd(II) species are anionic

chloropalladates, i.e. $\left[PdCl_n\left(H_2O\right)_{4-n}\right]^{2-n}$ (Ruiz *et al.*, 2000). The degree of ionization (α) of P4VP nanoparticles is dependent on the degree of crosslinking (i.e. [DVB]) (Dupin *et al.*, 2006), and therefore the respective values for each ranges of porosity were obtained from the experimental pH-titration curves (see Figure 4.2 of Chapter 4).

The experimental curves of D_{eff}/D_0 versus φ along with other model fits are shown in Figure 5.9. Even though the correlations (R^2 = 0.5770 for Figure 5.9 (a), and R^2 = 0.6374 for Figure 5.9 (b)) are poor, the model fits from Amsden's electrostatic obstruction-scaling model describe the trend better qualitatively after accounting for polymer network properties (C_∞), degree of ionization (α), relative size of polymer chain and solute (r_f, r_s), as compared to other obstruction models. Moreover, the values of scaling constant fitted (k_s) are close to that of other polymer-solute system, in terms of the order of magnitudes. For instance, Amsden *et al.* (2002) reported values of ca 36 $Å^{1.5}$ in crosslinked poly(acrylic acid) gel; whereas in another work, a value of 78 $Å^{1.5}$ for diffusion of bovine serum albumin (BSA) in calcium alginate hydrogel was reported (Amsden, 2001). The smaller value observed herein might be explained by the intrinsic difference of swollen P4VP network from other polyelectrolyte gel, as well as the uncertainties or errors in estimating C_∞ for P4VP networks at various pH. Besides, the porosity estimation using D_{DLS} data itself is at best an approximation to the real values, because of the large uncertainty in size measurement of large, water-filled swollen particles based on DLS principles. A better correlation might be achievable by having a more accurate value of these physical parameters input to the modeling.

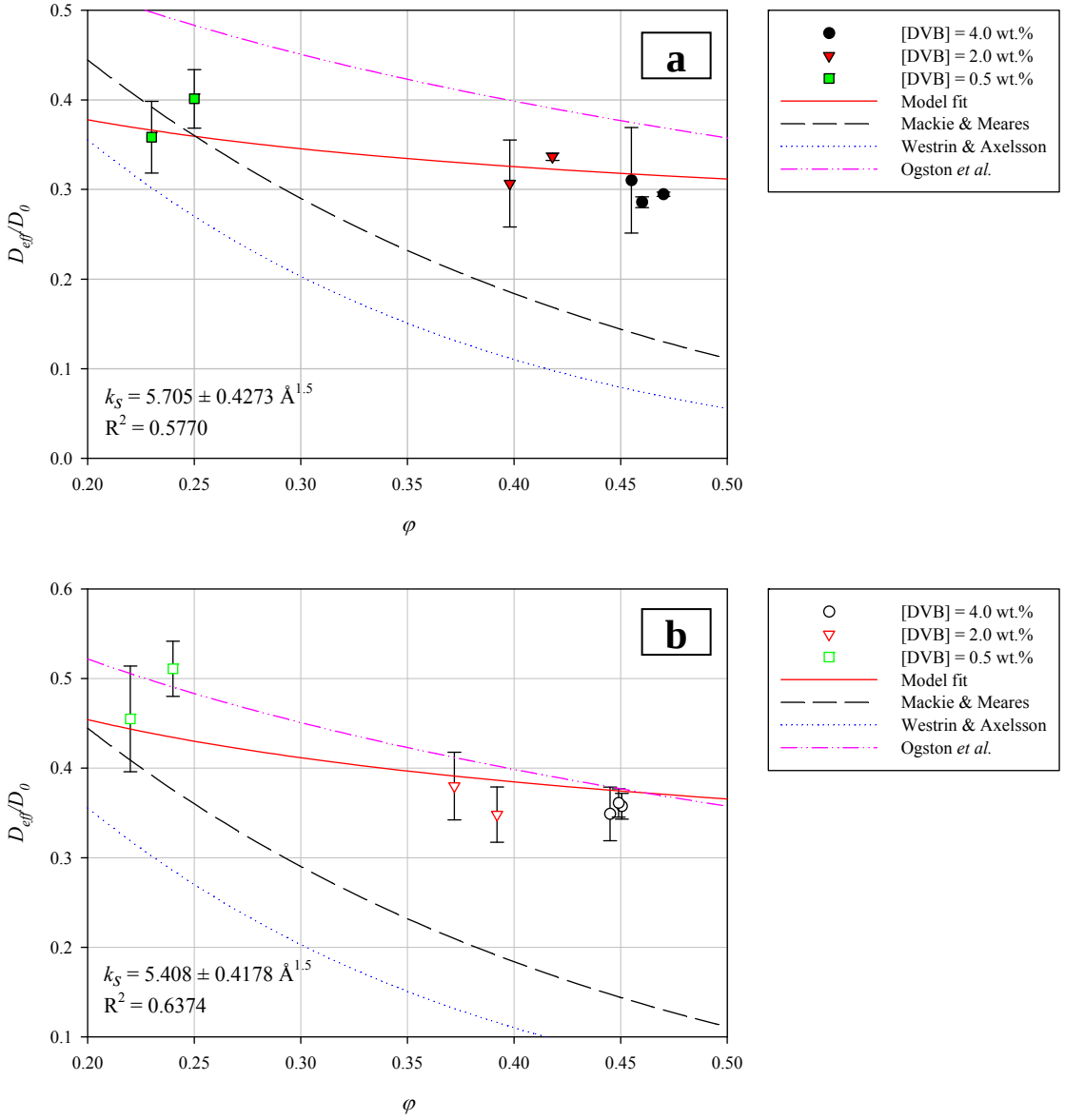

Figure 5.9 Plot of normalized diffusion coefficients for (a) pH 3 and (b) pH 1, fitted from adsorption kinetic data, versus polymer fraction (φ) along with various obstruction models. The solid red line is the model fit obtained using Amsden's model, whereas other lines plotted are calculated from the Mackie and Meares' model (long dash, black line), Muhr and Blanshard's model (dotted, blue line) and Ogston's model (pink, dash-dot line).

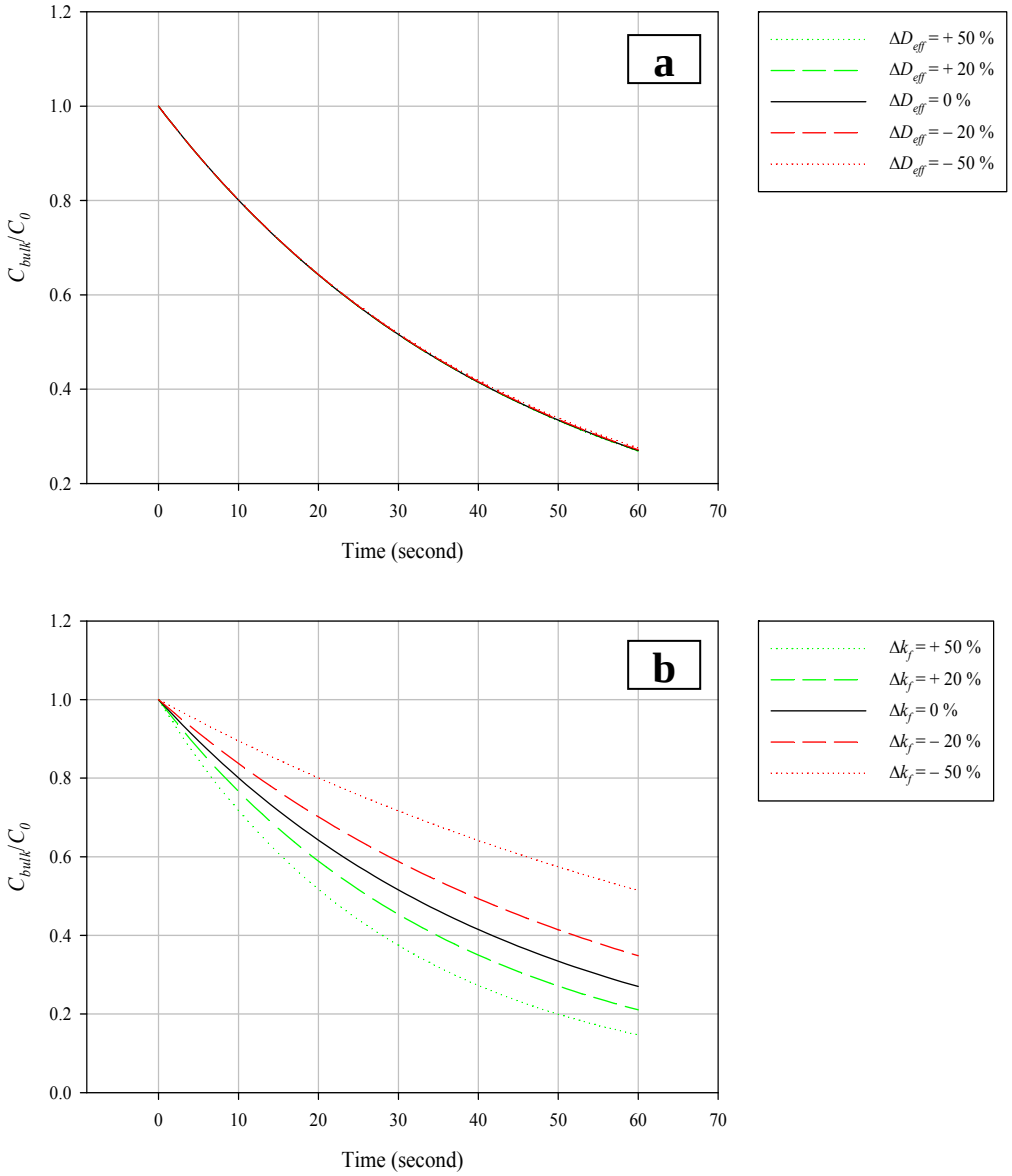

Figure 5.10 Sensitivity analysis of the fitted parameters (D_{eff}, k_f) using 2-*p* model. The simulated data is obtained from entry 1 of Table 5-6. The values of the model parameters are: $\varepsilon = 0.551$, $D_p = 0.5721 \times 10^{-6}$ cm^2/s, $k_f = 0.006471$ cm/s, $C_0 = 0.103$ mM. Each fitted coefficient is perturbed by ± 50 % and ± 20 %, where the simulated curves for perturbed D_{eff} and k_f are plotted in (a) and (b). The simulation was conducted using time interval of 1 second, i.e. 60 points per curve (excluding the point at time 0).

5.3.5 Sensitivity Analysis

To compare the relative importance of pore diffusion and film diffusion to the Pd(II) adsorption kinetic, a sensitivity analysis of the fitted coefficients (D_{eff}, k_f) was carried out. Each fitted coefficient was perturbed by ± 50 % and ± 20 %, and the simulated scenarios are plotted in Figure 5.10. For D_{eff}, the concentration curves display little

changes upon perturbation; whereas large variations in simulated curves are observed for k_f. This drastic difference implies that k_f yields greater influence among the two parameters. A slight change in k_f would result in noticeable difference in the Pd(II) adsorption kinetic. In other words, the film diffusion resistance is undeniably larger than that of pore diffusion, in line with the predicted features for ion-exchange reaction in resins of very small size by Helfferich (1962). By making the particles smaller, the pore diffusion resistance would eventually vanish as a result of shorter diffusion path length, and a switch in rate-determining step for the adsorption to take place.

5.4 Conclusion

Following Chapter 3 and Chapter 4, this chapter aims to reveal more insights into the mass transfer phenomenon involved during Pd(II) adsorption. The Pd-induced deswelling data from Chapter 3 was revisited, as analyzed along with the adsorption kinetic study. During "static adsorption", the volume transition (deswelling) as well as the diffusive penetration of metal ions through the P4VP polycationic network occurs simultaneously, though on a different rates. Deswelling of P4VP typically finishes within seconds ($\tau_{deswell}$ < 10 seconds in this work) or even tens of milliseconds (Yin *et al.*, 2008) for polymeric nanoparticles (or microgel particles) of colloidal sizes; whereas the entire Pd(II) adsorption would last more than 50 seconds, depending on the initial Pd(II) concentration and the solution pH. The estimated value of dimensionless Deborah number is less than unity, indicating that the palladium adsorption kinetics were diffusion-controlled rather than swelling-controlled (or deswelling rate of the P4VP network).

The kinetics of Pd(II) adsorption in stirred tank was investigated systematically wherein various experimental parameters (such as solution pH) were varied, and the resulting data were fitted to either the intraparticle diffusion (IPD) model (1-*p* model) or combined diffusion model (2-*p* model). Regression analysis with the IPD model that only accounts for intraparticle diffusion resistance yielded unrealistic diffusion coefficients; however the 2-*p* model fitted the Pd(II) adsorption process, as supported by evaluating the goodness-of-fit and the *F*-test. Modeling of the adsorption kinetic data also revealed that the adsorption process obeyed Fickian's laws of diffusion, which validates that, the deswelling was in fact more rapid than the adsorption process. The resistance of film diffusion should at least equal to or be greater than the pore diffusion resistance. The retardation effect observed for the Pd(II) diffusion coefficients fitted can be described qualitatively by the electrostatic obstruction-scaling model of Amsden (2001). The adsorption modeling approach described here can be generalized to other solute-adsorbent systems in order to quantify the retardation factor that governs the physical system. The OCFE computation algorithm can be readily implemented and is extendable to any physical processes which involve abrupt changes or steep slopes, yielding accurate numerical solutions (Finlayson, 1980).

CHAPTER 6

MEMBRANE FILTRATION SEPARATION OF THE PREPARED P4VP NANOPARTICLES AND THEIR FOULING BEHAVIORS

6.1 Introduction

The P4VP or P4VP-based nanoparticles showed good adsorption performance and fast sequestration kinetics for Pd(II), as presented in Chapter 4 and 5. In addition, the mechanical robustness of the prepared nanoparticles was extensively investigated in Chapter 3, in terms of their colloidal stability against coagulation/flocculation, and morphological stability against cyclic change in solution pH. However, the nanoparticles need to be effectively separated from the treatment process after use because of their possible environmental and health impact. Furthermore, it would be more economical to recover the nanoparticles for regeneration so that they can be reused in multiple cycles of adsorption-desorption processes. One solution is to augment the batch adsorber with membrane separation capability, similar to the MEUF and the DEUF processes described earlier.

The proposed system comprises five major steps, which can be operated in batch mode (see Figure 6.1). In Step 1 ("Adsorption"), the highly swollen P4VP-based nanoparticles that are narrowly-distributed in size and shape (see Chapter 3) are mixed with the Pd(II)-laden aqueous solution, and mixed for a reasonable length of time, to concentrate the chloropalladates to be separated from the feed (see Chapter 4). The adsorption equilibrium would usually be achieved typically after a few minutes, or maximally not more than 5 minutes for Pd(II) adsorption as shown in Chapter 4. In Step 2 ("Filtration-1"), the filtration of the Pd(II) adsorbed nanoparticle suspension is commenced, with a membrane with a smaller pore size that allows full retention of the nanoparticles. The Pd(II)-free solution is removed as permeate. In Step 3 ("Desorption"), the filtration is stopped and the Pd(II) adsorbed nanoparticles are treated with acidified thiourea solution (see Chapter 4) to regenerate the nanoparticles

and desorb the Pd(II). In Step 4 (“Filtration-2”), another run of filtration is used to separate and retain the regenerated nanoparticles, while the highly concentrated Pd(II) solution exits as permeate for recovery. In the final step (“Conditioning”), the nanoparticle suspension is re-conditioned, for instance, pH-adjustment. Lastly, the entire process starts all over from Step 1 to treat the next incoming batch of feed stream. The proposed process was conducted for investigating the palladium recovery with the P4VP nanoparticles, as demonstrated in Chapter 4.

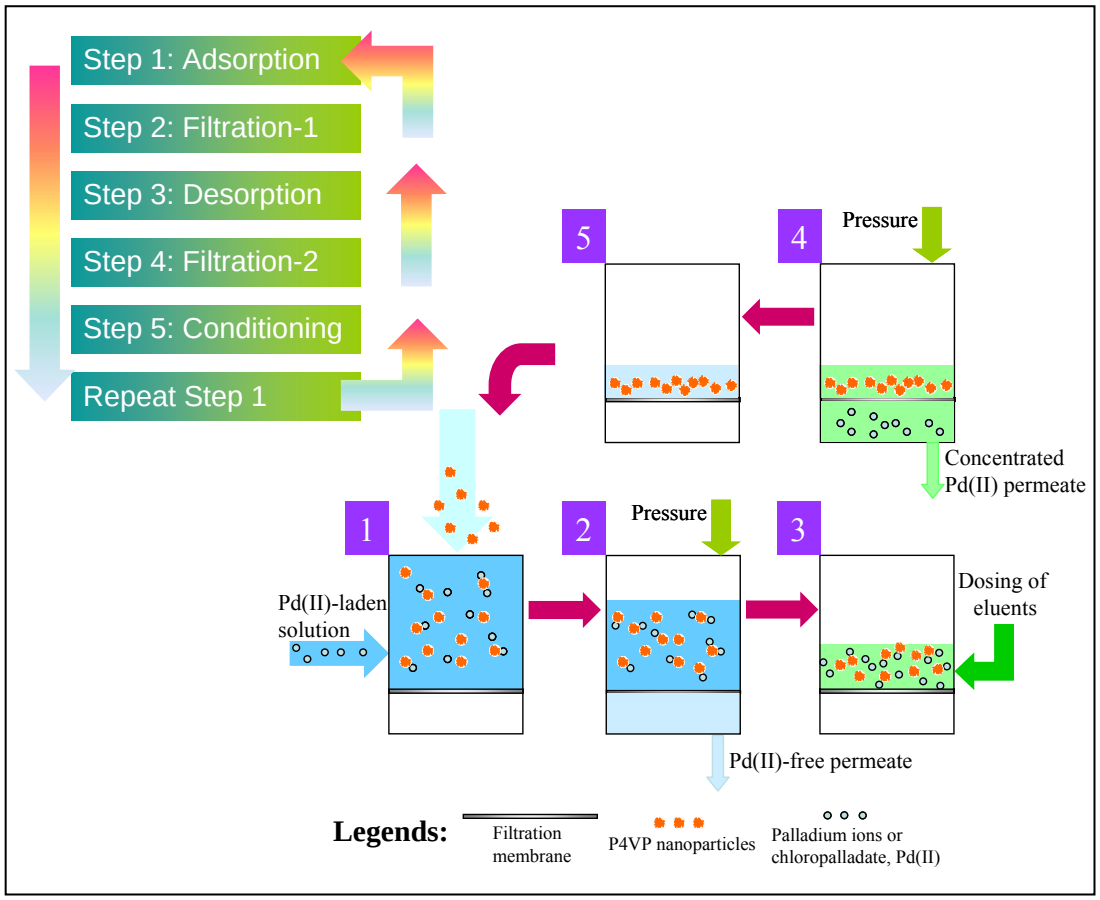

Figure 6.1 A schematic illustration of the hybrid adsorption-filtration process for adsorption and recovery of Pd(II) with P4VP-based nanoparticles.

In this study, highly uniform P4VP-based nanoparticles were successfully prepared. Hence, it is feasible to fully retain and separate the nanoparticles by selecting a membrane made of appropriate material, with a pore size smaller than the average

particle size of the nanoparticles used. When the nanoparticles are polydispersed in size, there is high chance for the smaller nanoparticles to be pulled into the membrane pores by the permeation drag, resulting pore blocking or plugging. This type of membrane fouling is often irreversible, and the extent of pore plugging can only be partially alleviated by energy-consuming cleaning technique, such as backwashing/flushing etc. (Hilal *et al.*, 2005). In this chapter, a commercially-available asymmetric-type membrane made of mixed cellulose ester (MCE) was selected and two types of monodispersed P4VP nanoparticles of different sizes were used. The separation/recovery efficiency of these two types of nanoparticles was investigated and their possible impact on the membrane fouling was examined. The fouling mechanisms caused by respective type of nanoparticle suspensions were identified and comparatively analyzed.

6.2 Materials and Methods

6.2.1 Materials

Membranes. A commercially available mixed cellulose ester (MCE) MF membrane (VCWP04700, Millipore) was chosen in this work. The membrane material consists of a mixture of cellulose acetate and cellulose nitrate, which render the membrane hydrophilic. The nominal pore size of the membrane is 0.1 μm, as rated by the manufacturer. Other specifications of the membrane from the manufacturer are summarized in Table 6.1. Each membrane disc (outer diameter = 47 mm) was trimmed down to a final diameter of approximately 43 mm that fitted the filtration cell used in the filtration experiments.

Table 6.1 Specifications of the MF membrane used in this work

Parameter	Value
Filter material	Mixed cellulose ester
Porosity	74%
Membrane thickness	105 μm
Membrane diameter	47 mm
Membrane pore Size	0.1 μm (manufacturer's pore rating)
Water flow rate (@ 10 psig)	1.5 ml/(min-cm^2)
Maximum operating temperature	55 °C
Bubble point at 23°C	≥ 14.1 bar, with air and water
Wettability	Hydrophilic
Membrane filter color	White
Membrane surface	Plain

Poly(4-vinylpyridine) nanoparticles. The two nominal sizes of the P4VP nanoparticles prepared and used in the filtration experiments are 250 nm and 60 nm. The pristine nanoparticles of 250 nm (denoted as P4VP250 in later sections) were prepared according to the SFEP method as described in Chapter 3 (Run A-2 of Table 3.1). The P4VP nanoparticles of 60 nm (denoted as P4VP060) were however impossible to obtain from the developed SFEP method without the use of PEGMA, which may complicate the subsequent analysis. To prepare NP060 without the aid of PEGMA, the nanoparticles were synthesized via a standard emulsion polymerization procedure (Lovell and El-Aasser, 1997). The experimental protocol was similar to that of Run A-2 of Table 3.1, except that 0.128 gram of cetylpyridinium chloride (CPC) was injected into the water before the monomer mixture was added. These nanoparticles were solely electrostatically stabilized (45.6 ± 3.2 mV and 49.1 ± 4.4 mV for P4VP250 and P4VP060 respectively, as measured by the ZetaPlus), and the effective hydrodynamic diameters (D_{DLS}) of the nanoparticle suspensions were measured using dynamic light scattering (DLS) with ZetaPlus-90PLUS, to check for their size monodispersity.

6.2.2 Characterization of Nanoparticles and Membranes

The shapes and morphologies of the as-prepared P4VP nanoparticles was observed with a field emission scanning electronic microscope (FESEM, JEOL, JSM-6700F, Japan). The sample preparation protocol for nanoparticle observation was described in Chapter 3. The structural characteristics and morphologies of surface and cross-section of the clean and fouled membranes were also examined. The clean membrane samples were prepared from the new, unused membrane. The fouled membrane samples were obtained from some selected filtration runs. The clean membrane was first soaked in ultrapure water to remove any residual wetting agents. The fouled membranes were first gently rinsed with dust-free, ultrapure water. Dry membrane samples were obtained by placing the selected membranes in a dessicator for more than 24 hours or till completely dried. Each piece of dried samples was carefully cut into a size that fits the FESEM observation stub and mounted onto the stub with double sided carbon tape. For the cross-section samples, liquid nitrogen was used to break up the wet membranes so as to minimize damages to the membrane structure (Ferlita *et al.* 2008). A sample with relative uniform edges was selected for the FESEM analysis. In addition, thin stripes of copper tape were placed on top of the cross-section samples to reduce sample charging. All samples were sputtered with platinum under a high vacuum condition before the FESEM observation. The FESEM micrographs of the surface of the clean membrane was analyzed with an image analysis software, *ImageJ* (MacBiophotonics *ImageJ*, Version 1.41n), to estimate the surface pore size of the membrane.

6.2.3 General Filtration Protocols

The set-up of the dead-end filtration system used for the nanoparticle filtration in this work was described earlier in Chapter 4. The schematic illustration of the set-up was shown in Figure 6.2. The effective filtration area of the filtration cell has been reduced to 1.18×10^{-3} m^2. All experiments were conducted at room temperature (22 ± 2 °C). The cumulative filtrate weight was measured by an electronic balance with an accuracy of 0.0001 g (PRECISA XT220A), and the data was recorded by a computer. The filtration cell and the pressurized reservoir were initially filled up with ultrapure water. The membrane was first soaked in the ultrapure water for 30 minutes to allow complete wetting of the membrane. Then, the membrane was placed in the filtration cell and compacted with the ultrapure water at 200 kPa (29.0 psi), until a steady permeate flux was obtained (usually overnight). Membrane compaction was conducted to maintain a relative constant hydraulic permeability of the membrane disc for the nanoparticle filtration later, as some studies have shown that pressure compaction of a fresh membrane would result a significant decrease (as much as 40 %) in the membrane permeability (Tarnawski & Jelen, 1986; Persson *et al.*, 1995), due to the reorganization of the polymeric fibrous structure under pressure (Zeman and Zydney, 1996). The ultrapure water in the reservoir was then quickly replaced with the P4VP nanoparticle suspensions. The filtration experiment was then commenced (operating pressure = 68.9 kPa, i.e. 10 psi) and the permeate weight-time data was continuously recorded at every ten seconds. Unlike that of Chapter 4, no magnetic stirring was used in this chapter. The filtration was stopped after running for a few hours or when the flux decline had ceased. At the end of each filtration run, the entire system was thoroughly flashed with ultrapure water to eliminate any nanoparticles remaining in the system and prevent cross-contamination in between successive

filtration runs. The nanoparticle suspension for each filtration run was freshly prepared before the experiment. Ultrapure water was used to adjust the suspension concentration when needed. For each filtration run, the concentrations of the nanoparticles in the feed suspension, filtrate or permeate and filtration retentate (concentrate) were quantified by measuring the suspension turbidity (absorbance at wavelength of 500 nm) with a UV/VIS spectrophotometer (HP Agilent 8453). For accurate quantification, the spectrophotometer was calibrated by measuring the UV/VIS absorbance values for a series of P4VP nanoparticle suspension of different concentrations. The correlation coefficient for the calibration curves was typically above 0.995.

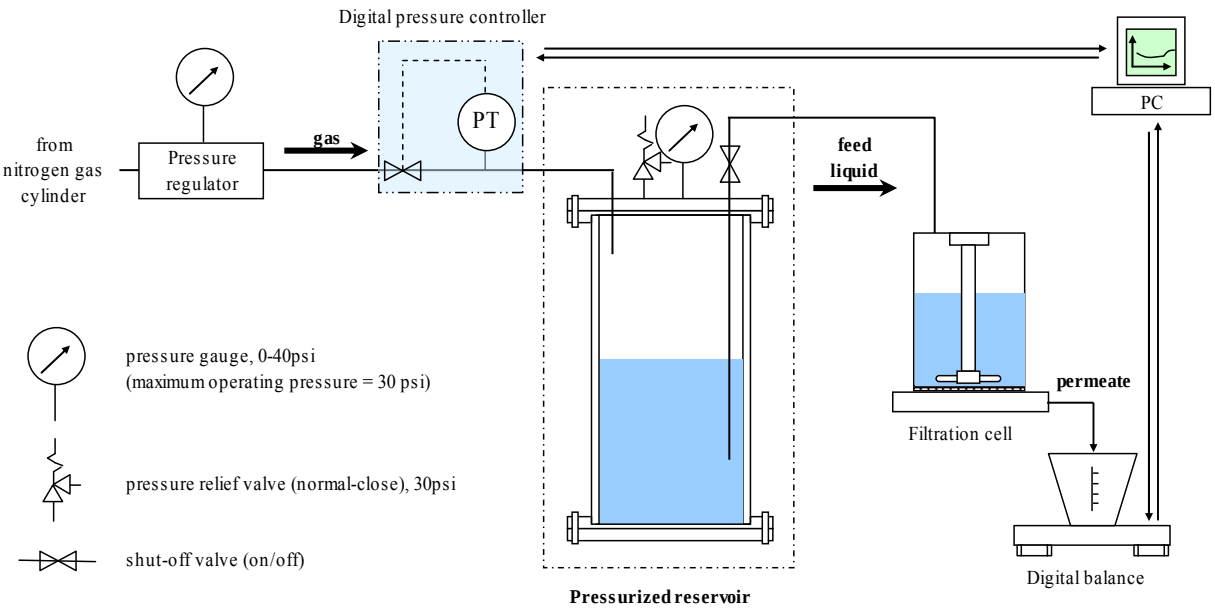

Figure 6.2 Schematic illustration of the filtration system used in this study.

6.2.4 Dead-end Filtration of Monodispersed Nanoparticle Suspensions.

All the filtration experiments were carried out under the same conditions (temperature, transmembrane pressure, pH and ionic strengths etc.), except that the particle sizes and particle concentrations were varied. Fresh membranes were used for each filtration run. The duration for each filtration run was typically 2 hour. During the

filtration of the nanoparticles suspension, the permeation flux would reduce gradually due to membrane fouling. An amount of 200 ml of the nanoparticle suspension with a selected concentration was freshly prepared before each filtration run. The clean membrane was firstly compacted with ultrapure water at a transmembrane pressure of 200 kPa (29.0 psi) until a steady flux was achieved. The flux recorded was taken as the membrane pure water flux and used to calculate the clean membrane resistance (R_m). The filtration cell was then disassembled, and the compacted membrane was visually inspected to check for any crack on the membrane. If any crack was found on the membrane, the membrane was replaced with a new piece and underwent compaction again. After inspection, the filtration cell was reassembled, and the freshly prepared nanoparticle suspension was placed in the reservoir. The filtration was then commenced. After each filtration run, the amount of the retentate in the filtration cell was measured gravimetrically. The concentrations of nanoparticles in the filtrate, retentate and the feed suspension were quantified as described earlier.

6.2.5 Filtration Data Processing

Reliable and accurate data post-processing method is crucial for performing flux calculation from experimental filtration data (Bowen and Williams, 2001). The data-collection program coded using LabVIEW® recorded the filtration data in term of the time (*t,* second or minute) and corresponding weight of the cumulative filtrate or permeate (*V*, gram or milliliter) collected during the filtration process. A data post-processing method to obtain other information, such as, flow rate and flux, was also coded. To remove any errors or noises from the recording system, several data smoothing algorithms (Pearson, 1986) such as 5 points moving average, were evaluated in this study. During the filtration, the flux continued to decrease as

membrane fouling occurred. Therefore, the first derivative of the cumulative volume, i.e. dV/dt, should continuously decrease. The second derivative, d^2V/dt^2 should diminish and approach to zero when the filtration reached steady state, i.e. the permeate flux acquired stable value. To capture these features accurately, a data-smoothing procedure that is based on penalized spline-approximation (Eilers and Marx, 1996) was chosen and coded for the experimental data processing (MATLAB®, R14SP3, The MathWorks, Natick, Massachusetts).

6.3 Results and Discussion

6.3.1 Membrane Surface, Morphology and Hydraulic Permeability

In the literature, it has been reported that the mixed cellulose ester (MCE) membranes have a fibrous network structure resulting in interconnected pore morphology with a board pore size distribution on the upper surface (Ho & Zydney, 1999). Both sides of the MCE membrane used in this study were observed by FESEM, with results as shown in Figure 6.3 (a) & (b). The FESEM micrographs clearly show that the morphology of the two surfaces was very different from each other, with much larger pore sizes on the bottom surface. Furthermore, the FESEM micrograph of the upper surface of the clean MCE membrane displayed no fibrous network structure. This unique asymmetric structure should contribute to its size-separation selectivity for the MCE membrane filter.

Conventional MF membranes can be categorized into two types: screen filters and depth filters. Screen filters have straight-through pores and all particles of particle size larger than the pore size are retained, whereas smaller particles could freely pass through the pores. On the other hand, depth filters are often characterized by a random,

tortuous porous structure and the particles are retained by interception or adsorption with the bulk porous network in the filter (Huisman, 2000). Depth filters usually has a higher 'dirty-handling' capacity due to their large interstitial spaces and voids as compared to screen filters. The retention of smaller particles by the depth filters are not uncommon (Block, 2001). Most of the polymeric microfiltration membranes are depth filters that consist of an isotropic network of polymer fibers, resulting in a highly interconnected pore structure and a fairly board distribution of pore sizes throughout the membrane (Ho & Zydney,1999).

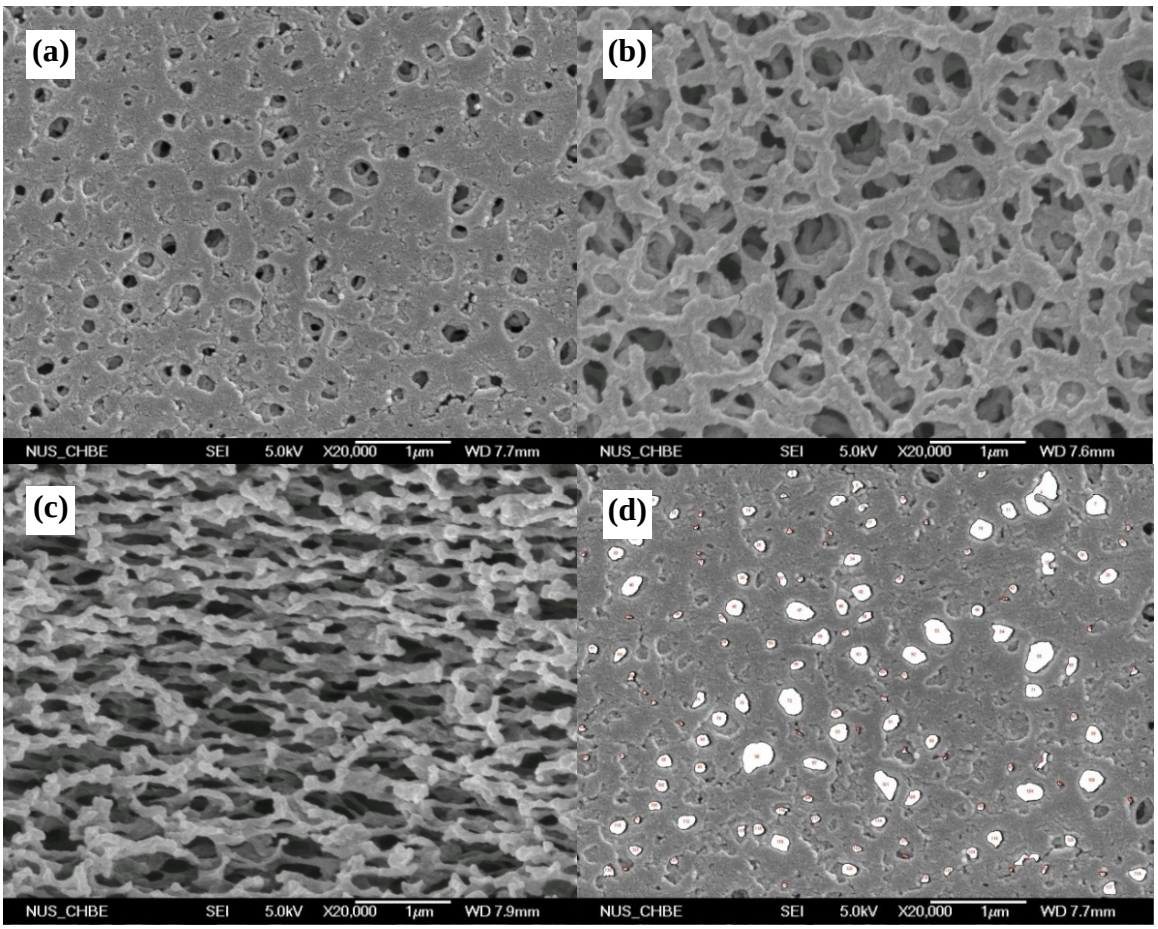

Figure 6.3 FESEM micrographs of the surfaces of the clean MCE membrane used in this study: (a) the upper surface, (b) the bottom surface, (c) the cross-section view (c), and (d) the top surface analyzed with *ImageJ*.

Though most current microfiltration processes employ homogenous (symmetric) depth-type membranes, there is growing interest in the use of asymmetric membranes. This is particularly true for particle removal applications in semiconductor industry and virus clearance in biopharmaceutical applications (Zeman & Zydney 1996). The IUPAC definition for asymmetric membrane refers to membranes which are constituted of two or more structural planes of non-identical morphologies (Koros *et al.*, 1996). Asymmetric membranes have a very thin and dense skin layer which serves as the selective barrier for incoming particles, and a much thicker porous substrate that provides the necessary mechanical stability. This asymmetric structure allows much greater hydraulic flow through the porous substrate. The fibrous structure with interconnected pores of the MCE membrane can be more clearly observed from the cross-section view of the membrane, as shown in Figure 6.3 (c). To assess the pore size distribution of the surface pores present on upper surface (Figure 6.3 (a)), the automated particle/hole counting algorithm of the *ImageJ* program was used. As shown in Figure 6.3 (d), most of the surface pores was detected and marked as white spots. The representative analysis result from the *ImageJ* analysis is shown Figure 6.4.

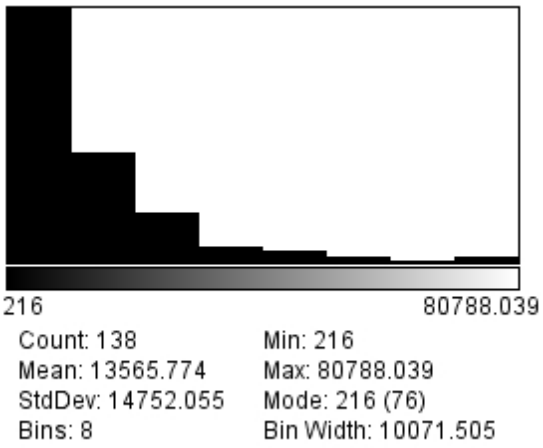

Figure 6.4 The representative surface pore area distribution as calculated by *ImageJ*.

The MCE membrane has a pore size rating of 0.1 μm (Millipore, 2009). From the pore area distribution plot in Figure 6.4, there are 138 surface pores detected on this micrograph. The maximum pore area was 80788.039 nm^2 and the minimum pore area was 216 nm^2, indicating a large polydispersity. More than half of the surface pore areas are in the range of 216 nm^2 to 10287 nm^2. The average surface pore area was given as 13565.664 nm^2, thus leading to a mean surface pore size of 150 nm or 0.15 μm (pore size = $[(4 \times \text{surface pore area})/\pi]^{1/2}$). The estimated average surface pore size is 50% larger than the rated pore size of 0.1 μm.

Secondly, the MCE membrane was shown to possess a fairly board range of surface pore on the upper surface, which essentially serves as the selective layer during the filtration. The smallest measured pore size was 0.02 μm, while pore size as large as 0.32 μm could be detected as well. Hence, it is difficult to define a single pore size for the MCE membranes used in this work. Nevertheless, it may be expected that particles of larger sizes than the membrane pore sizes cannot pass through the membrane, while those smaller may plug the pores directly upon permeation, or pass through the membrane pores. Therefore, the relative size ratio of the nanoparticles and membrane pores can result in different fouling mechanisms in effect.

Before the hydraulic permeability of the membranes was quantified, the membrane was compacted because it was observed that the permeability of the new, freshly trimmed membrane changed significantly after filtration with ultrapure water. A typical set of this experimental phenomenon is shown in Figure 6.5. As shown, the effect of membrane compaction effect is quite substantial for the MCE membrane used in this work. To assess the compressibility of the MCE membrane, more than 10

pieces of the membranes were compacted at 200 kPa (29 psi) for at least 24 hour, until steady ultrapure water flux (at 68.9 kPa or 10 psi) were observed. The results of the membrane compaction study showed that the mean steady ultrapure water flux is about 1.7×10^{-5} m^3/m^2-s or 62 L/m^2-h (ΔP = 68.9 kPa) (the membrane hydraulic resistance, $R_m \sim 4.6 \times 10^{12}$ m^{-1}) (Figure 6.6). Consequently, it was then assured that steady ultrapure water fluxes could be obtained by the membrane compaction protocol used. The values of all the steady state pure water flux obtained were well within ± 20 % of the average value.

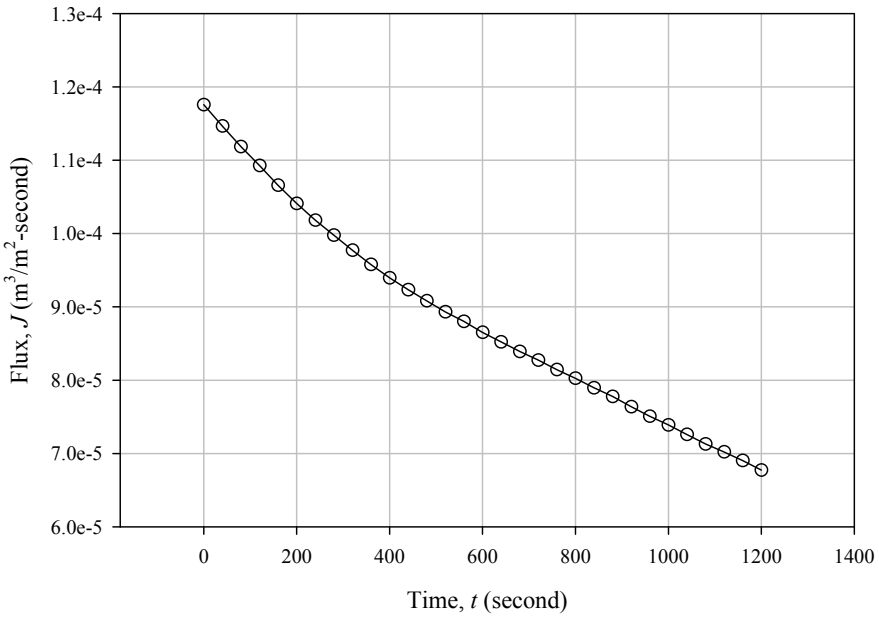

Figure 6.5 Typical ultrapure water flow rate during first 20 minutes of filtration (ΔP = 68.9 kPa).

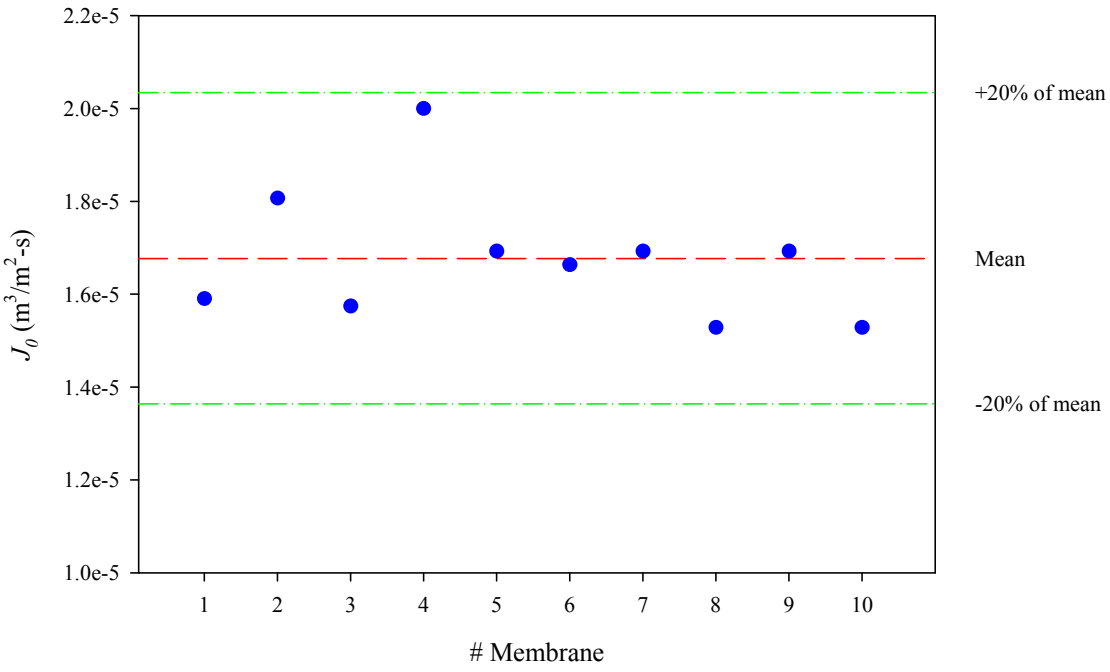

Figure 6.6 Plot of steady state clean water flux for 10 pieces of the membranes used in this work.

6.3.2 Membrane Filtration Behavior by Monodispersed Nanoparticle Suspensions

In membrane filtration processes, feed streams usually contain particles or colloids of various sizes. The occurrence of fouling phenomena, such as pore constriction, pore blocking and cake formation are greatly dependent on the particle sizes or distributions relative to the membrane pore size (Wakeman, 2007). Several fouling phenomena can occur simultaneously (Ho and Zydney, 2000; Yuan, 2001). A transition in fouling mechanism during filtration processes may occur (Tracy and Davis, 1994; Chan and Chen, 2004). All these complication resulted in difficulty to identify the dominant fouling mechanisms with respect to different particles sizes (Duclos-Orsello *et al.*, 2006). The primary objective of this part of the study was to investigate whether the nanoparticles can be effectively separated with a selected membrane and what the fouling phenomenon will be. The study was first conducted with the monodispersed nanoparticles (P4VP060 and P4VP250, see Figure 6.7) in suspensions of different concentrations. This study would provide some information

on more complicated cases where the nanoparticle suspensions are polydispersed for future study.

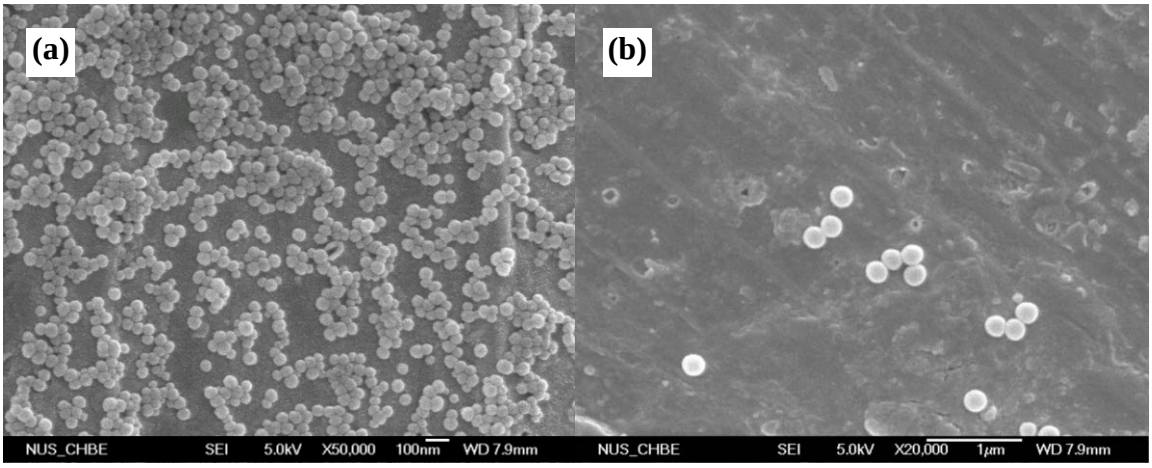

Figure 6.7 FESEM micrographs of the P4VP nanoparticles used in this work: (a) P4VP060 and (b) P4VP250.

The two types of P4VP nanoparticles prepared, i.e. P4VP060 and P4VP250, as shown in Figure 6.7, were spherical and uniform in size, in agreement with the results reported in previous chapter. The effective hydrodynamic diameters and the polydispersity index (μ) of the P4VP nanoparticle suspensions prepared are as follow: for P4VP250, D_{DLS} = 248.9 ± 5.2 nm, μ = 0.009; for P4VP060, D_{DLS} = 63.5 ± 3.1 nm, μ = 0.014. The polydispersity index measured for these nanoparticles are smaller than 0.020, indicating that the nanoparticles can be regarded as monodispersed. They were electrostatically stabilized with positive ζ -potential and made of the same chemical compositions. Therefore, the only essential difference between the two types of the nanoparticles was their physical dimensions. These two types of nanoparticles were used to demonstrate their different separation efficiency and fouling mechanisms. The dominant fouling mechanism for the smaller nanoparticles was expected to be led by internal fouling first, followed by cake filtration. Complete retention of the larger

nanoparticles was however expected, and cake formation should be the dominant fouling mode.

6.3.2.1 Separation/Rejection Efficiency

To determine whether the asymmetric MCE membrane is effective in recovering or separating the two types of nanoparticles, a series of filtration experiments were conducted as a function of nanoparticle concentrations in the feed suspensions. To assess the rejection performance, mass balance analysis was performed after each filtration run, and the results were tabulated in Table 6.2.

Table 6.2 Summary of nanoparticle concentrations measured for various nanoparticles suspensions and rejection percentages after each filtration.

	Feed Suspension		Retentate*		Filtrate**		Rejection$
	Volume (ml)	Concentration (ppm)	Volume (ml)	Concentration (ppm)	Volume (ml)	Concentration (ppm)	(%)
P4VP060	200	111.23	75	213.82	96.98	1.26	99.38%
	200	504.37	29	974.18	89.97	1.31	99.8%
	200	1042.55	80	1346.53	82.1	2.28	99.9%
P4VP250	200	113.86	62	312.5	129.01	0	100%
	200	567.41	66.5	845.94	102.31	0	100%
	200	1241.73	73	1526.27	83.96	0	100%

*: retentate refers to the suspension in the filtration cell.
**: Filtrate refers to the permeated suspension collected in the beaker on the digital balance.
$: Rejection (%) = $1 - \frac{residual\ nanoparticles\ in\ filtrate}{total\ nanoparticles\ in\ feed}$

The MCE membranes had a high separation or rejection efficiency for both types of the nanoparticles. The rejection percentages for the small P4VP060 nanoparticles were well above 99% and that for the large P4VP250 nanoparticles were essentially 100%, under all the three concentrations tested for each type of nanoparticles. The UV/VIS absorbance measured from the filtrates from P4VP250 filtrations were as low

as 10^{-3} A.U. in magnitude, which was well below the instrumental detection limit of the spectrophotometer. To cross-check whether any fugitive P4VP nanoparticles may have passed through the membrane, the filtrates were centrifuged to concentrate the nanoparticles if any, and the UV/VIS absorbance was measured again. Therefore, the rejection of P4VP250 was believed to be 100%. It should be noted that for full retention of nanoparticles, the pore diameter should be smaller than the particle diameter, as demonstrated in Table 6.2. The rejection of P4VP060 by the membrane was almost complete even though the membrane pore size was much larger than the nanoparticles. This could be attributed to the unique asymmetric structure of the MCE membrane which acts effectively as a depth filter. Upon entering the membrane pores, P4VP060 nanoparticles were captured by the tortuous networks as shown in Figure 6.3 (c).

6.3.2.2 Filtrate Volume versus Filtration Time

Figure 6.8 showed the experimental data for cumulative filtrate volume as a function of filtration time under the constant pressure, unstirred, dead-end filtration mode for different concentrations of (a) P4VP060 and (b) P4VP250. The filtrate volume was almost linearly increased with filtration time at very short time when the filtrations were just started ($t \leq 1000$ s), but decreased with the feed concentrations. As the filtration processes continued, the curves diverged after about 1000 s and the cumulative filtrate volume was higher for lower nanoparticles concentration. Given the equal filtration time, the total accumulated filtrate volume were much smaller for filtration of P4VP060, indicating that the membrane fouling was much more severe for the smaller nanoparticles.

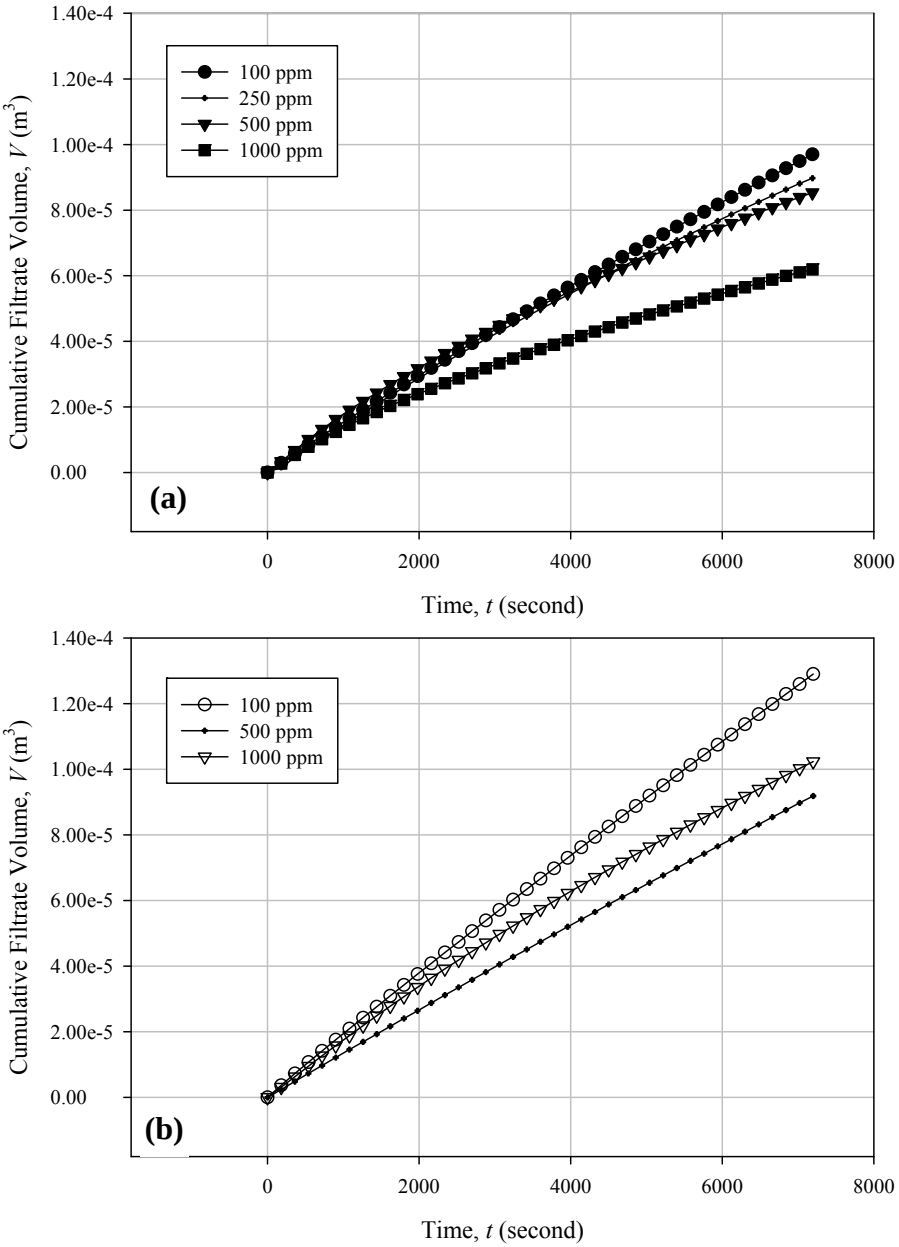

Figure 6.8 Plot of cumulative filtrate volume versus time for (a) P4VP060 and (b) P4VP250 (ΔP = 68.9 kPa).

6.3.2.3 Permeate Flux Ratio (J/J_0) versus Filtration Time

The data in Figure 6.8 were then processed and the values of filtrate flux (J) calculated were normalized to the initial flux (J_0) that was taken to be the steady-state clean water flux obtained prior commencing the nanoparticle filtration. A plot of the normalized flux (J/J_0) is shown in Figure 6.9 for better comparisons.

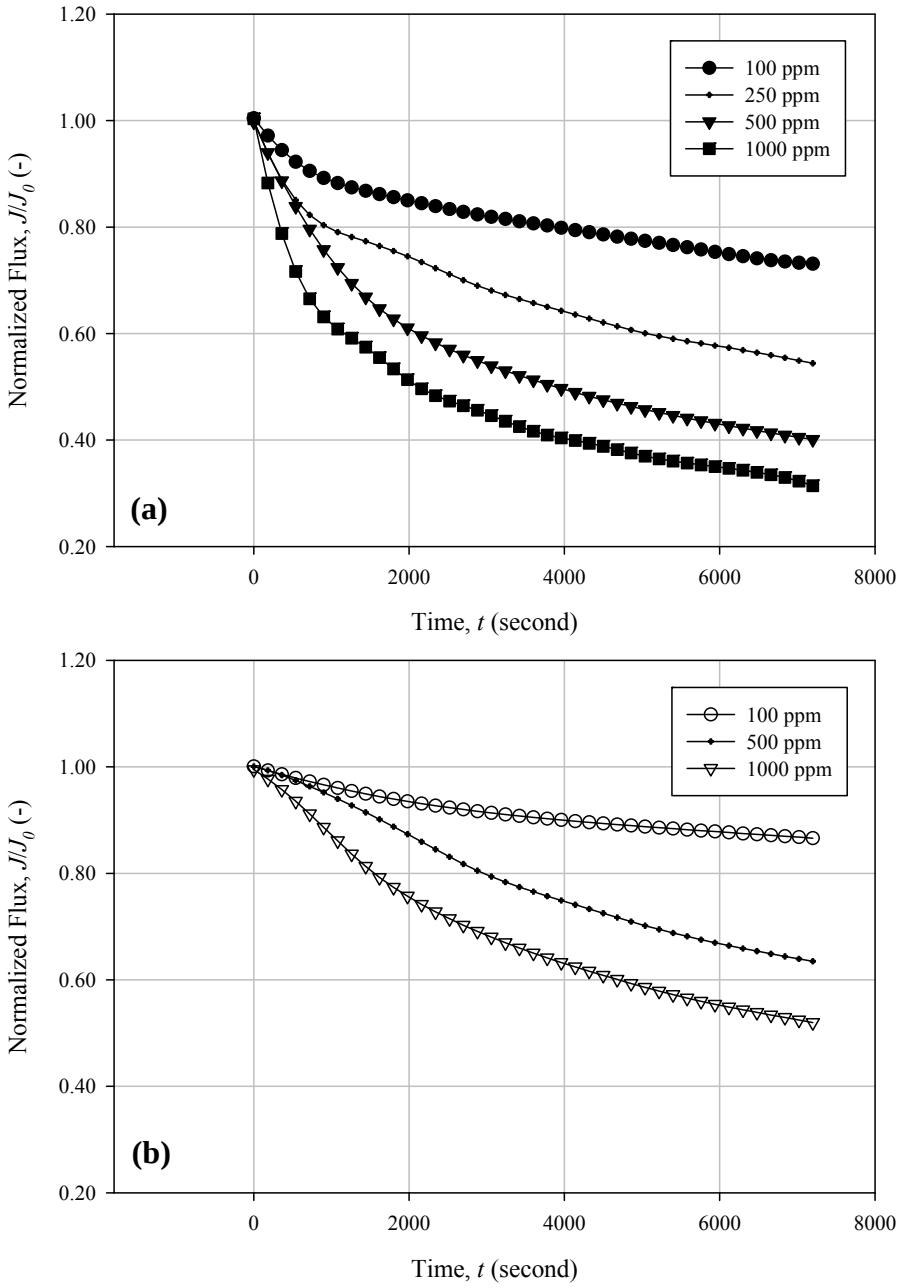

Figure 6.9 Plot of normalized flux versus time: (a) P4VP060 and (b) P4VP250.

For the smaller P4VP nanoparticles (i.e. P4VP060), the flux declined rapidly at the beginning of the experiments, in which the rate of decline increased with increasing nanoparticle concentration. At later times, the normalized flux in each case apparently approached a nearly constant value. In addition, the flux decline was always faster for P4VP060 than for P4VP250, indicating the hydraulic resistance increased at a faster pace for the former. For example, at the nanoparticle concentration of 100 ppm, the

flux decline after 2 hours' filtration for P4VP250 was only about 10%, but for the P4VP060 was more than 20%. Visual inspection of the membrane surface after the filtrations revealed than cake layers were formed in all filtration runs. Hence the difference in flux decline between the two types of nanoparticles may be attributed to the different inherent specific resistance of the cake layers formed in filtration (in addition to the possible pore blocking resistance for P4VP060). The Carman-Kozeny equation states that the specific particle resistance (α) of the cake is inversely proportional to the squared value of particle diameter (Zeman and Zydney, 1996):

$$\alpha = \frac{180(1-\varepsilon)}{\rho_p d_p^2 \varepsilon^3}$$

where ε is the porosity of the cake or particulate assemblage and ρ_p is the density of the particle. Thus, the hydraulic resistance of P4VP060 may be 17 times larger than that of P4VP250 assuming that the cakes formed from each type of nanoparticles have the equivalent porosity. Because of the higher specific cake resistance of P4VP060, the flux decline was logically higher.

6.3.2.4 Plot of Normalized Resistance (R_{total}/R_m)

The membrane fouling during microfiltration of colloids, for instance protein solutions, may switch from pore blockage to cake filtration (Ho and Zydney, 2000). As studied by some researchers (Tracy and Davis, 1994), the filtration flux data can be used to examine the underlying fouling mechanism by re-plotting the data in terms of total resistance, which is the sum of the fouling resistance accumulated during the filtration and the hydraulic resistance of the underneath membrane. The total resistance is defined by $R_{total} = \Delta P/(\mu \times J(t))$, where μ is the viscosity of the solution and $J(t)$ is the instantaneous filtration flux measured at time t. Tracy and Davis (1994)

observed that pore constriction or pore blockage happens when the plot of total resistance as a function of filtration time display concave up in the curve, whereas concave down for cake filtration. The results of the filtration runs were shown in Figure 6.10. The first plot (Figure 6.10 (a)) showed concaving up for all the P4VP060 filtrations during the early stage of filtrations ($t < 1000s$), which was consist with pore constriction or pore blockage mechanisms as proposed. In contrast, the curves at longer time ($t > 2000s$) were concave down, indicated cake filtration at long runs. The second plot (Figure 6.10 (b)); the curvatures of the curves were different from those in the first plot, even though the changes in curvatures were less clearly defined than the first one. The inflection point that connects the concave up and concave down regions indicates the transition in the filtration time where a switch from internal membrane fouling to external fouling such cake formation took place (Tracy and Davis, 1994; Wang and Tarabara, 2008). The inflection points occurred at longer time for filtrations with lower NPs concentrations for both plots, as indicated by the arrows in the plots and summarized in Table 6.3. Nonetheless, the identification of transition points from the total resistance plot seems to be ambiguous and subjective. Hence, the total resistance plot is not an effective way to analyze the transitions in fouling mechanism in this study.

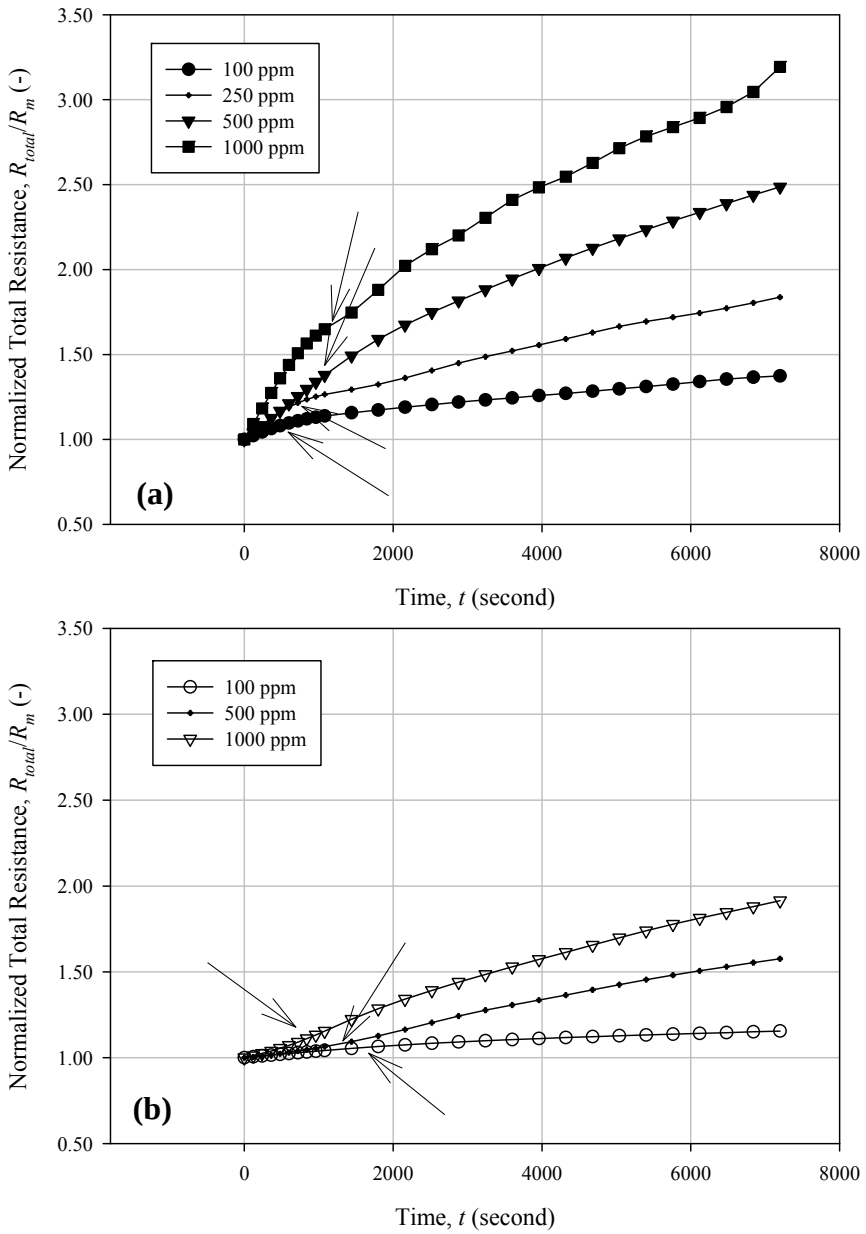

Figure 6.10 Plot of normalized total resistance versus time: (a) P4VP060 and (b) P4VP250.

Table 6.3 Summary of inflection points and R_{total}/R_m values at selected points

		Inflection point (s)	R_{total}/R_m	
			Inflection point	End of filtration
P4VP060	100 ppm	630	1.1	1.4
	250 ppm	840	1.2	1.9
	500 ppm	1000	1.4	2.5
	1000 ppm	1100	1.6	3.2
P4VP250	100 ppm	1700	1.05	1.14
	500 ppm	1300	1.08	1.6
	1000 ppm	700	1.1	1.9

It can be found in Figure 6.10 that the rate of resistance increase by the smaller P4VP060 was much higher than that of large ones (P4VP250) in the early stages. The resistance increased dramatically for the small NPs and the total resistances became more than doubled at the end of the run, whereas the total resistance only increased gradually and was much less for the much larger nanoparticles of P4VP250. The increase in total resistance for the P4VP060 is more likely an additive superimposition of both internal and external fouling. The former refers to pore constriction and pore blockage since P4VP060 are smaller than the pore size rating of the MCE membrane used. Furthermore, some surface pores on the surface are polydispersed as shown earlier, and some of the large pores may have allowed the passage of these small nanoparticles. The external fouling usually refers to the formation of cake layer. Many modeling studies have shown that the structure and formation of cake layer are a complex function of many parameters, such as ionic strength, pressure, temperature, solvent dielectric permittivity, etc. (Kim and Hoek, 2002; Kim *et al.*, 2006). ζ-potential plays a significant part in influencing the cake layer's volume fraction in this case. The greater ζ-potential yields a lower cake fraction (i.e. higher porosity) due to stronger EDL repulsion (Choi *et al.*, 2003). The high value of the ζ-potential for nanoparticles studied implied that the cake layer should be loosely packed which impose less hydraulic resistance. However, because of the much higher specific resistance of P4VP060 than P4VP250, the hydraulic resistance from the P4VP060 cake layers might be higher than that formed by P4VP250. Even though a thick cake layer (Figure 6.11) was built up after two hours of filtration with P4VP250, the increase in total resistance was less significant as compared to that of the P4VP060.

Figure 6.11 Photograph of air-dried fouled membrane after two hours of filtration with 1000 ppm P4VP250. Note the thick cake layer on the membrane surface.

6.3.2.5 Plots of Linearized Model Forms

Another approach to examine the fouling mechanism is to plot the filtration data in appropriate linearized forms derived from the original expressions for the classical pore blockage, pore constriction, and cake filtration models, as mentioned previously in Chapter 2. Figure 6.12 shows the pore blockage model analysis. The classical pore blockage model predicts that a plot of the filtration flux (J) versus filtration volume (V) would be linear. From Figure 6.12 (a), the model fitting shows a good agreement with the data in the initial stage for small nanoparticles (P4VP060), suggesting that the flux decline being dominated by the pore blockage mechanism. However, in the plot for the larger particles (P4VP250) (Figure 6.12 (b)), the fitting did not give good linear relationship, indicating that the fouling with large nanoparticles may mainly contribute to external fouling. The flux data in the later stage showed significant deviations from the linearity for both plots. Hence, pore blockage was no longer the major fouling mechanism after long filtration time.

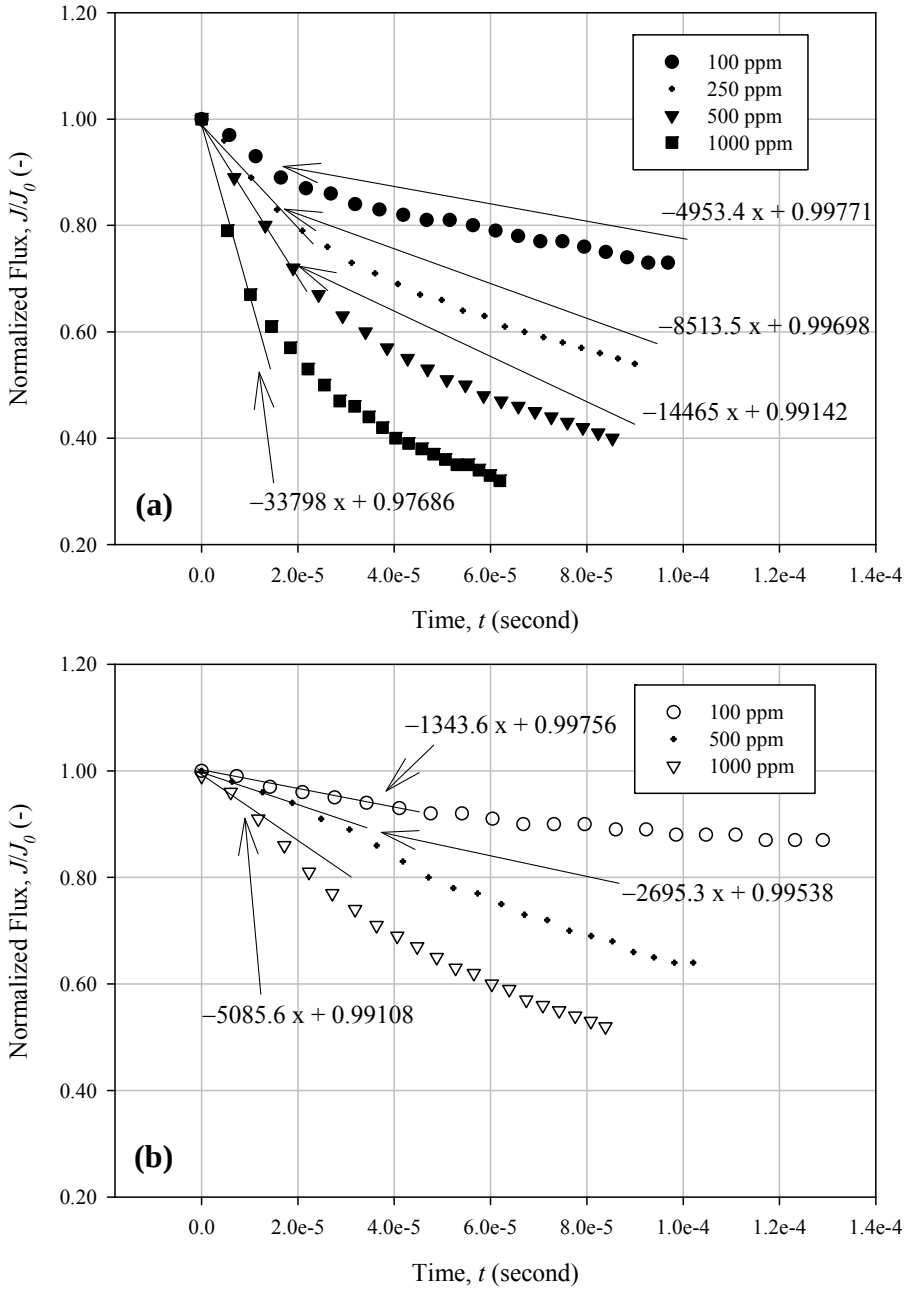

Figure 6.12 Plots of flux decline data as a function of nanoparticle concentration, plotted with pore blockage model: (a) P4VP060 and (b) P4VP250.

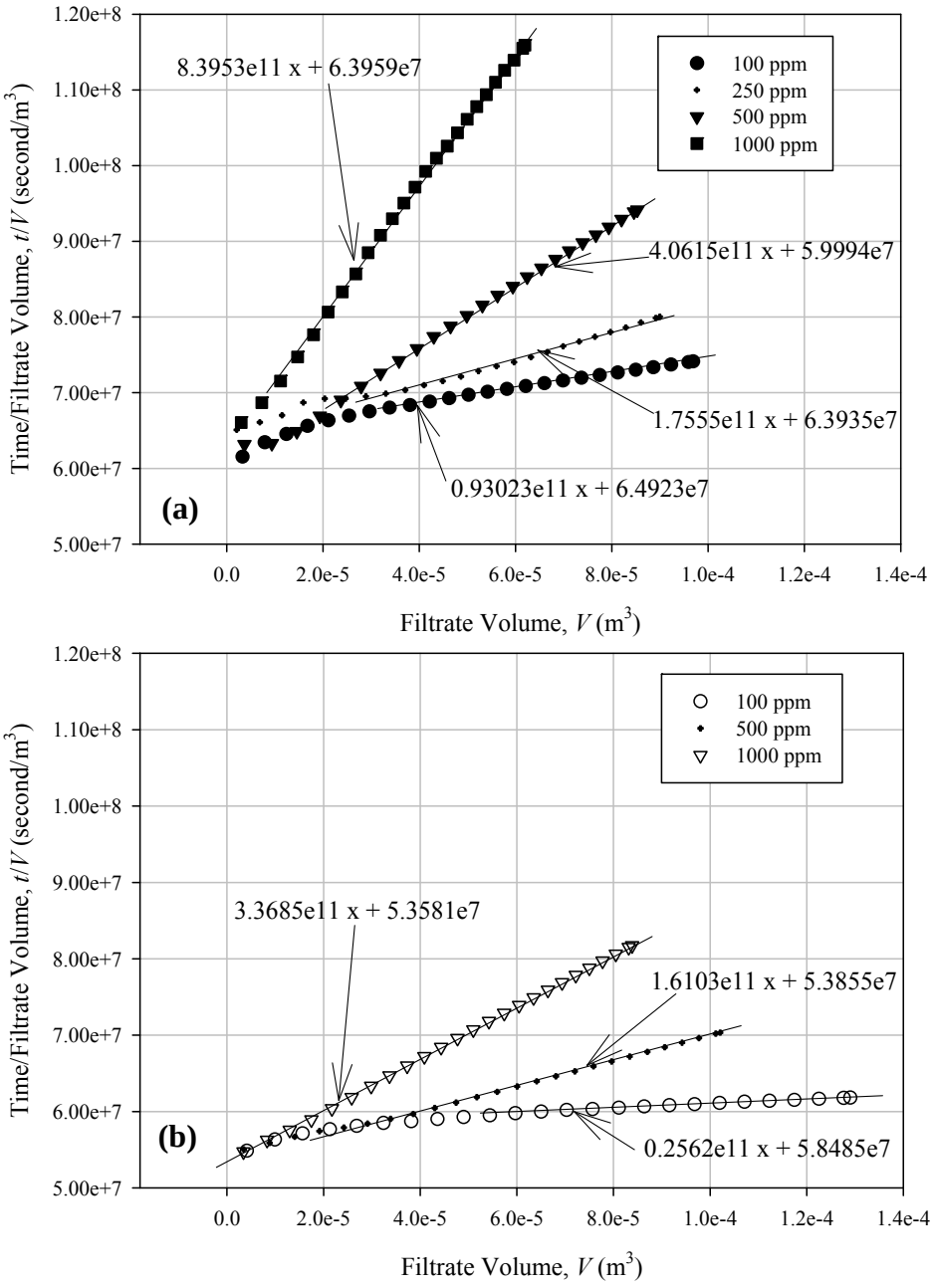

Figure 6.13 Plots of flux decline data as a function of nanoparticle concentration, plotted with cake filtration model: (a) P4VP060 and (b) P4VP250.

The classical cake filtration model predicts that a plot of t/V versus filtrate volume (V) should be linear. The analysis results are presented in the Figure 6.13. The straight lines plotted along with the processed curves clearly showed a good agreement with the cake formation model for most of the filtration data especially at the larger stage (where the V is large). Furthermore, the cake filtration model was better suited for the filtrations of P4VP250 because the larger nanoparticles were mostly retained and

accumulated on the membrane surface during the filtration, in agreement with the good linearity observed in Figure 6.13 (b).

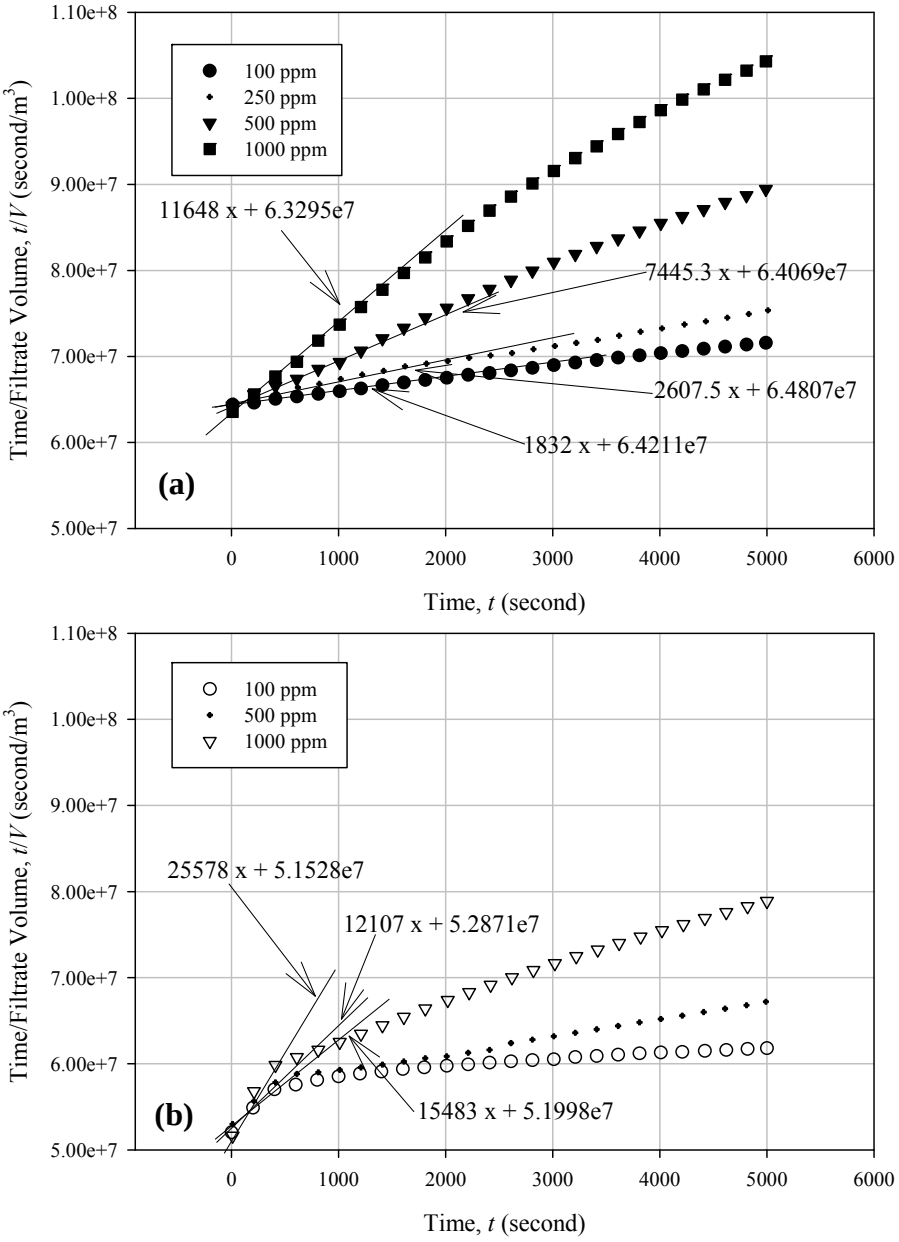

Figure 6.14 Plots of flux decline data as a function of nanoparticle concentration, plotted with pore constriction model: (a) P4VP060 and (b) P4VP250.

The classical pore constriction model predicts that t/V would change linearly with the filtration time (t). The data fitting according to this model are shown in Figure 6.14. Since pore constriction may mostly happen at the beginning of the filtrations, only the filtration data in the initial 90 minutes were analyzed with this model. The plots for

the small nanoparticles (P4VP060) clearly showed better agreement with the pore constriction model, as compared to the plot for filtration of P4VP250. The plots for the filtration of both the 100 ppm and 250 ppm P4VP060 suspension are almost straight for the entire run. For higher P4VP060 concentrations, i.e. 500 ppm and 1000 ppm, the straight line portions are only observed for the initial period. On the contrary, as shown in Figure 6.14 (b), the pore constriction model could not fit for the filtration data for the large nanoparticles (P4VP250) regardless of the concentration, indicating that pore constriction model was not the governing mechanism for the observed fouling phenomenon.

As shown earlier in Table 6.2, the rejection for P4VP060 generally increased with the nanoparticle concentrations in the feed suspensions, implying that the pore blocking or pore constriction by P4VP060 would have occurred during the filtration. The duration for which the small nanoparticles could travel through the pores or the length of pore constriction or pore blockage period was much shorter when the nanoparticle suspensions of higher P4VP060 concentration were filtered. The rejection rate increased by 0.5 % from the filtration run of 100 ppm P4VP060 to that of 500 ppm P4VP060; however, it was only increased by 0.1 % when the nanoparticle concentration was increased from 500 ppm to 1000 ppm. This enhanced rejection at higher nanoparticle concentrations can be explained by the Figure 6.13 (a), wherein the cake formation stage commenced earlier (as indicated by the starting point of the straight model fit for each run) when higher concentration of P4VP060 was filtered. The higher the amount of small nanoparticles was present, the earlier the cake started to form and the formed cake layer would limit the passage of P4VP060, resulting in higher apparent rejection performance.

Hwang *et al.* (2008) studied the dead-end microfiltration of poly(methyl methacrylate) particles with the diameters of 0.15 μm through two types of track-etched membranes (Isopore®) with the mean pore sizes of 0.2 and 0.4 μm. Through membrane blocking analysis, they demonstrated that the fouling was more severe when the disparity between the microfilter's pore size and particle diameter was larger. As the particle size was fixed at 0.15 μm (i.e. equivalent specific cake resistance), the observed phenomenon was caused because more particles can accumulate and block the larger pore. Transition in fouling regime from pore blocking to cake filtration was observed as well. From the model fitting shown, the membrane fouling with larger nanoparticles (P4VP250) can be attributed to the cake formation or cake filtration mechanism; whereas the small nanoparticles (P4VP060), may involve additional internal fouling mechanisms such as pore constriction and pore blocking. The relative size of the nanoparticle and the membrane pore is critical in determining the separation efficiency, hydraulic flux and filtration resistance. Selecting the pore size of the membrane filter to be smaller than the particle size of nanoparticles to be separated should lead to better process performance.

6.3.2.6 FESEM Micrography

The turbidity measurements with UV/VIS spectrophotometer were positive for all the filtrates collected from the filtration of P4VP060 at different concentrations. Hence, it was possible that some P4VP060 may have travel through the membrane and internal fouling may occur. FESEM was used to obtain direct visual evidence of the nanoparticles deposited within the membrane (Figure 6.15 (a)) or on the membrane surface (Figure 6.15 (b) and (c)).

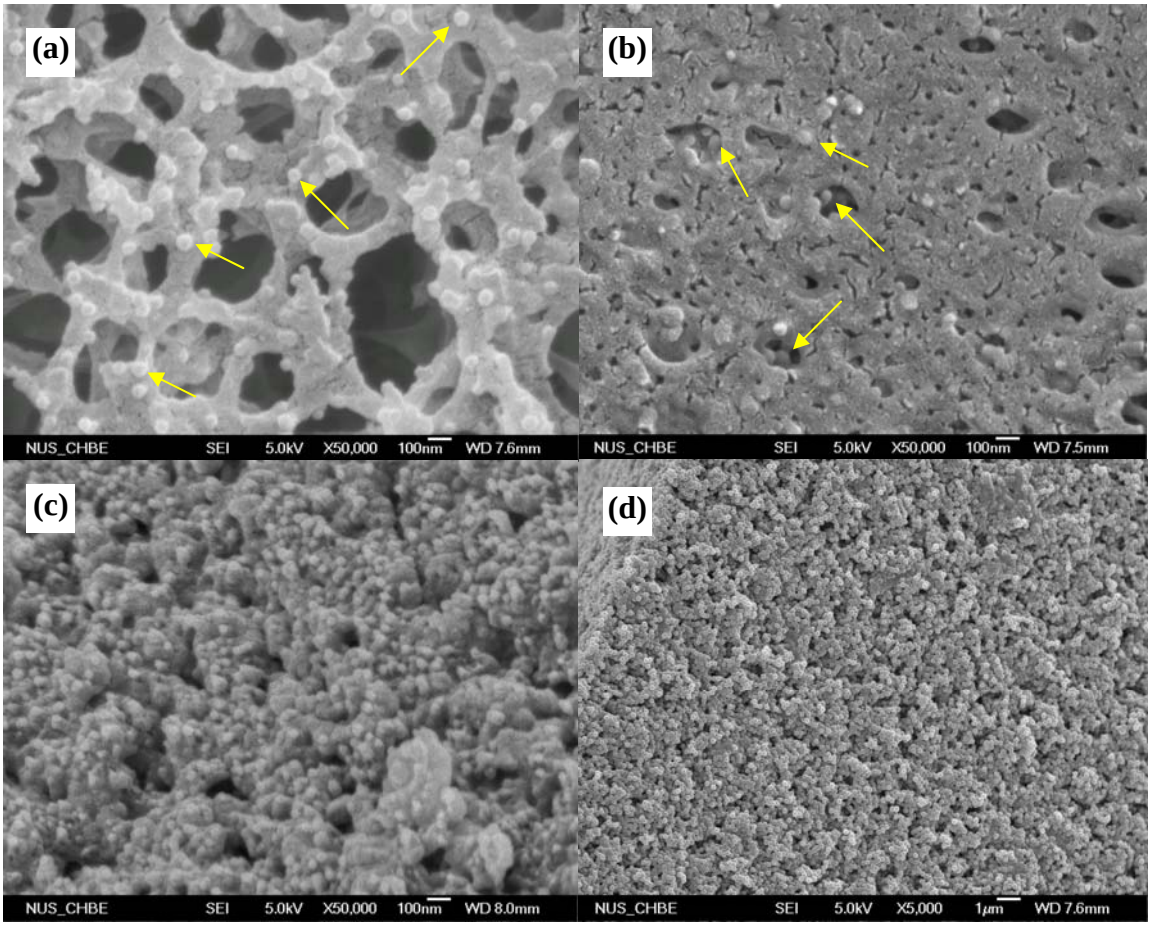

Figure 6.15 FESEM micrographs of fouled membranes: (a) cross-section view of a fouled membrane after filtration of 250 ppm P4VP060, (b) membrane surface fouled by 1000 ppm P4VP060 after cake layer was removed, (c) cake layer formed by 1000 ppm P4VP060 filtration, and (d) cake layer formed by 1000 ppm P4VP250 filtration. Arrows are drawn to indicate the deposited P4VP060 nanoparticles.

The deposition of nanoparticles on the fibrous network (Figure 6.15 (a)) and at the surface pore mouths (Figure 6.15 (b)) was observed, which supports the pore blocking and pore constriction fouling mechanisms. The FESEM results clearly provide evidence to support the earlier findings on the identification of fouling mechanisms during nanoparticle filtration, i.e. small NPs entered the membrane and deposited on the fiber structure during the filtration, causing internal fouling. A fouled membrane with the cake layer removed was examined with FESEM, as shown in Figure 6.15 (b). The membrane selected for this experiment was severely fouled by the 1000 ppm P4VP060 after 2 hours' of filtration and a thick cake layer was visually observed on

the surface (Figure 6.15 (c)). The image in Figure 6.15 (b) shows that the P4VP060 indeed entered the surface pores and closed up many of the surface pores.

From Figure 6.15 (c), it is observed that a loosely packed cake layer was formed. The spherical shape of dimensions in the range 60 ± 20 nm can be clearly distinguished. In summary, the FESEM micrographs clearly verified the fouling mechanisms of the nanoparticles smaller than the membrane surface pore, involving standard blocking, pore blockage and cake filtration. As cake formation was the only probable fouling mechanism for larger nanoparticles as shown earlier, no visual evidence were found from FESEM on pore blockage or pore constriction with P4VP250, except the cake layer formed on the membrane surface (Figure 6.15 (d)).

The results obtained in previous chapters confirm that the nanoparticles as an adsorbent can be effectively separated and recovered in the retentate by the membrane separation process. By controlling the ratio of nanoparticle size to membrane pore size, the dominant fouling mechanism can be manipulated and shifted to mainly cake formation with negligible involvement of internal fouling mechanism such as pore clogging or blocking. Even though there were significant amounts of cake formed from the dead-end filtration performed, cross-flow filtration may be employed to reduce the propensity of the nanoparticle suspension towards cake formation or concentration polarization (Hilal *et al.*, 2005; Kim *et al.*, 2006), during practical deployment of these nanoparticles as remedial agents for environmental applications.

6.4 Conclusion

The separation performance and fouling characteristics of the monodispersed nanoparticle suspensions in filtration were studied. The narrowly-distributed P4VP nanoparticles of two distinct sizes (60 nm and 250 nm) of identical chemical composition, together with a commercially available, asymmetric-type MCE membrane with a rated pore size of 0.1 μm were used to explore the effect of relative ratio of nanoparticle size to membrane pore size on membrane separation performance and fouling mechanisms. The separation or rejection efficiency for both small (P4VP060) and large (P4VP250) nanoparticles were well above 99%, except that minor losses of the small nanoparticles in the permeate were found. The different fouling behaviors of the 2 different sized nanoparticles were analyzed by the various models. The membrane fouling through cake formation dominated the filtration of P4VP250 nanoparticles, in which the flux decline was much slower as compared to that of the smaller P4VP060. Pore constriction and pore blockage were probably dominating the early portion of the filtration runs of P4VP060; however the differentiation between these two fouling modes was unsuccessful with the analysis tools discussed. Nevertheless, the results from the separation efficiency experiments and the FESEM were sufficient to support that the internal fouling occurred during the filtrations of P4VP060. On the other hand, only a minor pore blockage may exist during the filtrations of P4VP250 because some of the surface pores were larger than the P4VP250 nanoparticles, as confirmed by the *ImageJ* analysis. The minor blockage was believed to be caused by deposition in a few large pores on the membrane surface. Large nanoparticles could be intercepted and removed by the fibrous network of the membrane even when these particles could enter the membrane through the abnormally large surface pores, as confirmed by the mass balance analysis.

The fouling model analysis showed that the degree of membrane fouling with small P4VP060 nanoparticles was much more severe than that with larger nanoparticles, in terms of the hydraulic resistance and the rate of flux decline. None of the analysis tools employed herein can unambiguously determine the transition in fouling mechanisms, from internal fouling to external fouling. A more sophisticated model which allows integration of pore constriction, pore blockage, and cake filtration which may occur simultaneously or in sequential manner, such as the one proposed by Duclos-Orsello *et al.* (2006), can be used in future study.

CHAPTER 7

CONCLUSIONS AND RECOMMENDATIONS

7.1 Conclusions

The major objective of this thesis is to prepare a highly monodispersed nanoparticles as adsorbent for a potential use in hybrid adsorption-filtration process which can sequestrate and recover palladium. In addition, the robustness of the prepared nanoparticles was examined and optimized to enhance the reusability and mechanical stability of the nanoparticles. In this work, 4-vinylpyridine (4-VP) has been applied as the functional monomer responsible for metal sequestration and recovery. The use of the hydrophilic co-monomers, such as PEGMA and MATMAC, as well as the crosslinker, such as DVB and PEGDM, enabled the preparation of narrowly-distributed poly(4-vinylpyridine) (P4VP) nanoparticles in a wide size range, with enhanced colloidal stability and physical strength to withstand repeated cycles of swelling-deswelling. The following summarizes the findings and conclusions obtained in this research project.

In the first part of this work (Chapter 3), the spherical, narrowly-dispersed P4VP nanoparticles in the size range of 70 – 650 nm were successfully synthesized with the proposed two-pronged approach ("hydrophilic co-monomer addition" and "starve-fed") that was based on the surfactant-free emulsion polymerization method. Selection of co-monomers and crosslinkers in the polymerization recipes was crucial for obtaining P4VP-based nanoparticles with good colloidal and morphological stability. The nanoparticle robustness was examined from three aspects: colloidal stability, mechanical stability as tested in cyclic pH-swing swelling-deswelling, as well as simulated Pd(II) adsorption in acidic medium. The addition of PEGMA (degree of polymerization = 46) not only can enable the production of small P4VP-PEGMA nanoparticles (~ 70nm) but also confer

enhanced salt-tolerance to the prepared P4VP-based nanoparticles. P4VP-PEGMA nanoparticles crosslinked with 4 wt% of flexible, long chain PEGDM molecules (degree of polymerization = 9, and 13~14) were found to be extremely robust and remain physically intact and well-dispersed after five cycles of pH-swing swelling-deswelling. Swollen P4VP nanoparticles underwent deswelling in the presence of palladium ions and remained well-dispersed, indicating that the P4VP nanoparticles prepared would remain stable, even when the swollen polycationic networks were collapsed intramolecularly through the complexation with palladium ions.

In the second part of this work, the adsorption performance of the prepared P4VP nanoparticles was examined with respect to their adsorption capacity, sequestration kinetics as well as their regeneration and reuse. The P4VP nanoparticles were demonstrated to have high binding affinity towards palladium species, Pd(II) and the maximum adsorption capacity was as high as up to 6 mmole-Pd(II) per gram of the nanoparticles. In addition, the Pd(II) adsorption with the swollen nanoparticles reached adsorption equilibrium within short time of contact. Through adsorption isotherm study, the optimum pH for most effective Pd(II) removal was determined to be pH 3. Due to 'sponginess' and openness of the swollen P4VP networks, the Pd(II) sequestration kinetic was nearly independent of the particle size. Both XPS and FT-IR spectroscopy results confirmed that the pyridyl groups within the P4VP polymeric network are able to complex the Pd(II) through chemisorption, possibly via a combination of direct coordination and anion-exchange mechanisms. As the [HCl] increased, the amount of

Pd(II) bound diminished due to the competitive binding between the chloride ions and chloropalladate species for the protonated sites.

From the "static adsorption" tests, the deswelling of the swollen P4VP nanoparticles was found to complete before the adsorption equilibrium was achieved, indicating that the diffusive penetration of Pd(II) through the P4VP network was apparently unaffected. As discussed, the whole deswelling process of P4VP nanoparticles in this work typically lasted for few seconds ($\tau_{deswell}$ < 10 seconds in this work) or even tens of milliseconds, as reported by Yin *et al.* (2008) for other chemically similar, swollen polymeric nanoparticles of equivalent sizes; whereas the entire Pd(II) adsorption could take more than 50 seconds, depending on the initial Pd(II) concentration and the solution pH. The kinetics of Pd(II) adsorption in stirred tank were systematically studied and the resulting data were fitted to either the intraparticle diffusion (IPD) model (1-*p* model) or combined diffusion model (2-*p* model). The fitting with the IPD model that assumes intraparticle diffusion resistance only yielded unrealistic diffusion coefficients for Pd(II) which were far off from the reported values of self diffusion coefficient for various palladium species. In the contrary, the 2-*p* model fitted Pd(II) adsorption rate data better, as supported through the evaluation of the goodness-of-fit and the *F*-test. Modeling of the adsorption kinetic data also revealed that the Pd(II) adsorption process obeyed the Fickian's laws of diffusion. The calculated Biot number showed that the film diffusion resistances were much greater than that of the pore diffusion. This finding is consistent with the exploitation of nanoscale adsorbent: the shorter diffusion path renders the pore diffusion resistance to disappear and the rate-determining step switch to external film diffusion.

The retardation effect observed for the Pd(II) diffusion coefficients fitted were found to be described qualitatively by the electrostatic obstruction-scaling model of Amsden (2001).

The palladium adsorbed by the P4VP nanoparticles was quantitatively desorbed using acidified thiourea solution (0.1 M, pH 3). Through a dead-end stirred cell filtration set-up, the P4VP nanoparticles were shown to be reusable over five cycles of adsorption-desorption in the batch mode, without any apparent loss of the adsorption capacity. The successful Pd(II) adsorption and elution demonstrated in this work therefore support the proposition that the P4VP nanoparticles developed in this work are deployable for practical application. Unlike other nonporous nanoscopic adsorbents, for instance, Fe_3O_4 nanoparticles (Uheida *et al.*, 2006), the crosslinked P4VP nanoparticles are inherently highly porous and 'soft', due to Columbic repulsion-controlled network expansion and solvent impregnation. By tuning the input amount of the crosslinker in the polymerization recipes, one could effectively engineer the porosity of the swollen nanoparticles to either enhance the binding site accessibility or reduce the diffusion path length or resistance. The adsorption kinetic modeling approach described in this work can be generalized to other metal ion-nanoadsorbent systems to quantify the retardation factor that governs the physical system. The developed OCFE computation algorithm yields accurate numerical solutions and their implementation other physical systems are straightforward and easy (Finlayson, 1980).

The separation performance and fouling characteristics of the monodispersed nanoparticle suspensions in nanoparticle filtration were also studied to examine the effect of particle size to membrane pore size. Even though the P4VP060 nanoparticles are smaller than the pore size rating of the filter, the separation or rejection efficiency by the asymmetric-type MCE for both small (P4VP060) and large (P4VP250) nanoparticles exceeded 99%. Through various analysis methods, pore constriction and pore blockage were probably the operative fouling mechanism for P4VP060 during the short initial period of the filtration runs. A minor pore blockage might be involved in the filtrations of P4VP250 due to the presence of abnormally large surface pores that are equivalent in size or larger than the P4VP250 nanoparticles. Nonetheless, the depth-type interior of the membrane structure would have prevented the transmission of P4VP250, resulting in almost 100% rejection. The data obtained from this work suggest that membranes with pores that are smaller than the nanoparticles to be separated are preferred as they are less prone to internal fouling in the membrane and the breach in permeate quality (insufficient rejection) can be prevented. In short, a highly-efficient and recyclable P4VP nanoparticles for palladium recovery has been successfully synthesized and the prospects for industrial up-scale of these nanoparticles were demonstrated.

7.2 Recommendations

The results presented in this thesis provided insights on the facile preparation of highly adsorptive P4VP nanoparticles of narrow particle size distribution, and their use for metal removal and recovery. Future research may further address the process optimization of the recovery and reuse operation, another critical step (other than the adsorption) in

improving the overall techno-economic feasibility of the nanoparticles-based environmental technology.

A systematic study of the developed two-pronged SFEP method can be conducted by employing factorial design methodology. Through this systematic study, the effect of the experimental parameters (e.g. polymerization temperature, initiator concentration etc.) on the quality of the nanoparticles obtained (e.g. diameter, polydispersity index, polymerization yield etc.), and the possible interactions within the combination of experimental parameters chosen can be better described. In conjunction with factorial design, sensitivity analysis may be conducted to assess and improve the process robustness of the modified SFEP, facilitating the future up-scale of the method.

The microfiltration experiments may be extended to a range of P4VP nanoparticles of different concentrations. This would allow for better discrimination and understanding on the effect of ratio of particle size to membrane pore size on the separation/rejection performance (Hwang *et al.*, 2008). Asymmetric type membrane filters only represent a fraction of many membranes of industrial relevance nowadays. By expanding the range of membrane filter type, for example, isotropic type or sieve type microfilter, their separation performance in either separating or fractionating the nanoparticles from suspending mediums can be collected and comparatively analyzed (Brans *et al.*, 2007).

Next, a cross-flow filtration system can be employed for further investigation on the separation/filtration performance. The hydrodynamic shear imposed along the membrane

surface would have reduced the propensity towards the membrane fouling phenomenon observed in this work. The transmission and rejection of the nanoparticles should be examined closely and compared to that of dead-end filtration. Since the nanoparticles are highly charged in the aqueous mediums, the solution conditions (e.g. ionic strength, temperature) can be varied systematically, so that the resultant effect on the filtration behavior of the nanoparticles can be established. The data obtained could provide fundamental insight on the physicochemical interaction between the nanoparticles and the membranes, and the fouling mechanisms (Kim and Hoek, 2002; Kim *et al.*, 2006).

A more accurate and reliable tool such as that of Duclos-Orsello *et al.* (2006) may be used. A more sophisticated model which allows integration of pore constriction, pore blockage, and cake filtration that may occur simultaneously or in sequential manner would allow process engineer to identify the entrance into new fouling regime or the impact of the feed suspension on the membrane separation performance. As shown in this work, none of the analysis tools employed could unambiguously determine the transition of the fouling mechanisms for the whole filtration process.

Reference:

Abdurrahmanoglu, S., Okay, O. (2008) *Macromolecules*, **41**, 7759-7761.

Abiman, P., Wildgoose, G.G., Crossley, A., Compton, R.G. (2008) *J. Mater. Chem.*, **18**, 3948-3953.

Alexandratos, S.D., Crick, D.W. (1996) *Ind. Eng. Chem. Res.*, **35**, 635-644.

Alexia, G., Meireles, M., Aimar, P., Carvin, P. (2008) *Chem. Eng. Res. Design*, **86**, 1281-1293.

Altken, R.J., Creely K.S., Tran C.L. (2004) Nanoparticles: an occupational hygiene review. Institute of Occupational Medicine for the Health and Safety Executive 2004, London.

Alvarez-Lorenzo, C., Hiratani, H., Tanaka, K., Stancil, K., Grosberg, A.Y., Tanaka, T. (2001) *Langmuir*, **17**, 3616-3622.

Amalvy, J.I., Wanless, E.J., Li, Y., Michailidou, V., Armes, S.P., Duccini, Y. (2004) *Langmuir*, **20**, 8992-8999.

Amigoni-Gerbier, S., Larpent, C. (1999) *Macromolecules*, **32**, 9071-9073.

Amigoni-Gerbier, S., Desert, S., Guilik-Kryswicki, T., Larpent, C. (2002) *Macromolecules*, **35**, 1644-1650.

Amsden, B. (1998) *Macromolecules*, **31**, 8382-8395.

Amsden, B. (2001) *Macromolecules*, **34**, 1430-1435.

Amsden, B., Grotheer, K., Angl, D. (2002) *Macromolecules*, **35**, 3179-3183.

Anseth K.S., Bowman C.N. (1994) *Chem. Eng. Sci.*, **49**, 2207-2217.

Antonietti, M., Gröhn, F., Hartmann, J., Bronstein, L. (1997) *Angew. Chem. Int. Ed. Engl.*, **36**, 2080-2083.

Antonietti, M., Lohmann, S., Eisenbach, C.D., Schubert, U.S. (1995) *Macromol. Rapid Commun.*, **16**, 283-289.

Armenante, P.M., Kirwan, D.J. (1989) *Chem. Eng. Sci.*, **44**, 2781-2796.

Asai, S., Konishi, Y., Sasaki, Y. (1988) *J. Chem. Eng. Japan*, **21**, 107-112.

Baba, Y., Hirakawa, H. (1992) *Chem. Lett.*, **10**, 1905-1908.

Baek, K., Yang, J.-W. (2004) *Desalination*, **167**, 111-118.

Baes, C.F., Mesmer, R.E. (1977) *The hydrolysis of cations*, John Wiley & Sons, New York.

Bai R., Zhang X. (2001) *J. Colloid Interface Sci.*, **243**, 52-60.

Balzani, V., Ceroni, P., Gestermann, S., Kauffmann, C., Gorka, M., Vögtle, F. (2000) *Chem. Commun.*, 853-854.

Basila, M.R., Kantner, T.R., Rhee, K.H. (1964) *J. Phys. Chem.* **68**, 3197-3207.

Beamson, G., Briggs, D. (1992) *High Resolution XPS of Organic Polymers – The Scienta ESCA300 Database*, John Wiley and Sons, New York.

Bell, C.A., Smith, S.V., Whittaker, M.R., Whittaker, A.K., Gahan, L.R., Monterio, M.J. (2006) *Adv. Mater.*, **18**, 582-586.

Bellare, J.R., Kaneko, T., Evans, D.F. (1988) *Langmuir*, **4**, 1066-1067.

Benjamin, M.M., Hayes, K.F., Leckie, J.O. (1982) *J. Water Poll. Control Fed.*, **54**, 1472-1481.

Beolchini, F., Pagnanelli, F., de Michelis, I., Veglio, F. (2006) *Environ. Sci. Technol.*, **40**, 2746-2752.

Bernardis, F.L., Grant, R.A., Sherrington, D.C. (2005) *React. Funct. Polym.*, **65**, 205-217.

Bernocco, S., Ferri, F., Profumo, A., Cuniberti, C., Rocco, M. (2000) *Biophys. J.*, **79**, 561-583.

Biffis, A. (2001) *J. Mol. Catal. A Chem.*, **165**, 303-307.

Block, S.S. (2001) *Disinfection, sterilization, and preservation.* Lippincott Williams & Wilkins.

Bosman, A.W., Janssen, H.M., Meijer, E.W. (1999) *Chem. Rev.*, **99**, 1665-1688.

Bouvier-Fontes, L., Pirri, R., Magnet, S., Asua, J.M., Leiza, J.R. (2005) *Macromolecules*, **38**, 2722-2728.

Bowen, W.R., Williams, P.M. (2001) *J. Colloid Interface Sci.*, **233**, 159-163.

Brackman, J.C. (1991) *Langmuir*, **7**, 469-472.

Bradley, M., Bruno, N., Vincent, B. (2005a) *Langmuir*, **21**, 2750-2753.

Bradley, M., Ramos, J., Vincent, B. (2005b) *Langmuir*, **21**, 1209-1215.

Bradley, M., Vincent, B. (2005) *Langmuir*, **21**, 8630-8634.

Brans, G.A., van Dinther, A., Odum, B., Schröen, C.G.P.H., Boom, R.M. (2007) *J. Membr. Sci.*, **290**, 230-240.

Brandrup, J., Immergut, E.H., Grulke, E.A. (1999) *Polymer Handbook, 4th ed.*, New York: John Wiley & Sons.

Brazel, C.S., Peppas, N.A. (1999) *Biomaterials*, **20**, 721-732.

Budtova, T., Navard, P. (1997) *Macromolecules*, **30**, 6556-6558.

Budtova, T., Navard, P. (1998) *Macromolecules*, **31**, 8845-8850.

Burshtain, D., Wu, J., Melman, A., Mandler, D., Scherson, D.A. (2004) *Languir*, **20**, 4498-4502.

Byrne, R.H., Kump, L.R. (1993) *Geochim. et Cosmochim. Acta*, **57**, 1151-1156.

Calvo, P., Remunan-Lopez, C., Vila-Jato, J.L., Alonso, M.J. (1997) *Pharm. Res.*, **14**, 1431-1436.

Capek, I. (1999) *Radical Polymerization of Polyoxyethylene Macromonomers in Disperse Systems*, in Advances in Polymer Science 145, New York: Springer.

Capek, I. (2000) *Adv. Colloid Interface Sci.*, **88**, 295-357.

Chan, R., Chen, V. (2004) *J. Membr. Sci.*, **242**, 169-188.

Chanda, M., Rempel, G.L. (1993) *Ind. Eng. Chem. Res.*, **32**, 726-732.

Chang, Y.-C., Chen, D.-H. (2005). *J. Colloid Interface Sci.*, **283**, 446-451.

Chen, J.S., Vasiliev, A.N., Panarello, A.P., Khinast, J.G. (2007) *Appl. Catal. A*, **325**, 76-86.

Chen, L.-J., Lin, S.-Y., Chern, C.-S., Wu, S.-C. (1997) *Colloids Surf. A Physicochem. Eng. Asp.*, **122**, 161-168.

Chen, M.-Q., Chen, Y., Kaneko, T., Liu, X.-Y., Cheng, Y., Akashi, M. (2003) *Polym. J.*, **35**, 688-690.

Chen, M.-Q., Kishida, A., Serizawa, T., Akashi, M. (2000) *J. Polym. Sci. Part A Polym. Chem.*, **38**, 1811-1817.

Chen, Y.Y., Liang, C., Chao, Y. (1998) *React. Funct. Polym.*, **36**, 51-58.

Cheryan, M. (1998) *Ultrafiltration and Microfiltration Handbook*, CRC Press, Boca Raton, 345-483.

Choi, S.-W., Park, J.-M., Chang, Y., Yoon, J.Y., Haam, S., Kim, J.H., Kim, W.-S. (2003) *Sep. Purif. Technol.*, **30**, 69-77.

Chiellini, E., Orsini, L.M., Solaro, R. (2003) *Macromol. Symp.*, **197**, 345-354.

Christian, S.D., Tucker, E.E., Scamehorn, J.F., Lee, B.-H., Sasaki, K.J. (1989) *Langmuir*, **5**, 876-879.

Cohen, J.A., Khorosheva, V.A. (2001) *Colloids Surf. A: Physiochem. Eng. Aspects*, **195**, 113-127.

Colvin, V.L. (2003) *Nature Biotech.*, **21**, 1166-1170.

Costa, C., Rodrigues, A.E. (1985) *AIChE J.*, **31**, 1645-1654.

Crank, J. (1975) *The mathematics of diffusion*. Oxford: Clarendon Press.

Cushing, B.L., Kolesnichenko, V.L., O'connor, C.L. (2004) *Chem. Rev.*, **104**, 3893-3946.

Dalwadi, G., Benson, H.A.E., Chen, Y. (2005) *Pharm. Res.*, **22**, 2152-2162.

Dave G., Blanck H., Gustafsson K. (1979) *J. Chem. Tech. Biotechnol.*, **29**, 249-257.

Davies, M.C., Lynn, R.A.P., Hearn, J., Paul, A.J., Vickerman, J.C., Watts, J.F. (1995) *Langmuir*, **11**, 4313-4322.

Dawson, J.C., Le, H.V. (1996) *World Patent* WO/1996/002608.

Dendritech (2009) Dendrimer Price List, http://www.dendritech.com/pricing.html (June 20, 2010), Dendritech, Inc., Midland, Michigan.

Deslandes, Y., Mitchell, D.F., Paine, A.J. (1993) *Langmuir*, **9**, 1468-1472.

Diallo, M.S., Balogh, L., Shafagati, A., Johnson, J.H., Jr., Goddard, W.A., III, Tomalia, D.A. (1999) *Environ. Sci. Technol.*, **33**, 820-824.

Diallo, M.S., Christie, S., Swaminathan, P., Balogh, L., Shi, X., Lim, W., Papelis, C., Goddard, W.A., III, Johnson, J.H., Jr. (2003) *Langmuir*, **20**, 2640, 2651.

Diallo, M.S., Christie, S., Swaminathan, P., Johnson, J.H. Jr., Goddard, W.A. III. (2005) *Environ. Sci. Technol.*, **39**, 1366-1377.

Do, D. D. (1998). *Adsorption analysis: equilibria and kinetics*. London: Imperial College Press.

Downey, J.S., McIssac, G., Frank, R.S., Stöver, H.D. (2001) *Macromolecules*, **34**, 4534-4541.

Du, F., Baune, M., Kück, A., Thöming, J. (2008) *Sep. Sci. Technol.*, **15**, 3842-3855.

Duclos-Orsello, C., Li, W., Ho, C.-C.. (2006) *J. Membr. Sci.*, **280**,856-866.

Dupin, D., Fujii, S., Armes, S.P., Reeve, P., Baxter, S.M. (2006) *Langmuir*, **22**, 3381-3387.

Dupin, D., Rosselgong, J., Armes, S.P., Routh, A.F. (2007) *Langmuir*, **23**, 4035-4041.

Dykes, G.M. (2001) *J. Chem. Technol. Biotechnol.*, **76**, 903-918.

Eichenbaum, G.M., Kiser, P.F., Dobrynin, A.V., Simon, S.A., Needham, D. (1999) *Macromolecules*, **32**, 4867-4878.

Eilers, P.H.C., Marx, B.D. (1996) *Statist. Sci.*, **11**, 89-121.

Elmas, B., Onur, M.A., Şenel, S., Tuncel, A. (2004) *Colloids Surf. A-Physicochem. Eng. Aspects*, **232**, 253-259.

Fane, G.A., Fell, D.J.C.Kim, K.J. (1985) *Desalination*, **53**, 37-55.

Faust, S.D., Aly, O.M. (1987) *Adsorption processes for water treatment*, Butterworths, Boston.

Ferguson, C.J., Russell, G.T., Gilbert, R.G. (2002) *Polymer*, **43**, 4557-4570.

Ferguson, P., Sherrington, D.C., Gough, A. (1993) *Polymer*, **34**, 3281-3292.

Ferlita, R.R., Phipps, D., Safarik, J., Yeh, D.H. (2008) *Environ. Progress*, **27**, 204-209.

Fernández-Nieves, A., de las Nieves, F.J., Fernández-Barbero, A. (2004) *J. Chem. Phys.*, **120**, 374-378.

Fernández-Nieves, A., Fernández-Barbero, A., Vincent, B., de las Nieves, F.J. (2000) *Macromolecules*, **33**, 2114-2118.

Feeney, P.J., Napper, D.H., Gilbert, R.G. (1987) *Macromolecules*, **20**, 2922-2930.

Fillipi, B.R., Scamehorn, J.F., Taylor, R.W., Christian, S.D. (1997) *Sep. Sci. Technol.*, **32**, 2401-2424.

Fillipi, B.R., Brant, L.W., Scamehorn, J.F., Christian, S.D. (1999) *J. Colloid Interface Sci.*, **213**, 68-80.

Finlayson, B. (1980). *Nonlinear analysis in chemical engineering*. New York: McGraw-Hill.

Fortuny, M., Graillat, C., McKenna, T.F. (2004) *Ind. Eng. Chem. Res.*, **43**, 7210-7219.

Fritz, H., Maier, M., Bayer, E. (1997) *J. Colloid Interface Sci.*, **195**, 272-288.

Fujii, S., Armes, S.P., Araki, T., Ade, H. (2005) *J. Am. Chem. Soc.*, **127**, 16808-16809.

Fujiwara, K., Ramesh, A., Maki, T., Hasegawa, H., Ueda, K. (2007) *J. Hazard. Mater.*, **146**, 39-50.

Funke, W. (1996) In *Polymeric Materials Encyclopedia*, ed by Salamone J.C., 4360-4367, New York: CRC Press.

Gecol, H., Ergican, E., Fuchs, A. (2004) *J. Membr. Sci.*, **241**, 105-119.

Ghosh, G., Bhattacharya, P.K. (2006) *Chem. Eng. Sci.*, **119**, 45-53.

Gil, E.S., Hudson, S.M. (2004) *Prog. Polym. Sci.*, **29**, 1173-1222.

Gilbert, R.G. (1995) *Emulsion Polymerization: A Mechanistic Approach*, London: Academic Press.

Gittings, M.R., Saville, D.A. (1998) *Colloids Surf. A Physicochem. Eng. Asp.*, **141**, 111-117.

Glazunov, V.P., Odinokov, S.E. (1982) *Spectrochim. Acta*, **38A**, 339-408.

Gniewek, A., Trzeciak, A.M., Ziolkowski, J.J., Kepinski, L., Wrzyszcz, J., Tylus, W. (2005) *J. Cat.*, **229**, 332-343.

Göransson, A., Hansson, P., (2003) *J. Phys. Chem. B*, **107**, 9203-9213.

Govender, T., Stolnik, S., Garnett, M.C., Illum, L., Davis, S.S. (1999) *J. Control. Release*, **57**, 171-185.

Grisham, P.E., Nussbaum, J.H., Grodzinsky, A.J., Yarmush, M.L. (1990) *J. Chem. Phys.*, **93**, 4462-4472.

Guibal, E., Sweeney, N.V.O., Vincent, T., Tobin, J.M. (2002) *React. Funct. Polym.*, **50**, 149-163.

Guillaume, J.L., Pichot, C., Guillot, J. (1988) *J. Polym. Sci. Part A Polym. Chem.*, **26**, 1937-1959.

Guyot, A. (1988) *Pure & Appl. Chem.*, **60**, 365-376.

Gzara, L, Dhahbi, M. (2001) *Desalination*, **137**, 241-250.

Hansson, P. (1998) *Langmuir*, **14**, 4059-4064.

Harnish, B., Robinson, J.T., Pei, Z., Ramstrom, O., Yan, M. (2005) *Chem. Mater.*, **17**, 4092-4096.

Harriott, P. (1962) *AIChE J.*, **8**, 93-101.

Haruta, M. (1997) *Catal. Today*, **36**, 153-166.

Hazot, P., Delair, T., Pichot, C., Chapel, J.-P., Elaissari, A. (2003) *C. R. Chimie*, **6**, 1417-1424.

Henry, J.D.J., Lawler, L.F., Kuo, C.H.A. (1977) *AIChE J.*, **23**, 851-859.

He C., Liu J., Ye X., Xie L., Zhang Q., Ren X., Zhang G., Wu C. (2008) *Langmuir*, **24**, 10717-10722.

Hebrant, M., Tecilla, P., Scrimin, P., Tondre, C. (1997) *Langmuir*, **13**, 5539-5543.

Hebrant, M., Francois, N., Tondre, C. (1998) *Colloids Surf. A*, **143**, 77-88.

Helfferich, F. (1962) *Ion exchange*, New York: McGraw Hill.

Hermia, J. (1982) *Trans. IChemE*, **60**, 183-187.

Hiemstra, T., Venema, P., van Riemsdijk, W.H. (1996) *J. Colloid Interface Sci.*, **184**, 680-692.

Hilal, N., Ogunbiyi, O.O., Miles, N.J., Nigmatullin, R. (2005) *Sep. Sci. Technol.*, **40**, 1957-2005.

Ho, C.-C. (2001) *Effect of membrane morphology and structure on protein fouling during microfiltration.* PhD Thesis, University of Delaware.

Ho, Y.-S. (2006) *J. Hazard. Mater.*, **B136**, 681-689.

Ho, S., Critchley, K., Lilly, G.D., Shim, B., Kotov, N.A. (2009) *J. Mater. Chem.*, **19**, 1390-1394.

Ho, C.-C., Zydney, A.L. (1999) *J. Membr. Sci.*, **155**, 261-275.

Ho, C.-C., Zydney, A.L. (2000) *J. Colloid Interface Sci.*, **232**, 389-399.

Hu, J., Chen, G., Lo, I.M.C. (2005a). *Water Res.*, **39**, 4528-4536.

Hu, J., Lo, I.M.C., Chen, G.H. (2005b) *Langmuir*, **21**, 11173-11179.

Hu, J., Lo, I.M.C., Chen, G.H. (2007) *Sep. Purif. Technol.*, **56**, 249-256.

Huber, D.L. (2005) *Small*, **1**, 482-501.

Hubicki, Z., Leszcyńska, M., Łodyga, B., Łodyga, A. (2006) *Miner. Eng.*, **19**, 1341-1347.

Hubicki, Z., Wołowicz, A., Leszczyńska, M. (2008) *J. Hazard. Mater.*, **159**, 280-286.

Huisman, I.H. (2000) Microfiltration. In *Encyclopedia of Separation Science*, Wilson, I.D., eds., Academic Press: San. Diego.

Hunter, R.J. (2001) Association colloids. *Foundation of Colloid Science*, Oxford University Press, USA, 436-481.

Hwang, K.-J., Liao, C.-Y., Tung, K.-L. (2008) *Desalination*, **234**, 16-23.

Iglesias, M., Antico, E., Salvado, V. (1999) *Anal. Chim. Acta*, **381**, 61-67.

Ikeda, A., Suzuki, T., Aida, M., Fujii, Y., Itoh, K., Mitsugashira, T., Hara, M., Ozawa, M. (2004a) *J. Chromatogr. A*, **1041**, 195-200.

Ikeda, A., Yaita, T., Okamoto, Y., Shiwaku, H., Suzuki, S., Suzuki, T., Fujii, Y. (2007) *Anal. Chem.*, **79**, 8016-8023.

Ikkala, O.T., Ruokolainen, J., ten Brinke, G., Torkkeli, M., Serimaa, R. (1995) *Macromolecules*, **28**, 7088-7097.

Iqbal, J., Kim, H.-J., Yang, J.-S., Baek, K., Yang, J.-W. (2007) *Chemosphere*, **66**, 970-976.

Ismael, M., Tondre, C. (1992) *Langmuir*, **8**, 1039-1041.

Ismael, M., Tondre, C. (1993) *J. Colloid Interface Sci.*, **160**, 252-257.

Israelachvili, J. (1992) *Intermolecular and Surface Forces*; 2nd. Ed., Academic Press, London.

Jackson, C.L., Chanzy, H.D., Booy, F.P., Drake, B.J., Tomalia, D.A., Bauer, B.J., Amis, E.J. (1998) *Macromolecules*, **31**, 6259-6265.

Jadhav, S.V., Pangarkar, V.G. (1991) *Ind. Eng. Chem. Res.*, **30**, 2496-2503.

Jenkins, P., Snowden, M. (1996) *Adv. Colloid Interface Sci.*, **68**, 57-96.

de Jesús, E., Flores J.C. (2008) *Ind. Eng. Chem. Res.*, **47**, 7968-7981.

Ji, Y., Jain, S., Davis, R.J. (2005) *J. Phys. Chem. B*, **109**, 17232-17238.

Johansson, C., Hansson, P., Malmsten, M. (2007) *J. Colloid Interface Sci.*, **316**, 350-359.

Johansson, L., Skantze, U., Löfroth, J.-E. (1991) *Macromolecules*, **24**, 6019-6023.

John Gregory (2006) *Particles in water: properties and processes*, Boca Raton: Taylor & Francis.

Juang, R.-S., Xu, Y.-Y., Chen, C.-L. (2003) *J. Membr. Sci.*, **218**, 257-267.

Kanai, Y., Oshima, T., Baba, Y. (2008) *Ind. Eng. Chem. Res.*, **47**, 3114-3120.

Kanaras, A.G., Kamounah, F.S., Schaumburg, K., Kiely, C.J., Brust, M. (2002) *Chem. Commun.*, **20**, 2294-2295.

Kanazawa, R., Mori, K., Tokuyama, H., Sakohara, S. (2004) *J. Chem. Eng. Japan*, **37**, 804-807.

Kanel, S.R., Greneche,J.-M., Choi, H. (2006) *Environ. Sci. Technol.*, **40**, 2045-2050.

Kanel, S.R., Manning, B., Charlet, L., Choi, H. (2005) *Environ. Sci. Technol.*, **39**, 12-1298.

Kang, T., Park, Y., Yi, J. (2004) *Ind. Eng. Chem. Res.*, **43**, 1478-1484.

Kannurpatti, A.R., Anseth, J.W., Bowman, C.N. (1998) *Polymer*, **39**, 2507-2513.

Kawaguchi, H. (1999) Surface modification of polymer particles. *Fine particles: synthesis, characterization, and mechanisms of growth*, Sugimoto, T., ed., Marcel Dekker, New York, 647-659.

Kawaguchi, H. (2000) *Prog. Polym. Sci.*, **25**, 1171-1210.

Kawaguchi, S., Tano, K., Maniruzzaman, M., Ito, K. (2000) *Macromol. Symp.*, **150**, 101-108.

Kelland, D.R. (1998) *IEEE Trans. Magn.*, **34**, 2123-2125.

Kim, J.H., Chainey, M., El-Aasser, M.S., Vanderhoff, J.W. (1987) *J. Polym. Sci. Part A Polym. Chem.*, **27**, 3187-3199.

Kim, A.S., Hoek, E.M.V. (2002) *Environ. Eng. Sci.*, **19**, 373-386.

Kim, S., Marion, M., Jeong, B.H., Hoek, E.M.V. (2006) *J. Membr. Sci.*, **284**, 361-372.

Kim, J., Nayak, S., Lyon, L.A. (2005) *J. Am. Chem. Soc*., **127**, 9588-9592.

Klabunde, K.J., Stark, J., Koper, O., Mohs, C., Park, D.G., Decker, S., Jiang, Y., Lagadic, I., Zhang, D. (1996) *J. Phys. Chem.*, **100**, 12142-12153.

Klein, A., Daniels, E.S. (1997) In Emulsion Polymerization and Emulsion Polymers, ed. by Lovell P.A., El-Aasser M.S. New York: John Wiley & Sons.

Klepac, J., Simmons, D.L., Taylor, R.W., Scamehorn, J.F., Christian, S.D. (1991) *Sep. Sci. Technol.*, **26**, 165-173.

Kochkar, H., Turki, A., Bergaoui, L., Berhault, G., Ghorbel, A. (2009) *J. Colloid Interface Sci.*, **331**, 27-31.

Kononova, O.N., Kholmogorov, A.G., Mikhlina, E.V. (1998) *Hydrometallurgy*, **48**, 65-72.

Koper, O., Li, Y.-X., Klabunde, K.J. (1993) *Chem. Mater.*, **5**, 500-505.

Kopylova, V.D., Kargman, V.B., Saldadze, K.M., Kokorin, A.I., Suvorova, L.N. (1973) *Polym. Sci. U.S.S.R.*, 823-831.

Koros, W.J., Ma, Y.H., Shimidzu, T. (1996) *Pure Appl. Chem.*, **68**, 1479-1489

Krackeler, J.J., Naidus, H. (1969) *J. Polym. Sci. Part C*, **27**, 207-235.

Kramareva, N.V., Stakheev, A.Y., Tkachenko, O.P., Klementiev, K., Grunert, W., Finashina, E.D., Kustov, L.M. (2004) *J. Mol. Cat. A*, **209**, 97-106.

Kratz, K., Lapp, A., Eimer, W., Hellweg, T. (2002) *Colloids Surf. A Physicochem. Eng. Asp.*, **197**, 55-67.

Kuang, M., Wang, D., Möhwald, H. (2005) *Adv. Funct. Mater.*, **15**, 1611-1616.

Kumaresan, R., Sabharwal, K.N., Srinivasan, T.G, Rao, P.R.V., Dhekane, G. (2008) *Solvent Extr. Ion Exch.*, **26**, 643-671.

Larpent, C., Geniès, C., Delgado, A.P.D.S., Caminade, A.-M., Majoral, J.-P., Sassi, J.F., Leising, F. (2003) *Chem. Comm.*, 1816-1817.

Lefrancois, M., Malbois, G. (1971) *J. Catal.*, **20**, 350-358.

Leiza, J.R., Meuldijk, J. (2005) *Emulsion Copolymerisation: Process Strategies and Morphology* in *Chemistry and Technology of Emulsion Polymerisation* ed. by van Herk A., Oxford: Blackwell.

Leung, P.S. (1979) Surfactant micelle enhanced ultrafiltration. *Ultrafiltration membranes and applications*, Cooper, A.R., eds., Plenum Press, New York, 415-422.

LeVan, M.D., Carta, G. (2008) *Adsorption and Ion Exchange*, in *Perry's Chemical Engineer's Handbook* ed. Green D.W., Perry R.H., New York: McGraw-Hill.

Li, N., Bai, R. (2005) *Sep. Purif. Technol.*, **42**, 237-247.

Li, N., Bai, R., (2006) *Water Sci. & Technol.*, **54**, 103-113.

Li, X., Salovey, R. (2000) *J. Polym. Sci. Part A Polym. Chem.*, **38**, 1323-1336.

Li, X.-Q., Elliott, D.W., Zhang, W.-X. (2006) *Crit. Rev. Solid State Mater. Sci.*, **31**, 111-122.

Li, X.-Q., Zhang, W.-X. (2006) *Langmuir*, **22**, 4638-4642.

Li, X.-Q., Zhang, W.-X. (2007) *J. Phys. Chem. C.*, **111**, 6939-6946.

Lin, C.-C., Metters, A.T. (2006) *Adv. Drug Deliv. Rev.*, **58**, 1379-1408.

Lin, Y.-T., Sung, M., Sanders, P.F., Marinucci, A., Huang, C.P. (2007) *Sep. Purif. Technol.*, **58**, 138-147.

Lin, W., Zhou, Y., Zhao, Y., Zhu, Q., Wu, C. (2002) *Macromolecules*, **35**, 7407-7413.

Liu, W.-T. (2006) *J. Biosci. Bioeng.*, **102**, 1-7.

Liu, C., Bai, R. (2005) *J. Membrane Sci.*, **267**, 68-77.

Liu, J., Chew, C.H., Gan, L.M., Teo, W.K., Gan, L.H. (1997) *Langmuir*, **13**, 4988-4994.

Liu, J., Rieger, J., Huber, K. (2008) *Langmuir*, **24**, 8262-8271.

Liu, Z., Xiao, H., Wiseman, N. (2000) *J. Appl. Polym. Sci.*, **76**, 1129-1140.

Ledezma, R., Treviño, M.E., Elizalde, L.E., Pérez-Carrillo, L.A., Mendizábal, E., Puig, J.E., Leobandung, W., Ichikawa, H., Fukumori, Y., Peppas, N.A. (2002) *J. Controlled Release*, **80**, 357-363.

López, R.G. (2007) *J. Polym. Sci. Part A Polym. Chem.*, **45**, 1463-1473.

López-León, T., Carvalho, E.L.S., Seijo, B., Ortega-Vinuesa, J.L., Bastos-González, D. (2005) *J. Colloid Interface Sci.*, **283**, 344-351.

Loukidou, M.X., Karapantsios, T.D., Zouboulis, A.I., Matis, K.A. (2004) *Ind. Eng. Chem. Res.*, **43**, 1748-1755.

Lovell, P.A., El-Aasser, M.S. (1997) Emulsion polymerization and emulsion polymers. New York: John Wiley & Sons.

Loxley, A., Vincent, B. (1997) *Colloid Polym. Sci.*, **275**, 1108-1114.

Lyons, A.M., Vasile, M.J., Pearce, E.M. Waszczak, J.V. (1988) *Macromolecules*, **21**, 3125-3134.

Ma, G.H. (1999) Advances in preparations and applications of polymeric microspheres. *Polymer interfaces and emulsions*, Esumi, K., ed., Marcel Dekker, New York, 55-118.

Ma, G.H., Fukutomi, T. (1991) *J. Appl. Polym. Sci.*, **43**, 1451-1457.

Ma, H.-W., Liao, X.-P., Liu, X., Shi, B. (2006) *J. Membr. Sci.*, **278**, 373-380.

Ma, X., Cui, Y., Zhao, X., Zheng, S., Tang, X. (2004) *J. Colloid Interface Sci.*, **276**, 53-59.

Mackenzie, K., Frenzel, H., Kopinke, F.-D. (2006) *Appl. Catal. B*, **63**, 161-167.

Mackie, J.S., Meares, P. (1955) *Proc. R. Soc. London*, **A232**, 498-509.

Makino, H., Emi, H., Yamaguchi A., Iritani E., Namiki, N., Myojo, T., Yamamoto, K. (2008) Chapter 7: Environmental and Safety Issues with Nanoparticles. In *Nanoparticle Technology Handbook*, Hosokawa, M., Nogi, K., Naito, M., Yokoyama, T., eds., Elsevier Science, 385-417,.

Maniruzzaman, M,, Kawaguchi, S., Ito, K. (2000) *Macromolecules*, **33**, 1583-1592.

Marcus, Y. (1997) *Ion Properties*. New York: Marcel Dekker.

McNab, W.W., Jr., Ruiz, R., Reinhard, M. (2000) *Environ. Sci. Technol.*, **34**, 149-153.

Mika, A.M., Childs, R.F., Dickson, J.M. (2002) *J. Membr. Sci.*, **206**, 19-30.

Millipore (2009) MF-Millipore™ membrane filters. http://www.millipore.com/catalogue/module/c152 (March 29, 2009).

Molla, S.H., Bhattacharjee, S. (2005) *J. Membr. Sci.*, **255**, 187-199.

Molla, S.H., Bhattacharjee, S. (2008) *Langmuir*, **24**, 5659-5662.

Morris, G.E., Vincent, B., Snowden, M.J. (1997) *J. Colloid Interface Sci.*, **190**, 198-205.

Muhr, A.H., Blanshard, J.M.V. (1982) *Polymer*, **23**, 1012-1026.

Mulligan, C.N., Yong, R.N., Gibbs, B.F. (2001) *J. Hazard. Mater.*, **85**, 111-125.

Myakonkaya, O., Hu, Z., Nazar, M.F., Eastoe, J. (2010) *Chem. Eur. J.*, **16**, 11784-11790.

Nagata, S. (1975) *Agitation in solid-liquid systems.* In: *Mixing: principles and applications*. New York: Wiley.

Narita, T., Gong, J.-P., Osada, Y. (1998) *J. Phys. Chem. B*, **102**, 4566-4572.

Navarro R., Guzman J., Saucedo I., Revilla J. Guibal E. (2003) *Macrmol. Biosci.*, **3**, 552-561.

Ngai, T., Wu, C. (2005) *Langmuir*, **21**, 8520-8525.

Ni, H., Du, Y., Ma, G., Nagai, M., Omi, S. (2001) *Macromolecules*, **34**, 6577-6585.

Nilsson, P., Hansson, P. (2005) *J. Phys. Chem. B*, **109**, 23843-23856.

Nilsson, P., Unga, J., Hansson, P. (2007) *J. Phys. Chem. B* **111**, 10959-10964.

Nivas, B.T., Sabatini, D.A., Shiau, B.-J., Harwell, J.H. (1996) *Wat. Res.*, **30**, 511-520.

Nurmi, J.T., Tratnyek, P.G., Sarathy, V., Baer, D.R., James, E.A., Pecher, K., Wang, C., Linehan, J.C., Matson, D.W., Penn, R.L., Driessen, M.D. (2005) *Environ. Sci. Technol.*, **39**, 1221-1230.

Nyrkova, I.A., Semenov, A.N. (2005) *Faraday Discuss.*, **128**, 113-127.

O'Connor, A.J., Hatton, T.A., Bose, A. (1997) *Langmuir*, **13**, 6931-6940.

Ogston, A.G., Preston, B.N., Wells, J.D. (1973) *Proc. R. Soc. London*, **333**, 297-316.

Okasha, R., Hild, G., Rempp, P. (1979) *Eur. Polym. J.*, **15**, 975-982.

Okubo, M., Furukawa, Y., Shiba, K., Matoba, T. (2003) *Colloid Polym. Sci.*, **281**, 182-186.

Okubo, M., Kobayashi, H., Matoba, T., Oshima, Y. (2006) *Langmuir*, **22**, 8727-8731.

Okay, O. (2000) *Prog. Polym. Sci.*, **25**, 711-779.

Olah, A., Hempenius, M.A., Vancso, G.J. (2004) *Eur. Polym. J.*, **40**, 763-773.

Ottaviani, M.F., Bossmann, S., Turro, N.J., Tomalia, D.A. (1994) *J. Am. Chem. Soc.*, **116**, 661-671.

Ottaviani, M.F., Montalti, F., Turro, N.J., Tomalia, D.A. (1997) *J. Phys. Chem. B*, **101**, 158-166.

Ottewill, R.H., Satgurunathan, R. (1988) *Colloid Polym. Sci.*, **266**, 547-553.

Özdeğer, E., Sudol, E.D., El-Aasser, M.S., Klein, A. (1997) *J. Polym. Sci. Part A Polym. Chem.*, **35**, 3813-3825.

Ozin, G.A. (1992) *Adv. Mater.*, **4**, 612-649.

Pangarkar, V.G., Yawalkar, A.A., Sharma, M.M., Beenackers, A.A.C.M. (2002) *Ind. Eng. Chem. Res.*, **41**, 4141-4167.

Parajuli, D., Kawakita, H., Inoue, K., Funaoka, M. (2006) *Ind. Eng. Chem. Res.*, **45**, 6405-6412.

Pardey, A.J., Rojas, A.D., Yanez, J.E., Betancourt, P., Scott, C., Chinea, C., Urbina, C., Moronta, D., Longo C. (2005) *Polyhedron*, **24**, 511-519.

Parodi, A., Vincent, T., Pilsniak, M., Trochimczuk, A.W., Guibal, E. (2008) *Hydrometallurgy*, **92**, 1-10.

Parry, E.P. (1963) *J. Catal.*, **2**, 371-379.

Pathak, S., Greci, M.T., Kwong, R.C., Mercado, K., Prakash, G.K.S., Olah, G.A., Thompson, M.E. (2000) *Chem. Mater.*, **12**, 1985-1989.

Pearson, R.G. (1963) Hard and soft acids and bases. *J. Am. Chem. Soc.*, **85**, 3533-3539.

Pearson, C.E. (1986) *Numerical methods in engineering and science.* New York: Van Nostrand Reinhold Co.

Pelton, R. (2000) *Adv. Colloid Interface Sci.*, **85**, 1-33.

Peng S., Wu C. (1999) *Macromolecules*, **32**, 585-589.

Peng S., Wu C. (2001a) *Polymer*, **42**, 6871-6876.

Peng S., Wu C. (2001b) *J. Phys. Chem. B*, **105**, 2331-2335.

Peppas, N.A., Huang, Y., Torres-Lugo, M., Ward, J.H., Zhang, J. (2000) *Annu. Rev. Biomed. Eng.*, **2**, 9-29.

Persson, K.M., Gekas, V., Trägárdh, G. (1995) *J. Membr. Sci.*, **100**, 155-162.

Phenrat, T., Saleh, N., Sirk, K., Tilton, R.D., Lowry, G. V. (2007) *Environ. Sci. Technol.*, **41**, 284–290.

Pich, A., Lu, Y., Adler, H.-J. (2003) *Colloid Polym. Sci.*, **281**, 907-915.

Pinkrah, V.T., Snowden, M.J., Mitchell, J.C., Seidel, J., Chowdhry, B.Z., Fern, G.R. (2003) *Langmuir*, **19**, 585-590.

Polverari, M., van de Ven, T.G.M. (1994) *Colloids Surf. A Physicochem. Eng. Asp.*, **86**, 209-228.

Qi, L., Xu, Z. (2004) *Colloid. Surf. A*, **251**, 183-190.

Rao, C.R.M., Reddi, G.S. (2000) *Trends Anal. Chem.*, **19**, 565-586.

Rasmusson, M., Routh, A., Vincent, B. (2004) *Langmuir*, **20**, 3536-3542.

Rether, A., Schuster M. (2003) *React. Funct. Polym.*, **57**, 13-21.

Ripperger, S., Altmann, J. (2002) *Sep. Purif. Technol.*, **26**, 19-31.

Riseman, S.M., Massoth, F.E., Dhar, G.M., Eyring, E.M. (1982) *J. Phys. Chem.*, **86**, 1760-1763.

Ritchie, G.S.P., Sposito, G. (2002) Speciation in soils. *Chemical speciation in the environment*, Ure, A.M., Davidson, C.M., eds., Blackwell Science, Oxford, 237-264.

Romero-Cano, M.S., Martin-Rodriguez, A., Chauveteau, G., de las Nieves, F.J. (1998) *J. Colloid Interface Sci.*, **198**, 273-281.

Rotello, V.M. (2004) *Nanoparticles: building blocks for nanotechnology*, Kluwer Academic/Plenum Publishers, New York.

Rosensweig, R.E. (1985) *Ferrohydrodynamics*. Cambridge University: London.

Rossi, L.M., Vono, L.L.R., Silva, F.P., Kiyohara, P.K., Duarte, E.L., Matos, J.R. (2007) *Appl. Catal. A*, **330**, 139-144.

Roukolainen, J., ten Brinke, G., Ikkala, O., Torkkeli, M., Serimaa, R. (1996) *Macromoecules*, **29**, 3409-3415.

Roukolainen, J., Tanner, J., ten Brinke, G., Ikkala, O., Torkkeli, M., Serimaa, R. (1995) *Macromoecules*, **29**, 7779-7784.

Rouse, J.D., Bjornen, K.K., Taylor, R.W., Shiau, B.-J. (2004) Environ. Practice, **6**, 157-164.

Ruiz, M., Sastre, A.M., Guibal, E. (2000) *React. Funct. Polym.*, **45**, 155-173.

Ruiz, M., Sastre, A.M., Guibal, E. (2002) *Sep. Sci. Technol.*, **37**, 2385-2403.

Sabatini, D.A., Harwell, J.H., Hasegawa, M., Knox, R. (1998) *J. Membr. Sci.*, **151**, 87-98.

Sajjadi, S. (2007) *Langmuir*, **23**, 1018-1024.

Sajjadi, S., Brooks, B.W. (1999) *J. Appl. Polym. Sci.*, **74**, 3094-3110.

Sajjadi, S., Brooks, B.W. (2000) *Chem. Eng. Sci.*, **55**, 4757-4781.

Saleh, N., Sirk, K., Liu, Y., Phenrat, T., Defour, B., Matyjaszewski, K., Tilton, R.D., Lowry, G.V. (2007) *Environ. Eng. Sci.*, **24**, 45–57.

Sánchez, J.M., Hidalgo, M., Valiente, M., Salvadó, V. (2000) *J. Polym. Sci. Part A Polym. Chem*, **38**, 269-278.

Scamehorn, J.F., Sherill, C.D., Dawlat, E.-S.A., Uchiyama, H. (1994) *Sep. Purif. Technol.*, **29**, 809-830.

Sengupta, S., SenGupta, A.K. (2002) Trace heavy metals separation by chelating ion exchangers. *Environmental separation of heavy metals: engineering processes*, Lewis Publishers, Boca Raton, 45-96.

Serpe, M.J., Yarmey, K.A., Nolan, C.M., Lyon, L.A. (2005) *Biomacromolecules*, **6**, 408-413.

Shah, R., Devi, S. (1997) *Anal. Chim. Acta*, **341**, 217-224.

Shay, J.S., English, R.J., Spontak, R.J., Balik, C.M., Khan S.A. (2000) *Macromolecules*, **33**, 6664-6671.

Sherrington, D.C. (2001) *J. Polym. Sci. A Polym. Chem.*, **39**, 2364-2377.

Shin, S., Jang, J. (2007) *Chem. Comm.* 4230-4232.

Shouldice, G.T., Vandezande, G.A., Rudin, A. (1994) *Eur. Polym. J.*, **30**, 179-183.

Silva, V.M.T.M., Rodrigues, A.E. (2002) *AIChE J.*, **48**, 625-634.

Silverstein, R.M., Webster, F.X., Kiemle, D.J. (2005) *Spectrometric Identification of Organic Compounds*, John Wiley and Sons, New York.

Smedley, P.L., Kinniburgh, D.G. (2002) *Appl. Geochem.*, **17**, 517-568.

von Smoluchoski, M. (1921) *Electrische Endosmose und Strömungsströme*, in Greatz L. (Ed.) Handbuch der Elektrizität und des Magnetismus, Barth: Leipzig, Vol. 2, 366.

Snowden, M.J., Thomas, D., Vincent, B. (1993) *Analyst*, **118**, 1367-1369.

Song, Z., Poehlein, G.W. (1989) *J. Colloid Interface Sci.*, **128**, 486-500.

Song, Z., Poehlein, G.W. (1990) *J. Polym. Sci. Part A Polym. Chem.*, **28**, 2359-2392.

Steel, P.J. (1990) *Coord. Chem. Rev.*, **106**, 227-265.

Sweeney, S.F., Woehrle, G.H., Hutchison, J.E. (2006) Rapid purification and size separation of gold nanoparticles via diafiltration. *J. Am. Chem. Soc.*, **128**, 3190-3197.

Takahashi, K., Miyamori, S., Uyama, H., Kobayashi, S. (1997) *Macromol. Rapid. Commun.*, **18**, 471-475.

Talanova, G.G., Zhong, L., Bartsch, R.A. (1999) *J. App. Pol. Sci.*, **74**, 849-856.

Talanova, G.G., Zhong, L., Kravchenko, O.V., Yatsimiriskii, K.B., Bartsch, R.A. (2001) *J. App. Pol. Sci.*, **80**, 207-213.

Tan, K.L., Tan, B.T.G., Kang, E.T., Neoh, K.G. (1990) *J. Mol. Electron.*, **6**, 5-8.

Tanaka, T., Fillmore, D.J. (1979) *J. Chem. Phys.*, **70**, 1214-1218.

Tarnawski, V.R., Jelen, P. (1986) *J. Food Eng.*, **5**, 75-90.

Tauer, K. (2004) Latex particles. *Colloids and colloid assemblies: synthesis, modification, organization and utilization of colloid particles*, Caruso, F., ed., Wiley-VCH, Weinheim, 1-51.

Tien, C. (1994) *Adsorption calculations and modeling*, Butterworth-Heinemann, Boston.

Tobita, H., Aoyagi, N., Takamura, S. (2001) *Polymer*, **42**, 7583-7587.

Tomalia, D.A., Fréchet, J.M.J. (2002) *J. Polym. Sci. A Polym. Chem.*, **40**, 2719-2728.

Tondres, C., Son, S.-G., Hebrant, M., Scrimin, P., Tecilla, P. (1993) *Langmuir*, **9**, 950-955.

Tondre, C., Hebrant, M., Perdicakis, M., Bessiere, J. (1997) *Langmuir*, **13**, 1446-1450.

Tounissou, P., Hebrant, M., Tondre, C. (1996) *J. Colloid Interface Sci.*, **183**, 491-497.

Tracy, E.M., Davis, R.H.. (1994) *J. Colloid Interface Sci.*, **167**, 104-116.

Tratnyek, P.G., Johnson, R.L. (2006) *Nanotoday*, **1**, 40-48.

Tuncel, A. (2000) *Polymer*, **41**, 1257-1267.

Uheida, A., Iglesias, M., Fontàs, C., Hidalgo, M., Salvadó, V., Zhang, Y., Muhammed, M. (2006a) *J. Colloid Interface Sci.*, **301**, 402-408.

Uheida, A., Iglesias, M., Fontàs, C., Zhang, Y., Muhammed, M. (2006b) *Sep. Sci. Technol.*, **41**, 909-923.

Uno, T., Machida, K., Miyajima, K. (1968) *Spectrochim. Acta*, **24A**, 1749-1763.

Vanderhoff, J.W. (1981) *The Formation of Coagulum in Emulsion Polymerization* in *Emulsion Polymers and Emulsion Polymerization*, eds. Bassett D.R. and Hamielec A.E., 199-208, Washington: American Chemical Society.

Vatta, L.L., Kramer, J., Koch, K.R. (2007) *Sep. Sci. Technol.*, **42**, 1985-2002.

Vincent, B.; Edwards, J.; Emmett, S.; Jones, A. (1986) *Colloids Surf.*, **18**, 261-281.

Vincent, T., Parodi, A., Guibal, E. (2008) *React. Funct. Polym.*, **68**, 1159-1169.

Voorn, D.-J., Ming, W., van Herk, A.M. (2005) *Macromolecules*, **38**, 3653-3662.

Wakeman, R. (2007) *Sep. Purif. Technol.*, **58**, 234-241.

Walcarius, A., Etienne, M., Lebeau, B. (2003) *Chem. Mater.*, **15**, 2161-2173.

Wang, C., Tam, K.C., Tan, C.B. (2004) *Langmuir*, **20**, 7933-7939.

Wang, C., Yang, W., Fu, S. (2003) Functionlization of colloidal particles. *Colloidal polymers: synthesis and characterization*, Elaissari, A., ed., Marcel Dekker, New York, 93-116.

Wang, R., Liao, X., Shi, B. (2005) *Ind. Eng. Chem. Res.*, **44**, 4221-4226.

Wang, Y.-M., Pan, C.Y. (1999) *Colloid Polym. Sci.*, **277**, 658-665.

Wang, F., Tarabara, V. (2008) *J. Colloid Interface Sci.*, **328**, 464-469.

Watson, J.H.P., Cressey, B.A., Roberts, A.P., Ellwood, D.C., Charnock, J.M., Soper, A.K. (2000) *J. Mag. Mag. Mater.*, **214**, 13-30.

Wessling, R.A. (1968) *J. Appl. Polym. Sci.*, **12**, 309-319.

Westrin, B.A., Axelsson, A. (1991) *Biotechnol. Bioeng.*, **38**, 439-446.

Wiegert, T., Altmann, J., Ripperger, S. (1999) Crossflow electrofiltration in a pilot scale. *J. Membr. Sci.*, **159**, 253-262.

Wiesner, M.R., Aptel, P. (1996) Mass transport and permeate flux and fouling in pressure-driven processes. In *Water Treatment Membrane Processes: A Joint Project by Three of the Worlds Largest Agencies*, Mallevialle, J., Odenaal, P.E., Wiesner, M.R. ed., AWWA Research Foundation, American Water Works Association, 4.1-4.30.

Wilkinson, M.C., Hearn, J., Steward, P.A. (1999) *Adv. Colloid Interface Sci.*, **81**, 77-165.

de Witt, J.A., van de Ven, T.G.M. (1992) *Adv. Colloid Interface Sci.*, **42**, 41-64.

Wu, K.H., Wang, Y.R., Hwu, W.H. (2003) *Polym. Degrad. Stab.*, **79**, 195-200.

Xu, C., Sun, S. (2007) *Polym. Int.*, **56**, 821-826.

Xu, Y., Zhao, D. (2005) *Environ. Sci. Technol.*, **39**, 2369-2375.

Xu, Y., Zhao, D. (2006) *Ind. Eng. Chem. Res.*, **46**, 1758-1765.

Yagi, H., Motouchi, T., Hikita, H. (1984) *Ind. Eng. Chem. Process Des. Dev.*, **23**, 145-150.

Yang, G.H., Kang, E.T., Neoh, K.G., Zhang, Y., Tan, K.L. (2001) *Langmuir*, **17**, 211-218.

Yantasee, W., Warner, C.L., Sangvanich, T., Addleman, R.S., Carter T.G., Wiacek, R.J., Fryxell, G.E., Timchalk, C., Warner, M.G. (2007) *Environ. Sci. & Technol.*, **41**, 5114-5119.

Yavuz, C.T., Mayo, J.T., Yu, W.Y., Prakash, A., Falkner, J.C., Yean, S., Cong, L., Shipley, H.J., Kan, A., Tomson, M., Natelson, D., Colvin, V.L. (2006) *Science*, **314**, 964-967.

Yin, J., Dupin, D., Li, J., Armes, S.P., Liu, S. (2008) *Langmuir*, **24**, 9334 – 9340.

Yoshida, M. (1997) *Eur. Polym. J.* **33**, 943-948.

Yoshikawa, T., Umeno, D., Saito, K., Sugo, T. (2008) *J. Membr. Sci.*, **307**, 82-87.

Yu, K., Sommer, W., Weck, M., Jones, C.W. (2004) *J. Catal.*, **226**, 101-110.

Yu, K., Sommer, W., Richardson, J.M., Weck, M., Jones, C.W. (2005) *Adv. Synth. Catal.*, **347**, 161-171.

Yu, Q., Zhou, M., Ding, Y., Jiang, B., Zhu, S. (2007) *Polymer*, **48**, 7058-7064.

Yuan, W. (2001) *Fouling by humic acids during ultrafiltration and microfiltration for water treatment.* PhD.Thesis, University of Delaware.

Zagorodni, A.A. (2007) *Ion Exchange Materials-Properties and Applications*, Oxford: Elsevier.

Zaitsev, V.S., Filimonov, D.S., Presnyakov, I.A., Gambino, R.J., Chu, B. (1999) *J. Colloid Interface Sci.*, **212**, 49-57.

Zeman, L.J., Zydney, A.L. (1996) *Microfiltration and ultrafiltration: principles and applications.* New York: Marcel Dekker.

Zhai, G.Q., Kang, E.T., Neoh, K.G. (2003) *J. Membr. Sci.*, **217**, 243-259.

Zhang, W.-X. (2003) *J. Nanopart. Res.*, **5**, 323-332.

Zhou, X., Goh, S.H., Lee, S.Y., Tan, K.L. (1998) *Appl. Surf. Sci.*, **126**, 141-147.

Appendix A

Appendices for Chapter 3 - Additional figures

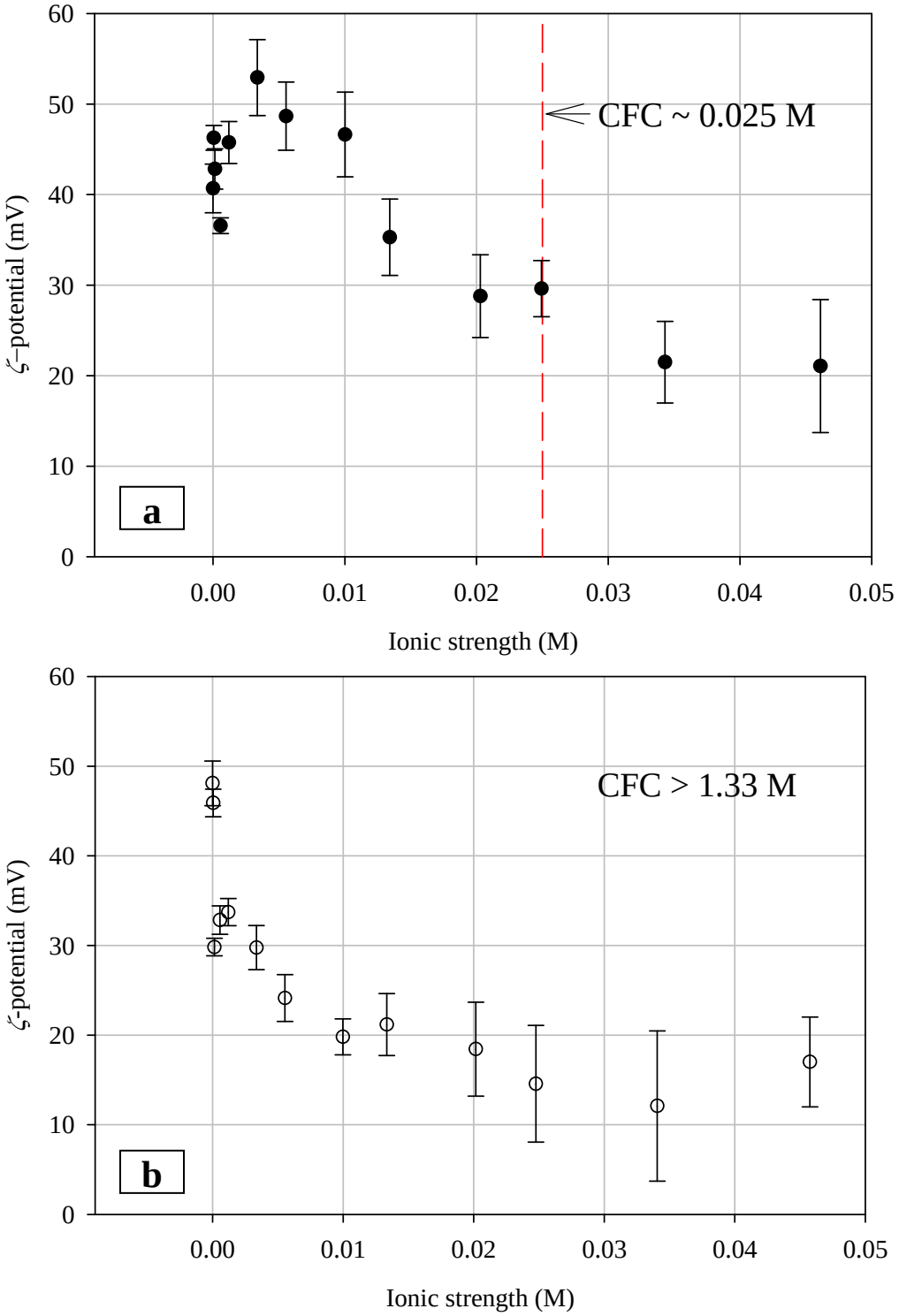

Figure A-1 Plot of the measured ζ-potentials against the ionic strength of the nanoparticle suspensions, for (a) the P4VP nanoparticles (A-4), and (b) the P4VP-PEGMA nanoparticles (B-4). Duplicate measurements were made to obtain each data point. Measurements for ionic strength higher than 0.05 M were unsuccessful due to the polarization of the palladium electrodes used at high salt content.

Explanation for lower apparent values of ζ–potential measured for P4VP-PEGMA nanoparticles in Figure A-1

In the presence of the surface-grafted PEG layers that originated from PEGMA, the charged groups (protonated amidine groups) located on the underlying particle surface of the P4VP-PEGMA nanoparticles gave rise to lower effective charge and lower apparent ζ–potentials. The reason is as follow: the uncharged or neutral polymer layers, either coated or covalently grafted onto the colloidal particles, would lower the electrophoretic mobility of the particles because of the increased drag force imposed upon the moving particles by the surface polymer layer during electrophoresis (Gittings and Saville, 2000; Ohshima, 2002; Hill *et al.*, 2003).

Reference:

Gittings M.R., Saville D.A. (2000) *Langmuir* **16**, 6416-6421.

Ohshima H. (2002) *J. Colloid Interface Sci.* **252**, 119-125.

Hill R.J., Saville D.A., Russel W.B. (2003) *J. Colloid Interface Sci.* **258**, 56-74.

Appendix B

Appendices for Chapter 4 (Part 2) - OCFE formulation for numerical solution of 2-*p* (combined diffusion) and 1-*p* models (IPD) used

Introduction

Kinetics of adsorption processes and its characterization has long been constituted as one of the important elements in either characterizing the inherent adsorption properties of the adsorbent of interest, or designing industrial adsorption process and equipment. A widely acceptable depiction of an adsorption process would consist of four consecutive stages: (1) transport of solute in the bulk fluid; (2) transport of the solute across the boundary layer surrounding the adsorbent particle (film-diffusion); (3) diffusion of solute within the pores of the adsorbent particle (intraparticle-diffusion); (4) adsorption/desorption of solute on the adsorbent surface (surface-reaction). Many theoretical and empirical model have been put forth to analyze and model the dynamics of adsorption process, by focusing either only one of the four processes abovementioned or a combination of few of them. Based on the selected rate-determining step(s), many analytical solutions have been derived; however, many of the mathematical solutions obtained have either assumed only linear form of adsorption isotherm model, or constant solute concentration in the bulk fluid, or absence of external mass transfer resistance. Analysis of the experimental adsorption data with the mathematical modeling tools which based upon those assumptions or simplification mentioned could be erroneous or inappropriate due to inadequate understanding of the actual physical processes inherent in the adsorption data, or ignorance of the mismatch between the ideal conditions wherein the models are adhered to, and the actual experimental conditions conducted.

The following sections illustrate the application of orthogonal collocation on finite elements (OCFE) method to numerically solve for the diffusion transient in adsorbents during adsorption processes based on 2-*p* model (combined diffusion = film + pore). Mass transfer resistance across external film (boundary layer/stagnant layer diffusion) is assumed not negligible, and therefore the full solution to the diffusion equations are sought via numerical computation as detailed herein.

Part I - Problem Statement

In most adsorption studies, the sorption of solutes by the binding sites, (for e.g. metal ions or organic pollutants) through physisorption, chemisorption or a combination of various binding mechanisms (ion-exchange, chelation), proceeds very fast relative to the diffusion of solute molecules through the network of pores. This physical intuition implies that local equilibrium between the solute in the pore fluid and the solute bound to the surface binding sites of the particle is established spontaneously, which is usually true except for molecular adsorption in carbon molecular sieve wherein the size of pore entrance is comparable to that of solutes (Do, 1995). The solute transport is assumed to follow Fickian's laws of diffusion. Consider the case of diffusion-controlled adsorption in a particle with arbitrary geometry, where R is the effective hydrodynamic radius of the particle, a radial differential mass balance is made over a small element of thickness Δr at the position r, followed by taking limit for Δr towards zero, and yields the following expression **(E-1)**.

$$\varepsilon \frac{\partial c}{\partial t} + (1-\varepsilon)\frac{\partial c_\mu}{\partial t} = \frac{1}{r^s}\frac{\partial}{\partial r}\left(r^s \cdot J\right),\ 0 \le r \le R \qquad \textbf{(E-1)}$$

where the diffusive flux (J) is defined as follow.

$$J = \varepsilon D_p \frac{\partial c}{\partial r} \qquad \textbf{(E-2)}$$

along with the boundary conditions **(BC)** and initial condition **(IC).**

BCs: $r = 0, \quad \dfrac{\partial c}{\partial r} = 0$ (geometric symmetry condition) **(BC-1a)**

$r = R, \quad \varepsilon D_p \dfrac{\partial c}{\partial r} = k_f \left(c_b - c\right)$ (finite film mass-transfer resistance) **(BC-1b)**

IC: $t = 0, \quad c = c_i$ (which is 0, for pore fluid initially filled only with solvents)

(IC-1)

The variable c_μ is volume-based, and it can be related to adsorption capacity (q) using the following relationship, i.e.

$$c_\mu(t,r) = 1000 \times \rho_p \times q(t,r) \quad \textbf{(E-3a)}$$

$$c_{\mu s} = 1000 \times \rho_p \times q_{\max} \quad \textbf{(E-3b)}$$

This expression **(E-1)** could be further simplified, by assuming that the solute diffusivity (D_p) remain constant throughout the particle (Do, 1998).

$$\varepsilon \frac{\partial c}{\partial t} + (1-\varepsilon)\frac{\partial c_\mu}{\partial t} = \varepsilon D_p \frac{1}{r^s}\frac{\partial}{\partial r}\left(r^s \frac{\partial c}{\partial r}\right), \; 0 \le r \le R, \quad \textbf{(E-4)}$$

where c is to be solved for $0 \le r \le R$.

This equation **(E-4)** could be expressed solely in c, by replacing c_μ with function of c via thermodynamic solute-partitioning models (adsorption isotherm models), such as Henry model or Langmuir model ($f(c)$).

$$\left[\varepsilon + (1-\varepsilon) f'(c)\right]\frac{\partial c}{\partial t} = \varepsilon D_p \frac{1}{r^s}\frac{\partial}{\partial r}\left\{r^s \frac{\partial c}{\partial r}\right\} \quad \textbf{(E-5)}$$

Note that the porosity parameter ε enters the expression to account for the liquid hold-up in pore fluid and solid phases separately. The shape parameter s has values of 0, 1 or 2 for planar, cylindrical or spherical geometry.

To convert the spatial domain into [0,1], the equation **(E-5)** is non-dimensionalized by allowing the following variables transformation **(TR-1)**. Langmuir isotherm model is applied.

$$y = \frac{c}{c_0} \qquad \textbf{(TR-1a)}$$

$$y_b = \frac{c_b}{c_0} \qquad \textbf{(TR-1b)}$$

$$y_i = \frac{c_i}{c_0} \qquad \textbf{(TR-1c)}$$

$$x = \frac{r}{R} \qquad \textbf{(TR-1d)}$$

$$\tau = \frac{\varepsilon D_p t}{R^2} \qquad \textbf{(TR-1e)}$$

$$c_\mu = f(c) = c_{\mu s}\frac{bc}{1+bc} \text{ (Langmuir isotherm model)} \qquad \textbf{(TR-1f)}$$

$$c_{\mu 0} = f(c_0) \qquad \textbf{(TR-1g)}$$

$$Bi = \frac{k_f R}{\varepsilon D_p} \qquad \textbf{(TR-1h)}$$

We then obtain the following equations **(E-6, E-7)** as well as the necessary conditions **(BC-2, IC-2)**.

$$G(y)\frac{\partial y}{\partial \tau} = \frac{1}{x^s}\frac{\partial}{\partial x}\left\{x^s \frac{\partial y}{\partial x}\right\} \qquad \textbf{(E-6a)}$$

or $$\frac{\partial y}{\partial \tau} = \frac{1}{G(y)}\left[\frac{s}{x}\frac{\partial y}{\partial x} + \frac{\partial^2 y}{\partial x^2}\right],\ 0 \le x \le 1, \quad \textbf{(E-6b)}$$

where $$G(y) = \varepsilon + (1-\varepsilon) f'(c_0 y) \quad \textbf{(E-7a)}$$

$$f'(c_0 y) = \frac{bc_{\mu s}}{\left[1 + bc_0 y\right]^2} \quad \textbf{(E-7b)}$$

BCs: $$x = 0,\quad \frac{\partial y}{\partial x} = 0 \quad \textbf{(BC-2a)}$$

$$x = 1,\quad \frac{\partial y}{\partial x} = Bi(y_b - y) \quad \textbf{(BC-2b)}$$

IC: $$\tau = 0,\quad y = y_i \quad \textbf{(IC-2)}$$

Part II - Domain Discretization

The domain [0,1] is divided into **NE** pieces of finite elements according to the methodology of the orthogonal collocation on finite elements (OCFE) (Finlayson, 1980), and the residuals at the collocation points located within each element are set to zero. In our current case, the region where steep gradients in concentration profile may occur is located near the particle surface (x→1). More elements with shorter length than those located near the core of the particle could therefore be located in this region to better capture steep gradients or sharp discontinuities when a layer of thin film exists to pose additional mass transfer resistance.

Transformation of the spatial variables is carried out within the *e-th* element as follow.

$$u = \frac{x - x^e}{\Delta x^e} \quad \textbf{(TR-2a)}$$

$$x = x^e + u\Delta x^e \quad \textbf{(TR-2b)}$$

$$\Delta x^e = x^{e+1} - x^e \quad \textbf{(TR-2c)}$$

For e-th element,

$$\frac{\partial y^e}{\partial \tau} = \frac{1}{G\left(y^e\right)}\left[\frac{s}{x^e + u\Delta x^e}\frac{1}{\Delta x^e}\frac{\partial y^e}{\partial u} + \frac{1}{\left(\Delta x^e\right)^2}\frac{\partial^2 y^e}{\partial u^2}\right], \text{ where } e = 1,..., NE \qquad \textbf{(E-8)}$$

BC become

$$u = 0, \quad \frac{\partial y^{e=1}}{\partial u} = 0 \text{ (for first element)} \qquad \textbf{(BC-3a)}$$

$$u = 1, \quad \frac{1}{\Delta x^e}\frac{\partial y^{e=NE}}{\partial u} = Bi\left(y_b - y^{e=NE}\right) \text{ (for last element)} \qquad \textbf{(BC-3b)}$$

and the IC becomes

$$\tau = 0, \quad y^e = y_i \text{ (for all element)} \qquad \textbf{(IC-3)}$$

An additional continuity condition **(CC)** is imposed on each collocation point at boundaries between elements.

$$\left.\frac{1}{\Delta x^{e-1}}\frac{\partial y^{e-1}}{\partial u}\right|_{\text{right end of } (e-1)\text{-th element}} = \left.\frac{1}{\Delta x^e}\frac{\partial y^e}{\partial u}\right|_{\text{left end of } e\text{-th element}}, \text{ for } e = 2,..., NE$$

(CC-1)

Part III - Orthogonal Collocation

The orthogonal collocation method is applied at each interior collocation point with the *e-th* element. The number of collocation point per element is **NP**, inclusive of u = 0 and u = 1. As the last collocation point of the *(e-1)-th* element is equivalent to the first collocation point of the *e-th* element, the total number of collocation point is **(NP – 1)*NE – 1**. See Figure B-1 for example calculation.

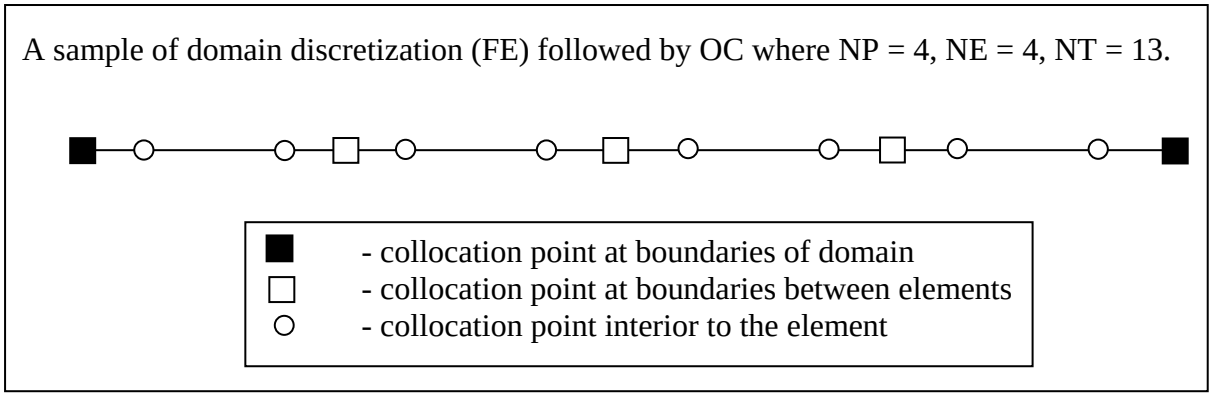

Figure B-1 Example calculation for the domain discretization process.

Introducing the following expressions,

$$\frac{\partial y^e}{\partial u}\left(u_J^e\right) = \sum_{I=1}^{NP} A_{J,I} y_I^e \qquad \textbf{(OC-1a)}$$

$$\frac{\partial^2 y^e}{\partial u^2}\left(u_J^e\right) = \sum_{I=1}^{NP} B_{J,I} y_I^e \qquad \textbf{(OC-1b)}$$

where A_{ji}, B_{ji} are the collocation matrices for first and second derivatives approximation, which are computed according to Villadsen and Michelsen (1979).

For *e-th* element, the residual at each *J-th* interior collocation point has the following form,

$$\frac{\partial y_J^e}{\partial \tau} = \frac{1}{G\left(y_J^e\right)}\left[\frac{s}{x^e + u\Delta x^e}\frac{1}{\Delta x^e}\sum_{I=1}^{NP} A_{J,I} y_I^e + \frac{1}{\left(\Delta x^e\right)^2}\sum_{I=1}^{NP} B_{J,I} y_I^e\right] \qquad \textbf{(E-9)}$$

where $J = 2,..., NP-1$ and $e = 1,..., NE$.

In addition, continuity of the function and first derivative between elements is transformed as well.

$$\frac{1}{\Delta x^{e-1}}\sum_{I=1}^{NP} A_{NP,I} y_I^{e-1} = \frac{1}{\Delta x^e}\sum_{I=1}^{NP} A_{1,I} y_I^e \text{ , for } e = 2,..., NE \qquad \textbf{(CC-2)}$$

The boundary conditions are as follow.

$$u = 0, \quad \frac{1}{\Delta x^{e=1}} \sum_{I=1}^{NP} A_{1,I} y_I^{e=1} = 0 \ \ (e = 1) \qquad \textbf{(BC-4a)}$$

$$u = 1, \quad \frac{1}{\Delta x^{e}} \sum_{I=1}^{NP} A_{NP,I} y_I^{e=NE} = Bi\left(y_b - y_{NP}^{e=NE}\right) \ (e = NE) \qquad \textbf{(BC-4b)}$$

Part IV - 'Finite-Volume' Problem

Additional constraints are imposed on the computation if the adsorption occurs in reservoir of finite volume, and therefore the solute concentration in the surrounding fluid is allowed to change with time (i.e. the total solute amount is constant). Simple mass balance shows the total loss of solute in the reservoir fluid equals to the product of the solute flux at the exterior surface of the adsorbent particle and the area of the exterior surface. The total number of adsorbent particles present in the reservoir is calculated as followed:

$$N_p = \frac{\left(\frac{m_p}{\rho_p}\right)}{\frac{4}{3}\pi R^3} \qquad \textbf{(E-10)}$$

where m_p and ρ_p are the total dry mass of the particles present and particle (swollen) wet density respectively. The latter could be calculated as follow.

$$(\rho_p = (1 - \varepsilon)\rho_s + \varepsilon\rho_f) \qquad \textbf{(E-11)}$$

The total loss of solute from the reservoir to the particles is therefore the product of the exterior particle surface area and the flux of solute **(E-2)**, multiplied by the total number of particles **(E-10)**. D_e represents the effective solute diffusivity across the particle, which could be replaced with εD_p if only the pore diffusion mechanism is

considered. The additional differential equation to be solved for is as follow, where c_b denotes the solute concentration in the surrounding fluid.

$$V\frac{\partial c_b}{\partial t} = -N_p\left(4\pi R^2\right)\left(\varepsilon D_p\right)\frac{\partial c(R,t)}{\partial r} = -\frac{3}{R}\left(\varepsilon D_p\right)\frac{\partial c(R,t)}{\partial r} \qquad \textbf{(E-12a)}$$

or, $$V\frac{\partial c_b}{\partial t} = -\frac{\left(s+1\right)}{R}\left(\varepsilon D_p\right)\frac{\partial c(R,t)}{\partial r} \qquad \textbf{(E-12b)}$$

which is generalized for arbitrary geometry.

The IC for **(E-12)** is as follow.

$$t = 0, \quad c_b = c_0 \qquad \textbf{(IC-3)}$$

To enforce consistency in usage of symbols for variables used in the previous and current section, both c and c_b are normalized to same reference concentration, i.e. the initial bulk solute concentration, c_0 (or c_{b0}).

The equation **(E-12b)** could be non-dimensionalized as follow,

$$\frac{\partial y_b}{\partial \tau} = -\left(s+1\right)K\,\frac{\partial y(1,\tau)}{\partial x} \text{ where } K = \frac{1}{V}\left(\frac{m_p}{\rho_p}\right) \qquad \textbf{(E-13)}$$

by variable transformation **(TR-1a, TR-1b, TR-1d, TR-1e)**, and the IC becomes as follow.

$$\tau = 0, \quad y_b = \frac{c_0}{c_0} = 1 \qquad \textbf{(IC-4)}$$

Recall that the mass transfer at the particle-fluid interface assumes the following condition, i.e.

$$x = 1, \quad \frac{\partial y}{\partial x} = Bi\left(y_b - y\right) \qquad \textbf{(BC-2b)}$$

which could be rearranged into the following expression.

$$\frac{\partial y(1,\tau)}{\partial x} = Bi\left(y_b(\tau) - y(1,\tau)\right). \qquad \textbf{(E-14)}$$

The last differential equation **(E-15)** is then obtained by substituting **(E-14)** into **(E-13)**.

$$\frac{\partial y_b}{\partial \tau} = -\frac{(s+1)}{V}\left(\frac{m_p}{\rho_p}\right) Bi\left(y_b(\tau) - y(1,\tau)\right) \qquad \textbf{(E-15)}$$

Part V - Computation Procedures

The discretized differential equations **(E-9)** in time domain are solved as initial-value problems (IVPs) with ODE Solver Suite, which is available in MATLAB®. A total of 8 elements (NE = 8), which consists of 5 collocation points (NP = 5) for each element, are used as default for domain discretization. The computation proceeds in two main steps. Firstly, the ODE solver guesses the y (or c) values at the interior collocation points with respect to time, that is (t,y_{guess}) (or (t,c_{guess})). Subsequently the user-provided smoothing routine is called to solve the matrix of algebraic equations **(M1)** which are assembled from the equations derived **(CC-2, BC-4a, BC-4b),** with the method of Gaussian elimination with Partial Pivoting. The computed values on the collocation points at boundaries between elements, as well as the values at the domain boundaries, will then be assembled along the whole spatial domain to yield a smooth, continuous curve (i.e. $c(t)$). The ODE solver then calculates the first derivative of the function and the residuals. The whole process is repeated if the total residual does not meet the error tolerance provided by user.

The suite of algebraic equations to be solved for is as follow.

$$e = 2,..., NE, \quad A_{NP,1} y_1^{e-1} + \left(A_{NP,NP} - \frac{\Delta x^{e-1}}{\Delta x^e} A_{1,1} \right) y_{NP}^{e-1} - \frac{\Delta x^{e-1}}{\Delta x^e} A_{1,NP} y_{NP}^{e}$$

$$= \frac{\Delta x^{e-1}}{\Delta x^e} \sum_{I=2}^{NP-1} A_{1,I} y_I^e - \sum_{I=2}^{NP-1} A_{NP,I} y_I^{e-1} \text{ where } y_{NP}^{e-1} = y_1^e . \quad \textbf{(AE-1a)}$$

$$e = 1, \quad A_{1,1} y_1^{e=1} + A_{1,NP} y_{NP}^{e=1} + 0 \cdot y_{NP}^{e=2} = -\sum_{I=2}^{NP-1} A_{1,I} y_I^{e=1} \quad \textbf{(AE-1b)}$$

$$e = NE, \quad 0 \cdot y_1^{e=NE-1} + \frac{H\left(y_{NP}^{e=NE}\right)}{\Delta x^e} A_{NP,1} y_{NP}^{e=NE-1} + \left(Bi + \frac{H\left(y_{NP}^{e=NE}\right)}{\Delta x^e} A_{NP,NP} \right) y_{NP}^{e=NE}$$

$$= Bi \cdot y_b - \frac{H\left(y_{NP}^{e=NE}\right)}{\Delta x^e} \sum_{I=2}^{NP-1} A_{NP,I} y_I^{e=NE} \quad \textbf{(AE-1c)}$$

where $y_{NP}^{e=NE-1} = y_1^{e=NE}$ **(AE-1d)**

The matrix of algebraic equations is then assembled as follow,

$$\text{i.e. } AA \cdot y_{bd} = B \quad \textbf{(M1)}$$

where $y_{bd} = \left[y_1^{e=1} \; y_{NP}^{e=1} \; y_{NP}^{e=2} \ldots y_{NP}^{e=NE-1} \; y_{NP}^{e=NE} \right]^T$ which is equivalent to $\left[y_1^{e=1} \; y_1^{e=2} \; y_1^{e=3} \ldots y_1^{e=NE} \; y_{NP}^{e=NE} \right]^T$. The matrix *AA* is sparse and tridiagonal, which lends great ease to computation. The y_{bd} (subscript *bd* denotes boundaries) could only be solved with iterative solver because the matrix *AA* as well as the *B* vector are functions of $y_{NP}^{e=NE}$.

Furthermore, the above algebraic equation **(AE-1)** is regrettably coupled to the differential equation **(E-16)** obtained from 'finite-volume' constraint, as the solute concentration in the bulk surrounding, *Y* (or $y_b(t)$) is required for calculating solute concentration in the pore fluid near the immediate particle surface. Both the bulk

concentration (Y) and the solute concentration in the pore fluid ($y(t)$) are then solved simultaneously during each iteration. The ODE solver computes both the solute time profile within the particle as well as that of reservoir over a predefined time interval $[t_1, t_n]$, by undergoing the following computation sequence.

1. The ODE solver will input a column of y trial into the subroutine *dydt* where the time derivatives at time t_1 will be calculated. Column y trial column consists of a series of guess for y at internal collocation points as well as the guess for the bulk fluid concentration, y_b, i.e.

   $$\left[y_2^{e=1}\ y_3^{e=1}\ \ldots y_{NP-1}^{e=1}\ y_2^{e=2}\ y_3^{e=2}\ \ldots y_{NP-1}^{e=2}\ \ldots y_2^{e=NE}\ y_3^{e=NE}\ \ldots y_{NP-1}^{e=NE}\ y_b\right]^T.$$

2. The subroutine *dydt* solves the $AA \cdot y_{bd} = B$ iteratively. The calculated y_{bd} is then used to calculate the time derivatives, and return the computed values to the ODE solver, i.e.

   $$\left[\frac{dy_2^{e=1}}{dt}\ \frac{dy_3^{e=1}}{dt}\ \ldots\ \frac{dy_{NP-1}^{e=1}}{dt}\ \frac{dy_2^{e=2}}{dt}\ \frac{dy_3^{e=2}}{dt}\ \ldots\ \frac{dy_{NP-1}^{e=2}}{dt}\ \ldots\ \frac{dy_2^{e=NE}}{dt}\ \frac{dy_3^{e=NE}}{dt}\ \ldots\ \frac{dy_{NP-1}^{e=NE}}{dt}\ \frac{dy_b}{dt}\right]^T.$$

3. The ODE solver calculates the errors between the calculated and expected values of time derivatives. If the errors fall below tolerance specified, the ODE solver then proceeds with new time t_2; otherwise, the ODE solver repeat step 1 abovementioned with new column of y trial, and adjusts the time step-size appropriately. This whole process repeats itself until the ODE solver finishes calculation for the whole time span $[t_1\ t_2\ \ldots t_n]$.

4. Once the ODE solver finishes the integration process over designated time interval, both the solute-uptake dynamic of the adsorbent and time-solute concentration profile of the reservoir are obtained, together with the radial-concentration profile within the particle.

As most of the adsorption isotherms data are reported in gravimetric unit q (mmole-solute/gram-adsorbent or mg-solute/gram-adsorbent) instead of volumetric unit c_μ, the uptake capacity q is calculated as follow.

$$q(t)\left(\frac{mmole-solute}{gram-adsorbent}\right)=\frac{V\left(c_0-c_0 y_b(t)\right)}{m_p} \qquad \textbf{(E-17)}$$

Part VI - Modeling

For 2-p model

To determine the D_p and k_f from the adsorption kinetic data, a nonlinear least-squares regression is required. For each experiment, the experimental data $(t,\ c)_{expt}$ is first normalized to yield $(\tau,\ y)_{expt}$, a nonlinear solver is then used to compute the $(\tau,\ y)_{model}$ via a code developed based on the OCFE formulation herein. The sum of squared errors (SS) between $(\tau,\ y)_{expt}$ and $(\tau,\ y)_{model}$ is computed and minimized till a optimum set of parameters ($D_p,\ k_f$) is obtained, which yields SS that is smaller that the error threshold (1e-6). In this work, the solver *lsqnonlin* from the Optimization Toolbox of MATLAB® is used to carry out the data fitting.

For 1-p model

Similar procedures are followed except only D_p is optimized and the k_f or Bi are set at default values of 100 or 1000 respectively, or even larger, to neglect the contribution

of film-transfer resistance to the diffusion process. This is equivalent to changing the **(BC-1b)** to the following conditions.

$r = R, \quad c = c_b$ (negligible film mass-transfer resistance) **(BC-5a)**

or $x = 1, \quad y = y_b$ (in dimensionless form) **(BC-5b)**

Reference:

Do D.D. (1998) *Adsorption Analysis: Equilibria and Kinetics*, London: Imperial College Press.

Finlayson B.A. (1980) *Nonlinear Analysis in Chemical Engineering*. New York: McGraw-Hill.

Villadsen J., Michelsen M. (1978) *Solution of Differential Equation Models by Polynomial Approximation*. New Jersey: Prentice Hall.

List of Symbols

Latin letters

$A_{J,I}$	First derivative collocation matrix (-)
$B_{J,I}$	Second derivative collocation matrix (-)
Bi	Biot number for mass transfer through film (-)
b	Binding affinity as referred from Langmuirian model (L/mmole)
c	Solute concentration in pore fluid (mmole/L)
c_b	Solute concentration in surrounding bath fluid (mmole/L)
c_i	Initial solute concentration in pore fluid (mmole/L)
c_μ	Sorbate concentration in solid phase (mmole/L)
$c_{\mu s}$	Saturation sorbate concentration in solid phase (mmole/L)
$c_{\mu 0}$	Initial sorbate concentration in solid phase (mmole/L)
c_0	Reference concentration (mmole/L)
D_p	Pore diffusivity (cm^2/s)
J	Solute flux into each particle ($mmole/cm^2$-s)
k_f	Mass transfer coefficient through external film (cm/s)
m_p	Mass of sorbent (dry mass basis) (g)
N_p	Total number of adsorbent particles (-)
q	Adsorption capacity of adsorbent (mmole/g)
q_{max}	Maximum adsorption capacity as referred from Langmuirian model (mmole/g)
r	Radial position (cm)
R	Effective hydrodynamic radius (cm)
s	Particle shape factor (0 for slab, 1 for cylinder, 2 for sphere) (-)
SS	Sum of squared errors (-)
t	Time (s)
u	Discretized, non-dimensionalized radius (-)
V	Volume of surrounding bath fluid (cm^3)
x	Non-dimensionalized radius (-)
y	Non-dimensionalized solute concentration in pore fluid (-)
y_b	Non-dimensionalized solute concentration in surrounding bath fluid (-)
y_i	Non-dimensionalized initial solute concentration in pore fluid (-)

Greek letters

ε	Sorbent porosity (-)
Δ	Increment in variable (-)
ρ_f	Fluid density (g/cm^3)
ρ_p	Sorbent density (wet mass basis) (g/cm^3)
ρ_s	Sorbent skeletal density (dry mass basis) (g/cm^3)
T	Non-dimensionalized time (-)

Subscripts

b	Bulk phase (surrounding bath fluid)
expt	Experimental data
i	Initial state for pore-fluid concentration
I, J	Indices of collocation matrices
μ	Solid phase (adsorbent)
max	Maximum or saturation state
model	Model prediction
NE	Total number of elements
NP	Total number collocation points
p	Adsorbent particle
s	Saturation state
T	Transposed state
0	Initial state or reference state

Superscripts

e	*e*-th element
s	Exponent, corresponding to that of particle shape factor